NATURE OF QUASAR DISK-WIND

Suk Yee Yong

ORCID: 0000-0002-5204-2902

Submitted in total fulfillment of the requirements of the degree of Doctor of Philosophy

School of Physics
Faculty of Science
The University of Melbourne

January 2020

Abstract

The brightest persistent astrophysical sources in the universe are quasars, a group of active galactic nuclei (AGN) that appear star-like and radiate across all wavelengths. The emitted radiation is believed to be powered by a supermassive black hole at the core of a galaxy. Matter that falls into the black hole is being fed onto the accretion disk, heating up the disk in the process due to friction. A wind emanating from the accretion disk, or a disk-wind, appears ubiquitous in these objects and acts as one effective way to generate the spectral lines observed in the quasar's spectrum. The broad spectral lines, originating from the broad line region (BLR), show diverse properties, specifically in velocity shift, line width, and degree of asymmetry. Yet, the exact structure of the BLR has remained perplexing due to its small size, which means it is unresolved even with the current astronomical instrumentation. Thus, simulations are important. By developing a model of the BLR, an informative analysis of the line profiles allows us to explore some of the key questions about the BLR, emphasising the shape of spectral lines, the disk-wind BLR, and the orientation.

We simulate line profile modelling using a simple kinematical disk-wind model of the BLR with radiative transfer in the high velocity limit. The model provides a framework to explore the characteristics of the emission line profile induced by the different geometries and kinematics of the BLR, including the opening angle of the wind and the geometry of the line emitting region. The effect of orientation in these systems is also examined.

As a first step, we use the model to simulate a narrow outflowing disk-wind, which has been described in the literature. The primary objective is to determine whether the observed emission line properties are consistent with a narrow wind scenario. We find that the line profiles are more blueshifted for a narrow polar wind model as opposed to intermediate and equatorial models. When viewing at pole-on angles, the simulated emission lines show a narrower line width, which is asymmetric and more blueshifted than that viewed edge-on. The blueward shift of the line profile increases as the line-of-sight and wind intersect. The model is also able to recover a shorter time delay in the red or blue side of the line profiles, consistent with observational evidence in reverberation mapping studies.

The second part of the thesis considers the properties of broad absorption line quasars

(BALQs). These objects are rare and often display a blueward absorption trough relative to the emission line. One interpretation of the velocity offsets is the unification based on orientation, whereby a BAL is viewed within a constrained narrow wind angle. In order to test whether the BALQs and non-BALQs can be distinguished by their emission features, we conduct statistical tests and machine learning on the two populations. We find that their continuum and emission features are qualitatively similar, which contradicts the narrow disk-wind model in the geometric unification. Therefore, we propose a model of the disk-wind comprising a wide wind opening angle with multiple dense radial streams, where the BAL is detected when the line-of-sight crosses these streams.

These findings have lead us to the discovery of a novel orientation indicator of quasars in the ultraviolet-optical regime. We propose a simple yet robust angle-of-viewing probe using the correlation between the velocity shifts and line widths. Our idea is shown to be qualitatively consistent with other orientation proxies. We also perform a wide angle disk-wind simulation and successfully retrieve the predicted correlation with inclination.

In addition, we extend our model to estimate the bias in the virial black hole mass due to the scale factor f, which is related to the unknown nature of the BLR. Using a wide disk-wind configuration, we retrieve the f factors for a range of inclination angle. The f factor shows significant dependence with orientation, characterisation of the line width, and location of the emission region in the wind. Therefore, using a constant f value biases the estimation of the mass of the black hole.

Declaration

This is to certify that:

1. the thesis comprises only my original work towards the PhD except where indicated in the Preface,
2. due acknowledgement has been made in the text to all other material used,
3. the thesis is fewer than 100 000 words in length, exclusive of tables, maps, bibliographies, and appendices.

Suk Yee Yong

Preface

While the majority of the work presented in this thesis is that of the author, some sections are the result from collaborations. Any work that is not my own is cited appropriately in the text. Additional details are outlined below.

Chapter 1 presents a review of the active galactic nuclei, which is entirely the work of the author. References are cited in the text.

Chapter 2 presents a review of the observational properties of spectral lines in the broad line region. The work is based on the following publication, which is entirely the work of the author. References are cited in the text.

- Yong, S. Y., King, A. L., Webster, R. L., Bate, N. F., O'Dowd, M. J., & Labrie, K. (2018). Using the Properties of Broad Absorption Line Quasars to Illuminate Quasar Structure. *MNRAS*, 479, 4153–4171. ADS: 2018MNRAS.479.4153Y. doi: 10.1093/mnras/sty1540, Section 1

Chapter 3 presents a kinematical disk-wind modelling of the broad line region. The work is based on the following publications, under the supervision of Rachel Webster and Anthea King with comments and suggestions from Nicholas Bate, Kathleen Labrie, and Matthew O'Dowd.

- Yong, S. Y., Webster, R. L., & King, A. L. (2016). Black Hole Mass Estimation: How Good is the Virial Estimate? *PASA*, 33, e009. ADS: 2016PASA...33....9Y. doi: 10.1017/pasa.2016.8, Section 2.1
- Yong, S. Y., Webster, R. L., King, A. L., Bate, N. F., O'Dowd, M. J., & Labrie, K. (2017). The Kinematics of Quasar Broad Emission Line Regions Using a Disk-Wind Model. *PASA*, 34, e042. ADS: 2017PASA...34...42Y. doi: 10.1017/pasa.2017.37, Section 1 and Section 2

Chapter 4 presents analyses of the emission line properties using a kinematical disk-wind model with narrow opening angle. The work is based on the following publication, under the supervision of Rachel Webster and Anthea King with comments and suggestions from Nicholas Bate, Kathleen Labrie, and Matthew O'Dowd.

- Yong, S. Y., Webster, R. L., King, A. L., Bate, N. F., O'Dowd, M. J., & Labrie, K. (2017). The Kinematics of Quasar Broad Emission Line Regions Using a Disk-Wind Model. *PASA*, 34, e042. ADS: 2017PASA...34...42Y. doi: 10.1017/pasa.2017.37

Chapter 5 presents analyses of emission properties in broad absorption line quasars. The work is based on the following publication, under the supervision of Anthea King and Rachel Webster with comments and suggestions from Nicholas Bate, Kathleen Labrie, and Matthew O'Dowd.

- Yong, S. Y., King, A. L., Webster, R. L., Bate, N. F., O'Dowd, M. J., & Labrie, K. (2018). Using the Properties of Broad Absorption Line Quasars to Illuminate Quasar Structure. *MNRAS*, 479, 4153–4171. ADS: 2018MNRAS.479.4153Y. doi: 10.1093/mnras/sty1540

Chapter 6 presents analyses of novel and various orientation indicators of quasars. The work is based on the following publication, under the supervision of Rachel Webster and Anthea King with comments and suggestions from Nicholas Bate, Kathleen Labrie, and Matthew O'Dowd.

- Yong, S. Y., Webster, R. L., King, A. L., Bate, N. F., Labrie, K., & O'Dowd, M. J. (2020). Determining quasar orientation. *MNRAS*, 491(1), 1320–1334. ADS: 2020MNRAS.491.1320Y. doi: 10.1093/mnras/stz3074

Chapter 7 presents analyses of the bias in black hole mass estimation. The work is based on the following publications, under the supervision of Rachel Webster and Anthea King.

- Yong, S. Y., Webster, R. L., & King, A. L. (2016). Black Hole Mass Estimation: How Good is the Virial Estimate? *PASA*, 33, e009. ADS: 2016PASA...33....9Y. doi: 10.1017/pasa.2016.8
- Yong, S. Y. & Webster, R. L. (2019). Black hole mass estimation: Modelling the biases. In *2019 6th International Conference on Space Science and Communication (IconSpace)* (pp. 139–143). doi: 10.1109/IconSpace.2019.8905923

Chapter 8 summarises the findings presented in the thesis, which is entirely the work of the author.

Acknowledgements

The accomplishment of this thesis would have been impossible to achieve without the help from various individuals.

First and foremost, an utmost gratitude to my supervisor, Rachel Webster, for her continuous encouragement, guidance, and inspiration. Her vast insight has enriched my understanding, not only in astronomy, but also in life skills. I will always be grateful to her for offering me this opportunity.

A heartfelt thanks to my co-supervisor, Anthea King, for being a great mentor and always being accommodating when I randomly dropped by her office asking questions. Many thanks to my collaborators, Nick Bate, Kathleen Labrie, and Matt O'Dowd, for the enlightening discussions during our weekly teleconference.

A big thanks to my PhD review panels, Andrew Melatos and Ann Robert, for providing invaluable advice over our occasional conversations.

Thanks also to the people from the astrophysics group at the University of Melbourne for creating a welcoming and learning environment.

Finally, a special thanks to my family for being caring and believing in me throughout the years. This journey would not have been accomplishable without their unfaltering support.

This research has made use of the VizieR catalogue access tool, CDS, Strasbourg, France. The original description of the VizieR service was published in Ochsenbein et al. (2000). This research made use of the Python libraries including open source packages such as `astropy` (Astropy Collaboration et al. 2013), `ipython` (Pérez & Granger 2007), `matplotlib` (Hunter 2007), `numpy` (van der Walt et al. 2011), `pandas` (McKinney 2010), `scikit-learn` (Pedregosa et al. 2011), and `scipy` (Jones et al. 2001).

Table of Contents

List of Figures

List of Tables

List of Acronyms

Abbreviations

AGN	**A**ctive **g**alactic **n**uclei
BAL	**B**road **a**bsorption **l**ine
BALQ	**B**road **a**bsorption **l**ine **q**uasar
BEL	**B**road **e**mission **l**ine
BH	**B**lack **h**ole
BI	**B**alnicity **i**ndex
BL Lac	**BL Lac**ertae
BLR	**B**road **l**ine **r**egion
BLRG	**B**road **l**ine **r**adio **g**alaxy
CSS	**C**ompact **s**teep **s**pectrum
DPEL	**D**ouble-**p**eaked **e**mission **l**ine
DR	**D**ata **R**elease
E1	**E**igenvector **1**
EW	**E**quivalent **w**idth
FeLoBAL	Iron (**Fe**) **lo**w-ionisation **b**road **a**bsorption **l**ine
FR	**F**anaroff-**R**iley
FSRLQ	**F**lat-**s**pectrum **r**adio-**l**oud **q**uasar
FWHM	**F**ull **w**idth at **h**alf **m**aximum
GPS	**G**igahertz-**p**eaked **s**pectrum
HERG	**H**igh-**e**xcitation **r**adio **g**alaxy
HiBAL	**H**igh-**i**onisation **b**road **a**bsorption **l**ine
HIL	**H**igh-**i**onisation **l**ine
HWHM	**H**alf **w**idth at **h**alf **m**aximum
LERG	**L**ow-**e**xcitation **r**adio **g**alaxy
LIL	**L**ow-**i**onisation **l**ine
LINER	**L**ow-**i**onisation **n**uclear **e**mission line **r**egion

LoBAL	**Lo**w-ionisation **b**road **a**bsorption **l**ine
ML	**M**achine **l**earning
NAL	**N**arrow **a**bsorption **l**ine
NEL	**N**arrow **e**mission **l**ine
NLR	**N**arrow **l**ine **r**egion
NLRG	**N**arrow **l**ine **r**adio **g**alaxy
OVV	**O**ptically **v**iolently **v**ariable
QSO	**Q**uasi-**s**tellar **o**bject
RL	**R**adio-**l**oud
RM	**R**everberation **m**apping
RQ	**R**adio-**q**uiet
SDSS	**S**loan **D**igital **S**ky **S**urvey
SED	**S**pectral **e**nergy **d**istribution
SSRLQ	**S**teep-**s**pectrum **r**adio-**l**oud **q**uasar
UFOs	**U**ltra-**f**ast **o**utflow**s**
USS	**U**ltra-**s**teep **s**pectrum
UV	**U**ltra**v**iolet
WA	**W**arm **a**bsorber

Physical Constants

c	Speed of light	$2.998 \times 10^{8}\,\mathrm{m\,s^{-1}}$
G	Gravitational constant	$6.674 \times 10^{-11}\,\mathrm{m^{3}\,kg^{-1}\,s^{-2}}$
k_{B}	Boltzmann constant	$1.381 \times 10^{-16}\,\mathrm{erg\,K^{-1}}$
m_{e}	Electron mass	$9.109 \times 10^{-31}\,\mathrm{kg}$
m_{p}	Proton mass	$1.673 \times 10^{-27}\,\mathrm{kg}$
$M_{\odot}$	Solar mass	$1.989 \times 10^{30}\,\mathrm{kg}$
pc	Parsec	$3.086 \times 10^{18}\,\mathrm{cm}$
σ_{T}	Thomson scattering cross section	$6.652 \times 10^{-25}\,\mathrm{cm^{2}}$

CHAPTER 1

Active Galactic Nuclei (AGN)

1.1 Background

The quest to search for a unified model of active galactic nuclei (AGN) has been a perpetual theme of interest since AGN were first discovered. As the name suggests, an AGN is distinct from a normal galaxy in that it harbours an active nucleus in the centre. An AGN appears star-like and emits tremendous radiation over a wide range of the electromagnetic spectrum at wavelengths from gamma-rays up to radio waves. The brightest persistent sources belong to one of the AGN classes known as quasars. Quasars are observable up to redshifts of $z \sim 7$, with the two highest found so far: ULAS J1120+0641 at $z = 7.09$ (Mortlock et al. 2011) and more recently ULAS J134208.10+092838.61 at $z = 7.54$ (Bañados et al. 2018), which entitles it to be the highest redshift quasar known. Hence, they are among the most distant objects and reveal insight into the early stages of the universe.

1.2 Structure of AGN

An AGN is often depicted as axisymmetric with the following components: black hole (BH), accretion disk, broad line region (BLR), dusty torus, narrow line region (NLR), and sometimes a radio/optical jet. This model is known as the unified scheme of AGN and a classical example of this is illustrated in Fig. 1.1. Looking at the picture, it is clear that the observable emission relies on the direction from which the AGN is observed. This gives rise to the distinct observed characteristics of AGN, which are the basis for orientation-based unification schemes. In essence, it is possible to discern the type of AGN from the viewing angle. Further discussion on this topic is found in § 1.3.

In the core of AGN lies the supermassive BH, encircled by a flattened accretion disk. Within close proximity to the central active BH of $\sim 0.01\,\mathrm{pc}$, the BLR is found.

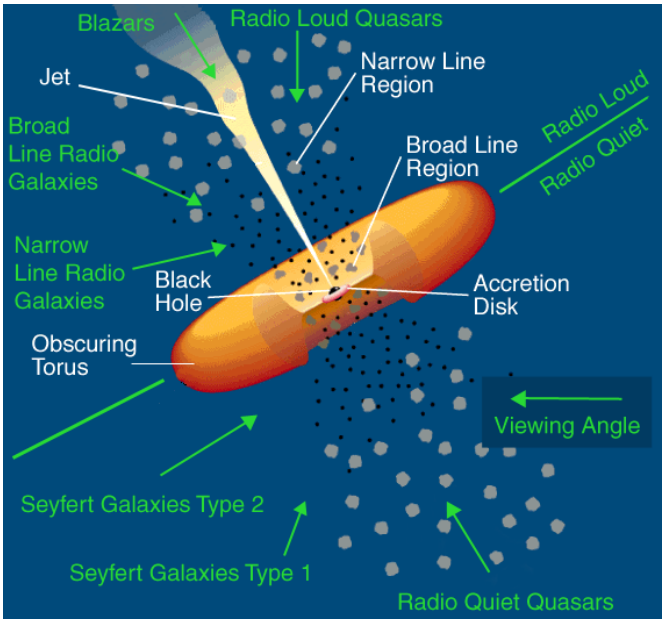

Figure 1.1: A schematic structure of AGN. The main components are stated in white and the AGN classes by orientation are stated in green. Image credit: Urry & Padovani (1995).

The BLR in Fig. 1.1, which is depicted as an ensemble of clouds, is one out of the many possible BLR models. In general, the models can be classified into two major groups, namely the cloud and the disk wind models. The area beyond the accretion disk and BLR, between $\sim 0.1\,\mathrm{pc}$ and $\sim 10\,\mathrm{pc}$ with respect to the BH, is surrounded by the torus. At a greater distance of $\sim 100\,\mathrm{pc}$ from the source centre, there exists the NLR. In some instances, either a one-sided or biconical relativistic radio jet is launched from the vicinity of the central BH along the BH axis of rotation. Estimates of their distances relative to the centre of BH are presented in Fig. 1.2.

1.2.1 Black Hole (BH) Paradigm

It is a long-held belief that a supermassive BH dwells in the centre of AGN's host galaxy. The accretion of matter onto the BH acts as an immense energy powerhouse of AGN. As the BH continues to accrete matter, a flattened structure, an accretion disk, is formed around the BH orbiting with Keplerian orbital velocities of

$$v_{\mathrm{K}} = \sqrt{\frac{GM_{\mathrm{BH}}}{r}}, \tag{1.1}$$

where G is the gravitational constant, M_{BH} is the mass of the BH, and r is the radius of the orbit.

The first observational evidence of the existence of accretion disk in AGN is the big blue bump (BBB) feature (Malkan & Sargent 1982). The BBB is an excess flux in

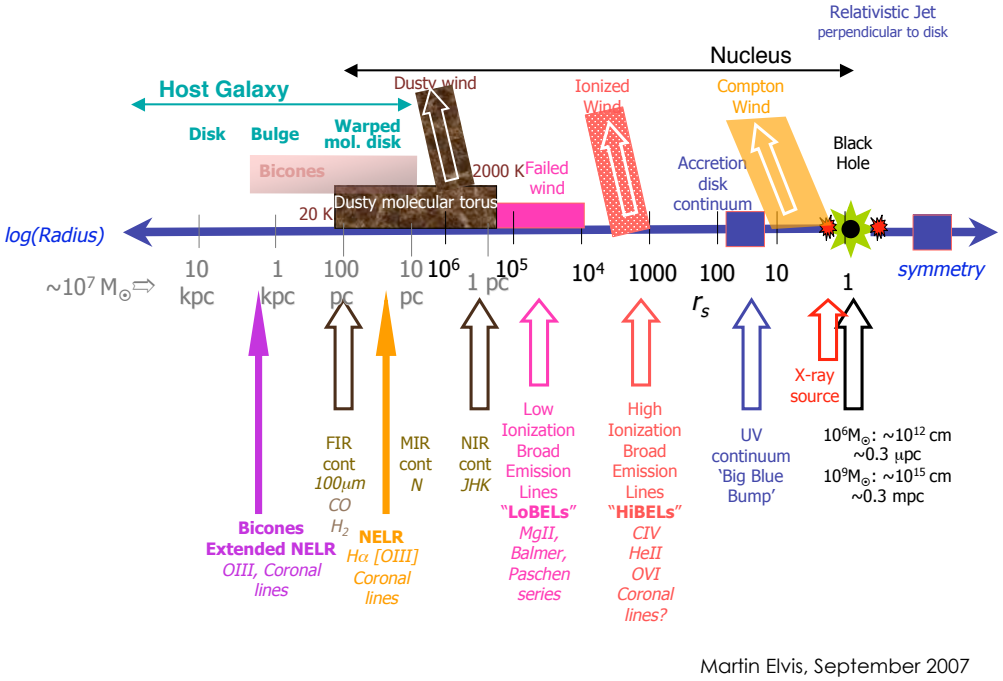

Figure 1.2: Components of AGN and their relative sizes from the centre of the ionising source. Image credit: http://hea-www.harvard.edu/~elvis/QuasarScales.pdf.

the continuum towards the ultraviolet (UV) domain of a spectrum and spectral energy distributions (SEDs) of AGN. As a result, AGN appears like a blue star in an optical image. It is speculated that the BBB is caused by the thermal emission of the gas from the accretion disk (Shields 1978; Malkan & Sargent 1982). However, simple modelling of an accretion disk does not match the observed UV/optical continuum (see review by e.g., Koratkar & Blaes 1999).

The local emission from the accretion disk is assumed to be emitted as a perfect blackbody. According to the conservation of energy, a conversion of gravitational potential energy of the infalling gas to electromagnetic radiation is required. The material in the disk spirals inward towards the rotating BH due to gravity and is converted to energy at a mass accretion rate of $\dot{M}$ with efficiency factor, η. The observed luminosity, L, is linked to $\dot{M}$ and η by

$$L = \eta \dot{M} c^2, \tag{1.2}$$

where c is the speed of light.

Owing to the conservation of angular momentum, the angular momentum gained has to be counterbalanced by the transfer of angular momentum outwards from the centre of the BH. During this process, the temperature rises as heat is dissipated through viscous forces. This removes the angular momentum of inflowing gas and causes the release of thermal radiation. When the gravitational and radiation pressure forces are at equilibrium, the maximum luminosity is achieved. When this condition is achieved for

spherical accretion, it is called the Eddington luminosity, which is expressed as

$$L_{\rm Edd} = \frac{4\pi G M m_{\rm p} c}{\sigma_{\rm T}}, \tag{1.3}$$

where M is the mass of the object, $m_{\rm p}$ is the mass of proton, and $\sigma_{\rm T}$ is the Thomson scattering cross section.

From Eq. (1.2) and Eq. (1.3), the infall mass accretion rate in the Eddington limit is then

$$\dot{M}_{\rm Edd} = \frac{L_{\rm Edd}}{\eta c^2} \simeq 2.22 M_8 \left(\frac{\eta}{0.1}\right)^{-1} M_\odot\,{\rm yr}^{-1}, \tag{1.4}$$

where M_8 is the BH mass in units of $10^8\,M_\odot$, and $M_\odot$ is solar mass. In a simple case where the infalling plasma with opacity of ionised hydrogen is assumed, the Eddington luminosity is estimated to be $L_{\rm Edd} \simeq 1.26 \times 10^{38}\,(M/M_\odot)\,{\rm erg\,s^{-1}}$.

In certain cases, the formation of a highly energetic collimated jet is ejected along the rotation axis and orthogonal to the plane of the disk. The cause of this phenomenon might be that the excess gravitational energy in the inflowing gas is converted to outflowing kinetic energy, which is manifested in the form of radio jet. It is assumed that the source of jet emission is mainly synchrotron radiation. The structure and the viewing angle to the jet have also influenced AGN classification by radio morphology (see § 1.3).

1.2.2 Broad Line Region (BLR)

As the BLR is close to the central BH, it is the best probe to understand the driving mechanisms of AGN. Although the BLR is spatially unresolved including in the nearest AGN, valuable information is attainable through observational studies of the continuum and emission lines. The BLR size measured from the BH is approximately ~ 0.01–$1.0\,{\rm pc}$ (Beckmann & Shrader 2012). This region is mostly occupied by photoionised gas with large hydrogen column density of $N_{\rm H} \sim 10^{23}\,{\rm cm^{-2}}$ (Netzer 2013). The fraction of the sky as viewed from the central ionising source that is covered by the line-emitting gas or the covering factor can be estimated from the strength of the emission lines, described by the equivalent width (EW). The covering factor of the BLR is around 10% (Peterson 2006).

The BLR consists of high velocity hot gases. Only permitted and semi-forbidden broad lines are emitted from the BLR. The absence of broad forbidden lines implies that these lines are collisionally de-excited so the density in this region is extremely high. In particular, the electron density, $n_{\rm e}$, is sufficiently high compared to the critical densities, $n_{\rm c}$, of every forbidden transition. The notation for semi-forbidden ions ends with a single square bracket, for example C III]. Forbidden ions are designated with

square brackets at both ends, for example [O III].

The BLR electron density can be constrained by the forbidden [O III] λ5007 and semi-forbidden C III] λ1909 lines. Given that $n_{\mathrm{c,[O\,III]}} \approx 10^6\,\mathrm{cm^{-3}}$ and $n_{\mathrm{c,C\,III]}} \approx 10^{10}\,\mathrm{cm^{-3}}$, the lower and upper limits of the electron density are between $10^8\,\mathrm{cm^{-3}}$ and $10^{10}\,\mathrm{cm^{-3}}$, respectively. A rough estimate of the electron density in the BLR is taken to be $n_\mathrm{e} \approx 10^9\,\mathrm{cm^{-3}}$ (Osterbrock 1989).

The broad emission lines (BELs) originated in the BLR have line widths measured by the full width at half maximum (FWHM) of more than $10^3\,\mathrm{km\,s^{-1}}$ and extending to $> 10^4\,\mathrm{km\,s^{-1}}$. A typical BEL width in FWHM is $\approx 5000\,\mathrm{km\,s^{-1}}$. There are similarities in the relative emission line strengths of AGN spectra and those seen in ionised gas regions, for example planetary nebulae and H II regions. This can be explained as these gases reach photoionisation equilibrium at similar temperature of $T \approx 10^4\,\mathrm{K}$, which occurs when the rate of photoionisation is equivalent to the rate of recombination. For $T \approx 10^4\,\mathrm{K}$, the thermal line width or line-of-sight velocity dispersion is about $v_\mathrm{th} \approx 10\,\mathrm{km\,s^{-1}}$ using

$$v_\mathrm{th} \approx \sqrt{\frac{k_\mathrm{B}T}{m_\mathrm{p}}}, \tag{1.5}$$

where k_B is the Boltzmann constant.

Assuming that the width of the line is purely broadened by thermal motions, a typical BEL width of FWHM$\approx 5000\,\mathrm{km\,s^{-1}}$ corresponds to $T \gtrsim 10^9\,\mathrm{km\,s^{-1}}$. This value is substantially higher than the expected temperature from photoionisation equilibrium. In order to explain this discrepancy, it is evident that another broadening process is necessary. This mechanism is usually interpreted as the Doppler shifts from bulk motions of the gas in the BLR (Peterson 1997). Line profiles that have large Doppler widths may signify that they emerged from a deep gravitational potential region, such that the velocity is dominated by Keplerian motion.

Although numerous studies on the BLR have shown great progress, inferring the true structure, kinematics, and dynamics of the BLR continues to be elusive. The BLR tends to be complex and displays a wide variation of observational features for different sources. One of the principal objectives in this thesis is to investigate the nature of this line-emitting gas region, which will be further elaborated in the next chapter.

1.2.3 Dusty Torus

A toroidal shaped circumnuclear medium or torus with size of a few parsecs envelopes the area beyond the BLR and accretion disk. The range of gas density is within $n_\mathrm{e} \sim 10^4$–$10^7\,\mathrm{cm^{-3}}$ with a large variation in column density (Netzer 2013). The high opacity and optically thick torus blocks almost all wavelengths apart from the infrared

wavelengths. In the optical and UV regimes, the direct emission arising from the BLR and disk is fully hidden by the intervening material in the torus when viewed from certain directions. This leads to the unique observational properties of AGN spectra. In particular, the torus plays a vital role in the classical orientation-based unification scheme. The differences in AGN classes are essentially due to the anisotropic obscuration of the nucleus (see § 1.3). The separation between type 1 and type 2 AGN depends on whether the line-of-sight is unobstructed by the torus such that the BEL is visible.

The torus is mainly composed of dust, hot ionised gas, and warm molecular gas. There are several suggestions on the density distribution of the dust in the torus, whether it is homogeneously smooth (Pier & Krolik 1992, 1993), clumpy (Krolik & Begelman 1988; Nenkova et al. 2002, 2008; Elitzur & Shlosman 2006; Tristram et al. 2007), or a mixture of both (Stalevski et al. 2012; Assef et al. 2013). Though the exact structure of the torus remains unclear, the current favoured model is a clumpy torus. It was first proposed by Krolik & Begelman (1988) that the dust in this region was distributed in optically and geometrically thick clouds or clumps. In this case, the dust temperature and the distance are not linearly dependent. There is a vast variation in the dust temperature for a given distance from the centre of ionising source, and thus some disk emissions are still able to penetrate through.

A plausible signature of the dusty torus is the prominent silicate dust features of the SED (Jaffe et al. 2004; Siebenmorgen et al. 2005; Hao et al. 2005; Sturm et al. 2005). Type 2 AGN or edge-on objects exhibit silicate dust in absorption, while type 1 AGN or face-on objects display suppression of silicate dust in emission. Early radiative transfer simulations of the torus modelled using smooth uniform dust distributions are unable to accurately reproduce the silicate features, which yield excess silicate emission in face-on sources (Pier & Krolik 1992, 1993).

Subsequently, the clumpy torus geometry was first modelled by Nenkova et al. (2002) using one-dimensional radiative transfer code. They demonstrated that the clumpy medium is able to weaken the 10 μm silicate emission in the SED of type 1 AGN. However, it is argued that the model relies on the input parameters instead of the dust distribution as the silicate features in smooth and clumpy models are similar (Dullemond & van Bemmel 2005; Stalevski et al. 2012). In order to better comprehend the role of torus in the unification scheme, there has been advancement on the development of radiative transfer codes of higher dimensions with more realistic assumptions (Dullemond & van Bemmel 2005; Hönig et al. 2006; Schartmann et al. 2008; Stalevski et al. 2012).

1.2.4 Narrow Line Region (NLR)

The uniqueness of the NLR is that it is the only spatially resolved AGN emission component in the optical and UV regimes. This makes the NLR spectrum among the most studied observational characteristic in AGN. The physical conditions in the NLR

differ from the BLR. The size of the NLR is $\sim 10^2$–10^4 pc, which is several orders of magnitude larger than the size of the BLR (Beckmann & Shrader 2012). The gas in this region has low column density of $N_{\rm H} \sim 10^{20-21}\,{\rm cm}^{-2}$ and small covering factor of about a few percentage (Netzer 2013).

The lines emitted from this region are narrow with FWHM$< 1000\,{\rm km\,s}^{-1}$. These lines are identified as the narrow emission lines (NELs). A typical NEL has line width of FWHM$\sim$ 400–500 $\rm km\,s^{-1}$, about ten times smaller than that of BEL. In addition to permitted and semi-forbidden lines, the appearance of forbidden lines, such as [O II], [O III], and [N II], implies a low density environment in the NLR. The electron gas density is typically around the range of $n_{\rm e} \sim 10^3$–$10^5\,{\rm cm}^{-3}$ (Beckmann & Shrader 2012). This indicates a cooler and slower moving gas residing in the NLR.

The model of the obscuring torus is further supported by the discovery of conical or biconical structures along the jet axis in the extended NLR of type 2 AGN (e.g., Pogge 1989; Tadhunter & Tsvetanov 1989). The far-side cone might not be detectable because of geometric and projection effects. It is suggested that this ionisation cone is due to the anisotropic ionising continuum being shadowed by the obscuring material from the torus. The opening angle of the ionisation cone ranges between $\sim 30^\circ$ and $\sim 110^\circ$ with linear size of 15 pc to 18 kpc scale (Wilson & Tsvetanov 1994). The flux ratio of [O III] λ5007 to Hα in the interior of the cone is larger than unity, implying that the inner part is filled with low density gas ionised by the continuum. This ratio is smaller within the exterior of the cone, which means that the ionisation process of the gas is dominated by starlight.

It has been shown that stratification also occurs in the NLR. There is a proportional relationship between the average velocity dispersion and ionisation parameter of the forbidden lines (Dasyra et al. 2011). This is in agreement with the decreasing ionisation states of the lines further from the centre of the BH, similar to the stratification of the BLR.

1.3 Unification and Taxonomy of AGN

Since the discovery of AGN, there have been many studies to understand a multitude of aspects of these objects. With the emergence of assorted AGN types and their distinct phenomena, attempts to unify them have always been a prevailing aim (e.g., Antonucci 1993; Urry & Padovani 1995). Numerous terminologies are also imposed to describe the different AGN. It is most likely that even the latest comprehensive compilation of the AGN zoo in Padovani et al. (2017, Table 1) is incomplete and there are AGN subgroups yet to be identified. Some of these will be addressed in the following subsections.

1.3.1 Unifying AGN

The unified model of AGN governed by orientation is not particularly a new idea (Antonucci 1993; Urry & Padovani 1995). The diversity of the observational characteristics in AGN spectra have invoked various classification systems. In past years, this framework has been improvised, which inevitably leads to the increasing complexity (see reviews by e.g., Netzer 2015; Padovani et al. 2017). The main classification schemes, including those which are traditional and recently established, will be described next.

1.3.1.1 Radio-loud versus Radio-quiet

AGN can be categorised into two groups, radio-loud (RL) or radio-quiet (RQ), depending on their radio loudness. Classically, the definition of radio loudness is assessed using the radio luminosity at frequency of 5 GHz ($L_{5\,\mathrm{GHz}}$; e.g., Peacock et al. 1986; Miller et al. 1990) and the radio-to-optical flux density ratio (R; e.g., Schmidt 1970; Kellermann et al. 1989). Radio objects with $L_{5\,\mathrm{GHz}} < 10^{24}\,\mathrm{W\,Hz^{-1}\,sr^{-1}}$ (or $\sim 10^{31}\,\mathrm{erg\,s^{-1}\,Hz^{-1}}$) and $R \lesssim 10$ are RQ, while $L_{5\,\mathrm{GHz}} > 10^{25}\,\mathrm{W\,Hz^{-1}\,sr^{-1}}$ (or $\sim 10^{32}\,\mathrm{erg\,s^{-1}\,Hz^{-1}}$) and $R > 10$ are RL.

So far, high energy gamma-ray signals have only been detected from RL AGN. There are a few candidates from RQ AGN, namely NGC 1068, NGC 4945 (Teng et al. 2011), ESO 323-G077, and NGC 6814 (Ackermann et al. 2012a), but none are convincing cases. NGC 1068 and NGC 4945, are both Seyfert 2 galaxies, and are speculated to be associated with starburst galaxies (Ackermann et al. 2012b), while ESO 323-G077 and NGC 6814 are possibly due to chance spatial coincidences (Ackermann et al. 2012a). This might imply that RQ AGN are actually gamma-ray quiet, rather than radio-quiet. Consequently, it has also been suggested that the RL vs. RQ dichotomy should be replaced by jetted vs. non-jetted, which is more descriptive of their differences (Padovani 2016, 2017). In this case, three characteristics are found to differentiate a jetted from non-jetted AGN: (i) presence of highly relativistic jets, (ii) strong gamma-ray emission of $\gtrsim 1\,\mathrm{MeV}$, and (iii) excess radio emission in the far-infrared and radio relationships.

RL objects show radio jets and comprise around 10–20% of the AGN population (e.g., Kellermann & Pauliny-Toth 1966; Katgert et al. 1973; Fanti et al. 1977; Smith & Wright 1980; Sramek & Weedman 1980; Strittmatter et al. 1980; Miller et al. 1990; Stern et al. 2000; Ivezić et al. 2002). Following the Fanaroff-Riley (FR; Fanaroff & Riley 1974) classification, the RL sources are separated according to the structure of the radio emission. Qualitatively, the sources are differentiated based on the ratio of the separation between the highest surface brightness regions on opposite sides of the central galaxy and the source coverage evaluated from the lowest brightness contour, and any compact component located on the central galaxy was disregarded. The ratio is < 0.5 for objects in FR class I (FR I), and otherwise for those in FR class II (FR

II). Additionally, FR I are low luminosity sources, and hence have lower radio power compared to FR II. FR I sources are edge-darkened or core-brightened, meaning the brightness diminishes the farther away from the galaxy centre. In contrast, FR II sources are edge-brightened with brighter extended radio emission region surrounding the lobe. A third class, FR 0, has also been proposed to accommodate radio galaxies that match the radio characteristics of FR I, but show a factor of ~ 30 more core-domination and lack pronounced extended radio emission (Baldi et al. 2015). Examples of FR I, FR II, and FR 0 objects are portrayed Fig. 1.3.

Nevertheless, it is noticed that the FR morphological class is incomplete and

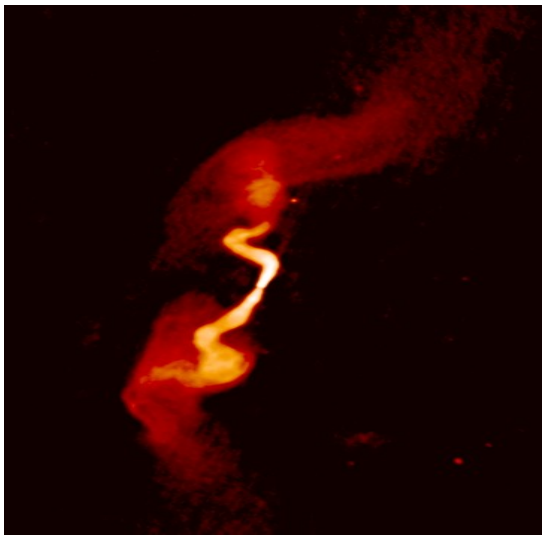

(a) Radio galaxy 3C 31 (NGC 3833) at 1.4 GHz in FR I class

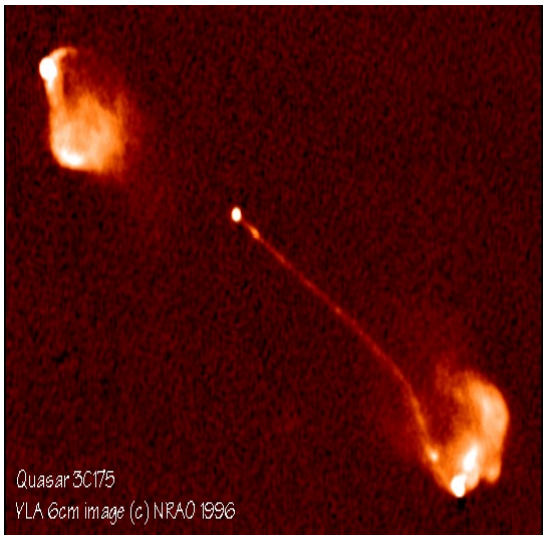

(b) Radio quasar 3C 175 at 5.0 GHz in FR II class

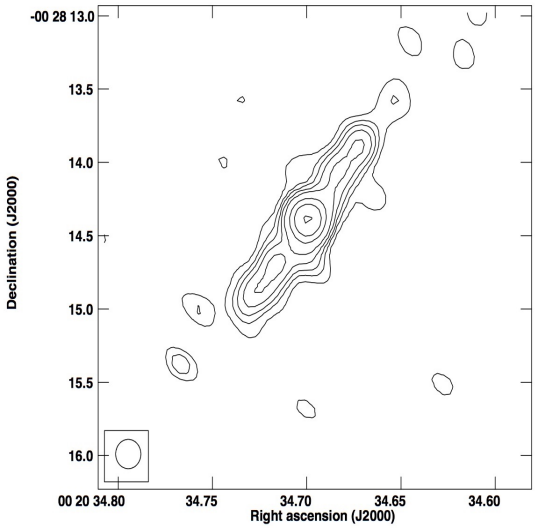

(c) Radio source ID 547 at 7.5 GHz in FR 0 class

Figure 1.3: Map of radio sources in each FR class. Images credit for subfigures: (a), (b) NRAO/AUI, and (c) Baldi et al. (2015).

unable to entirely segregate the diversity of all RL AGN (Hine & Longair 1979). Another criterion based on the excitation level of emission lines in the optical spectra of RL AGN has also been adopted (Hine & Longair 1979; Laing et al. 1994; Jackson & Rawlings 1997; Best & Heckman 2012). Those with high-excitation narrow lines are referred to as high-excitation radio galaxies (HERGs, also known as radiative-mode RL AGN), while those that have weak lines or lack of this feature are low-excitation radio galaxies (LERGs, also known as radio-mode or jet-mode RL AGN). They tend to have different accretion rates (e.g., Best & Heckman 2012; Russell et al. 2013; Mingo et al. 2014; Gürkan et al. 2014; Fernandes et al. 2015), with the former accretion in a radiatively efficient manner and the latter in a radiatively inefficient way (also see § 1.3.1.2). In addition, the host galaxies of HERGs are less massive and bluer compared to those of LERGs (e.g., Tasse et al. 2008; Hickox et al. 2009; Smolčić 2009; Best & Heckman 2012; Janssen et al. 2012). Indeed, there are considerable overlaps between the FR I/II and LERG/HERG criteria, but the relation is not one-to-one. Low and high luminosity radio sources that are commonly linked with FR I and II classes are mostly LERGs and HERGs respectively (Best & Heckman 2012). However, there are some FR II sources that are also LERGs (e.g., Laing et al. 1994).

1.3.1.2 Type 1 versus Type 2

In the AGN unification scheme, it is believed that the different classifications of AGN, such as Seyfert 1, Seyfert 2, quasar, and blazar, are based on the orientation of the AGN with respect to the line-of-sight of the observer (see Fig. 1.1). Generally, there are two orientation unified models, which differ from one another by their wavelength regimes. In the optical regime, the distinction between AGN of type 1 and type 2 is associated with the obscuring dusty torus. In the radio scheme, a combination of torus and jet determines the radio morphologies of quasars (see § 1.3.4). While the similarity in both situations is most likely the symmetry axis, they have disparate orientation dependences. The former is subjected to the composition and optical depth of the obscuring material, whereas the latter is affected by the beaming pattern. Essentially, these models might also depend on other physical parameters, e.g., BH mass and mass accretion rate.

Based on the width of the emission lines in an AGN spectrum at optical wavelength, AGN are divided into different types. The optical spectra of several groups of AGN are shown in Fig. 1.4. A normal galaxy spectrum is also provided for comparison. Both BELs and NELs are present in the spectrum of type 1 AGN, but type 2 has only NELs. AGN of type 0 show weak or unusual emission lines. This is seen in the BL Lacertae (BL Lac) object spectrum, which can be easily identified by the relatively featureless emission continuum. The corresponding AGN classification scheme from Beckmann & Shrader (2012) is provided in Table 1.1. There are also other AGN groups which are not listed, such as low-ionisation nuclear emission line region (LINER). The main classes

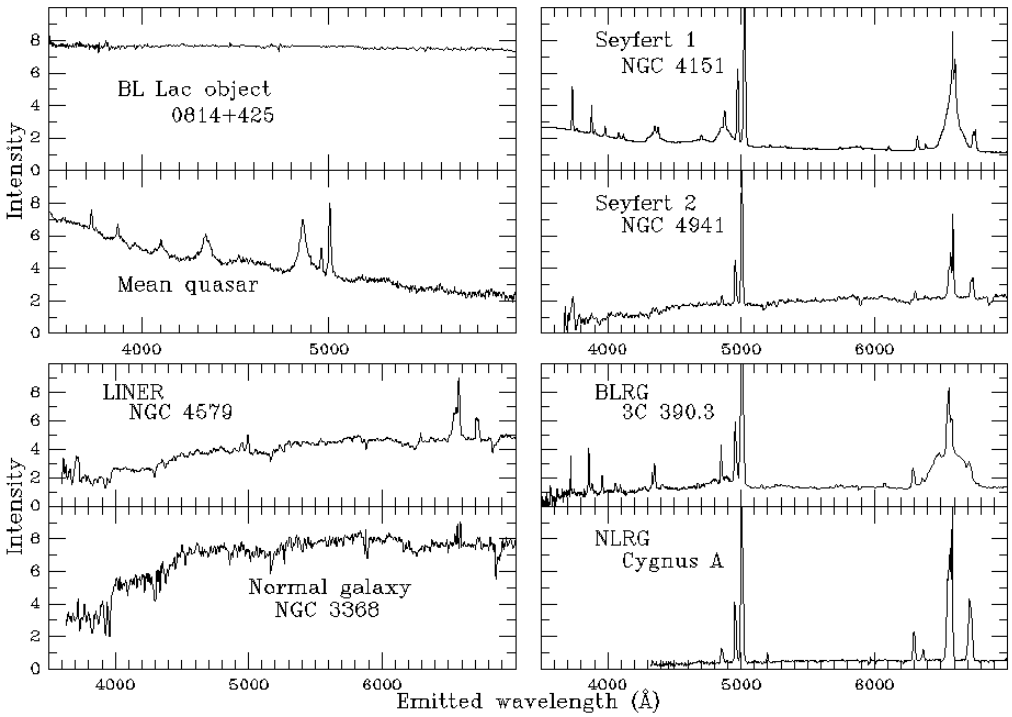

Figure 1.4: Spectra of different classifications of AGN. Image credit: http://pages.astronomy.ua.edu/keel/agn/spectra.html.

and their abbreviations are briefly reviewed in the following subsections.

Some AGN are alike in a sense that they are both in the same type and radio morphology categories. The distinction is mainly determined by their luminosities, specifically the luminosity of the AGN's nucleus, L_{AGN}, and the luminosity of the host galaxy, L_{host}. High luminosity AGN, such as quasars, have nuclei that outshine the host galaxy. AGN with low luminosities, for example Seyferts, are fainter or have comparable brightness to their host galaxies.

Within the framework of unification models based on orientation, type 1 objects are unobscured AGN viewed at low inclination angle or pole-on relative to the rotation axis of the accretion disk. This enables a direct view of the continuum and emission from the BLR, and hence contribute to the BELs. Type 2 AGN are seen edge-on as the line-of-sight between the observer and direct emission is obscured by the torus. The dusty torus surrounding the BLR, shields the BELs and direct radiation from the central ionising source. This is apparent as only NELs are observed in the optical domain.

There have been clues that strengthen the AGN classification with additional dependence on the mode and efficiency of the accretion process (e.g., Hardcastle et al. 2007; Russell et al. 2013; Mingo et al. 2014; Heckman & Best 2014). A more generic classification has also been suggested, distinguishing AGN into radiative-mode or jet-mode (Heckman & Best 2014). In this viewpoint, AGN in radiative-mode (or high-excitation) accrete matter through an optically thick accretion disk (Shakura & Sunyaev

Table 1.1: AGN classifications adopted from Beckmann & Shrader (2012).

Type	Line width	Radio-quiet	Radio-loud	Luminosity
Type 1	Broad+narrow	Seyfert 1 QSO	BLRG Quasar: SSRLQ, FSRLQ	$L_{\rm AGN} \leq L_{\rm host}$ $L_{\rm AGN} \geq L_{\rm host}$
Type 2	Narrow	Seyfert 2 Type 2 QSO	NLRG Type 2 quasar	$L_{\rm AGN} \leq L_{\rm host}$ $L_{\rm AGN} \geq L_{\rm host}$
Type 0	Unusual		Blazar: BL Lac, OVV	$L_{\rm AGN} \geq L_{\rm host}$

1973), which aligns with the conventional orientation unified picture of Urry & Padovani (1995). They are radiatively efficient and emit at luminosities above $\sim 1\%$ of Eddington limit. AGN that accrete below this limit are jet-mode (or low-excitation) AGN. The bulk energy of these objects is fuelled via radiatively-inefficient or advection-dominated accretion flows (Narayan & Yi 1994) and is released kinetically in the form of two-sided collimated jets (Merloni & Heinz 2007). Radiative-mode AGN encompass Seyferts and quasars, which also include both type 1 and 2 AGN. Examples of jet-mode AGN are LINERs and absorption line systems. Although the orientation model is still controversial, it provides a simple link among the AGN types.

1.3.2 Seyfert Galaxies

Historically, Seyfert galaxies are the first class of AGN to be discovered by Seyfert (1943). They are typically classified into two common groups, type 1 and type 2 Seyferts, or Seyfert 1 and Seyfert 2 for short. The dichotomy between Seyfert 1 and Seyfert 2 is the presence of BELs. Seyfert 1 shows both BELs and NELs, while Seyfert 2 shows only NELs (Khachikian & Weedman 1974). However, it is apparent that there exist an intermediate Seyfert subclasses, Seyfert 1.2, 1.5, 1.8, and 1.9, depending on the strength of the broad relative to the narrow component of the emission lines in optical regime (Osterbrock 1977, 1981). For instance, the broad Hβ Balmer component is strong in Seyfert 1.2, but is weaker for Seyfert 1.8. Seyfert 1.5 is an intermediate type object between that of type 1 and 2. A more quantitative scheme is proposed based on the ratio between the [O III λ5007] line flux and the total Hβ line flux (Whittle 1992; Winkler 1992). The Seyfert subclassifications are presented in Table 1.2.

In the standard unified model of AGN, the Seyferts appear to be low luminosity RQ AGN. The different Seyfert types are attributed to orientation (Antonucci 1993; Urry & Padovani 1995). All Seyfert galaxies are inherently the same but viewed at varying inclination angle. When observed pole-on, the unobstructed view of the BLR and accretion disk causes the BELs feature, as detected in Seyfert 1 galaxies. The absence of

Table 1.2: Seyfert classifications.

Seyfert Type	Presence of[a]		[O III]/Hβ Flux Ratio	
	Hβ	Hα	Whittle 1992[b]	Winkler 1992[c]
Type 1	Yes	Yes	[O III]/H$\beta \leq 0.3$	[O III]/H$\beta \leq 0.2$
Type 1.2	Yes	Yes	$0.3 <$ [O III]/H$\beta \leq 1.0$	$0.2 <$ [O III]/H$\beta \leq 0.5$
Type 1.5	Yes	Yes	$1.0 <$ [O III]/H$\beta \leq 4.0$	$0.5 <$ [O III]/H$\beta \leq 3.0$
Type 1.8	Yes	Yes	$4.0 <$ [O III]/Hβ	$3.0 <$ [O III]/Hβ
Type 1.9	No	Yes		

[a] Classified by presence of broad Hβ and Hα from Osterbrock (1977, 1981).
[b] Flux ratio of [O III] and Hβ from Whittle (1992).
[c] Flux ratio of [O III] and Hβ from Winkler (1992).

BELs in the optical spectra of Seyfert 2 galaxies are due to being observed edge-on where the line-of-sight of the observer is blocked by the dusty torus. Intermediate Seyfert types are those viewed between pole-on and edge-on such that the BELs are partially obscured along the line-of-sight, and hence lower broad to narrow emission lines strength.

This perspective is supported by the spectropolarimetric surveys of some Seyfert 2 galaxies (e.g., Antonucci & Miller 1985; Miller & Goodrich 1990; Tran et al. 1992; Tran 1995; Young et al. 1996; Heisler et al. 1997; Moran et al. 2000). The polarised optical BELs in these objects hint the existence of hidden BLR, in which Seyfert 2 consists of Seyfert 1 nucleus with obscured continuum and BLR. However, it is reported that the hidden BLR is not ubiquitous in every Seyfert 2 as only around 50% of them exhibit this component (Tran 2001, 2003). Several explanations suggest that the visibility of the hidden BLR is likely connected to an AGN physical quantity, either the luminosity (Lumsden & Alexander 2001; Elitzur & Ho 2009) or accretion rate (Nicastro 2000; Nicastro et al. 2003), and is not solely due to orientation effect. The BLR is found to be missing in AGN with low luminosity of $< 5 \times 10^{39}\,(M/10^7\,M_\odot)^{2/3}\,\mathrm{erg\,s^{-1}}$ and low radiative efficiency of $\lesssim 10^{-4}$ (Elitzur & Ho 2009). On the other hand, some argue that its absence is because the stronger emission from the host galaxy dilutes the emission from the AGN, which results in a weaker polarised light and lowers the chance of being detected (Alexander 2001; Gu et al. 2001).

1.3.3 Radio Galaxies

Radio galaxies are AGN with jets and are analogous to the RL version of Seyfert galaxies. The type 1 and type 2 radio galaxies are the broad line radio galaxy (BLRG) and narrow line radio galaxy (NLRG) respectively. While Seyferts are hosted by spiral galaxies, radio galaxies are often elliptical galaxies. Either one or two jets are observed in a radio galaxy. The strong polarised light and non-thermal particles from the relativistic jet suggest that the emission across the entire electromagnetic spectrum is due to synchrotron radiation.

1.3.4 Quasars

The most luminous group among all AGN was first identified in the 1960s. Due to the star-like appearance in the optical image, this object earns the name quasi-stellar radio source or coined as quasar by Chiu (1964). The major breakthrough was made by Schmidt (1963) as he managed to identify the quasar 3C 273 with redshift of 0.158. A few years later, Sandage (1965) announced the discovery of a more abundant population of RQ objects that resemble the optical properties of quasars, which he called quasi-stellar galaxies or now formally recognised as quasi-stellar objects (QSOs). The difference in terminology between quasar and QSO is that the former is RL while the latter is designated for RQ source.

Following the unification scheme for low luminosity Seyferts, obscured high luminosity AGN with only NELs should correspondingly exist. The detection of these objects is more arduous since quasars of type 2 are fainter in comparison to their type 1 counterparts. A type 2 high luminosity AGN is later identified by Kleinmann et al. (1988). Subsequently, a larger sample of these candidates were found at low redshift (e.g., Zakamska et al. 2003; Reyes et al. 2008) and also at high redshift (e.g., Alexandroff et al. 2013). Around 15% of low redshift and high luminosity type 2 AGN are RL objects (Lal & Ho 2010).

Additionally, the RL quasars are subdivided according to their radio continuum shape. The two subdivisions are the steep-spectrum RL quasar (SSRLQ) and the flat-spectrum RL quasar (FSRLQ). FSRLQs are also within the blazar AGN class. The SED of the radio sources roughly follows a power-law dependence, which is described by the flux density, $F_\nu \propto \nu^{-\alpha_\nu}$, where ν is the frequency and α_ν is the radio spectral index. SSRLQs usually have extended lobe-dominated radio structures and steep slope continuum with $\alpha_\nu \geq 0.5$, whereas the compact core-dominated FSRLQs display flat spectra with $\alpha_\nu < 0.5$. In the traditional orientation-based unified model, the core-dominated FSRLQs are subset of lobe-dominated SSRLQs, where they are viewed pole-on along the line-of-sight (Antonucci 1993).

Various subgroups of SSRLQ also exist, such as ultra-steep spectrum (USS), gigahertz-peaked spectrum (GPS), and compact steep spectrum (CSS) radio sources. Radio sources that show $\alpha_\nu > 1$ are classified as USS sources and are efficient candidates to identify high redshift radio galaxies (e.g., Chambers et al. 1988; Roettgering et al. 1994, 1997; De Breuck et al. 2001). Both GPS and CSS sources are compact and powerful radio objects that have convex radio spectra with pronounced spectral peaks at high ($\sim 1\,\mathrm{GHz}$) and low ($< 500\,\mathrm{GHz}$) frequencies, respectively (see reviews by e.g., O'Dea 1998; Sadler 2016). About 10% GPS and 30% CSS objects constitute the bright radio source population (O'Dea 1998).

By convention, the name quasar often refers to both RQ and RL populations. Hereafter, the term quasar indicates type 1 RQ and RL high luminosity AGN, in

particular those that have BELs, unless specified otherwise. The study of quasars is the primary emphasis and will be a recurring theme.

1.3.5 Blazars

Blazars are plausibly a subclass of core-dominated RL quasars or radio galaxies seen pole-on relative to the jet angle. As observed from this angle, the radiation from the relativistic jet is boosted by Doppler beaming. The ejected synchrotron radiation dampens the continuum and emission lines. As a consequence, they exhibit high polarisation and rapid variability in their emission.

Blazars are subdivided into BL Lac and FSRLQ, which differ from one another in their optical spectra. The optically violently variable (OVV) quasars are under FSRLQs. As indicated previously, broad permitted lines are present in a FSRLQ spectrum, akin to those of quasars. Conversely, there is rarely any emission or absorption lines in the optical spectrum of BL Lac object due to the strong synchrotron radiation.

1.3.6 Other Enigmatic AGN

The emergence of the so-called changing-look AGN poses a challenge to the traditional orientation unification scheme. The term is initially applied to describe X-ray AGN that transition from Compton-thin ($N_{\rm H} \lesssim 10^{24}\,{\rm cm}^{-2}$) to Compton-thick, or vice versa (e.g., Guainazzi 2002; Matt et al. 2003; Bianchi et al. 2005; Puccetti et al. 2007; Risaliti et al. 2009; Marchese et al. 2012; Miniutti et al. 2014; Ricci et al. 2016). Optical changing-look AGN exhibit variation in the brightness and switch AGN type (e.g., from type 1 to type 1.8–2.0, or vice versa) with rapid disappearance/appearance of their BELs (e.g., Collin-Souffrin et al. 1973; Tohline & Osterbrock 1976; Penston & Perez 1984; Cohen et al. 1986; Storchi-Bergmann et al. 1993; Aretxaga et al. 1999; Shappee et al. 2014; Denney et al. 2014; LaMassa et al. 2015; Runnoe et al. 2016; McElroy et al. 2016; Gezari et al. 2017).

Several reasons to explain this scenario have been considered. The dramatic changes in the observed flux could be caused by the movement of obscuring dusty material from the clumpy torus (e.g., Elitzur 2012). Another scenario is that it is due to the variation in accretion rate (e.g., Penston & Perez 1984; Elitzur et al. 2014). The lower accretion activity results in lack of emission to ionise the BLR gas, therefore reducing the strength of the emission lines. A different suggestion is that the stellar tidal disruption events or supernova events by the BH lead to a sudden burst in brightness and subsequent dimming (Eracleous et al. 1995; Merloni et al. 2015; Blanchard et al. 2017).

1.3.7 Universal AGN Picture

Although the geometric unification picture seems to be an over-simplification of the various AGN types, most observational AGN phenomena can be interpreted within this foundation. It still provides a reasonable representation of the actual AGN system. The unique spectral signature of different AGN across the whole electromagnetic bands reflects the complexity of the AGN. Similarities between the AGN properties are also seen, indicating some overlap among the subclasses. This highlights the difficulty in acquiring a universal unification scheme of AGN.

1.4 Outline of the Thesis

The thesis revolves around these themes: shape of spectral lines, disk-wind of BLR, and orientation in the unification scheme. Chapter 2 introduces observational characteristics of the BLR. The topic on disk-wind is reviewed in Chapter 3, including the theory and a few existing disk-wind models. Our approach to model the disk-wind BLR is then outlined. Using a narrow disk-wind configuration, Chapter 4 explores the trends in the line profile shapes. Chapter 5 uses observational data to statistically examine a subclass of quasars based on their spectral features and concludes by introducing a BLR disk-wind model with wide range of angles. In light of these results, Chapter 6 presents a unique and robust method to determine the orientation of quasars in the UV-optical domain. We delve into the application side of the modelling in Chapter 7 and investigate the bias in the estimates of the black hole masses. Summary and future implications of the work are discussed in Chapter 8.

CHAPTER 2

Observables of the Broad Line Region

This chapter, specifically part of Section 2.1, is based on the publication:

- *Yong, S. Y., King, A. L., Webster, R. L., Bate, N. F., O'Dowd, M. J., & Labrie, K. (2018). Using the Properties of Broad Absorption Line Quasars to Illuminate Quasar Structure.* MNRAS, *479, 4153–4171. ADS: 2018MNRAS.479.4153Y. doi: 10.1093/mnras/sty1540, Section 1*

Abstract

For more than half-century, the BLR has been rigorously studied. There have been growing pursuits to constrain the BLR based on the key features in AGN spectra. In spite of the long history, the true nature of the BLR is still enshrouded in mystery as novel findings are often discovered. The results from pioneering studies reveal that the structure of BLR is much more sophisticated. With the emerging vast surveys, such as the Sloan Digital Sky Survey (SDSS), statistical analyses on the observational characteristics of AGN spectra using large samples have been made possible. These will enable the extraction of general information on the BLR spatial and kinematical structures. In this chapter, the diverse observational characteristics of the quasar spectra emitted from the BLR are reviewed.

2.1 Broad Emission Line (BEL)

The optical-ultraviolet BELs are the most distinguishing feature of a quasar optical spectrum. These lines originate from the BLR, which is situated close to the central ionising source (accretion disk). There have been various studies to understand the relationship between the geometry and dynamics of the BLR and the BEL profiles (e.g. Sulentic et al. 2000; Gaskell 2009; Grier 2013; Pancoast et al. 2014). The absence of forbidden broad lines suggests that the BLR consists of dense regions that suppress the formation of these lines through collisional de-excitation of the gas.

The most notable broad lines are the hydrogen Lyα and hydrogen Balmer series lines Hα, Hβ, and Hγ. Some emission lines are heavily blended due to the broadened Doppler widths. These lines are hard to be distinguished separately and are often measured together, for example Lyα+N V, Si IV+O IV], and C III]+Si III]. Several lines also appear as doublet or multiplets, for instance O VI $\lambda\lambda$1032, 1038, N V $\lambda\lambda$1239, 1243, Si IV $\lambda\lambda$1394, 1403, C IV $\lambda\lambda$1548, 1551, Mg II $\lambda\lambda$2796, 2803, and Fe II multiplets. Based on the ionisation state of the lines, they are grouped into high-ionisation lines (HILs) or low-ionisation lines (LILs). HILs are such as He II, He I, O VI, N V, and C IV, while LILs are such as Mg II, Ca II, O I, Hα, and Hβ.

Some clues to the nature of the BLR can be found by considering the unique properties of the BEL profiles. The shape of the BEL profiles and relative line strengths in a quasar spectrum vary from source to source and reflect the dynamics and geometry of the BLR. Typically, a BEL has FWHM of $\sim 5000\,\mathrm{km\,s^{-1}}$, but can be broader than $10\,000\,\mathrm{km\,s^{-1}}$ (Peterson 1997). The emission line strengths vary between different line species in the same object or the same line in distinct objects, suggesting different ionisation conditions.

The EW is usually used to measure the strength of the emission or absorption lines relative to the underlying continuum flux. It is defined as the width measured using the rectangular area from the continuum which has equal area to that covered by the spectral line:

$$\mathrm{EW} = \int \frac{f(\lambda) - f_c(\lambda)}{f_c(\lambda)}\,\mathrm{d}\lambda \approx \frac{f_{\mathrm{line}}}{f_c}, \tag{2.1}$$

where $f(\lambda)$ is the measured specific flux across the entire spectral line at wavelength λ, $f_c(\lambda)$ is the continuum specific flux, and f_{line} is the total line specific flux. A sketch of the line measurements with FWHM and EW is displayed in Fig. 2.1.

The main attributes of selected emission lines from Vanden Berk et al. (2001), in particular the velocity shifts, skewness, EW, and ionisation potential, are listed in Appendix A. The measurements are estimated based on the generated median composite spectrum of over 2200 SDSS quasar samples at redshift $0.04 \leq z \leq 4.79$, shown in Fig. 2.2. In general, the properties are quite different depending on the ionisation

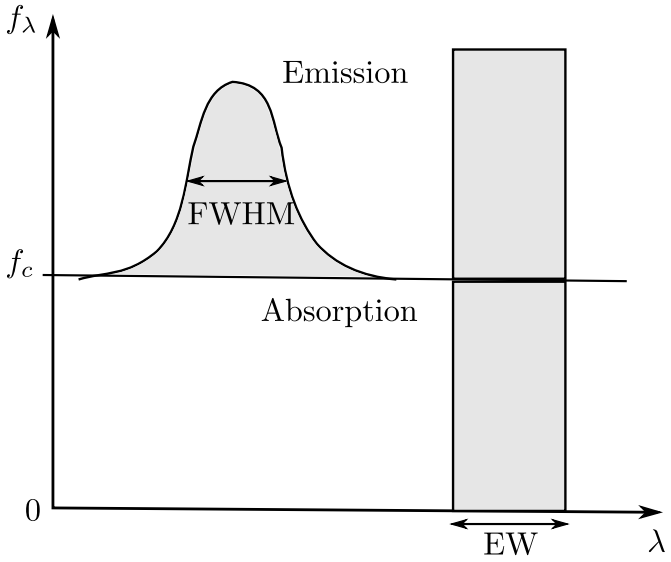

Figure 2.1: Measure of line width using full width at half maximum (FWHM) and line strength using equivalent width (EW). The area in each shaded region is equal.

species.

There appears to be a trend in the BELs for different ionisation states of the ions. Lines with higher ioninisation, like C IV, have broader line widths than those from lower ionisation species, such as Mg II (e.g. Shuder 1982; Mathews & Wampler 1985; Netzer 2013). It suggests that the BLR is likely to have a stratified structure, in a sense that species with high ionisation potential are located nearer to the central of the ionising source. Low ionisation ions are less gravitationally bounded and situated at larger distance.

Results from reverberation mapping (RM), a technique to estimate the time delay of the variations in the emission line flux relative to the continuum flux, also show evidence that the BLR has a stratified ionisation structure (Kollatschny 2003; Peterson et al. 2004). The HILs and LILs are observed to arise at different relative distances from the inner accretion disk. RM studies find that the HILs are emitted from regions closer to the continuum source than the LILs (Gaskell & Sparke 1986; Clavel et al. 1991; Peterson & Wandel 1999; Kollatschny 2003; Peterson et al. 2013; Bentz et al. 2016). This reinforces the view that the location of the HIL regions are different from that of the LIL regions.

2.1.1 Velocity Shifts

Often, emission line profiles are shifted relative to the systemic velocity of the quasar. The forbidden NLR lines, such as [O III], are located further away at kiloparsec from the centre of the BH and are usually assumed to be at the systemic redshift of the quasar, within $\sim 50\,\mathrm{km\,s^{-1}}$ (Hewett & Wild 2010) of the systemic host galaxy velocity. Their

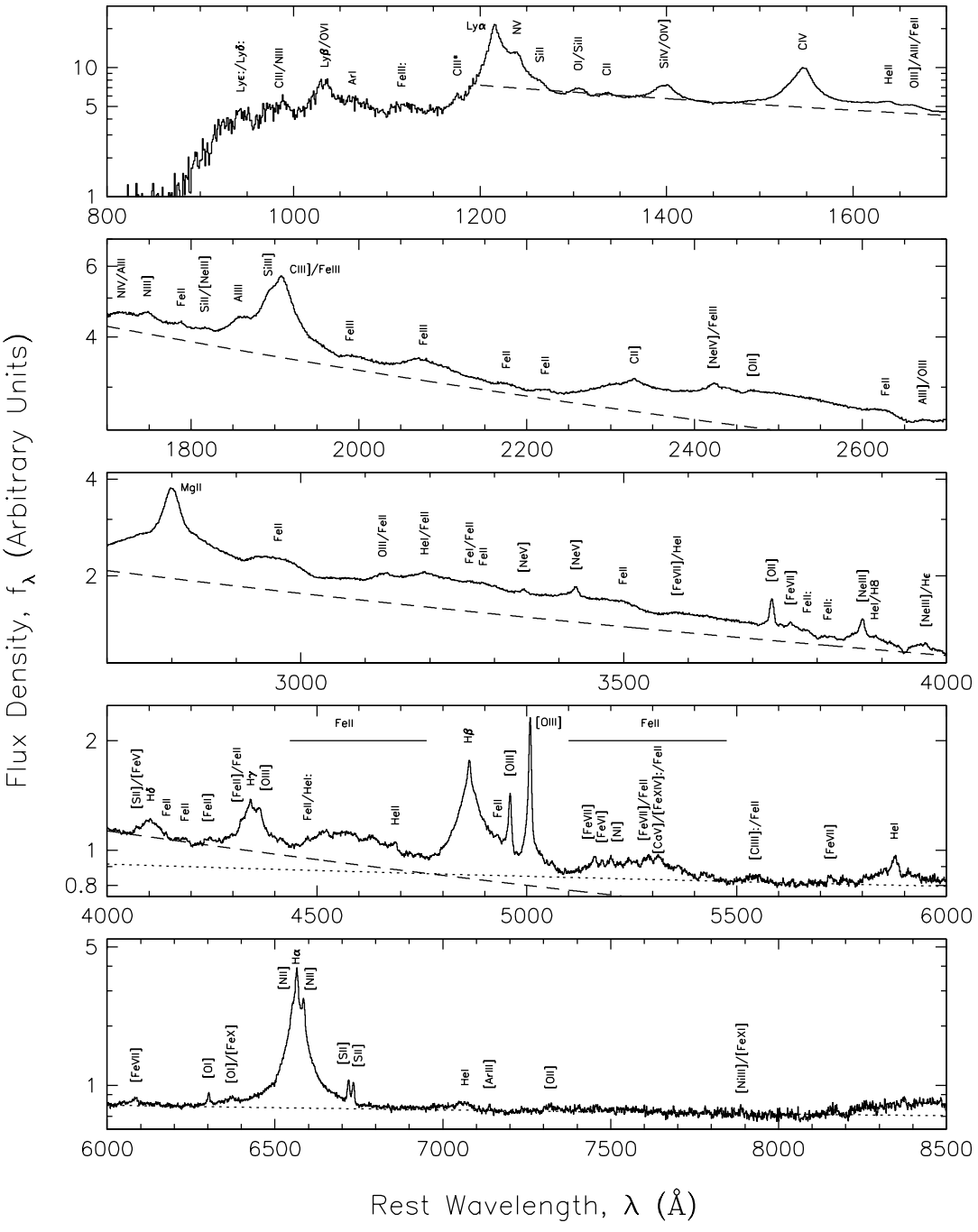

Figure 2.2: Median quasar composite spectrum from Vanden Berk et al. (2001). Ambiguous lines are labelled with trailing colon (:). The dashed and dotted lines show power-law continuum fits.

redshifts in low redshift quasars of $z < 1$ are consistent with the host galaxies redshifts measured using stellar absorption lines (Gaskell 1982) and 21 cm wavelength neutral hydrogen emission line observations (Hutchings et al. 1987). LILs, such as Mg II, have average systemic velocities comparable to that of [O III] line, and hence are often used in cases where the [O III] line lies outside the observed wavelength range (Carswell et al. 1991; McIntosh et al. 1999). Hereafter, the convention adopted is that negative velocity denotes blueshift with line peak towards the low end of the wavelength, while positive velocity corresponds to redward shift towards the high end of the wavelength. This is illustrated in Fig. 2.3.

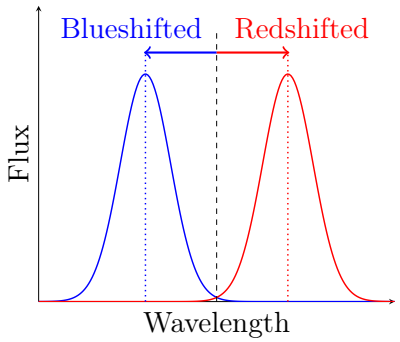

Figure 2.3: The adopted notation for velocity shifts. The vertical dashed line represents the centre of a reference line and the dotted blue and red lines are centre of the lines shifted bluewards and redwards, respectively.

A blueshift is also commonly observed between HILs and LILs. This velocity shift was first reported by Gaskell (1982), and further confirmed by Wilkes (1986), Espey et al. (1989), Tytler & Fan (1992), McIntosh et al. (1999), Vanden Berk et al. (2001), and Shen et al. (2016). In addition, there is a negative relationship between the velocity shifts and ionisation potential, whereby the blueshift increases with higher ionisation line (Gaskell 1982; Wilkes 1986; Espey et al. 1989; Tytler & Fan 1992; McIntosh et al. 1999; Vanden Berk et al. 2001; Shen et al. 2016). Some of the major emission lines velocity shifts with respect to [O III] forbidden line from Vanden Berk et al. (2001) are given in Appendix A, with negative value delineates blueshift. This indicates that the HILs have different dynamics to the LILs and are likely to originate from a different parts of the BLR.

While the source of the offsets in emission lines remains uncertain, the factors that might contribute to the shifts are the redshift, luminosity, and radio type of the AGN. Using FSRLQ sample of redshift $0.2 \lesssim z \lesssim 2.3$, Gaskell (1982) found that the HILs are blueshifted with respect to the NELs and LILs by $\sim 600\,\mathrm{km\,s^{-1}}$. For a redshift range of $1.3 \lesssim z \lesssim 2.4$, Espey et al. (1989) obtained a slightly higher HIL blueshift of $\sim 1000\,\mathrm{km\,s^{-1}}$. The shift can extend over $4000\,\mathrm{km\,s^{-1}}$ for optically selected sources with high luminosity (Corbin 1990).

On the other hand, low redshift objects exhibit different trend in velocity shifts, depending on their radio morphologies. Boroson & Green (1992) demonstrated for quasars at redshift $z \lesssim 0.5$ that LIL Hβ line is shifted toward both blue and red sides from the systemic velocity for RQ objects, but only toward the red for RL objects. Marziani et al. (1996) confirmed for a sample of $z \lesssim 0.8$ AGN that there is a difference in the kinematics of RQ and RL objects.

However, McIntosh et al. (1999) argued that the radio type dependency is not detected in luminous quasars with high redshifts of $2.0 \lesssim z \lesssim 2.5$. Instead, they found a luminosity dependence in their samples, in a sense that there is an increment in redward shift of Hβ line relative to the systemic. By using RQ quasars at $1.5 \lesssim z \lesssim 2.2$ from the SDSS, Richards et al. (2002, 2011) verified that the HIL C IV is blueshifted by $\sim 800\,\mathrm{km\,s^{-1}}$ with respect to the LIL Mg II line and is more blueshifted as the luminosity increases. Both radio type and luminosity dependences are observed by Richards et al. (2011). They reported that C IV blueshift in RL quasars is smaller $\sim 360\,\mathrm{km\,s^{-1}}$ and is weakly correlated with luminosity compared to those of RQ quasars. The link between the blueshift of HILs and luminosity is also proven by Shen et al. (2016) using quasar spectra from SDSS RM project.

Though there are conflicting results, the findings have been getting consistent. The application of large and high quality data samples will provide a tighter velocity shift correlation with other parameters, and hence grant further insights into the geometry and kinematics in the BLR.

2.1.2 Asymmetry

The shape of the BEL profiles differ from one another and some of them often display line asymmetries. Asymmetry is used to describe the degree of symmetry or skewness of an emission line. Hereafter, the convention applied to define the line asymmetry is depicted in Fig. 2.4. Both sides are evenly distributed for a symmetric line (Fig. 2.4b). A negative or blueward asymmetric line profile has broader and more flux on the blue wing (Fig. 2.4a). In contrast, the red wing is more intense than the blue wing in a positive or redward asymmetric line profile (Fig. 2.4c). The skewness of selected emission line profiles adopted from Vanden Berk et al. (2001) are presented in Appendix A. The asymmetry is calculated by using Pearson's coefficient of skewness, that is $3(\mathrm{mean} - \mathrm{median})/\sigma_\lambda$, where σ_λ is the root mean square wavelength dispersion.

The emission lines display wide variation in shapes and degrees of asymmetry (Corbin & Francis 1994; Corbin 1995; Corbin & Boroson 1996; Marziani et al. 1996; Corbin 1997). Various studies relate line asymmetries, particularly for the C IV and Hβ lines, to radio types and orientation of quasars (Marziani et al. 1996; Corbin 1997). These studies find that in RL sources the Hβ line is redshifted and red asymmetric,

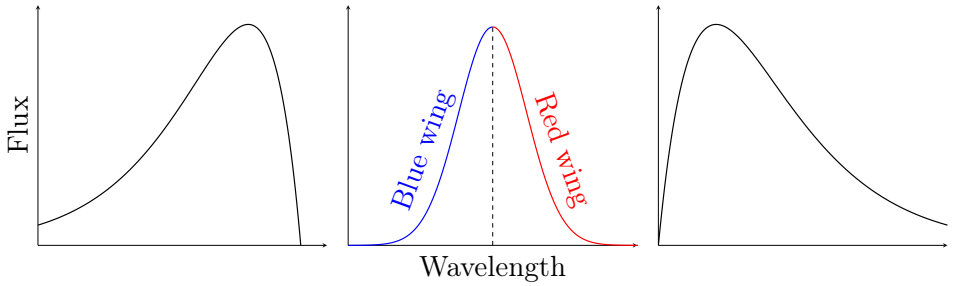

(a) Bluewards asymmetry (b) Symmetric (c) Redwards asymmetry

Figure 2.4: The adopted notation for line asymmetry. The vertical dashed line represents the centre of the line.

while the C IV line remains unshifted and symmetric. For RQ sources, the C IV line is blueshifted and blue asymmetric, while the Hβ line is unshifted and symmetric.

An interpretation is that the anisotropic line emission is due to a combination of obscuration and the kinematics of the wind. Consider that the motion of the wind is outflowing, the line profile shape will be influenced by the projected angle along the line-of-sight of the observer relative to the accretion disk. If viewed at low inclination angle or close to pole-on, the opaque disk will block most of the emission from the opposite side of the disk. Consequently, the red wing of the emission line is diminished, while the blue wing is stronger since the projected line-of-sight velocity is towards the observer. As the inclination angle increases, the receding wind at the far end starts to be visible and contributes to the line flux on the red wing. Part of the emission comes from both ends of the outflowing wind and the line becomes symmetric when viewed close to edge-on.

2.1.3 Double-peaked Emission Line (DPEL)

Some AGN show line profiles with broad double-peaked emission lines (DPELs) or double-peaked emitters, as shown in Fig. 2.5. This characteristic is reminiscent to those seen in cataclysmic variable stars (e.g., Young & Schneider 1980), which are binary star systems with white dwarf as the primary component and mass transferring companion star as the secondary component. It is considered as a direct kinematical evidence for Keplerian motion in accretion disk (e.g., Horne & Marsh 1986), and hence accretion disk models are often invoked to fit the shape of the DPELs (Chen et al. 1989; Chen & Halpern 1989; Eracleous et al. 1995). The two peaks in a DPEL profile are caused by the disk rotation, whereby the approaching side will produce a blue peak and the residing side will yield a red peak. Due to Doppler boosting and gravitational redshifting, DPEL is typically asymmetric with stronger blue peak than the red peak (Chen et al. 1989; Chen & Halpern 1989), though DPELs with stronger red peak are also found (e.g., Eracleous et al. 1995).

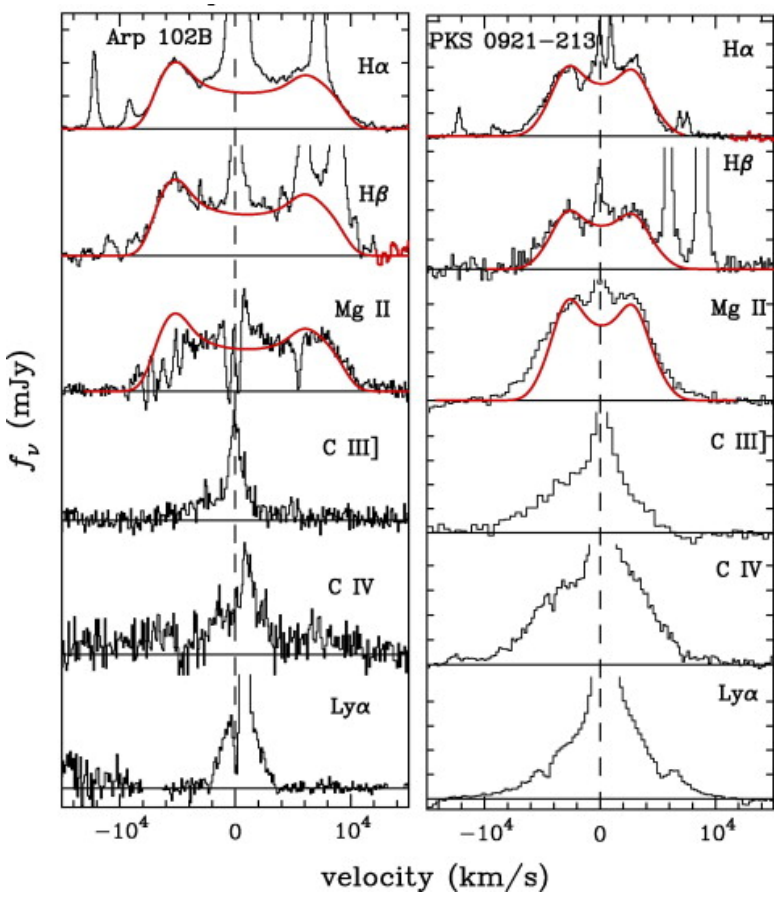

Figure 2.5: Double-peaked emission lines from Eracleous et al. (2009). The red solid line is the disk model using best fit Hα line.

Alternative scenarios for the origin of DPELs have also been suggested. These include a binary supermassive BH formed through galaxy mergers, (Begelman et al. 1980; Gaskell 1983; Peterson et al. 1987) a bipolar outflow (Zheng et al. 1990), and a spherical BLR illuminated by an anisotropic continuum source (Wanders et al. 1995; Goad & Wanders 1996). However, all of these ideas have been rejected as they are inconsistent with those from theoretical expectations and observations of DPELs (see reviews by e.g., Eracleous & Halpern 2003; Gezari et al. 2007).

DPELs are mainly found in LILs, for instance Balmer lines and occasionally Mg II lines, while none has been identified in UV resonance lines, like Lyα and C IV. The lack of two peaks in the UV lines might imply that the conditions in the accretion disk are optically thick and highly dense for these line such that they are unable to be emitted from the disk (Halpern et al. 1996). Only a small fraction of AGN are double-peaked emitters. Double-peaked Balmer lines are present in around 20% of RL AGN at $z < 0.4$ (Eracleous & Halpern 1994, 2003) and about 4% of all AGN in the SDSS catalogue at $z < 0.3$, where 76% are RL AGN and 12% are LINERs (Strateva et al. 2003). The chances of finding a DPEL in RL objects are also 1.6 times higher compared to in RQ objects (Strateva et al. 2003).

Since a Keplerian rotating disk BLR is assumed to be ubiquitous, this leads to the question of why the emission line profiles of AGN are rarely double-peaked and are predominantly single-peaked. Various schemes have been discussed by Eracleous & Halpern (2003) to tackle this dilemma and essentially linking the DPEL AGN with the general AGN population. One of the factors is the size of the disk (Dumont & Collin-Souffrin 1990; Jackson et al. 1991; Rokaki et al. 1992). In particular, a small ratio of outer to inner disk radius of $\lesssim 100$ yields a double-peaked line profile. If the disk radius is large, the two peaks appear to combine and create a single-peaked line profile. Alternatively, a face-on orientation will also create the same effect (Corbin 1997).

Additionally, the inclusion of wind component to the photoionised accretion disk model has been shown to explain well not only the DPELs, but also the emission and absorption lines phenomenology (Murray & Chiang 1997). The resulting line profile depends on the radiative transfer effects. Regions in the wind that have high optical depth and substantial radial velocity shear will enable the line photons to escape along the directions of low projected velocity. The non-axisymmetric disk emissivity also reduce the emission from disk regions with large projected velocity, and therefore produce single-peaked line profiles. While the deficit of emission at small projected velocity in optically thin wind generates double-peaked lines.

Extensive spectroscopic monitoring campaigns have been conducted over timescales of months to years in order to study the variability of the DPELs in a few AGN. For example, Arp 102B (Sergeev et al. 2000; Shapovalova et al. 2013), 3C 390.3 (Veilleux & Zheng 1991; Sergeev et al. 2002; Jovanović et al. 2010; Shapovalova et al. 2010; Popović et al. 2011; Sergeev et al. 2011), 3C 332 (Gezari et al. 2007), and NGC 1097 (Storchi-Bergmann et al. 2003). The relative flux of the blue and red peaks in some

sources (e.g., 3C 390.3 and NGC 1097) also display occasional fluctuation between the two peaks, causing changes in the line profile asymmetry.

2.2 Broad Absorption Line (BAL)

A subpopulation of quasars display absorption trough bluewards with respect to the emission line (e.g. Weymann et al. 1991), though redshifted troughs have also been identified (Hall et al. 2013). Depending on the width of the absorption lines, the absorbers are classified into broad absorption lines (BALs), narrow absorption lines (NALs), and mini-BALs. BALs have typical velocity widths that extend to tens of thousands $\mathrm{km\,s^{-1}}$ and are often blueshifted relative to the rest frame of the emission line. NALs show lower absorption line widths of less than a few hundred $\mathrm{km\,s^{-1}}$. Absorption troughs with intermediate widths are called mini-BALs. The estimates of the detection rate in increasing order are mini-BALs, BALs, and NALs, with $\sim 5\%$, $\sim 20\%$, and $\sim 45\%$, respectively (Hamann et al. 2012). It is also found that the percentage of AGN with intrinsic outflows can be as large as $\sim 70\%$ (Ganguly & Brotherton 2008; Hamann et al. 2012).

The absorption lines can also be separated into intrinsic and intervening absorbers. Intrinsic absorbers consist of gas that is physically associated to quasars. Intervening absorbing materials are those produced in foreground galaxies, interstellar, or intergalactic media along the quasar line-of-sight. BALs are intrinsic to quasars. An example of intrinsic BAL profiles in the low-ionisation BAL quasar H1413+117 acquired from O'Dowd et al. (2015), is portrayed in Fig. 2.6. The lines are C IV, Si IV, N V, and Al III. Meanwhile, NALs can be either one, but the majority are intervening absorbers. Traditionally, NALs falling within $5000\,\mathrm{km\,s^{-1}}$ from the quasar systemic redshift (associated absorption lines) have higher possibility of being intrinsic, while those that are larger than this cutoff are from intervening systems (e.g., Weymann et al. 1979; Foltz et al. 1986).

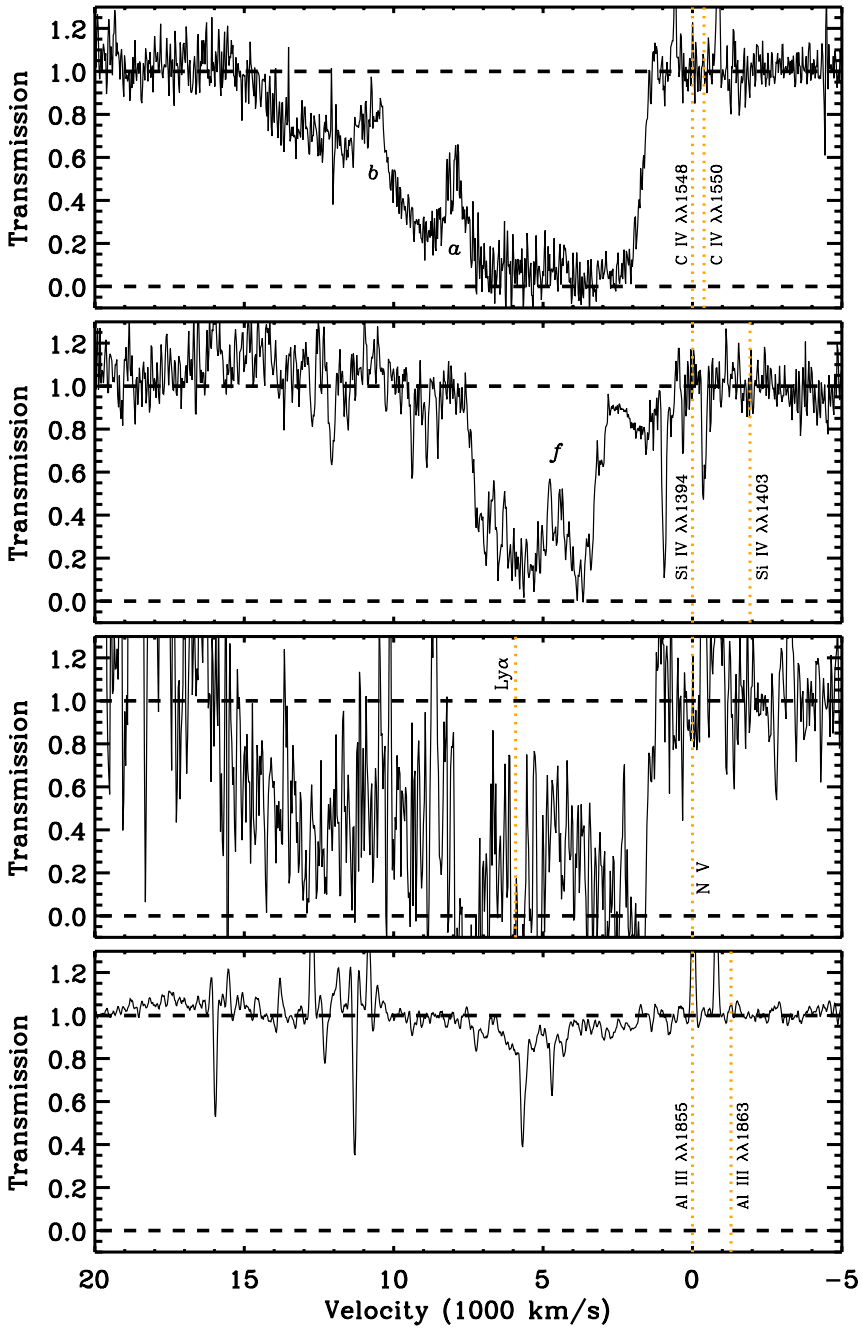

Figure 2.6: Intrinsic broad absorption line (BAL) profiles for C IV, Si IV, N V, and Al III of low-ionisation BAL quasar H1413+117 from O'Dowd et al. (2015).

CHAPTER 3

Quasar Disk-wind

This chapter is based on the publications:

- *Yong, S. Y., Webster, R. L., & King, A. L. (2016). Black Hole Mass Estimation: How Good is the Virial Estimate?* PASA, *33, e009. ADS: 2016PASA...33...9Y. doi: 10.1017/pasa.2016.8, Section 2.1*
- *Yong, S. Y., Webster, R. L., King, A. L., Bate, N. F., O'Dowd, M. J., & Labrie, K. (2017). The Kinematics of Quasar Broad Emission Line Regions Using a Disk-Wind Model.* PASA, *34, e042. ADS: 2017PASA...34...42Y. doi: 10.1017/pasa.2017.37, Section 1 and Section 2*

Abstract

The structure and kinematics of the BLR in quasars are still not well established. One popular BLR model is the disk-wind model that offers a geometric unification of a quasar based on the angle of viewing. We construct a simple kinematical disk-wind model combined with radiative transfer in the Sobolev, or high velocity, limit.

3.1 Background

It is becoming common that the idea of accretion and outflow process are closely intertwined and important in astrophysical systems. Observational evidence for this phenomenon have been identified in several astronomical objects including cataclysmic variable (CV) stars (e.g., Cordova & Mason 1982), X-ray binaries (e.g., Ponti et al. 2012), and AGN (e.g., Weymann et al. 1991). The outflow is often posited to arise from the base of the accretion disk, albeit many aspects of the physics behind these processes are still not fully grasped. The exact acceleration mechanisms of the outflow remain debatable. Postulated outflow models also have to be fully self-consistent and match the prediction of observables. In this chapter, outflow models and the driving mechanisms are reviewed in § 3.1. Our BLR modelling approach is presented in § 3.2 and summarised in § 3.3.

3.1.1 Outflows in Quasars

One compelling piece of evidence of outflowing materials is the P Cygni profile in a spectrum of a star. The name is derived from P Cygni, a luminous blue variable star, whose spectrum shows intense emission lines with absorption lines bluewards. These features are caused by an expanding shell of gas or a stellar outflowing wind. An illustration of the formation of the classic P Cygni line profile is shown in Fig. 3.1. When the wind material is between the observer and the star, absorption line is created. It also appears blueshifted from the centroid since the photons are approaching the line-of-sight of the observer. An emission line is produced from the rest of the expanding shell, though the material at the far side along the observer's line-of-sight is occulted by the star. It tends to be fairly symmetric due to the contributions from the positive and negative projected velocities. The P Cygni profile is then the combination of both spectral features. In general, the term P Cygni profile is applied to other celestial objects with similarly shaped spectral lines.

A plausible signature of outflows in a substantial fraction of quasars is the existence of absorption lines. As the characteristics of a BAL and the classic P Cygni profile are similar, this leads to the possibility that some degree of outflowing wind is also present in quasars. However, BALs in quasars show a wide variety of shapes instead of just smooth P Cygni line profiles. The absorption trough of a BAL can appear detached from its corresponding emission line. This implies that quasar outflows are more complex than the simplistic argument of a smooth and spherically symmetric atmosphere inferred from stellar winds.

Most BAL quasars are probed in the UV waveband but some in X-ray waveband have also been found. Some BAL X-ray spectra show ultra-fast outflows that have mildly relativistic outflow velocities of $\gtrsim 0.1c$ (e.g., Chartas et al. 2002; Reeves et al. 2003; Chartas et al. 2003). These objects can even have high Hydrogen column densities in the range of 10^{22}–$10^{24}\,\mathrm{cm}^{-2}$. Similar to BALs, the NALs are also detected in both UV and X-ray regimes. The UV NALs can appear at blueshifted velocities of more than ten of thousands $\mathrm{km\,s}^{-1}$ and even $\gtrsim 50\,000\,\mathrm{km\,s}^{-1}$ from the emission lines (e.g., Jannuzi et al. 1996; Hamann et al. 1997; Narayanan et al. 2004). High velocity NAL outflows are also reported in X-ray spectra that extend $\gtrsim 60\,000\,\mathrm{km\,s}^{-1}$ (e.g., Chartas et al. 2009). It is plausible that systems with high velocity outflows are in the host galaxy.

Quasar outflows are vital candidates to provide clues into the AGN feedback mechanisms that are responsible for the coevolution between the supermassive BHs and their host galaxies (see e.g., Kormendy & Ho 2013; King & Pounds 2015). The gas and dust from young galaxies can be carried away by the outflows, contributing to the metal-rich environment in the local universe and even regulating star formation in interstellar and intergalactic media (e.g., Silk & Rees 1998; Kauffmann & Haehnelt 2000; Granato et al. 2004; Di Matteo et al. 2005; Fabian 2012). Therefore, quasar outflows reveal broader insight not only into the physical properties, but also into galaxy evolution and the surrounding environment.

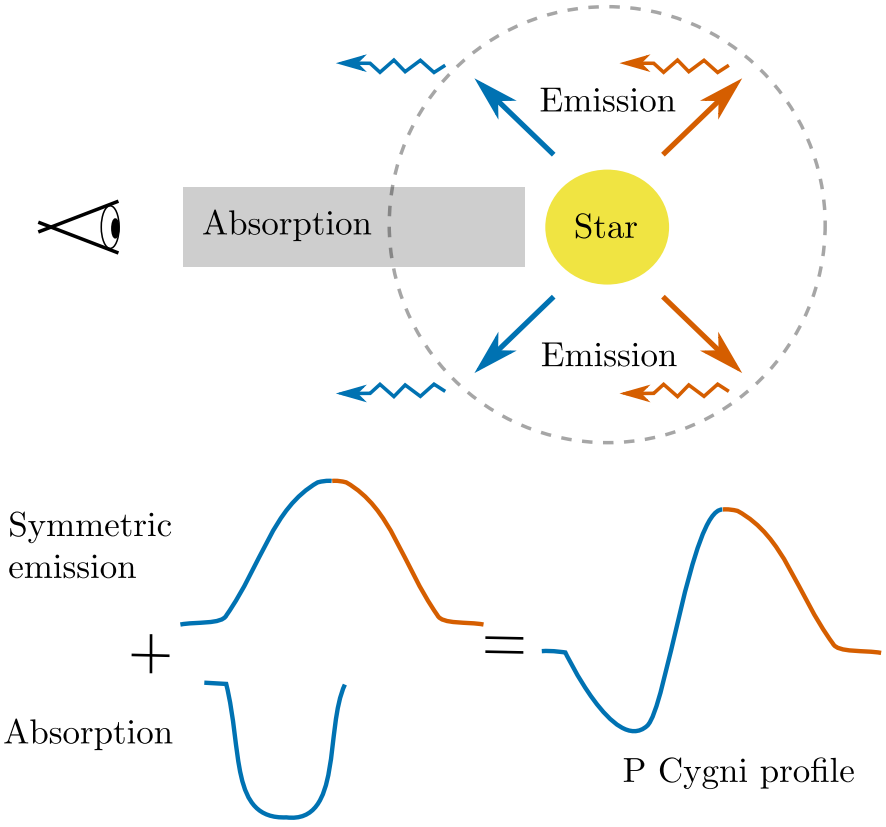

Figure 3.1: Formation of P Cygni profile.

3.1.2 Driving Mechanisms

For a quasar outflow to occur, some sort of force on the gas is required to dominate over gravity. A brief discussion on plausible driving forces is reviewed in Proga (2007). Currently, the driving mechanism of the wind is still unclear. The three major drivers that have been proposed are thermal or gas pressure (Weymann et al. 1982; Begelman et al. 1991), radiation pressure due to spectral lines or line driving (Shlosman et al. 1985; Arav et al. 1994; Murray et al. 1995), and magnetocentrifugal pressure due to the accretion disk (Blandford & Payne 1982; Emmering et al. 1992; Konigl & Kartje 1994). This can be represented by the radiation magnetohydrodynamics (MHD) equation, specifically the equation of motion which is given by

$$\rho\frac{D\mathbf{v}}{Dt} + \rho\nabla\Phi = -\nabla P + \frac{1}{4\pi}(\nabla \times \mathbf{B}) \times \mathbf{B} + \rho\mathbf{F}_{\rm rad}, \tag{3.1}$$

where D/Dt is the Lagrangian or the convective derivative. The quantities ρ, $\mathbf{v}$, Φ, P, $\mathbf{B}$, and $\mathbf{F}_{\rm rad}$ are the mass density, velocity, gravitational potential, pressure, magnetic field strength, and total radiation force per unit mass, respectively. Then, the three terms on the right-hand side of Eq. (3.1) describe the thermal pressure gradient, magnetic Lorentz force, and radiation force. A short description of these launching mechanisms is presented in the following sections.

3.1.2.1 Thermal or Gas Pressure Driven

Quasars reside in a matter-rich environment, and hence are energetic sources of radiation. The heating of the gas in the accretion disk causes thermal expansion. When the thermal velocity of the gas surpasses the local escape velocity, a thermal pressure driven wind is formed. For this scenario to occur, the temperature needs to be high, around a Compton temperature of $\sim 10^7$ K, and at a large distance from the BH where the local escape velocity is small (e.g., Chelouche & Netzer 2005). A thermal driven wind is less likely to dominate below Compton temperature.

It has been shown through detailed photoionisation and dynamical modelling that the thermally driven wind model can explain the observed highly ionised low velocity X-ray absorption features or warm absorbers (WAs) seen in some Seyfert galaxies (Chelouche & Netzer 2005). The inclusion of adiabatic cooling can also substantially reduce the maximum temperature to be lower than the Compton temperature. However, a thermal wind model fails to drive the outflow at large scales as adiabatic cooling causes the wind to decelerate too rapidly (Everett & Murray 2007). For the wind to remain isothermal, other heating sources, which are yet to be identified, are necessary. Alternative means to accelerate the wind must also be introduced to explain outflows with extreme velocities.

3.1.2.2 Radiation Pressure or Line-driven

The theory of a line-driven wind has long been established by Castor et al. (1975) from the studies of stellar winds in hot stars. They showed that the radiation force equation can be expressed as

$$\mathbf{F}_{\rm rad} = \frac{\sigma_{\rm e} F}{c} M(t), \tag{3.2}$$

where $\sigma_{\rm e}$ is the mass scattering coefficient of the free electron and F is the total flux. The factor $\sigma_{\rm e}F/c$ is the force caused by continuous absorption. The force multiplier function, $M(t)$, is a function of the optical depth variable, t, which determines the fraction of force driven by a spectral line and the force due to electron scattering.

If all lines are optically thick, $M(t)$ approaches zero. This occurs when the gas is highly ionised and radiation pressure due to electron scattering will dominate. If all lines are optically thin or the gas is partially ionised, the line driving force will dominate. The force multiplier reaches a maximum value of $M_{\rm max}$ and is found to be about $\sim 10^3$ (e.g., Castor et al. 1975; Abbott 1982; Gayley 1995). This provides an estimate of the lower bound on the luminosity for efficient line driving wind $L > L_{\rm Edd}/(1 + M_{\rm max})$ or $L \gtrsim 0.0005\, L_{\rm Edd}$ with $M_{\rm max}$ of 2000.

A promising observational indication of radiatively driven outflows in quasars is the discovery of a line-locking feature (e.g., Turnshek 1984; Foltz et al. 1987). This signature is associated with narrow and blueshifted absorption characteristics seen in a pair of different ionisation lines separated by a line doublet spacing. One of the most studied line-locked pairs is Lyα and N V, with a small hump observed in the absorption trough of BAL quasars blueshifted at $\sim 5900\,{\rm km\,s^{-1}}$ from the centre of the line (e.g., Weymann et al. 1991; Korista et al. 1993). It is well-known as the ghost of Lyα and hints that radiative pressure is likely to have a role in accelerating the wind (e.g., Arav et al. 1995; Arav 1996, but see also Cottis et al. 2010).

Generally, disk-wind models driven by radiative acceleration are fairly robust especially in explaining the BEL and BAL properties in AGN (e.g., Murray et al. 1995; Elvis 2000). The mechanism is inspired by that from hot stars (e.g., Lamers & Cassinelli 1999). Two major considerations are required to implement line driving developed for hot stars to quasars. First is the difference in structure. The winds in hot stars have roughly spherically symmetric geometry, whereas quasars are assumed to be axisymmetric. Second is the difference in SED. The radiation emitted from hot stars is mainly in UV, while quasars emit both in UV and X-ray domains. As a consequence, the X-ray radiation can over-ionise the gas, and hence prevent the formation and acceleration of UV lines in the wind via line driving. For this reason, some sort of shielding gas is needed to protect the wind from the strong X-ray photons. This issue is familiarly known as the over-ionisation problem and any viable line-driven model has to address this matter. By taking these factors into account, some hydrodynamic simulations have

successfully incorporated a line driving mechanism to model AGN (e.g., Proga et al. 2000; Proga & Kallman 2004).

3.1.2.3 Magnetically Driven

Although line driving is an attractive mechanism in producing outflows in AGN, it is inadequate to cover low luminosity objects and high ionisation state gases (e.g., Chelouche & Netzer 2005). Thermal driving is only significant provided that the accretion disk is heated to a sufficiently high temperature and at radius far away from the central ionising source. This indicates that some other mechanisms, like magnetic force, is necessary to accelerate the wind.

Several studies in favour of a magnetic wind model have been conducted (e.g., Blandford & Payne 1982; Emmering et al. 1992; Bottorff et al. 1997, 2000). One robust and successful method to transport angular momentum in the accretion disk is through magnetorotational instability (Balbus & Hawley 1991). There are two subgroups of magnetic Lorentz force. Using the vector triple product identity, the Lorentz force can be expanded as

$$\frac{1}{4\pi}(\nabla \times \mathbf{B}) \times \mathbf{B} = \frac{1}{4\pi}(\mathbf{B} \cdot \nabla)\mathbf{B} - \frac{1}{8\pi}\nabla B^2. \tag{3.3}$$

The first factor on the right-hand side of Eq. (3.3) is the magnetic tension in field lines or magnetocentrifugal force due to the rise of the angular velocity in the radial direction. The second factor is the magnetic pressure, which is related to the horizontal gradient pressure formed in the vertical direction.

The seminal paper by Blandford & Payne (1982) describes how magnetic tension launches the wind from the disk. The behaviour of the magnetic field lines is analogous to 'bead on a rigid wire'. A bead of gas can be ejected from the wire of fast rotating magnetic field line, depending on the geometry of the field. For a centrifugally driven outflow of gas, it requires the poloidal magnetic field to be at inclination of more than 30° relative to the normal of the disk surface.

The observational features in AGN that can be described by radiative pressure winds have been shown to also deemed feasible with magnetocentrifugal winds. The applications of MHD models include BAL outflows (e.g., Emmering et al. 1992), as well as the reproduction of the shape and variability of the emission line profiles (e.g., Bottorff et al. 1997). The magnetic wind also solves one of the main complications in line-driven wind, that is the over-ionisation problem. Since it does not involve radiation pressure, a magnetic wind can play a crucial role, especially in systems with low luminosity, such as young stellar objects or sources over-ionised by strong radiation, like AGN (e.g., Pelletier & Pudritz 1992; Konigl & Kartje 1994; Ouyed & Pudritz 1997; Ustyugova et al. 1999; Krasnopolsky et al. 1999). Additionally, a magnetically driven wind might also aid other

driving mechanisms to accelerate the outflow more efficiently (de Kool & Begelman 1995; Everett 2005). The wind remains dense as it is confined by magnetic fields and is able to accelerate radiatively. Some authors have considered models combining both magnetic and line driving mechanisms (Konigl & Kartje 1994; de Kool & Begelman 1995; Proga 2003; Everett 2005).

Though the magnetic wind model seems rather universal, there are still a few issues. Notably, the origin of large-scale magnetic fields is unclear. As it is difficult to test against observations, inferring the properties of the wind, such as the mass-loss rate, has also become a hurdle. Indeed, extensive work is needed to address all the concerns.

3.1.3 Disk-Wind Models

In recent years, there has been a significant improvement in the quality of the data along with better instrumentation and larger surveys to better understand the line-emitting region. Despite this, the nature of the BLR is still an open question. Numerous BLR models have been proposed to explain the observed characteristics of line profiles in AGN spectra with the main aim of developing a scheme to unify all AGN. Among the various proposed models of the BLR are the discrete cloud and disk-wind models (see reviews by e.g., Korista 1999; Eracleous 2006). The discrete cloud model consists of discrete optically thick gas clouds photoionised via the continuum source emission. Although this model is capable of explaining the observed spectral characteristics, it suffers from a few complications. One main issue is the confinement problem: without a way to confine the clouds, they would simply evaporate (see review by e.g., Mathews & Capriotti 1985). Several solutions to this problem have been suggested, such as a hot intercloud medium (Krolik et al. 1981) and magnetic fields (Rees 1987).

Models associated with winds accelerated by some driving mechanisms are attractive and have gained attention over the years. Meanwhile, rare observations of double-peaked line profiles in AGN (e.g., Eracleous & Halpern 1994, 2003; Strateva et al. 2003) indicate that the velocity is likely to be dominated by Keplerian motion, favouring accretion disk models (Chen et al. 1989; Eracleous et al. 1995). Hence, a combination of disk and wind components is often invoked to depict the BLR as it provides a natural avenue to transfer angular momentum from the accretion disk and is free from the confinement problem. Examples of such models include thin winds (Elvis 2000, 2004), large disk radii winds (Murray et al. 1995), failed dusty disk-winds (Czerny & Hryniewicz 2011), line-driven winds (Shlosman et al. 1985; Proga et al. 2000; Proga & Kallman 2004), MHD driven winds (Blandford & Payne 1982; Emmering et al. 1992; Konigl & Kartje 1994; Bottorff et al. 1997, 2000; Elitzur & Shlosman 2006), or hybrid of radiative pressure and MHD driven winds (de Kool & Begelman 1995; Everett 2005). Some notable candidates for a disk-wind BLR are reviewed in the following subsections.

3.1.3.1 Elvis — Funnel-shaped Thin Shell Outflow Model

Elvis (2000, 2004) introduced a simple phenomenological structure of quasar to account for the observed emission and absorption phenomenology, including BELs, BALs, NALs, and X-ray WAs. The model has a biconical outflow as shown in Fig. 3.2. A narrow wind is emitted vertically off the base of the accretion disk at a distance of $\sim 10^{16}$ cm from the black hole. The wind then bends radially outward and is accelerated by radiative pressure. The wind is $\sim 60°$ from the rotation axis with opening angle of $\sim 10°$, which represents the covering fraction of quasars with BAL. BALs are seen in a spectrum when looking directly through the wind. NALs and WAs are detected when viewing across the cylindrical part of the wind. Meanwhile, high-ionisation BELs are embedded in a cool phase ($\sim 10^4$ K) of the wind and low-ionisation BELs are originated from the accretion disk but further out. There is no absorption features when the line-of-sight and the wind are not coincide.

In a recent paper, Elvis (2017) suggested a 'quasar rain' model using wind and thermal instabilities to explain the origin of the BLR, which is displayed in Fig. 3.3. In general, the quasar rain model predicts three forms of cool gas in the BLR, namely BEL clouds, low ionisation phase of WAs, and X-ray eclipsing clouds. The cool condensations in BEL clouds are formed naturally at sub-escape velocity in the warm ($\sim 10^6$ K) radiatively driven accretion disk-wind. The rapid variation in the X-ray ionising continuum moves the WA gas into stable regions. This causes the BEL clouds to condense out of WA wind, and hence creating the cool phase for BEL clouds. Since these BEL clouds are dense with high column densities, they are unable to accelerate by radiative pressure. They will stall and rain back toward the black hole, leading to an inflow motion as observed in most velocity-resolved RM (e.g., Gaskell 1988; Koratkar & Gaskell 1989; Crenshaw & Blackwell 1990; Korista et al. 1995; Ulrich & Horne 1996). These clouds or 'raindrops' are highly supersonic compared to the outflow of WA and only survive for a few months. Consequently, this might produce narrow cometary shape of the BEL clouds found in asymmetric X-ray ellipses (Maiolino et al. 2010).

3.1.3.2 Emmering et al. — Disk-driven Hydromagnetic Wind Model

A way to solve the cloud confinement problem encountered in cloud models is by magnetic pressure (Rees 1987). Emmering et al. (1992) developed a magnetic accretion disk-wind model consisting of clouds in an attempt to explain the observed BEL features. The outflow of clouds are embedded along the streamlines of a centrifugally driven MHD wind. A cartoon of their model is illustrated in Fig. 3.4.

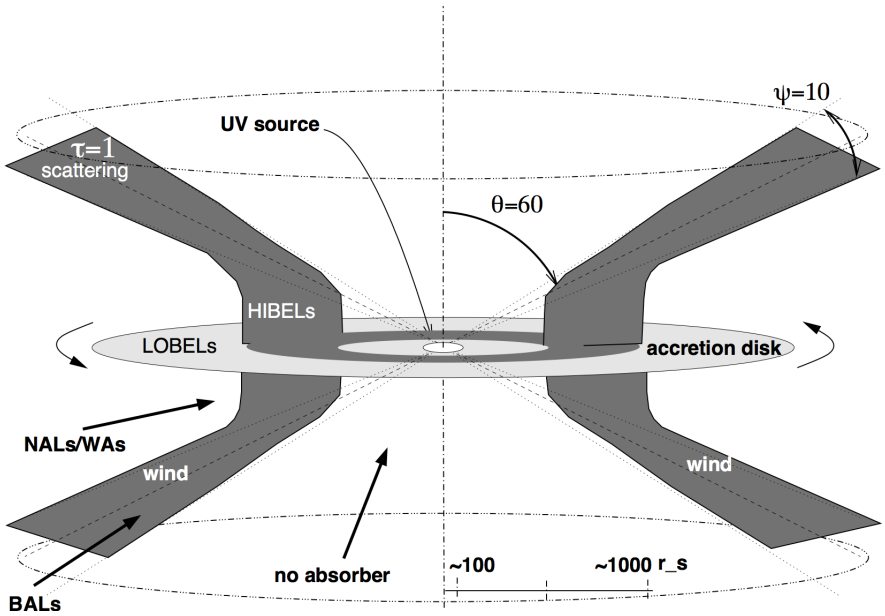

Figure 3.2: A schematic of funnel-shaped thin shell outflow model proposed by Elvis (2004).

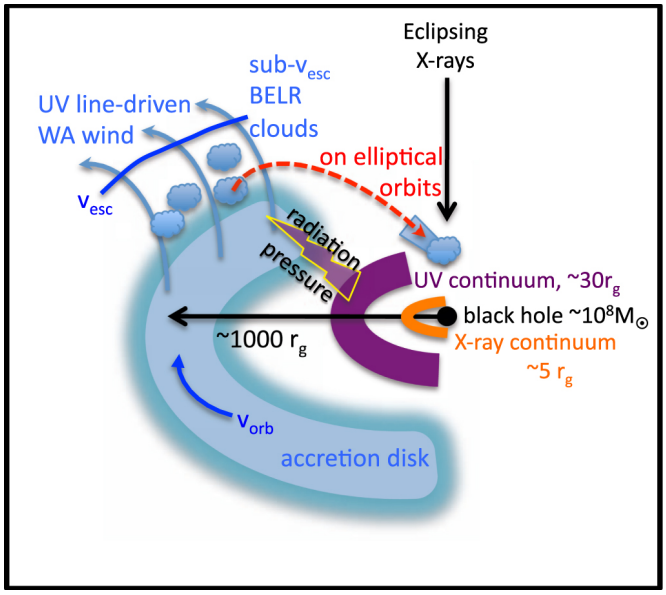

Figure 3.3: A schematic of quasar rain proposed by Elvis (2017).

Small dense and cool molecular clouds are flung away from the exterior parts of the accretion disk via magnetic field. The exposure to the UV ionising flux from the interior parts of the disk causes the ensemble of clouds to become photoionised, and thus producing emission lines. The broaden wings of the line profile is likely caused by electron scattering of $\sim 10^6$ K intercloud medium, where the clouds are either situated close to the disk or inside the corona. They demonstrated that the estimated values for the ionising flux, electron density, filling factor, and velocity agree with those from observations.

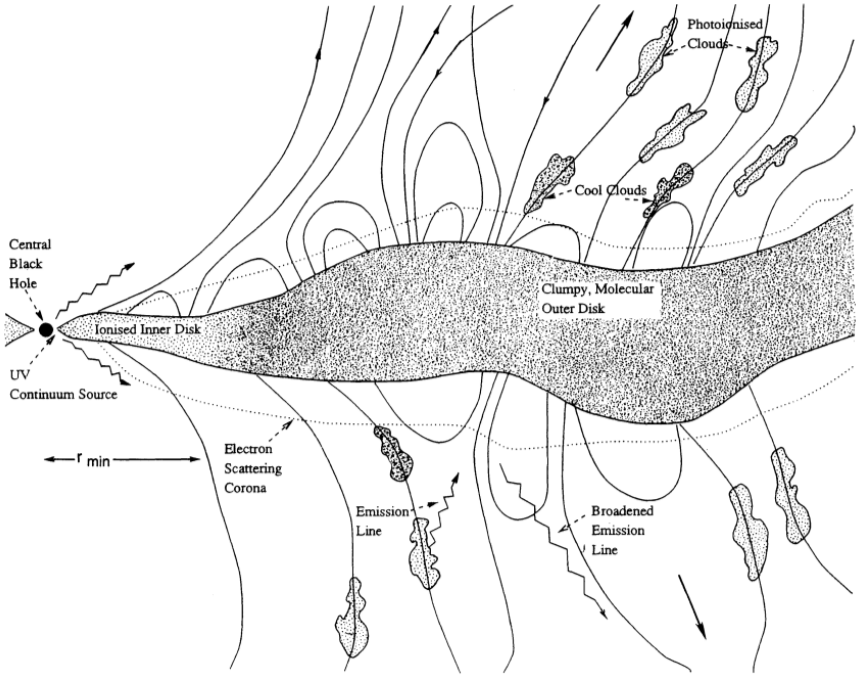

Figure 3.4: A schematic of disk-driven hydromagnetic wind model proposed by Emmering et al. (1992).

3.1.3.3 Everett — Hybrid Radiatively and Magnetically Driven Wind Model

The disk-driven hydromagnetic wind model is originally proposed by Konigl & Kartje (1994). The apparent achievement of this model in describing the radiative characteristics of young stellar objects has prompted them to apply it to AGN, considering that these objects are both similar in some aspects. Everett (2005) further improved the model with more realistic prescriptions of the radiatively accelerated MHD wind by including photoionisation. The two key components in play are the 'shield' and the 'wind', as portrayed in Fig. 3.5. Both components are intentionally separated for simplistic approximations of the simulation. The 'shield' is the inner part of the outflow facing the BH and is basically a shielding gas solely driven by magnetic field acceleration. As it absorbs the ionising radiation, it protects the outer part of the wind from becoming

over-ionised. The exterior wind past the shield is optically thin, which accelerates off the accretion disk via radiative and magnetocentrifugal forces.

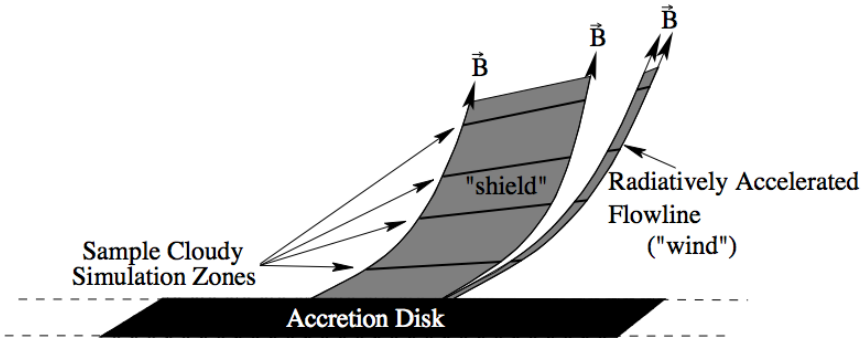

Figure 3.5: A schematic of hybrid radiatively and magnetically driven wind model proposed by Everett (2005).

Subsequent work by Gallagher & Everett (2007) suggested a cold dusty outflow as an additional component into the model. The distinct outflow regions are possibly governed by different driving mechanisms. The X-ray shielding gas might be magnetically accelerated, while the UV absorbing wind might be radiatively accelerated. The dusty outflow is accelerated by UV radiative pressure, and plausibly magnetic forces, on dust grains.

Keating et al. (2012) enhanced the hybrid model of Everett (2005) with dust opacity embedded to construct the shape of the infrared SEDs. Using their model as a framework, Gallagher et al. (2015) examined the effects of various model parameters on the dusty disk-wind model. They demonstrated that the generated mid-infrared SED is consistent with the predicted fraction of type 1 and type 2 AGN.

3.1.3.4 Murray et al. — Line-driven Disk-wind Model

The model suggested by Murray et al. (1995) is composed of a smooth wind emanating off an accretion disk with launch radius of 10^{16} cm from a $10^8\ M_\odot$ BH. Radiation pressure further accelerates the outflowing wind to terminal velocity of $\sim 0.1c$. The wind is near planar and forms an opening angle of $\sim 5°$. This cloudless model also implies that it is not susceptible to the confinement problem. An illustration of the proposed structure is depicted in Fig. 3.6.

A vital ingredient in this model is the postulated 'hitchhiking' gas, a thick dense layer of gas at the inner edge of the wind that hinders the wind from being over-ionised due to the X-ray source at the centre. It acts as a shield from the strong ionising source and effectively accelerates the outflow via radiation pressure on UV resonance lines. The BELs are produced naturally from the base of the wind where the density is high, while BALs are formed when the line-of-sight intersects the wind.

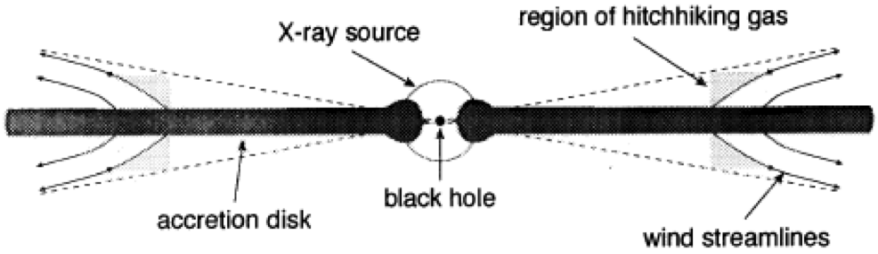

Figure 3.6: A schematic of line-driven disk-wind model proposed by Murray et al. (1995).

Several subsequent series of papers by Chiang & Murray (1996) and Murray & Chiang (1997) attempt to access the robustness of the model. With the addition of radiative transfer effects, they showed that their model is able to effectively explain most of the observed BEL characteristics. These include modelling an earlier response in the red side of the emission line profile that matches with many velocity-resolved RM objects, and generating single-peaked emission line profile.

3.1.3.5 Proga et al. — Hydrodynamic Line-driven Disk-wind Model

The basis of the numerical hydrodynamic simulation for radiatively driven wind developed by Proga et al. (1998, 1999) was initially used for a white dwarf. Later, Proga et al. (2000) and Proga & Kallman (2004) improved the method and extended the functionality to AGN outflows. Their model, as displayed in Fig. 3.7, consists of a central engine radiating ionising X-rays and UV photons. The line-driven wind is launched from a geometrically thin and optically thick Keplerian disk. The accretion disk has inner edge radius of $3r_{\rm S}$, where $r_{\rm S} = 2GM_{\rm BH}/c^2$ is the Schwarzschild radius, and spans up to outer radius of 1000 times larger than the inner radius.

They demonstrated that a line-driven wind can be formed for the case of a $10^8\,M_\odot$ black hole accreting at a rate of $1.8\,M_\odot\,{\rm yr}^{-1}$ with disk luminosity of $0.5\,L_{\rm Edd}$. The density and poloidal component velocity field maps for this system are presented in Fig. 3.8. There are three components of the flow. The polar region contains hot, low density, and high photoionisation parameter gas, while warm, dense, and fast gas occupies the equatorial region. A transitional zone also exists in between whereby hot outflows are unable to escape.

The line force is less likely to dominate in the polar region since the gas is highly ionised. On the other hand, the high density and low ionised gas enables the wind to be driven radiatively from the inner disk of the equatorial region, with wind covering factor of ~ 0.2 at opening angle $\theta \sim 70^\circ$ relative to the rotation axis of the disk. The process causes the density to decrease with increasing temperature and photoionisation parameter, which continues until the gas is fully ionised. In this situation, the line force becomes inefficient at ejecting the material and the gas returns to the accretion disk. This 'failed wind' scenario is required to shield the fast stream of gas in the equatorial

region from X-ray radiation, and hence ensuring line force at outer region of $\lesssim 10^{16}$ cm. However, the disk-wind is unstable and dense knots are produced within a couple of years.

While Proga et al. (2000) assume that the X-ray and UV radiation from the central engine contribute equally, Proga & Kallman (2004) consider that the dominant contribution of 90% is from the UV band. They reported that the solution of the flow also relies on the luminosity and the BH mass of the system. When the disk luminosity is lower than $0.1\,L_{\rm Edd}$, no wind is created since the decrease in the wind mass flux density causes the the wind to be more vulnerable to over-ionisation. For a source with disk luminosity of about $0.5\,L_{\rm Edd}$, the one that has a higher BH mass of $\gtrsim 10^7\,M_\odot$ will be easier to generate line-driven wind.

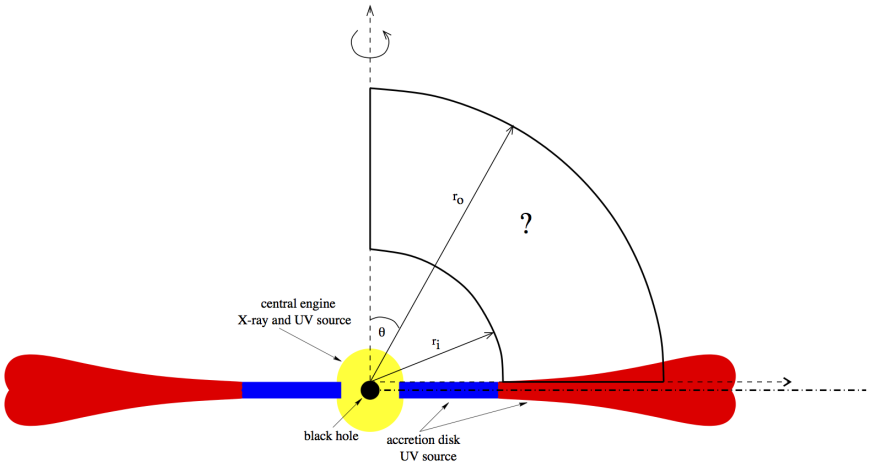

Figure 3.7: A schematic of hydrodynamic line-driven disk-wind model proposed by Proga et al. (2000).

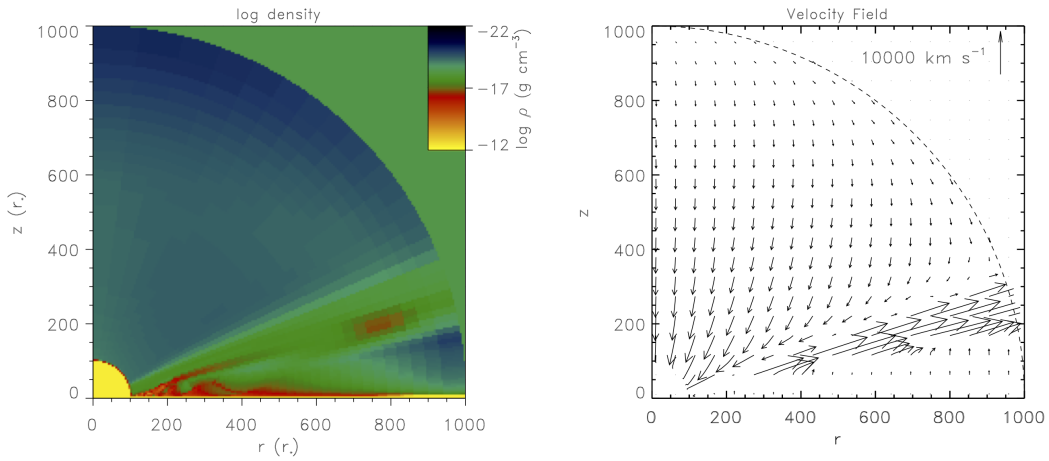

(a) Density map

(b) Poloidal velocity field map

Figure 3.8: Map of disk-wind solution from Proga et al. (2000).

3.2 Kinematical Disk-wind Model

In this section, we introduce our BLR disk-wind modelling approach. The kinematics of our BLR disk-wind model is adopted from Shlosman & Vitello (1993), designed initially for CVs. The similarities in the geometries, kinematics, and ionisation state between CVs and AGN, suggest this model can be implemented to study the characteristics of AGN (Higginbottom et al. 2013, 2014; Matthews et al. 2016). A schematic of the model is depicted in Fig. 3.9. We also incorporate radiative transfer effects to generate the line profiles using the Sobolev (high velocity gradient) approximation, following previous work (Chiang & Murray 1996; Murray & Chiang 1997; Flohic et al. 2012).

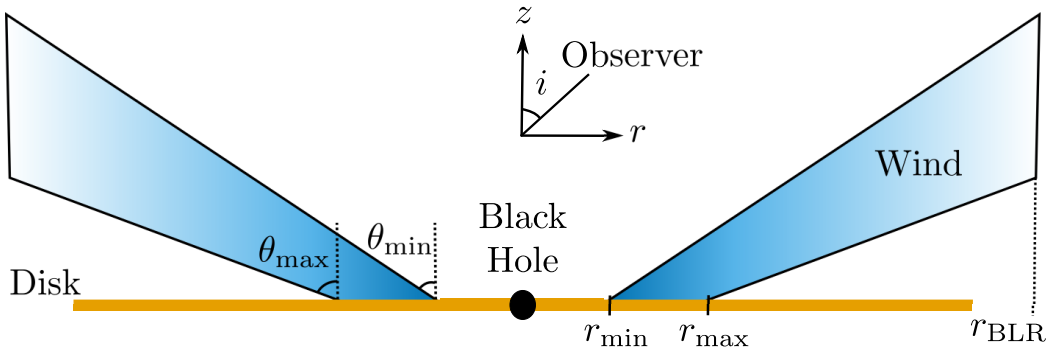

Figure 3.9: A sketch of the geometry and main parameters of our cylindrical disk-wind model.

3.2.1 Wind Kinematics

The BLR model of size $r_{\rm BLR}$ with $M_{\rm BH}$ BH at the centre is assumed to have an axially symmetric geometry, which we describe using cylindrical coordinates (r, ϕ, z). The radial and azimuthal coordinates, r and ϕ, are located on the xy-plane, which is defined as the plane of the accretion disk surface. The z-axis is defined as the rotation axis of the disk. The angle between the z-axis and the line-of-sight of the observer is defined by the inclination angle, i.

The disk-wind model is described by two main components: the accretion disk and wind. The accretion disk is assumed to be flat and geometrically thin, but optically thick such that the far side of the disk is obscured. A conical outflowing wind emanates from the accretion disk with inner and outer radii of $r_{\rm min}$ and $r_{\rm max}$. The boundary of the wind opening angle is between $\theta_{\rm min}$ and $\theta_{\rm max}$. The wind streamline spirals upwards in a three-dimensional helical motion at a constant opening angle, θ, given by

$$\theta = \theta_{\rm min} + (\theta_{\rm max} - \theta_{\rm min})x^{\gamma}, \tag{3.4}$$

where $x = (r_0 - r_{\rm min})/(r_{\rm max} - r_{\rm min})$, r_0 is the origin position of a single streamline, and γ is used to adjust the concentration of the streamlines toward either the inner or outer boundaries of the wind. Throughout our investigations we have set $\gamma = 1$, which corresponds to even angular spacing between the streamlines.

The total velocity at any given point inside the wind is expressed in terms of the poloidal velocity, v_l, and rotational velocity, v_ϕ. The poloidal velocity describes the velocity component along the streamline, which consists of a combination of the radial component, v_r, and vertical component, v_z. It specifies the velocity in the rz-plane, which is given by

$$v_l = v_0 + (v_\infty - v_0)\left[\frac{(l/R_v)^\alpha}{(l/R_v)^\alpha + 1}\right], \tag{3.5}$$

where v_0 is the initial poloidal wind velocity at the surface of the disk (set arbitrarily at $6\,{\rm km\,s^{-1}}$; Higginbottom et al. 2013; Shlosman & Vitello 1993), $l = [(r - r_0)^2 + z^2]^{1/2}$ is the distance along a poloidal streamline, R_v is the wind acceleration scale height characterising the scale at which the wind reaches half its terminal velocity v_∞, and α is a power-law index that controls the shape of the acceleration profile. Furthermore, v_l is correlated to v_r and v_z such that $v_r = v_l \sin\theta$ and $v_z = v_l \cos\theta$. In our model, the asymptotic wind velocity or the terminal velocity, v_∞, is taken to be equal to the escape velocity, $v_{\rm esc} = (2GM_{\rm BH}/r_0)^{1/2}$.

The initial rotational velocity on the surface of the disk is presumed to be Keplerian, $v_{\phi,0} = (GM_{\rm BH}/r_0)^{1/2}$. The assumption that the wind conserves specific angular momentum implies that the rotational velocity decreases linearly as the wind is accelerated radially outwards, given by

$$v_\phi = v_{\phi,0}\left(\frac{r_0}{r}\right). \tag{3.6}$$

For a particular point (r, z) in the wind, the density, ρ is determined using the mass continuity equation

$$\rho(r, z) = \frac{r_0}{r}\frac{{\rm d}r_0}{{\rm d}r}\frac{\dot{m}(r_0)}{v_z(r, z)}, \tag{3.7}$$

where the factor $(r_0/r)({\rm d}r_0/\,{\rm d}r)$ scales as the streamline area increases with outflowing wind. The mass-loss rate per unit surface of the disk, $\dot{m}$, is

$$\dot{m}(r_0) = \dot{M}_{\rm wind}\frac{r_0^\lambda \cos\theta(r_0)}{\int {\rm d}A\, r_0'^\lambda \cos\theta(r_0')}, \tag{3.8}$$

where $\dot{M}_{\rm wind}$ is the total mass-loss rate of the wind, λ is the mass-loss rate exponential, and the term $\cos\theta$ represents the angle formed between the streamline and the disk. A uniform mass-loss with radius is indicated by $\lambda = 0$. Here, $\dot{M}_{\rm wind}$ is taken to be equivalent to $\dot{M}_{\rm acc}$. The notations for the model parameters are listed in Table 3.1.

There is strong evidence that the gas in the BLR is stratified, with high ionisation lines situated closer to the ionising source than the low ionisation lines (Peterson & Wandel 1999; Kollatschny 2003; Peterson 2014). To mimic the stratified structure of the wind, we separate the wind into 'wind zones' of 4 rows and 4 columns that consist of

narrow streams of cones, as illustrated in Fig. 3.10. An individual zone is designated by the location of its row and column $[a, b]$, starting from the base of the wind, closest to the central ionising source, to increasing radial distance.

Table 3.1: Notation for the model parameters.

Parameter	Notation
Black hole mass	$M_{\rm BH}$ $(M_\odot)$
BLR size	$r_{\rm BLR}$ (cm)
Wind radius	$r_{\rm min}$; $r_{\rm max}$ (cm)
Wind opening angle	$\theta_{\rm min}$; $\theta_{\rm max}$
Concentration of streamline	γ
Initial poloidal velocity	v_0 $(\mathrm{km\,s^{-1}})$
Scale height	R_v (cm)
Acceleration power law index	α
Mass-loss rate exponent	λ
Total mass-loss rate	$\dot{M}_{\rm wind}$ $(M_\odot\,\mathrm{yr^{-1}})$

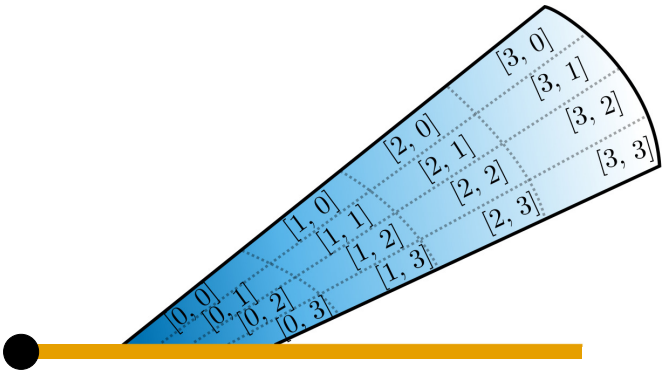

Figure 3.10: A sketch of the 'wind zones' numbered by rows and columns, from bottom to top and left to right.

3.2.2 Disk-wind Radiative Transfer

When the flow speed is much larger than the mean thermal speed of the gas, radiation at a given frequency as seen by a fixed observer comes primarily from a unique mathematical surface (iso-velocity surface). In such situations, the full radiative transfer can be treated by the approximate escape probability method or Sobolev approximation. In this case, the wind opacity in a given direction mostly depends on the velocity gradient in that direction. Following Rybicki & Hummer (1978, 1983) prescriptions, the monochromatic

specific luminosity, $\mathcal{L}_\nu$, with frequency ν in the direction $\hat{n}$ over volume V is given by

$$\begin{aligned}\mathcal{L}_\nu^{\mathrm{S}}(\hat{n}) &= \int I_\nu \, \mathrm{d}V \\ &= \int k(r_s) S_\nu(r_s) \frac{1 - e^\tau}{\tau} \delta \left[\nu - \nu_0 \left(1 + \frac{v_{\mathrm{los}}}{c} \right) \right] \mathrm{d}V, \end{aligned} \tag{3.9}$$

where I_ν is the intensity. The integrated line opacity, $k(r_s)$, and source function, $S(r_s)$, are written as functions of spherical radius. We have taken a fiducial $S'(r_s) = k(r_s)S(r_s) \propto r_s^{-\beta}$ as a power law function with exponent, $\beta \simeq 1$. Assuming that the line-of-sight does not intersect multiple resonant surfaces, which occurs when $v_{\mathrm{los}}/c = (\nu - \nu_0)/\nu_0$, where v_{los} is the line-of-sight velocity of the particle and ν_0 is the central frequency.

Within the Sobolev approximation, the optical depth is

$$\tau = \frac{\xi}{|Q|}, \tag{3.10}$$

where the $\xi = kc/\nu_0$. Roughly, the value of $\xi = 1\,\mathrm{s}^{-1}$ will yield an optically thin wind with $\tau < 1$, while $\xi = 10^{10}\,\mathrm{s}^{-1}$ for an optically thick wind. The parameter $Q \equiv \hat{n} \cdot \mathbf{\Lambda} \cdot \hat{n}$ is the double-dot product of the strain tensor, $\mathbf{\Lambda}$, with the line-of-sight vector, $\hat{n}$, and describes the gradient along the line-of-sight wind velocity. In cylindrical coordinates, Q is expressed as

$$\begin{aligned} Q = \sin^2 i [\Lambda_{rr} \cos^2 \phi + \Lambda_{\phi\phi} \sin^2 \phi - 2\Lambda_{r\phi} \sin\phi \cos\phi] \\ \cos i [2\Lambda_{rz} \sin i \cos\phi + \Lambda_{zz} \cos i - 2\Lambda_{\phi z} \sin i \sin\phi]. \end{aligned} \tag{3.11}$$

Due to azimuthal symmetry, the contribution from $\partial/\partial\phi = 0$ and the elements of the strain tensor (Chajet & Hall 2013) are as follows

$$\begin{aligned} \Lambda_{r\phi} = \frac{1}{2}\left(\frac{\partial v_\phi}{\partial r} - \frac{v_\phi}{r} \right), \quad \Lambda_{rz} = \frac{1}{2}\left(\frac{\partial v_r}{\partial z} + \frac{\partial v_z}{\partial r} \right), \\ \Lambda_{\phi z} = \frac{1}{2}\frac{\partial v_\phi}{\partial z}, \quad \Lambda_{rr} = \frac{\partial v_r}{\partial r}, \quad \Lambda_{\phi\phi} = \frac{v_r}{r}, \quad \Lambda_{zz} = \frac{\partial v_z}{\partial z}. \end{aligned} \tag{3.12}$$

3.2.3 Emission Line Construction

Since this study is focussed on understanding the kinematical signatures of BELs, no attempt has been made to include the effects of photoionisation. After the kinematical disk-wind model is initialised, the code proceeds by populating particles within the boundaries of each 'wind zone'. A Monte Carlo simulation is implemented to generate a large number of particles. Random points are first created in spherical coordinates (l, ϕ, θ) such that the wind forms an angle θ at a particular l in the 'wind zone'. The coordinates are then transformed to cylindrical coordinates (r, ϕ, z) in order to evaluate the projected velocity along the line-of-sight, v_{los}. For a given zone, the v_{los} is computed

for a range of inclination angles, i, from 5° to 85°, and binned into histograms. The counts in each bin are weighted by a density distribution and intensity from radiative transfer. To produce a smooth line profile, the distribution is also convolved using a Gaussian kernel with standard deviation of 3 bins. These steps are repeated for every 'wind zone'. A discussion on the histogram binning is elaborated in § 3.2.4.

The resulting line profiles are purely based on the kinematics of the wind with an optical depth correction. Photoionisation is excluded in our simulations. This should not have a significant effect on the line profiles derived from local sections of the wind, within which incident flux is relatively constant. In addition, plausible clumpiness in the wind (Matthews et al. 2016) and obscuration by the dusty torus (Krolik & Begelman 1988) are not included.

3.2.4 Density Estimation

Density estimation is often applied in statistics and is a useful technique to estimate the underlying probability density function of the observed data. In essence, the emission line profile created is an estimate of the probability of a random data point along a particular line-of-sight velocity. One common representation of the density estimation is a histogram.

A histogram is a nonparametric density estimator, in a sense that less rigid distributional assumptions are made on the probability distribution of the variable. It is constructed by binning the data ranges into intervals of equal bin width and then tallying the data points within each interval. Generally, there is no definitive rule to determine the optimal number of bins. However, the graphical presentation of the data depends on the choice of bin width. The number of bins is inversely proportional to the bin size, so the number of bins increases with decreasing bin width. The size of the bin serves as a smoothing parameter and regulates the bias-variance trade-off. If the bin width chosen is small (high variance), the density estimation will be more precise, but it will also yield a noisier distribution. In contrast, if the bin width is wide (high bias), the density distribution will be smoother since noise from randomness in sample is reduced, but this will induce loss of valuable relations.

Although there are several rules of thumb, the number of bins is calculated using the square-root of the total number of samples. This was chosen for simplicity and also because the choice plays a secondary role as the histogram will be further smoothed by convolving with a Gaussian kernel. In addition, the histogram is also normalised to display the relative counts that fall into the respective bin.

As a comparison, Fig. 3.11 displays the effect of changing the amount of smoothing governed by the standard deviation or width of the Gaussian kernel for single- and double-peaked line profiles. For a small kernel width of $\sigma = 1$, the line profiles match well with the original histogram (yellow), especially the maximum peak. One drawback

is that they are also more prone to random noise, which makes it difficult to evaluate the line profile statistics. Although with $\sigma = 2$, the emission line profile seems to be able to capture the major structure of the data distribution for single-peaked case, it is still slightly noisy for the double-peaked case. With increasing Gaussian kernel width, the distribution becomes smoother. However, this will also incur an increase in bias and subsequently yield an over-smoothed line profile. The height of the peaks is mildly diminished and both sides of the line profile wing are broader, which leads to a biased line profile measurements. For the rest of the line profile creation, the histogram is convolved with a Gaussian kernel of standard deviation 3 pixels since it provides a reasonable visualisation of the underlying shape of the distribution.

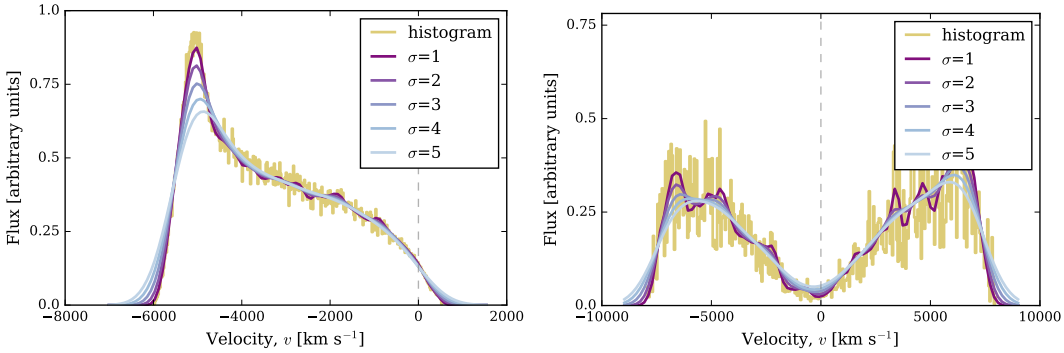

(a) Single-peaked

(b) Double-peaked

Figure 3.11: Degree of smoothing dependence on the choice of standard deviation of the Gaussian kernel, σ. The original histogram is displayed in yellow. The dashed grey vertical line shows the systemic centroid of the line.

3.3 Summary

In this chapter, we have introduced one of the favoured BLR models, which is the disk-wind model. We developed a simple kinematical disk-wind BLR model with the incorporation of radiative transfer in the Sobolev limit. This model provides a major framework for the subsequent chapters, giving an insight into the structure of the BLR.

CHAPTER 4

Narrow Disk-wind Model

This chapter is based on the publication:

- *Yong, S. Y., Webster, R. L., King, A. L., Bate, N. F., O'Dowd, M. J., & Labrie, K. (2017). The Kinematics of Quasar Broad Emission Line Regions Using a Disk-Wind Model.* PASA*, 34, e042. ADS: 2017PASA...34...42Y. doi: 10.1017/pasa.2017.37*

Abstract

Based on the kinematical disk-wind model described in the previous chapter, we explore the model in the context of a narrow outflowing wind angle. We examine how angle of viewing affects the observed characteristics of the emission line, especially the line widths and velocity offsets. The line profiles were found to exhibit distinct properties depending on the orientation, wind opening angle, and region of the wind where the emission arises.

At low inclination angle (close to face-on), we find the shape of the emission line is asymmetric with narrow width and significantly blueshifted. As the inclination angle increases (close to edge-on), the line profile becomes more symmetric, broader, and less blueshifted. Additionally, lines that arise close to the base of the disk wind, near the accretion disk, tend to be broad and symmetric. The relative increase in blueshift of the emission line with increasing wind vertical distance is larger for polar winds compared with equatorial winds. By considering the optical thickness of the wind, single-peaked line profiles are recovered for the intermediate and equatorial outflowing wind. The model is also able to reproduce a faster response in either the red or blue sides of the line profile, consistent with reverberation mapping studies. A quicker response in the red side is achieved in the model with a polar wind and intermediate wind opening angle at low viewing angle. The blue side response is faster for an equatorial wind seen at high inclination.

4.1 Background

The immense power of a quasar comes from accreting mass onto the central black hole via the accretion disk. During the accretion process, gravitational potential energy is converted into radiation via viscous dissipation, creating the continuum we observe. The emitted continuum radiation photoionises the surrounding gas, which is deep in the potential well of the black hole, allowing the formation of the BLR. Since the BLR is too small spatially to be resolved by modern telescopes even for the most nearby objects, its geometry, kinematics, and dynamics remain elusive.

The goal of this thesis is to provide qualitative constraints on BEL models through simple kinematical modelling of a basic disk-wind model. We explore the effect of orientation on the shapes of the emission lines for outflowing winds with narrow opening angles. The details of the line shapes, in particular the line widths and velocity offsets, will hopefully enable us to describe the kinematics and dynamics of the BLR. The overview is as follows. § 4.1 provides complementary information on the emission lines. The details on modelling the disk-wind are explained in § 4.2. § 4.3 presents the generated line profiles. In § 4.4, the implications of wind opening angle, inclination angle, and wind region on the line widths and velocity offsets are explored. The conclusions are given in § 4.5.

4.1.1 Shape of Emission Line

A common feature of a quasar spectrum in the optical and UV regimes is the BELs. The properties of BELs provide crucial details on the nature of the BLR. The BEL profiles show wide diversity in their widths and shapes. Their line widths commonly exceed $10^3\,\mathrm{km\,s^{-1}}$ and can extend to $10^4\,\mathrm{km\,s^{-1}}$. In general, the width of the HILs, such as C IV, are found to be broader than the LILs, such as Mg II (e.g., Shuder 1982; Mathews & Wampler 1985). The variation in line profile shapes reflects the dynamics of the emitting gas in the BLR. This provides valuable information on the structure and geometry of the emission line region.

It has been known for several decades that there is an offset between different ionisation lines (e.g., Gaskell 1982; Wilkes 1986; Espey et al. 1989; Tytler & Fan 1992; McIntosh et al. 1999; Vanden Berk et al. 2001; Shen et al. 2016). The HILs are usually seen blueshifted relative to LILs. This blueshift can be interpreted as a consequence of an outflowing wind component and obscuration by the disk (Gaskell 1982; Leighly 2004; Richards et al. 2011), and is one of the major motivators for the disk-wind model.

4.1.2 Variability of Emission Line

One of the techniques used to probe the structure of the BLR is RM (Blandford & McKee 1982; Peterson 1993). This method measures a time delay between emission line flux variations and continuum flux variations. Analyses based on RM results infer that the BLR has a stratified ionisation structure (Peterson & Wandel 1999; Kollatschny 2003; Peterson et al. 2004). The HILs are found to have a shorter time lag compared to that of LILs. This suggests that the HILs are located closer to the central engine, while the LILs are situated further out (Gaskell & Sparke 1986; Clavel et al. 1991; Peterson & Wandel 1999; Kollatschny 2003).

Variability in the line profile provides a way to extract information on the geometry and kinematics of the BLR (e.g., Bahcall et al. 1972; Blandford & McKee 1982; Capriotti et al. 1982; Horne et al. 2004; Pancoast et al. 2011). By measuring the time delays of emission lines as a function of line-of-sight velocity, a velocity-delay map can be constructed, which makes it possible to predict whether the BLR dynamics are dominated by inflow, outflow, or rotation (Horne et al. 2004). Different studies have reached the following conclusions: an asymmetric velocity profile with faster response in the red or blue wing of the line tends to be associated with infall or outflow, respectively; for virialised gas motion, the velocity profile is symmetric with quicker response in the line wings compared to the line core. Through analyses of the recovered velocity-delay maps from velocity-resolved RM, most objects show combinations of infall and rotation since the red side of the line wing tends to have a shorter lag than the blue side (e.g., Gaskell 1988; Koratkar & Gaskell 1989; Crenshaw & Blackwell 1990; Korista et al. 1995; Ulrich & Horne 1996; Kollatschny 2003; Bentz et al. 2010; Grier et al. 2013). However, a signature of outflow, with the blue line wing leading, has been found in some objects (e.g., NGC 3227, Denney et al. 2009).

4.2 Modelling the Narrow Wind

The prescription of the wind kinematics is as provided in § 3.2. Additionally, we also investigate the effects of optical depth and time delay of the emission lines. We choose to examine two optical depth cases, one where ξ is $1\,\mathrm{s}^{-1}$ and another where ξ is $10^{10}\,\mathrm{s}^{-1}$. These values were chosen so that the optical depth of all the points in the wind are optically thin, $\tau < 1$, in the first case, and optically thick for the other.

The time lag of each particle due to the light travel time is determined from the centre of the ionising source. During the line profile creation, the line profile is separated into the blue and red sides from the median velocity, and the mean time delays, $\langle\tau\rangle$, are calculated for both sides. The difference in mean time delay between the blue and the red side, $\langle\tau_\mathrm{b}\rangle - \langle\tau_\mathrm{r}\rangle$, is then calculated for every zones.

4.2.1 Parameter Choice

The geometry of the narrow wind is similar to the models proposed by Murray et al. (1995) and Elvis (2000, 2004) to describe the phenomenology of BELs and BALs in quasars. In our model, the vertical component of the wind proposed in Elvis (2000, 2004), where the wind is lifted vertically off the disk before being accelerated outwards, is not incorporated.

The list of parameters in the model is shown in Table 4.1. Two of the main parameter values, specifically the black hole mass and wind radius, are selected according to the funnel disk-wind model proposed by Elvis (2000, 2004). This is based on one of the most extensive RM AGN, Seyfert 1 NGC 5548, which is estimated to have $M_{\rm BH} \sim 7 \times 10^7\,M_\odot$ with lower and upper limit wind radii of ~ 10 light-days (2.59×10^{16} cm or $175\,r_{\rm g}$, where $r_{\rm g} = GM_{\rm BH}/c^2$ is the gravitational radius) and ~ 30 light-days (7.77×10^{16} cm or $526\,r_{\rm g}$) from the emitting region size of HIL C IV and LIL Mg II respectively (Clavel et al. 1991; Peterson & Wandel 1999).

The size of the BLR wind region is bounded within $r_{\rm BLR} = 2 \times 10^{17}$ cm, in both radius and height. The value is chosen such that the effects of the poloidal velocity can be seen. This fiducial radius generally agrees with results from RM and microlensing. For a quasar with black hole mass of $M_{\rm BH} \sim 10^8\,M_\odot$, RM studies found that the size of the BLR using Balmer lines is about 1×10^{17}–5×10^{17} cm (Wandel et al. 1999; Kaspi et al. 2000). Microlensing measurements of the quasar QSO 2237+0305 estimates the BLR radius for HIL C IV to be $\sim 2 \times 10^{17}$ cm with $M_{\rm BH} \sim 10^{8.3}\,M_\odot$ (Sluse et al. 2011). For $M_{\rm BH} \sim 4 \times 10^8\,M_\odot$ BAL quasar H1413+117, the BLR size is $\gtrsim 2.9 \times 10^{16}$ cm (O'Dowd et al. 2015).

Based on the evidence that the fraction of BAL quasars is around 20% of the overall quasar population (Weymann et al. 1991; Hewett & Foltz 2003; Knigge et al. 2008; Allen et al. 2011), we set the wind to have a narrow opening angle of 10°. This is obtained assuming that the fraction is associated to $\sin\theta = 20/100$, which yields $\theta \lesssim 11.5°$. However, due to the anisotropic continuum radiation from the accretion disk, the fraction of BALs in optical flux-limited samples might be larger when the outflowing wind opening angle is close to equatorial (Krolik & Voit 1998). Scattering attenuation of the continuum may also induce substantial bias on the true BAL covering fraction (Goodrich 1997). These factors are ignored for simplicity. We test ranges of minimum and maximum narrow wind opening angles from polar ($\theta_{\rm min} = 5°; \theta_{\rm max} = 15°$), intermediate (e.g., $\theta_{\rm min} = 40°; \theta_{\rm max} = 50°$), to equatorial ($\theta_{\rm min} = 75°; \theta_{\rm max} = 85°$). The intersections of the wind zone with inclination angle will be presented in § 4.2.2.

The acceleration scale height, R_v, is set to 25×10^{16} cm. The power law index that adjusts the acceleration of the wind, α, is taken to be 1, such that the acceleration increases slowly with increasing poloidal distance. Assuming an accretion efficiency of $\eta = 0.1$, the total mass accretion rate for a source with high luminosity of $L \approx 10^{46}\,{\rm erg\,s^{-1}}$

and black hole mass of $10^8\,M_\odot$ is $\dot{M}_{\rm acc} \approx 2\,M_\odot\,{\rm yr}^{-1}$ (Peterson 1997). The total mass-loss rate of the wind, $\dot{M}_{\rm wind}$, is fixed to be equal to the total mass accretion rate, $\dot{M}_{\rm acc} = 2\,M_\odot\,{\rm y}^{-1}$. The kinematics of the outflow for the fiducial BLR disk-wind model will be elaborated in § 4.2.3. Quantitative effects due to different choices of some parameter values will be explored in § 4.4.6.

Table 4.1: Adopted parameter values in the fiducial narrow wind model.

Parameter	Notation	Value
Black hole mass	$M_{\rm BH}$ $(10^8\,M_\odot)$	1.0
BLR size	$r_{\rm BLR}$ $(10^{16}\,{\rm cm})$	20.0
	$r_{\rm BLR}$ (light-days)	77.2
	$r_{\rm BLR}$ $(r_{\rm g})$	1354.1
Wind radius	$r_{\rm min}$; $r_{\rm max}$ $(10^{16}\,{\rm cm})$	1.0; 2.0
	$r_{\rm min}$; $r_{\rm max}$ (light-days)	3.9; 7.7
	$r_{\rm min}$; $r_{\rm max}$ $(r_{\rm g})$	67.7; 135.4
Wind opening angle	$\theta_{\rm min}$; $\theta_{\rm max}$	Within 10°
Scale height	R_v $(10^{16}\,{\rm cm})$	25.0
	R_v (light-days)	96.5
	R_v $(r_{\rm g})$	1692.6
Acceleration power law index	α	1.0
Total mass-loss rate	$\dot{M}_{\rm wind}$ $(M_\odot\,{\rm yr}^{-1})$	2.0

4.2.2 Wind Zone

As aforementioned, the rationale of partitioning the wind into 'wind zones' is to resemble the stratification of the different ionisation lines in the BLR geometry, which is consistent with the evidence of different time lags measured for LILs and HILs in RM studies. Essentially, this approach provides a way to examine the emission line properties in distinct emitting zone. To get an insight on which wind zones intersect with the sight lines, illustrations of the narrow winds viewed at various inclination angles are depicted in Fig. 4.1.

In all cases, a close to pole-on viewing angle of $i = 5°$ intercepts none of the wind zones, even for the polar wind since the initial baseline radius does not start at the centre of the rotation axis. A viewing angle near edge-on of $i = 85°$ will certainly intersect zones $[0, b]$ for all narrow wind models, and additionally zones $[a, 3]$ for equatorial wind. Meanwhile, a viewing angle at $i = 45°$ crosses zones $[0, b]$ in polar wind model, mostly zones $[a, 0]$ in intermediate wind model, but none in the equatorial wind model.

These are particularly useful in identifying the trends in the line width and blueshift of the line profiles, as will be shown later in the findings. In brief, when the line-of-sight and the outflowing wind are close to or intersect one another, the line profile will be

broader and more blueshifted[1]. Though, it is also subjected to other factors including the wind zone position and the angle of outflow.

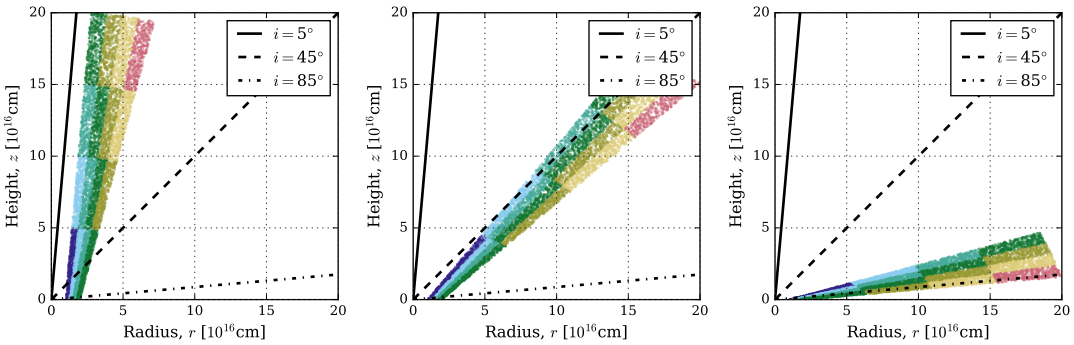

(a) Polar wind 5°–15° (b) Intermediate wind 40°–50° (c) Equatorial wind 75°–85°

Figure 4.1: Plot of intersections between wind zones and inclination angle. The discrete colours merely to distinguish the generated random points in each zone.

4.2.3 Wind Velocity and Density

Before delving into the characteristics of the line profile, first lets examine the kinematics of the narrow disk-wind model with the specified fiducial parameter values given in Table 4.1. The physical properties of the outflow, which include the velocity components, total velocity, velocity gradient, and density, for three wind opening angles are shown in the contour plots in Figs. 4.2 to 4.4.

Initially, the wind is driven off the base of the accretion disk. For regions close to the streamline of the wind, the wind velocity is governed by the rotational component, v_ϕ, and can be as large as $\sim 12\,000\,\mathrm{km\,s^{-1}}$. This is due to the fact that matter is accreted into the disk and subsequently contributes to the Keplerian motion. As the wind spirals upward in a helical movement, the wind gradually gains an increase in the poloidal velocity while the rotational velocity continues to decrease. At some point, the poloidal part of the wind will dominate and be larger than the rotational part. This transition occurs at different positions depending on the angle of the wind, which can be seen in the total velocity plot. The total velocity is a combination of these two velocity components and represents the unprojected total velocity, i.e., without accounting for the projection onto the line-of-sight. Radially further from this location, a significant portion of the wind velocity comes from the poloidal term. It can achieve $\sim 8000\,\mathrm{km\,s^{-1}}$ at maximum height or a radius of 2×10^{17} cm.

One of the primary factors that determines whether a line profile will be single-peak is through the velocity gradient, defined by the poloidal over rotational velocity shear $|(\mathrm{d}v_l/\,\mathrm{d}r)/(\mathrm{d}v_\phi/\,\mathrm{d}r)|$ (Chiang & Murray 1996; Murray & Chiang 1997). If the poloidal

[1]Negative velocity indicates blueshift and positive velocity indicates redshift (see Fig. 2.3).

shear is greater than the rotational shear $|(\mathrm{d}v_l/\,\mathrm{d}r)/(\mathrm{d}v_\phi/\,\mathrm{d}r)| \gtrsim 1$, then there is a higher likelihood of photons to travel radially, which will lead to the formation of single-peaked emission lines. As shown in Fig. 4.2d, it is challenging for the polar wind model to attain single-peaked lines since the ratio is never more than 1 regardless of the wind zones. In contrast, the intermediate Fig. 4.3d and equatorial narrow wind Fig. 4.4d are able to satisfy this limit for all wind zones except those that are near the wind base. Due to the higher rotational shear in those regions, the line profiles are expected to remain double-peaked. The radial shear increases as the wind travels further away; therefore, the increased ratio.

Considering the case for a uniform mass-loss rate of $\lambda = 0$, the densities for the intermediate and equatorial wind models have roughly the same range of values within $\sim 10^{-18}$–$10^{-12}\,\mathrm{g\,cm^{-3}}$, whereas the range is slightly smaller within $\sim 10^{-17}$–$10^{-13}\,\mathrm{g\,cm^{-3}}$ for polar wind model. However, the variation in the densities are different in each model. The density gradient in polar wind model seems to be flatter compared to that of intermediate and equatorial wind. The inverse relationship between the density and poloidal velocity implies that the regions near the base of the outflow will be denser and becoming less dense with increasing poloidal distance, which complies with the continuity and mass conservations.

While the results presented here are for specific models, they serve as a vital insight on the motion of the particles in the BLR wind. Accordingly, this will enable us to infer whether a region in the wind is dominated by rotational or poloidal velocity component, and hence predicts the shape of the line profile. § 4.4.6 will be dedicated to explore the sensitivity to the parameters.

4.3 Emission Line Profiles

The width and relative velocity shifts of the emission lines are highly dependent on the wind opening angles, inclination, and 'wind zone' position. We investigate the effects of changing these parameters on the line properties. Figures 4.5 and 4.6 present the generated emission lines as a function of viewing angle, $i = 5°$–$85°$, for optically thin wind with $\xi = 1\,\mathrm{s^{-1}}$ and optically thick wind with $\xi = 10^{10}\,\mathrm{s^{-1}}$. Each panel in the 'wind zones' represents the location in the wind as defined in Fig. 3.10. The emission line profiles in some zones exhibit small structures. This is caused by a resolution issue and primarily affects zones with a huge density variation, specifically those near the base of the wind $[0,\, b]$.

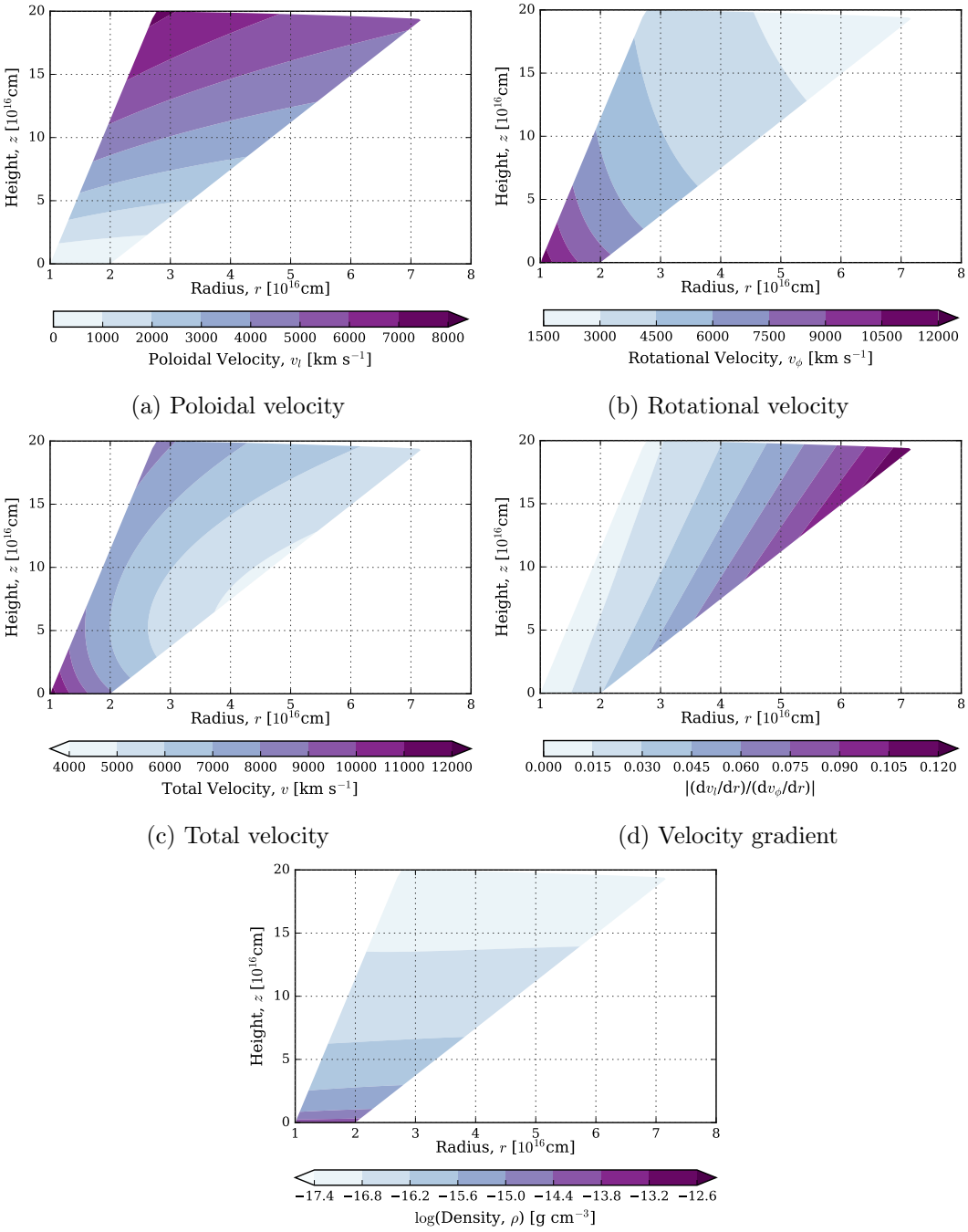

(a) Poloidal velocity

(b) Rotational velocity

(c) Total velocity

(d) Velocity gradient

(e) Density

Figure 4.2: Contour plot of outflow kinematics for polar wind with opening angle of 5°–15°.

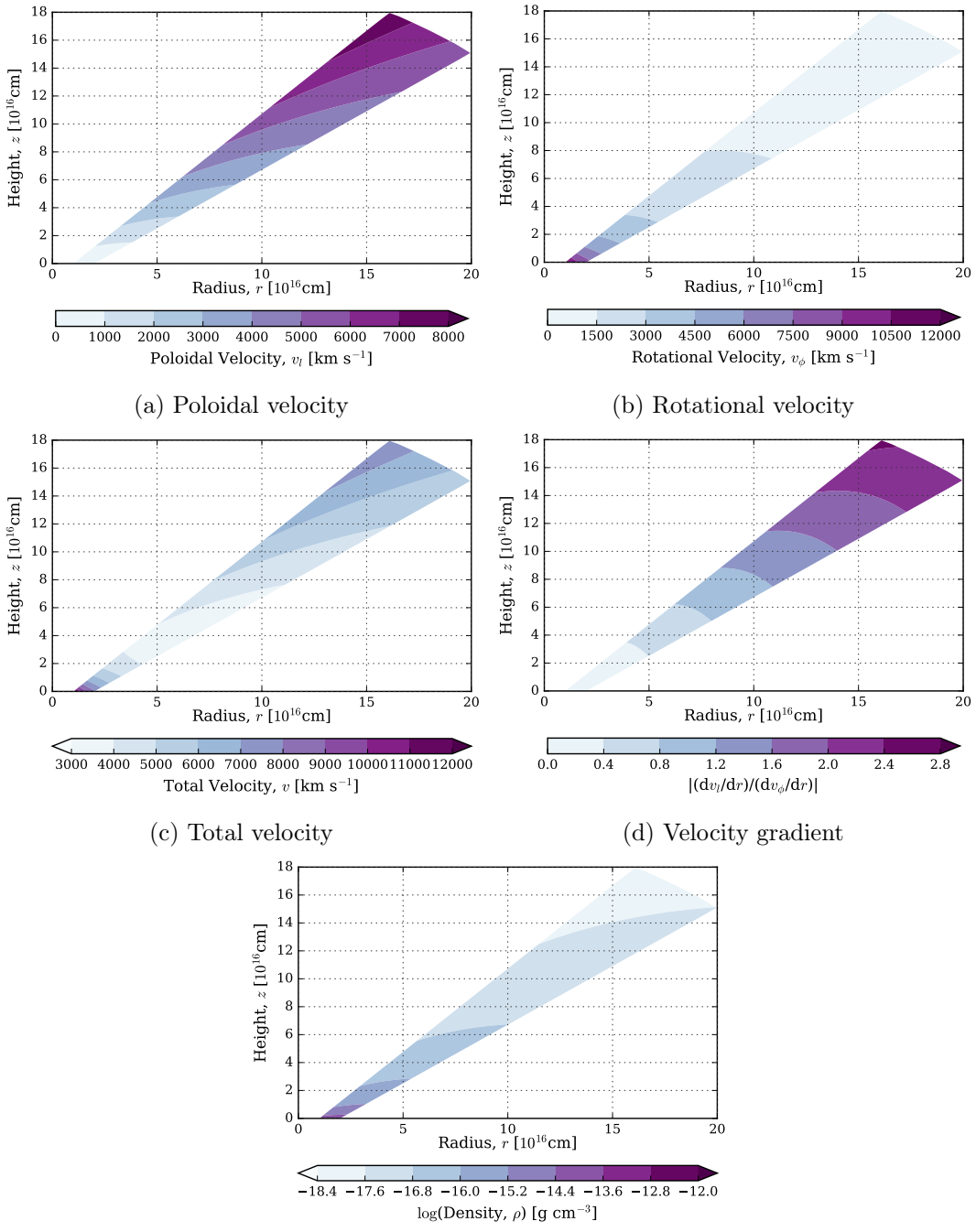

(a) Poloidal velocity

(b) Rotational velocity

(c) Total velocity

(d) Velocity gradient

(e) Density

Figure 4.3: Contour plot of outflow kinematics for intermediate wind with opening angle of 40°–50°.

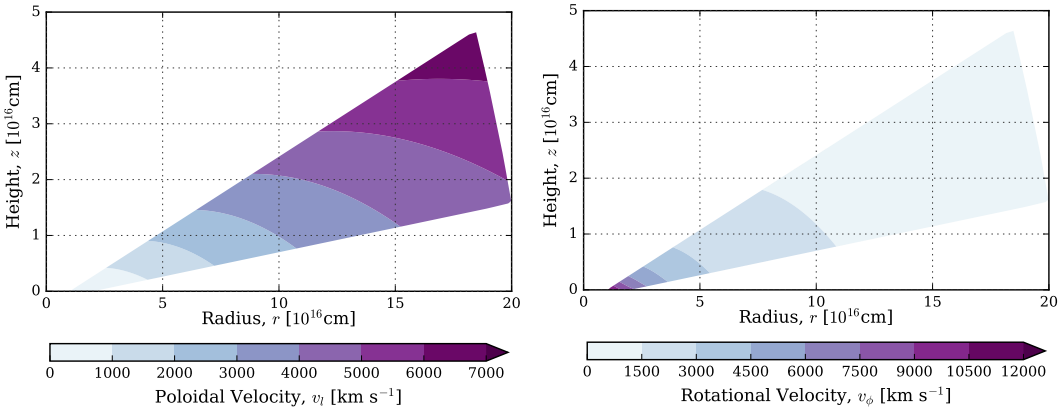

(a) Poloidal velocity

(b) Rotational velocity

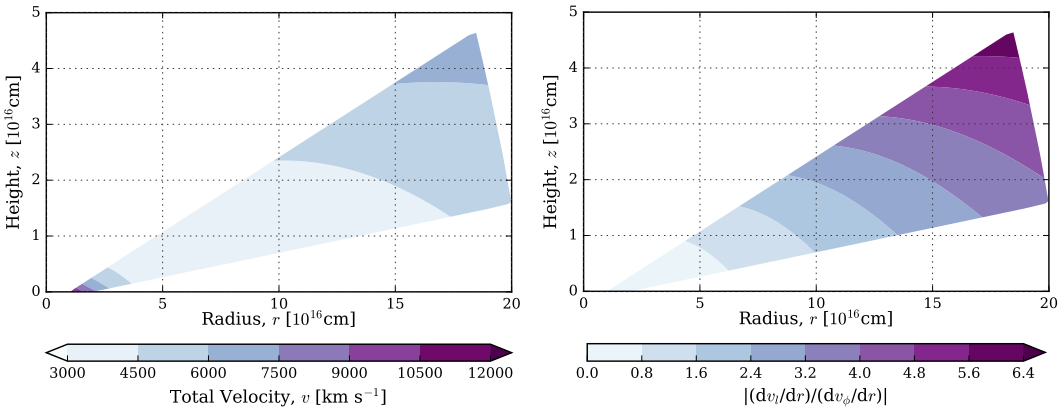

(c) Total velocity

(d) Velocity gradient

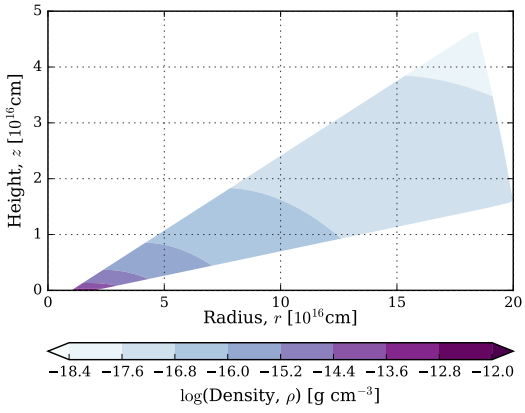

(e) Density

Figure 4.4: Contour plot of outflow kinematics for equatorial wind with opening angle of 75°–85°.

4.3.1 Emission Line Shape

In all cases, the line profiles are broadest at the base of the wind [0, b]. The line widths also decrease with increasing poloidal distances. However, for intermediate (Figs. 4.5b and 4.6b) and equatorial (Figs. 4.5c and 4.6c) wind opening angles, the widths start to become broader at a point above half of the total poloidal distance, i.e., 'wind zones' of [2, b] and [3, b], due to an increase in poloidal velocity.

The emission lines also tend to be more blueshifted, i.e., towards the negative side from the central axis of the line profile, as the wind travels farther away off the base in the direction of increasing height from [0, b] to [3, b]. This effect is more prominent for the polar outflowing wind (Figs. 4.5a and 4.6a) but is present in all wind models. For more equatorial winds, the relative velocity shift of the emission lines between regions is reduced. The line profiles become more redshifted in the direction of increasing horizontal distance from [a, 0] to [a, 3].

At high inclination angles close to $i = 90°$ (edge-on), the line profiles are roughly symmetric and less blueshifted relative to the axis centre. The lines are also broader compared to those for face-on viewing angle around $i = 0°$. When the viewing angle is close to face-on, the lines are asymmetric and exhibit a negative velocity offset. The differences are less pronounced in wind regions near the wind base.

A comparison between Figs. 4.5 and 4.6 illustrates the effects of optical depth on the line profiles. In the $\xi = 1\,\mathrm{s}^{-1}$ case, the wind is optically thin, while the $\xi = 10^{10}\,\mathrm{s}^{-1}$ case yields an optically thick wind. In the intermediate and equatorial wind, the double peaks combined to form a single peak line profile for the $\xi = 10^{10}\,\mathrm{s}^{-1}$ case, except for zones nearest to the base. However, the line profiles for the polar wind still exhibit double-peaked features even when the emission is optically thick. This is because the velocity shear $|(\mathrm{d}v_l/\,\mathrm{d}r)/(\mathrm{d}v_\phi/\,\mathrm{d}r)|$ is low (Chiang & Murray 1996; Murray & Chiang 1997). Single-peaked lines are expected to form when the radial shear is larger than the Keplerian shear as photons are more likely to escape radially in this case.

4.3.2 Time Delay

Figures 4.7 and 4.8 display the difference between mean time delays of blue and red sides, $\langle\tau_\mathrm{b}\rangle - \langle\tau_\mathrm{r}\rangle$, at varying opening angles of the wind and viewing angles for the two conditions of optical depth. The wind is optically thin using $\xi = 1\,\mathrm{s}^{-1}$ in Fig. 4.7 and optically thick with $\xi = 10^{10}\,\mathrm{s}^{-1}$ in Fig. 4.8. The mean time delays are colour-coded by their values. A negative difference (blue) implies the blue side response is faster than the red side of the line, and vice versa for positive value (red). Since the time delay is grouped into the blue and red parts from the median line-of-sight velocity of the line profile, a quicker response in the red side does not necessarily correspond to inflowing

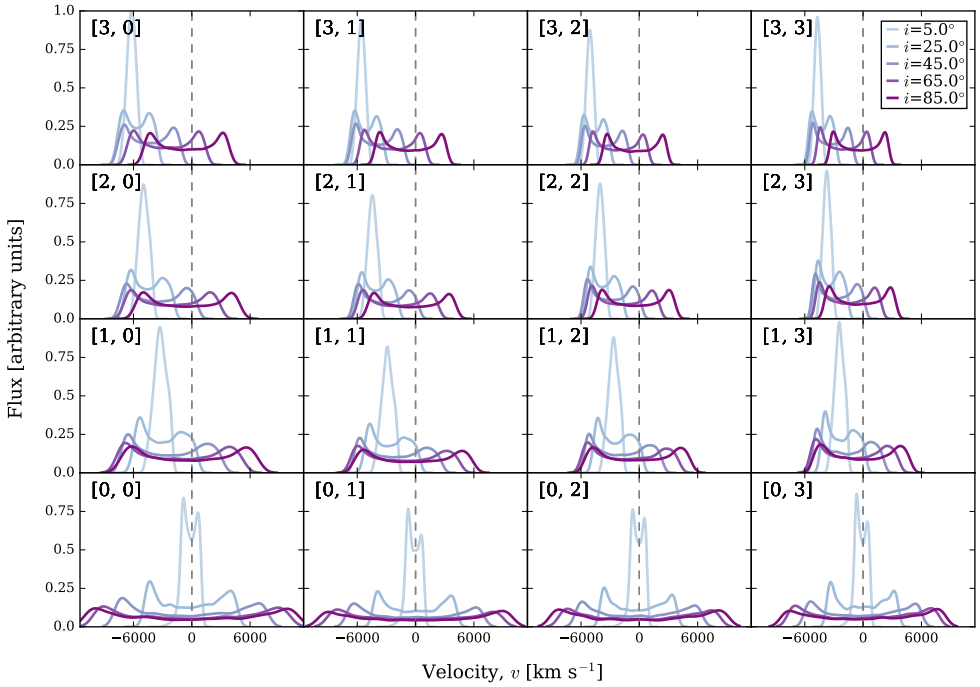

(a) Optically thin polar wind with opening angle of 5°–15°

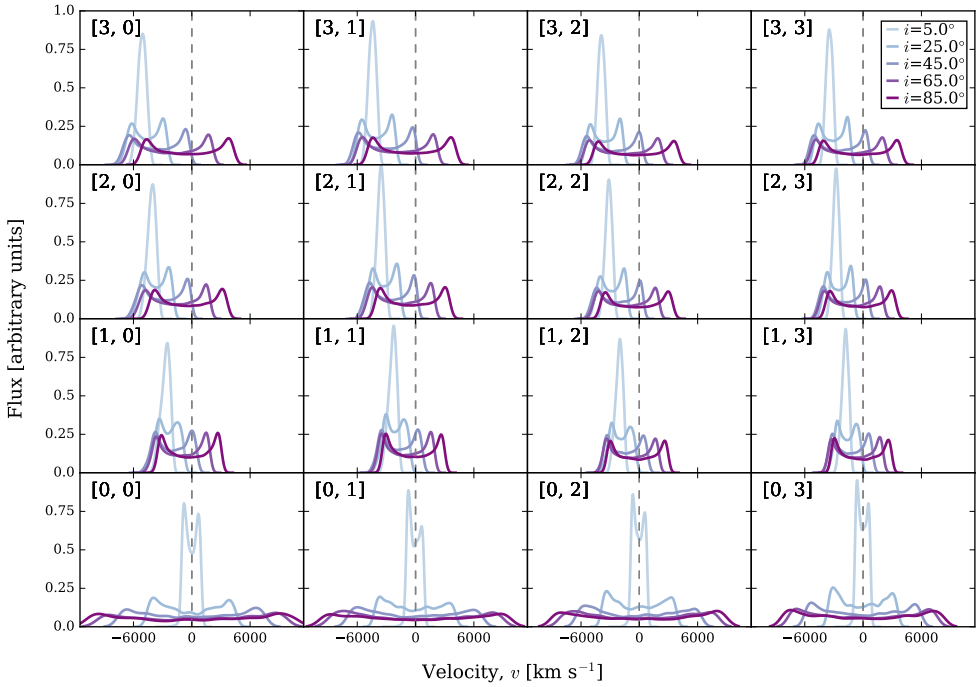

(b) Optically thin intermediate wind with opening angle of 40°–50°

Figure 4.5: Simulated emission line profiles as a function of inclination angle for optically thin wind with $\xi = 1\,\mathrm{s}^{-1}$. The position of the 'wind zone' $[a, b]$ is indicated on the top left of each panel. The dashed line shows the systemic centroid of the line.

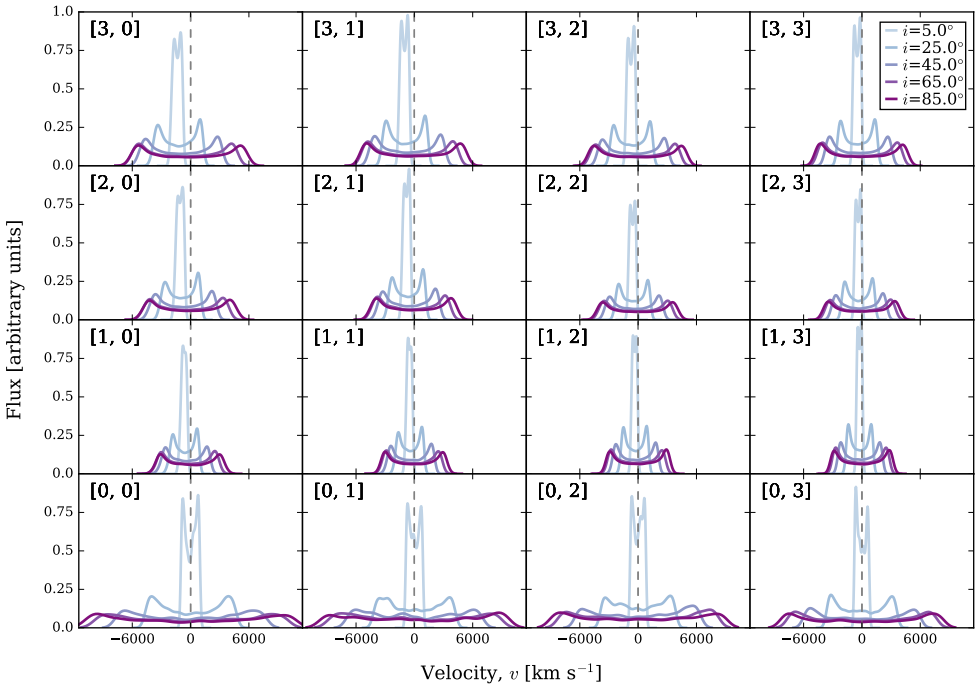

(c) Optically thin equatorial wind with opening angle of 75°–85°

Figure 4.5: — Continued

motion in our model. In the cases where the red side responds quicker than the blue, all or a significant fraction of the particles that make up the red side have a negative line-of-sight velocity (i.e. outflowing). Therefore, when the red side responds quicker than the blue side, it simply means that the median time delay to the parts of the wind with larger negative $v_{\rm los}$ is longer than the delay to the parts with a more positive $v_{\rm los}$.

Most zones in the polar wind model and a few zones in the intermediate wind model, particularly at small angle of viewing, have a positive difference in the mean time delay. This indicates that red side of the line profile responds quicker compared to the blue side. In contrast, the equatorial wind model exhibits shorter lag in the blue side than the red side. The differences are more noticeable at large inclination angles. In all cases, as the inclination angle increases towards edge-on, the difference in mean time delay decreases, i.e., the response in the blue side is becoming faster than the red side.

Changing the optical thickness to a higher value results in smaller time lags of blue side. The mean time delays for the polar wind are generally all positive except for a few zones when the wind is viewed close to edge-on. The intermediate and polar wind show signatures of faster red side response in the zones close to the base in the optically thick wind but not in the optically thin wind.

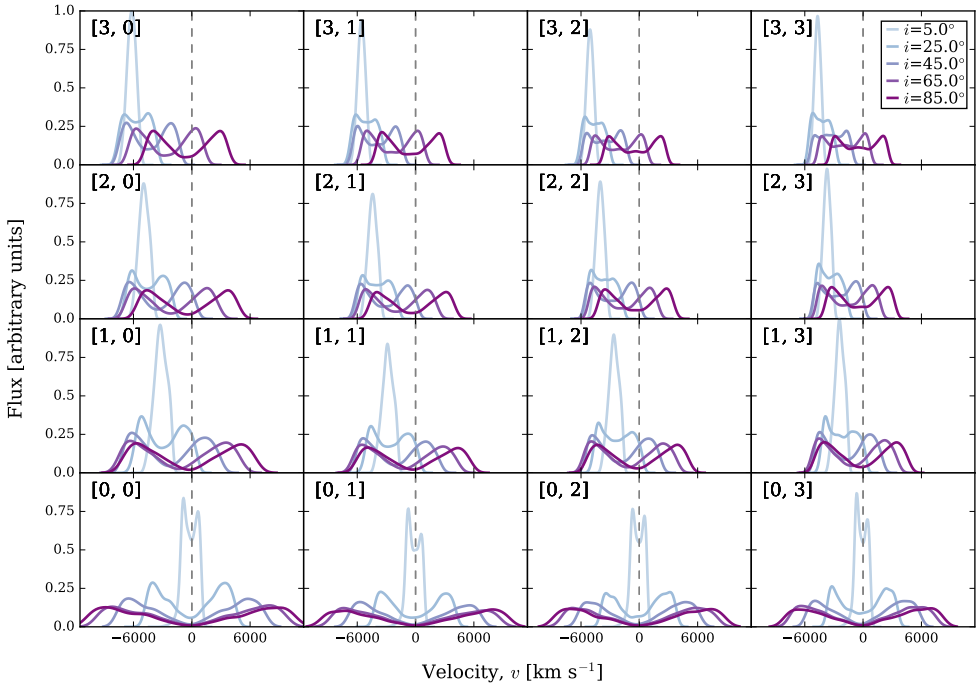

(a) Optically thick polar wind with opening angle of 5°–15°

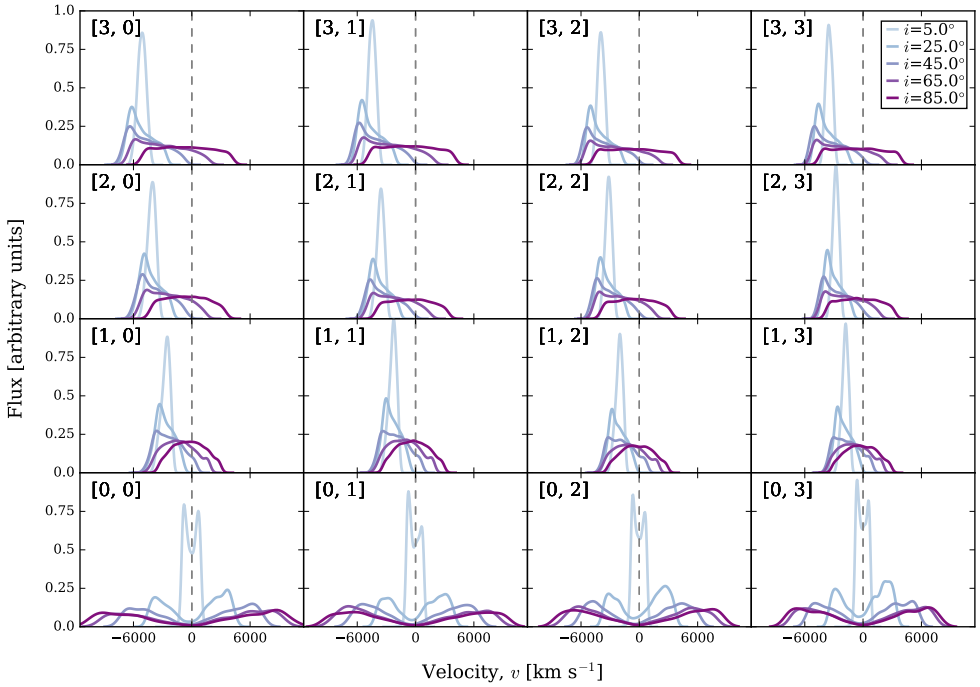

(b) Optically thick intermediate wind with opening angle of 40°–50°

Figure 4.6: Simulated emission line profiles as a function of inclination angle for optically thick wind with $\xi = 10^{10}\,\mathrm{s}^{-1}$. The position of the 'wind zone' $[a, b]$ is indicated on the top left of each panel. The dashed line shows the systemic centroid of the line.

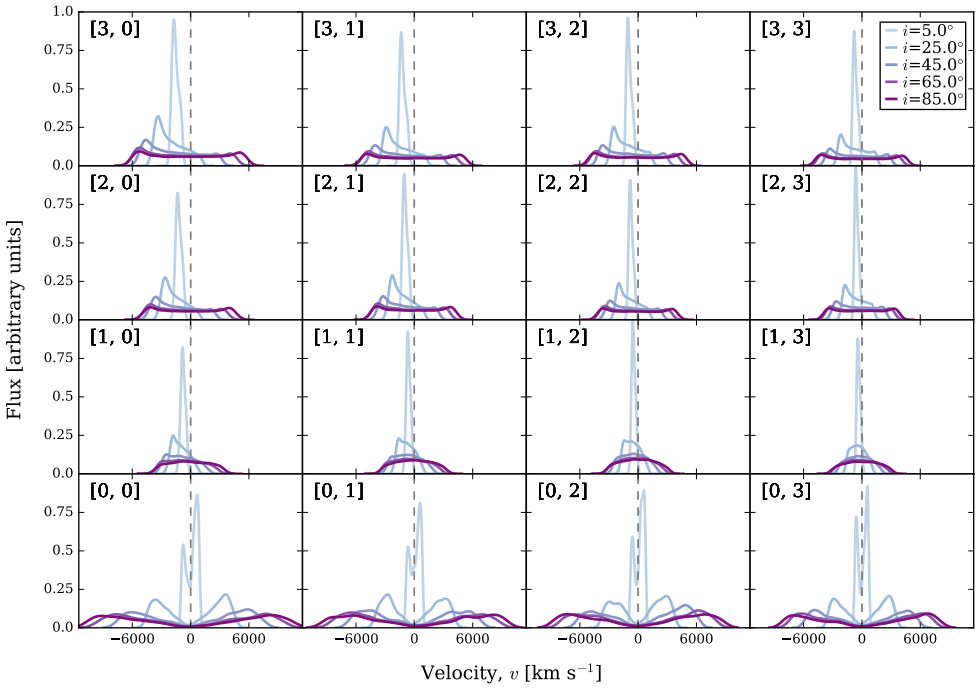

(c) Optically thick equatorial wind with opening angle of 75°–85°

Figure 4.6: — Continued

4.4 Discussion

Understanding the wind properties that give rise to the diversity of quasar broad line profiles has crucial consequences in inferring the structure of the BLR. When line profiles predicted from given models are compared to the observed emission lines, they can be used to infer the kinematics and dynamics of the line emitting region. In this section, we perform a qualitative analysis on a disk-wind model characterised by a flattened rotating accretion disk and a narrow outflowing helical wind.

4.4.1 Wind Opening Angle

Several authors have considered a multitude of combinations of disk and wind BLR components, but in reality, the main distinction between the models is the opening angle of the wind. Our simulation with the intermediate wind opening angle is similar to that proposed by Elvis (2000, 2004), but without the vertical outflow, which is imposed to justify narrow absorption lines. Our equatorial wind model also resembles Murray et al. (1995) model, though their model has a wider opening angle with the wind closer to the base of the disk.

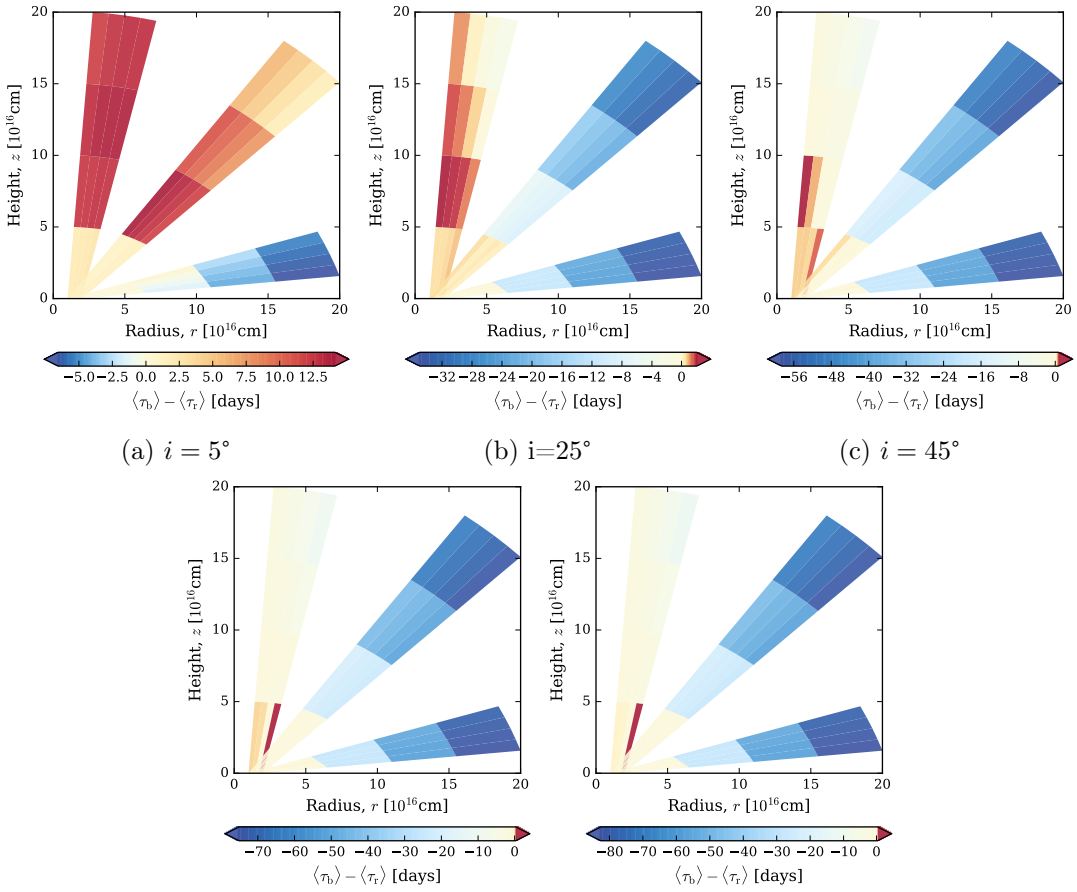

(a) $i = 5°$ (b) i=25° (c) $i = 45°$

(d) $i = 65°$ (e) $i = 85°$

Figure 4.7: Difference between mean time delay of blue and red sides for optically thin wind at various wind opening angles and inclination angles. The narrow winds in each plot: *left*: polar, *middle*: intermediate, and *bottom*: equatorial.

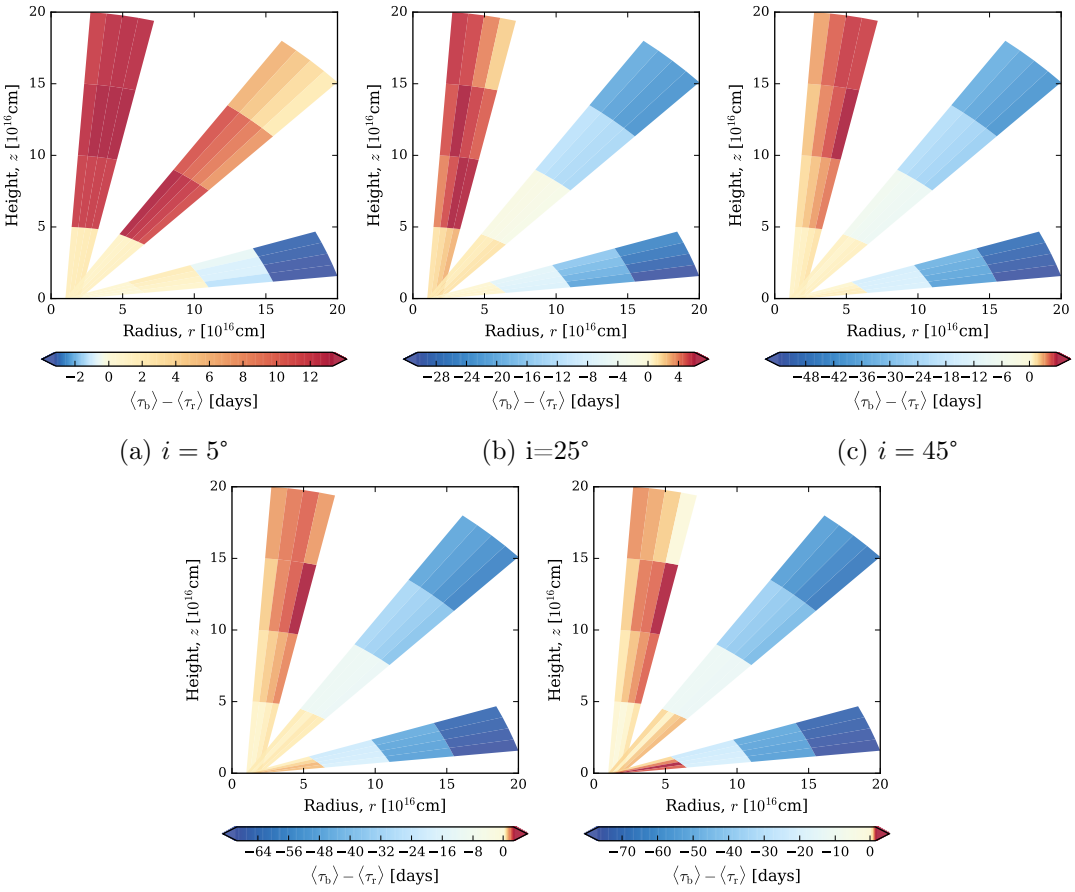

(a) $i = 5°$ (b) i=25° (c) $i = 45°$

(d) $i = 65°$ (e) $i = 85°$

Figure 4.8: Difference between mean time delay of blue and red sides for optically thick wind at various wind opening angles and inclination angles. The narrow winds in each plot: *left*: polar, *middle*: intermediate, and *bottom*: equatorial.

Based on Figs. 4.5 and 4.6, an equatorial wind model, like that of Murray et al. (1995), produces more symmetric and less blueshifted emission line profiles. As the wind opening angle is shifted towards polar, the profiles tend to become more asymmetric with higher blueshifts. Since the wind is outflowing, this indicates that the most of the wind is travelling towards the observer and smaller fraction is projected in the opposite direction. The increase in blueshift implies that the majority of the wind velocity is aligned with the line-of-sight of the observer.

4.4.2 Inclination Angle

The degree of line asymmetry tends to increase with decreasing inclination. Chajet & Hall (2013, 2017) produced similar findings using a model combining the improvised accretion disk-wind model of Murray & Chiang (1997) and the magnetohydrodynamic model of Emmering et al. (1992). We find that the line profiles are symmetric when viewed near edge-on and asymmetric near face-on. This trend is a simple consequence of the outflowing wind. For low inclination objects, the poloidal or outflowing velocity dominates the observed line-of-sight velocity. Meanwhile, in high-inclination-angle objects, the line-of-sight velocity is dominated by the rotational velocity component, which has roughly equal approaching and receding velocity components.

The line profiles also tend to be more blueshifted for smaller inclination angle than those seen at high inclination. Following a similar explanation, the direction of the outflowing wind determines the strength of the blueshift. Viewing the object face-on, the projected wind velocity is towards the line-of-sight of the observer. Assuming that the far side of the emission is obscured by the optically thick accretion disk, this yields an overall bluewards shift of the line. In the optically thick wind (Fig. 4.6), the emission line gradually becomes more blueshifted as the line-of-sight approaches and intersects the opening wind region within $\theta_{\rm min}$ and $\theta_{\rm max}$ (see also Fig. 4.1). When the inclination angle passes the emitting region and moves closer towards edge-on, the lines become less blueshifted since the line-of-sight is now travelling away from the wind. In addition, the Keplerian rotation component significantly contributes to the projected velocity and hence, the increase in line width. These findings are consistent with the results from Chajet & Hall (2013, 2017) line profile modelling.

4.4.3 Wind Zone Position

Depending on the spatial location of the line emission region in the wind, there will be a variation in the physical properties of the emission lines. The width of the line profile is broader and approximately symmetric near the base of the streamline. This is expected since the rotational velocity or Keplerian motion is dominant close to the surface of the

accretion disk. As the wind travels outwards in poloidal distance, the rotational velocity starts to decrease, while the poloidal component of the velocity gradually increases. This contributes to the narrowing of the line profile for regions further out until at a certain point where the poloidal velocity is significant, and consequently broadens the line profile. This transition is particularly strong in more equatorial winds as demonstrated in Fig. 4.5b–Fig. 4.5c and Fig. 4.6b–Fig. 4.6c.

Earlier studies have shown that the shape of the emission line profile depends on the ionisation level of the line. HILs, like C IV, are often broader in comparison to LILs, like Mg II and Hβ (e.g., Osterbrock & Shuder 1982; Mathews & Wampler 1985). The distinct line shapes indicate different physical conditions in the line emitting region and thus, it is possible to infer the relative spatial location of the line in the outflowing wind. It is expected that the LILs will lie close to the base of the wind further from the black hole, in a region of higher density (Ruff et al. 2012), while the HILs will lie closer to the ionising source, and higher in the wind, reflecting both the rotational and the poloidal wind components. This explains the reliability of the LILs in black hole estimation (e.g., McLure & Jarvis 2002; Shen et al. 2008; Rafiee & Hall 2011; Mejía-Restrepo et al. 2016) and the observed velocity offset of the HILs with the systemic velocity of the system compared to that of the LILs (Hewett & Wild 2010).

The relative positions of the HILs and LILs agrees with the blueshifting trend in our model. The blueward shift in the line is higher for 'wind zones' close to the ionising source relative to zones further away but near the base of the wind. This is consistent with the observed blueshift of HILs with respect to LILs (e.g., Gaskell 1982). C IV HILs that display large blueshifts of $> 2000\,\mathrm{km\,s^{-1}}$ tend to be dominated by non-virial motion (Coatman et al. 2016). In our model, the blueshifting is most prominent for polar wind opening angle due to the reason mentioned in previous section. The emission lines in the equatorial wind only show slight blueshifts with larger poloidal distance.

4.4.4 Optical Depth

In the optically thin wind situation, most of the simulated lines presented are double-peaked, which are rarely observed (Eracleous & Halpern 1994, 2003; Strateva et al. 2003). The profiles are generally single-peaked for viewing angle close to face-on. However, 'wind zones' that are close to the accretion disk and for polar outflowing wind opening angle, always show double-peaked profiles.

As suggested by Chiang & Murray (1996) and Murray & Chiang (1997), one of the determining elements for a line profile to be single-peaked is a larger velocity gradient in the poloidal compared to the rotational, $|(\mathrm{d}v_l/\,\mathrm{d}r)/(\mathrm{d}v_\phi/\,\mathrm{d}r)| \gtrsim 1$ since the light is more readily transmitted in a radial direction. In our model, this ratio is always less than 1 in all 'wind zones' for a polar outflowing wind (Fig. 4.2d). Consequently, the profiles remain double-peaked regardless of the optical thickness of the wind. In the intermediate

and equatorial wind models, the rotational shear at regions close to the accretion disk is also higher than the radial shear. Hence the double-peaked line profiles. However, the radial shear increases with poloidal distance and the photons are more likely to escape radially along the line-of-sight, which results in the observed single-peaked lines (Figs. 4.3d and 4.4d).

4.4.5 Time Delay

The response of the BEL flux to changes in the ionising continuum flux reflects the geometric configuration of the BLR. The side closest to the observer is seen to vary with changes in the continuum flux earlier (Gaskell 2009). Generally, a shorter lag in the red side of the line is associated with inflow motion, while a shorter blue side response is related to outflow motion. Many objects monitored in velocity-resolved RM are detected to have the red side of the line profile leading the blue side and hence, disfavouring outflow models and supporting inflow cases (e.g., Gaskell 1988; Koratkar & Gaskell 1989; Crenshaw & Blackwell 1990; Korista et al. 1995; Ulrich & Horne 1996). However, using the spherical disk-wind model of Murray et al. (1995), Chiang & Murray (1996) demonstrated that it is possible to attain earlier response in the red side of the line by taking into account radiative transfer effects due to the radial and rotational components of the velocity.

Our kinematical narrow wind model is also able to recreate the shorter time delay in the red or blue side of the line for both optically thin and thick winds. The time lag in the red side is quicker than the blue side for polar and intermediate wind opening angles, especially when the viewing angle is close to face-on. This is in accordance with Type 1 objects seen at low inclination angle. A strong indication of outflowing winds with shorter lag in the blue side is exhibited in equatorial winds at high viewing angle.

4.4.6 Parameter Sensitivities

The results presented assume the model parameters described in § 4.2.1. However, despite the exact values chosen for this analysis, the underlying trends in line widths and blueshifts at varying viewing angles and outflowing wind should remain true over a large range of parameters. In order to test this, we inspect how changing the values of some parameters affects the shape of the line profile. An individual free parameter is varied while assuming the values for the rest of the parameters fixed using those from Table 4.1. Note that since full radiative transfer and photoionisation are not implemented in our modelling, changes in the spectral energy distribution shape and luminosity of quasar spectra due to changing the physical black hole parameters, such as the black hole mass

and accretion efficiency, are not accounted for. Instead, we concentrate on investigating the following key points:

- Shape of the line profile.
- Properties of the line profile: line width, blueshift, and asymmetry.
- Variation in density.

Further caveats on the modelling are mentioned in § 4.4.7.

We found that changing the source function power law exponent, β, in the radiative transfer equation only slightly changes the line profile width and asymmetry. At regions far from the surface of the disk, the increase in β yields narrower emission lines in the equatorial wind model. This trend is in agreement with the Murray & Chiang (1997) studies. For intermediate wind angles, the lines are narrower with less flux on the blue wing and slightly more on the red wing. However, in all wind models, zones near the base display broader lines with higher β. The rest of the zones for a polar wind also show line profiles broader on the red side and slightly narrower on the blue side. This trend is likely because zones have smaller poloidal velocity shear than rotational shear with $|(\mathrm{d}v_l/\,\mathrm{d}r)/(\mathrm{d}v_\phi/\,\mathrm{d}r)| < 1$.

The widths of the line profiles were found to be broader with increasing black hole mass. They scale roughly $\propto M_{\mathrm{BH}}^{1/2}$ as expected from virial motion, assuming other parameters are kept constant. The parameter γ is used to specify the separation in the streamline opening angle, θ, for the bounded initial radius at the base, r_0. Fig. 4.9 demonstrates the changes in θ with increasing r_0 for different γ in the intermediate wind opening angle of 40°–50°. Since the sole difference in the physical parameters compared to other models is the inner and outer limit of the wind angle, similar exponential growth for higher γ is also shown in the narrow polar and equatorial wind models. As predicted, γ of 1 corresponds to a linear increment between θ and r_0.

The rate of wind acceleration can be regulated by the quantity α. For a large α value, the poloidal velocity near the base of the accretion disk starts slow initially but gradually increases at around R_v. On the other hand, a smaller α implies a faster initial poloidal velocity. These variations are displayed in Fig. 4.10.

The density of the wind is dependent on the parameters λ and $\dot{M}_{\mathrm{wind}}$, as shown in Fig. 4.11. A negative mass-loss rate exponential leads to a decreasing local mass-loss rate as the radius increases. By lowering the mass-loss rate of the wind, the density decreases and causes a change in ionisation states. In all scenarios, the qualitative trends in the line profile shapes are fairly similar.

4.4.7 Caveats

Several caveats are noteworthy in our modelling. The values of ξ in the optical depth function were selected to represent an optically thin or thick wind. Although these conditions are shown to suppress the double peaks to a single peak, a more sensible

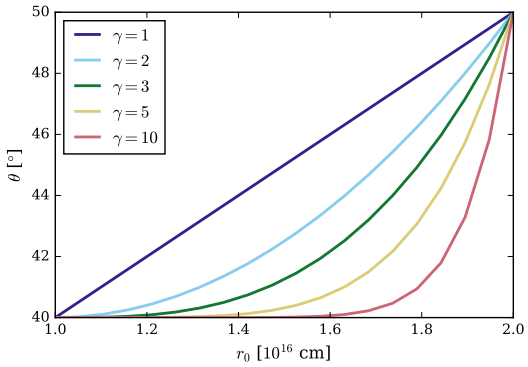

Figure 4.9: Plot of streamline opening angle, θ, as a function of baseline radius, r_0, for various concentration of streamline, γ, shown for intermediate wind opening angle of 40°–50°. Other parameter values are as defined in Table 4.1.

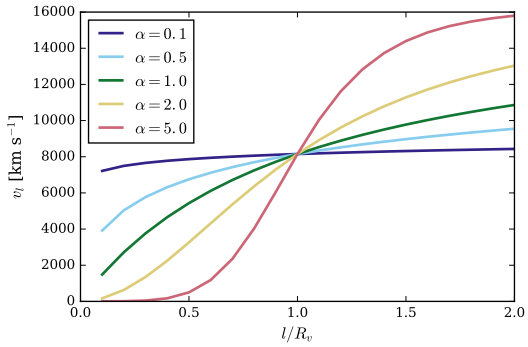

Figure 4.10: Plot of poloidal velocity, v_l, as a function of ratio between poloidal distance and scale height, l/R_v, for various acceleration power law index, α. Other parameter values are as defined in Table 4.1.

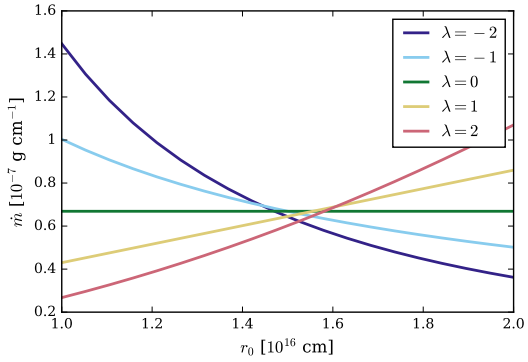

Figure 4.11: Plot of local mass-loss rate per unit surface of the disk, $\dot{m}$, as a function of baseline radius, r_0, for various mass-loss rate exponent, λ. Other parameter values are as defined in Table 4.1.

value obtained through photoionisation simulations should further clarify the effects of optical depth on the emission lines. There is also a possibility for radiative transfer in multiple scattering surfaces (Rybicki & Hummer 1978).

Though our modelling assumes that the line profiles are generated locally within each zone, in a realistic context, variations in density can induce significant fluctuations in the ionising state. The density ranges at different opening angles are $\sim 10^{-17}$–$10^{-13}\,\mathrm{g\,cm^{-3}}$ (Hydrogen number density, $n_{\mathrm{H}} \sim 6 \times 10^{6\text{–}10}\,\mathrm{cm^{-3}}$) for polar wind, $\sim 10^{-18}$–$10^{-13}\,\mathrm{g\,cm^{-3}}$ ($n_{\mathrm{H}} \sim 6 \times 10^{5\text{–}10}\,\mathrm{cm^{-3}}$) for intermediate wind, and $\sim 10^{-18}$–$10^{-12}\,\mathrm{g\,cm^{-3}}$ ($n_{\mathrm{H}} \sim 6 \times 10^{5\text{–}11}\,\mathrm{cm^{-3}}$) for equatorial wind. Huge variations in densities are seen for $[0, b]$ 'wind zones' that are close to the base of the accretion disk. The difference can be up to three orders of magnitude $\sim 10^{-16}$–$10^{-13}\,\mathrm{g\,cm^{-3}}$ for polar winds and up to four orders of magnitude for intermediate and equatorial winds with ranges of $\sim 10^{-17}$–$10^{-13}\,\mathrm{g\,cm^{-3}}$ and $\sim 10^{-16}$–$10^{-12}\,\mathrm{g\,cm^{-3}}$ respectively. The densities vary approximately an order of magnitude for the rest of the 'wind zones'. Although most emission lines are effective at emitting over a large range of densities (Korista et al. 1997), ionisation changes over these density ranges could dramatically affect the emergent line profiles. As the wind travels further in poloidal distance, the changes in density are less. The model can be enhanced by taking into account the complexity of the BLR structure, such as incorporating photoionisation.

4.4.8 Comparison with Other Studies

Different models of quasar wind geometries have been tested against the observations by a number of authors. Marin et al. (2015, and references therein) considered different models to explain the observed polarisation dichotomy between Type 1 and 2 AGN. This dichotomy shows Type 1 quasars typically have polarisation parallel to the system axis, while for Type 2, the polarisation is perpendicular to the axis. They found that a two-phased outflowing wind with a bending angle of 45° is able to explain this dichotomy. However, their predicted polarisations depend quite strongly on the clumpiness of the wind and the line-of-sight. Similarly Young et al. (2007) modelled the structures observed in polarized light of the BAL quasar PG1700+518, and found the general geometric structure of both the BLR wind and the electron scattering wind responsible for the polarisation consistent with an outflowing wind, with a poloidal launching angle.

Other authors are challenging the idea that quasars follow a simple unification model, depending only on black hole mass and accretion rate (for example, Matthews et al. 2017; DiPompeo et al. 2017, and references therein). In DiPompeo et al. (2017), evidence is presented for evolutionary differences affecting the amount of obscuration in quasars and Matthews et al. (2017) concluded that BAL quasars are viewed from similar angles to non-BAL quasars, and/or geometric unification cannot explain the fraction of BALs in quasar samples.

Detailed hydrodynamic simulations of a line-driven wind have illustrated the possibility of over-ionising the wind, leading to a reduction in efficiency of the line-driving. This illustrates the complexity of the BLR region demanded by observations, which require shielding of the outflowing winds (Proga et al. 2000; Higginbottom et al. 2014).

4.5 Summary

We have explored the properties of BELs, specifically the widths and velocity offsets, using a dynamical disk-wind model with radiative transfer in the Sobolev limit. The effect of orientation for narrow angle of outflowing wind is analysed. We have considered several factors that contribute to the different BEL features, which include inclination angle, angle of outflow, and position of the emission region in the wind.

When viewed face-on, the emission line profile is asymmetric and narrow. The profile is blueshifted since the wind is approaching the observer. The blueshift increases as the inclination angle moves toward the opening angle of the wind and decreases as the viewing angle recedes from the emitting wind. The profile is symmetric and broader as the viewing angle approaches edge-on. At wind regions close to the accretion disk surface, the emission line is symmetric with broader width than a line emitted further out. The emission line profile has a larger blueshift with increasing vertical distance along the wind from the central ionising source, particularly for polar wind opening angle. The blueshifting effect decreases as the angle of outflowing wind tends towards equatorial.

By taking into account the correction for optical depth, single-peaked emission lines are formed for the intermediate and equatorial wind. Due to the relatively small poloidal velocity gradient compared to the rotational shear found in the polar wind, the lines are double-peaked even after applying the optical depth correction.

We have also demonstrated that an ouflowing wind model is capable of generating a shorter lag in the red or blue sides of the line. This suggests that outflowing winds are not ruled out when the red side of the emission line responds on a quicker time frame than the blue side, as has previously been implied.

CHAPTER 5

Broad Absorption Line Quasar (BALQ)

This chapter is based on the publication:

- *Yong, S. Y., King, A. L., Webster, R. L., Bate, N. F., O'Dowd, M. J., & Labrie, K. (2018). Using the Properties of Broad Absorption Line Quasars to Illuminate Quasar Structure.* MNRAS, *479, 4153–4171. ADS: 2018MNRAS.479.4153Y. doi: 10.1093/mnras/sty1540*

Abstract

A key to understanding quasar unification paradigms is the emission properties of broad absorption line quasars (BALQs). The fact that only a small fraction of quasar spectra exhibit deep absorption troughs blueward of the broad permitted emission lines provides a crucial clue to the structure of quasar emitting regions. To learn whether it is possible to discriminate between the BALQ and non-BALQ populations given the observed spectral properties of a quasar, we employ two approaches: one based on statistical methods and the other supervised machine learning classification, applied to quasar samples from the Sloan Digital Sky Survey. The features explored include continuum and emission line properties, in particular the absolute magnitude, redshift, spectral index, line width, asymmetry, strength, and relative velocity offsets of high-ionisation C IV λ1549 and low-ionisation Mg II λ2798 lines.

We consider a complete population of quasars, and assume that the statistical distributions of properties represent all angles where the quasar is viewed without obscuration. The distributions of the BALQ and non-BALQ sample properties show few significant differences. None of the observed continuum and emission line features are capable of differentiating between the two samples. Most published narrow disk-wind models are inconsistent with these observations, and an alternative disk-wind model is proposed. The key feature of the proposed model is a disk-wind filling a wide opening angle with multiple radial streams of dense clumps.

5.1 Background

In § 3.2, we developed a simple kinematical thin disk-wind model, enabling a qualitative understanding of both the emission line widths and the offsets of line centroids. The results of those analyses demonstrate that the properties of the BELs are highly dependent on the viewing angle, wind opening angle, and wind region. In Chapter 4, we find that the shape of the emission line profile is narrow and asymmetric when viewed face-on. In contrast, the emission line is broad and symmetric for an edge-on geometry. The relative blueshift is larger as the line-of-sight is aligned with the outflowing wind. Additionally, a polar narrow wind model exhibits higher blueshift compared to that of equatorial wind model. The aim of these investigations was to relate the measured attributes of the BELs to the observed in the context of a disk-wind model for the BLR.

Investigating the differences in emission properties between the BALQ and non-BALQ populations can therefore shed light on the geometry and origin of the observed BALs. In this study, we attempt to group the BAL and non-BAL quasars into their respective classes using statistical tests and supervised machine learning for classification. The investigated features include continuum properties, particularly the absolute magnitude, redshift, and spectral index, and additionally the characteristics of high- and low-ionisation emission lines, specifically the FWHM, asymmetry, EW, and velocity offsets of C IV λ1549 and Mg II λ2798 emission lines. We explicitly consider whether the differences between the BALQs and the non-BALQs can be explained by either of the postulated paradigms, and if so, what constraints are required on the model. Throughout this analysis, we assume that the BELs and BALs arise in the same disk-wind and we refer to this region as the BLR.

The outline of this chapter is as follows. We discuss plausible explanations for the BAL phenomenology in § 5.1. In § 5.2, we describe the selection criteria for the data sample of quasars and how they were separated into BAL and non-BAL populations. The statistical tests and machine learning algorithms employed are outlined in § 5.3. The results from the two methods are presented in § 5.4, followed by discussion in § 5.5 where we examine the use of the observable BAL signatures in the context of evolutionary and orientation in a narrow disk-wind paradigms. This analysis motivates us to present a revised BLR model in § 5.6. Finally, a summary is provided in § 5.7.

5.1.1 BAL Phenomenology

One of the main explanations for the BAL phenomenon and its relative rarity is a unification/orientation model that assumes all AGN possess BAL outflows but these outflows are narrow and BAL features are only observed when the observer's line-of-sight intersects the outflow. If the presence of a broad absorption feature results from a

specific angle of viewing, the signature should be evident in the characteristics of the BELs. This is true no matter if the BLR is assumed to be co-spatial with BAL outflows, or not, or which BLR model (Keplerian disk, equatorial disk-wind, poloidal wind, etc.) is adopted. This study compares the measurable characteristics of BELs in quasars with and without BALs, to further understand the geometry of the BLR and BAL outflows.

Only a fraction of quasars are BALQs. A common measure of a BAL is the balnicity index (BI; Weymann et al. 1991), which describes the amount of absorption blueward of the line:

$$\mathrm{BI} = \int_{-25\,000}^{-3000} \left[1 - \frac{f(v)}{0.9}\right] C(v)\,\mathrm{d}v, \tag{5.1}$$

where $f(v)$ is the normalised flux density as a function of velocity, v, relative to the centre of emission line. The value of C is either 0 or 1. It equals to unity when the term in the square bracket is continuously positive for at least $2000\,\mathrm{km\,s^{-1}}$, and zero otherwise. Traditional BALs are defined to have $\mathrm{BI} > 0\,\mathrm{km\,s^{-1}}$. Depending on the ionisation potential of the absorbed lines, BALQs are further separated into three subcategories: high-ionisation BAL (HiBAL) quasars, low-ionisation BAL (LoBAL) quasars, and iron low-ionisation BAL (FeLoBAL) quasars. HiBAL quasars show absorption from high-ionisation species, for example C IV, N V, and Si IV, and are the most common type of BALQ. LoBAL quasars show absorption from high-ionisation species as well as absorption from low-ionisation species, such as Mg II, Al III, and Al II. FeLoBAL quasars are the rarest type of BALQ and are LoBALs with additional absorption lines from Fe II or Fe III complexes.

5.1.2 Orientation Interpretation

There are two primary explanations for the BAL phenomenon in quasars. One interpretation that we mentioned earlier is a unification model based on orientation. It is believed that all quasars have BAL outflows since the characteristics of the emission line and continuum of BALQs and non-BALQs are found to be similar (Weymann et al. 1991). The fact that only a small fraction $\sim 15\%$ of quasars display BAL features (Hewett & Foltz 2003; Reichard et al. 2003; Knigge et al. 2008; Gibson et al. 2009) might be due to orientation effects, such that a BAL is seen when the line-of-sight intersects the covering angle of the outflow. This leads to the notion of wind emanating from the accretion disk or the disk-wind model.

The disk-wind model is often depicted as a biconical wind with a narrow opening angle of $\sim 10°$–$20°$ to account for the small fraction of BALQs, from which the BELs and BALs arise (Murray et al. 1995; Elvis 2000, 2004). However, for a narrow wind, we might expect different physical characteristics in the BELs between the BALQs and non-BALQs since they are observed from different directions (see also Chapter 4,

Matthews et al. 2017). For example, BALs viewed through a polar narrow wind will have narrower and more blueshifted line profiles than those of non-BALs observed from non-polar angles. In contrast, the line profile will be broad and less blueshifted in BALQs with equatorial narrow wind opening angle. We would expect different BEL properties for the two population when viewed from different orientations for any general flattened axisymmetric BLR models as shown by Collin et al. (2006), Goad et al. (2012), and Braibant et al. (2017). An orientation explanation is not a new concept. Orientation has also been commonly used in the literature to differentiate between the types of AGN, either type 1 or type 2, and based on radio morphology, either RL or RQ (Antonucci 1993; Urry & Padovani 1995).

In a recent paper by Matthews et al. (2017), the distribution of the BEL EW values for both BALQ and non-BALQ are compared to test the geometric unification model. They find similarities between the EWs of both populations, which contradicts the idea that a BAL originates from an equatorial outflowing wind coming off a geometrically thin but optically thick accretion disk. These authors conclude that either (i) the continuum emission is inconsistent with a geometrically thin accretion disk, (ii) the viewing angles for BALQ and non-BALQ are the same (i.e., at low inclination angles close to face-on), or (iii) geometric unification is unable to justify the BAL fraction in quasar samples.

5.1.3 Evolutionary Interpretation

An alternative interpretation for the BAL phenomena is that the BALQ represents a stage in the evolution of quasars. In this scenario, BALQs are young quasars residing in a gas- and dust-rich environments enveloped by a high covering fraction cocoon (e.g., Hamann & Ferland 1993; Voit et al. 1993; Becker et al. 2000). After some time they blow off their dusty shroud and become the more common non-BALQs.

The spectrum of a BALQ is found to be redder compared to a non-BALQ spectrum with LoBAL quasars redder than HiBAL quasars (Weymann et al. 1991; Sprayberry & Foltz 1992; Brotherton et al. 2001; Reichard et al. 2003; Trump et al. 2006; Gibson et al. 2009), suggesting a quasar transition from FeLoBALs, LoBALs, HiBALs, and finally to non-BALs. If the BAL phenomenon is an evolutionary stage of a quasar, then we might expect no difference between BEL characteristics of the two populations, but a difference in spectral slope and maybe differences in accretion rates and/or black hole masses. It is also possible that the BAL phenomenon is a combination of both explanations (Gallagher et al. 2007; Allen et al. 2011; DiPompeo et al. 2013).

5.1.4 Two-sample Empirical Distribution Function Tests

To determine whether two samples are likely to be drawn from the same population, a two-sample (2s) statistical test based on the empirical distribution function (EDF) can be conducted. For an ordered set of n independent and identically distributed random samples $(x_1, x_2, \ldots, x_n)$, the EDF represents the fraction of elements in the sample that are less than or equal to x. This can be expressed as

$$F_n(x) = \begin{cases} 0 & \text{if } x < x_1, \\ i/n & \text{if } x_i \leq x < x_{i+1} \text{ for } i = 1, \ldots, n-1, \\ 1 & \text{if } x \geq x_n. \end{cases} \tag{5.2}$$

The two well-known EDF tests are Kolmogorov–Smirnov (K–S) and Anderson–Darling (A–D) tests. Both are non-parametric statistical methods that are free from any assumption about the probability distribution of the data and test the null hypothesis, H_0, that the samples belong to the same distribution.

The K–S statistic was first proposed by Kolmogorov (1933, 1941) and Smirnov (1939) and belongs to the supremum type EDF statistic. For a 2s K–S test, the K–S statistic, denoted as D_{nm}, is calculated from the supremum or the maximum absolute difference of two EDFs, $F_n(x)$ and $F_m(x)$, with sample sizes of n and m:

$$D_{nm} = \sup_x |F_n(x) - F_m(x)|. \tag{5.3}$$

The A–D statistic was introduced by Anderson & Darling (1954) and was further developed by Darling (1957); Pettitt (1976). It belongs to the square type EDF statistic. Given two random samples $(x_1, x_2, \ldots, x_n)$ and $(y_1, y_2, \ldots, y_m)$, the 2s A–D statistic can be written as

$$A^2_{nm} = \frac{1}{nm} \sum_{i=1}^{N-1} \frac{(M_i N - ni)^2}{i(N-i)}, \tag{5.4}$$

where $N = m + n$ is the combined samples and M_i is the number of samples in x that is less than or equal to the ith smallest element in the combined samples. Compared to the K–S test, the A–D test is more sensitive to the changes at the tails of the distributions (Engmann & Cousineau 2011).

5.1.5 Machine Learning (ML) Algorithms

With the advent of big data era, many promising resources have been developed to handle the challenge. One of these tools is machine learning (ML). The term machine

learning refers to a technique that enables computers to learn information based on data and experiences without being explicitly programmed. It is closely linked with statistics in respect of performing predictions. ML is broadly applied to untangle real world problems. From winning the American quiz game show, Jeopardy, with the IBM Watson computer system (Ferrucci et al. 2010), to automating rovers for space missions (McGovern & Wagstaff 2011), the applications of ML extend to many fields.

ML can be branched into supervised learning, unsupervised learning, and reinforcement learning. With supervised learning, the outputs are already established and the learning process attempts to predict the outcome of an event given prior knowledge of other outcomes. In contrast, the outputs are not provided in unsupervised learning. The algorithm then seeks to discover the inherent pattern in the data. Reinforcement learning is an automated approach whereby machine learns by interacting with the environment. It decides the ideal course of action based on its past trials in order to acquire the greatest reward or outcome.

In supervised learning, a model is trained using a training dataset given inputs where the desired outputs are identified beforehand. A set of features to be examined is used as the input to make predictions on the outputs. The feature is also known by its many names such as attribute, input, and explanatory variable. Outputs are also called classes, labels, outcomes, response variables, and targets. There are two subdivisions of supervised learning, namely classification and regression problems, which differ depending on the type of labels. For classification, the label is categorical or discrete, while it is continuous for regression. For the purposes of this study, we use supervised ML for binary classification problems and only review these methods.

Various ML algorithms have been developed to solve different tasks. This ideology is clearly captured by the "No Free Lunch" theorems. There are two of these theorems, one for supervised ML (Wolpert 1996) and another for optimisation (Wolpert & Macready 1997). Essentially the main message conveyed is that there is no unique algorithm that works perfectly in every scenario and is free from any drawbacks. A model is often based on some simplifications of the actual reality, which is achieved by making assumptions. Generally, the assumptions might hold for one situation but possibly fail for other. For this reason, it is vital to examine a variety of algorithms to assess the performance of the model.

A good ML model will strive to achieve a balanced bias-variance trade-off. Bias measures the error between the expected predictions and the actual values, while variance error measures the consistency of the model predictions in the training dataset. A model will suffer underfitting (high bias) when it is far too simple, and is therefore unable to grasp the underlying pattern in the data. In this case, the learning algorithm performs badly on both the training and test dataset. On the other hand, a model suffers from overfitting (high variance) when it is extremely complex, for example containing too many parameters. This model is able to perform exceedingly well on the training data, but has a poor performance on the test dataset. Hence, managing the trade-off is crucial

in selecting an optimal model that will generalise well on real world data. We investigate several algorithms that will be described in detail next.

5.1.5.1 Decision Tree

Decision tree (Breiman et al. 1984) is a predictive model that uses a series of observations and sample splitting according to those observations to make conclusions about the possible classification of an input. The training process starts at the tree root node, i.e., the origin of all branches, and the samples are split into branches of child nodes. At a node, all features are considered and the split is chosen that maximises the purity of the children sample given the parent sample. The purity of the sample can be thought of as the least amount of mixing between the different classifications. In the case, where the parent node is a mix of objects with a classification of either A or B, the perfect split (aka the split that gives the maximum purity) would perfectly split the sample with classification A into one child node and objects with classification B into the other child node. This purity can rarely be achieved after one split. Therefore, the splitting procedure is iterated at each child node until the samples are perfectly separated or upon reaching the specified minimum number of samples at the node. The final node is called the terminal or leaf node, and the predicted outcome is given at this point.

Technically, the objective function of the decision tree algorithm is to maximise the impurity decrease at each split. The impurity decrease, $\Delta I(s,t)$, evaluates the quality of a split s given node t. In the binary case, the parent node at t is separated into two child nodes, the left ($t_{\rm L}$) and the right ($t_{\rm R}$):

$$\Delta I(s,t) = I(t) - \frac{N_{t_{\rm L}}}{N_t} I(t_{\rm L}) - \frac{N_{t_{\rm R}}}{N_t} I(t_{\rm R}), \tag{5.5}$$

where N_t, $N_{t_{\rm L}}$, and $N_{t_{\rm R}}$ are the number of samples in the parent, left, and right nodes, respectively. The quantity $I(t)$ is the purity in the sample and $\Delta I(s,t)$ describes the changes in purity from the parent node to the left and right child nodes.

The two common impurity measures, $I(t)$, are the Gini index (Gini 1921) and the Shannon entropy (Shannon 1948). The Gini index minimises the probability of misclassification and is defined as

$$I_{\rm G}(t) = \sum_{i=1}^{c} p(i|t)[1 - p(i|t)]. \tag{5.6}$$

The parameter $p(i|t)$ is the fraction of samples that are in class c at node t. For binary classification, this can be simplified to

$$I_{\rm G}(t) = 2p(i|t)[1 - p(i|t)]. \tag{5.7}$$

The impurity function using Shannon entropy maximises the amount of information in the tree. This is given by

$$I_{\mathrm{H}}(t) = -\sum_{i=1}^{c} p(i|t) \log_2 p(i|t) \tag{5.8}$$

and for the binary problem

$$I_{\mathrm{H}}(t) = -p(i|t) \log_2 p(i|t) - [1 - p(i|t)] \log_2 [1 - p(i|t)]. \tag{5.9}$$

The impurity decrease based on Gini index, $\Delta I_{\mathrm{G}}(s,t)$, is also known as Gini impurity, while it is termed information gain, $\Delta I_{\mathrm{H}}(s,t)$, using Shannon entropy.

A quantitative representation of the feature importances can be allocated based on how much they contribute to the prediction during the training process. For a single decision tree, T, the importance of variable X_j (Breiman et al. 1984) is given by

$$\mathrm{Imp}(X_j, T) = \sum_{t \in N_T} \mathbb{1}(X_j, t) \frac{N_t}{N} \Delta I(s,t), \tag{5.10}$$

where N_t/N is the proportion of samples at node t and $\Delta I(s,t)$ is the impurity decrease of a split s at t as specified in Eq. (5.5). The quantity $\mathbb{1}(X_j, t)$ is an indicator function that equals 1 when node t splits on input variable X_j and 0 otherwise.

5.1.5.2 Random Forest

Random forest (Breiman 2001) is an ensemble of decision trees. A collection of trees is built from random samples of the training set generated by bootstrap sampling without replacement. The final classification is obtained via averaging all the votes from each trees. By combining multiple independently trained decision trees, the variance captured by individual trees in the forest is reduced.

By taking the mean of Eq. (5.10), the equation can be extended to calculate the feature importance trained with random forest algorithm (Breiman 2001) by taking the mean of Eq. (5.10) from a number of trees, which is also known as the mean decrease impurity:

$$\mathrm{Imp}(X_j) = \frac{1}{N_T} \sum_{T} \mathrm{Imp}(X_j, T), \tag{5.11}$$

where N_T is the number of trees in the forest. The value is normalised to have a sum of unity. If Gini index is used as the impurity function, consequently the equation is sometimes called the Gini importance or mean decrease Gini.

5.1.5.3 Logistic Regression

Logistic regression (Cox 1958), also called logit regression or maximum-entropy classification, belongs to a generalised linear model. It is used to predict the probability of being one of two possible classifications based on the input features. The regions that separate the input space into its respective class are called the decision boundaries. If there exists a region that perfectly divides the two classes, then the classes are linearly separable and the decision boundary is called a hyperplane.

Logistic regression algorithm attempts to search for the optimal hyperplane in the input features by maximising the log likelihood function. The hyperplane has a linear form that can be written as a combination of the predictor variables $\vec{x}$ and the corresponding weight vector $\vec{w}$:

$$z = w_0 + w_1 x_1 + \ldots + w_m x_m = w_0 + \sum_{i=1}^{n} w_m x_m = w_0 + \vec{w}^T \vec{x},$$

where n is the number of samples, m is the number of features, and w_0 is the intercept or bias. The probability model is characterised by a logistic or sigmoid function

$$P(y = \pm 1 | \vec{x}, \vec{w}) = \frac{1}{1 + \exp[-y(w_0 + \vec{w}^T \vec{x})]}, \tag{5.12}$$

which can be interpreted as the conditional probability that a sample belongs to class y given feature $\vec{x}$ and weight $\vec{w}$.

Consider the training vectors of n samples for binary class $(\vec{x}^{(i)}, y^{(i)})$ and $y \in \{-1, +1\}^n$, where $\vec{x}^{(i)} \in \mathbb{R}^d$ is a d-dimensional real vector and $i = 1, \ldots, n$. The logistic regression solves the following optimisation problem:

$$\min_{w_0, \vec{w}} \frac{1}{2} \vec{w}^T \vec{w} + C \sum_{i}^{n} \log[1 + \exp(-y^{(i)}(w_0 + \vec{w}^T \vec{x}^{(i)}))], \tag{5.13}$$

where the first term is the L2 regularisation. The misclassification penalty is controlled by the parameter $C = 1/\lambda$, which is the inverse of the regularisation parameter, λ. It controls the trade-off between large decision boundaries and correctly identified $\vec{x}^{(i)}$. Smaller C value implies that the optimisation will be less strict on penalising misclassification and seeks a hyperplane with larger decision bounds. Conversely, large C means weak regularisation and tends to impose higher penalties on misidentified points. This leads to a stricter decision bound.

The probability is then compared with a threshold of 0.5 to determine either the object is in y binary class -1 or $+1$. If the likelihood is greater than the threshold, the object will be predicted as a $+1$, and vice versa if it is less. The weight function is iteratively calculated using a training sample and is chosen to minimise the deviations between the predicted classification given a trial weight function and the known

classification.

5.1.5.4 Support Vector Machine (SVM)

Support vector machine (SVM; Boser et al. 1992; Cortes & Vapnik 1995) is a discriminative classifier with the aim of obtaining a maximum margin hyperplane that divides the classes. This is illustrated in Fig. 5.1. Margin is defined as the distance between the closest points, i.e., the support vectors, and the hyperplane. In a linear model, the hyperplane is a linear combination of input vector, $\vec{x}$, and is written as $w_0 + \vec{w}^T\vec{x}$, where $\vec{w}$ is the weight vector and w_0 is the intercept.

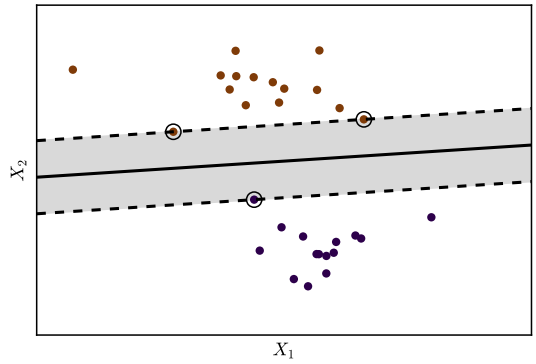

Figure 5.1: Separating hyperplane for samples from two classes using two features, X_1 and X_2, trained with linear SVM. The hyperplane is indicated by the solid line. The margin is the grey shaded region between the two dashed lines with circled points on the boundary as the support vectors.

Given the training vectors of n samples for binary class $(\vec{x}^{(i)}, y^{(i)})$ and $y \in \{-1, +1\}^n$, where $\vec{x}^{(i)} \in \mathbb{R}^d$ is a d-dimensional real vector and $i = 1, \ldots, n$. The objective function to be optimised consists of solving the primal problem:

$$\begin{aligned} \min_{w_0, \vec{w}, \vec{\xi}} \quad & \frac{1}{2}\vec{w}^T\vec{w} + C\sum_{i}^{n}\xi^{(i)} \\ \text{subject to} \quad & y^{(i)}(w_0 + \vec{w}^T\vec{x}^{(i)}) \geq 1 - \xi^{(i)}, \\ & \xi^{(i)} \geq 0, \forall i. \end{aligned} \tag{5.14}$$

The slack parameter, $\xi^{(i)}$, is introduced to relax the constraints on the margin. Similar to logistic regression, the penalty is governed by C. If the value is large, the algorithm will try to enforce a small margin hyperplane such that all the points are grouped correctly, and vice versa for small value of C.

This optimisation problem can also be represented in its dual form:

$$\begin{aligned} \max_{\alpha} \quad & \sum_{i}^{n} \alpha_i - \frac{1}{2} \sum_{i} \sum_{j} \alpha_i \alpha_j y^{(i)} y^{(j)} \vec{x}^{(i)T} \cdot \vec{x}^{(j)}, \\ \text{subject to} \quad & 0 \leq \alpha_i \leq C, \\ & \sum_{i}^{n} \alpha_i y^{(i)} = 0, \forall i, \end{aligned} \tag{5.15}$$

where α_i is the Lagrangian multiplier. Solving the dual problem yields the weight coefficient and intercept:

$$\vec{w} = \sum_{i}^{n} \alpha_i y^{(i)} \vec{x}^{(i)} \tag{5.16}$$

$$w_0 = y^{(i)} - \vec{w}^T \vec{x}^{(i)}. \tag{5.17}$$

The predictions for unseen data can be made using

$$\text{sign} \left(w_0 + \sum_{i}^{n} \alpha_i y^{(i)} \vec{x}^{(i)T} \cdot \vec{x}^{(j)} \right). \tag{5.18}$$

A technique called kernel trick can be implemented with SVM. The idea is to apply functions, i.e., kernels, to map inputs from a low dimensional space to higher dimensional feature spaces, $\phi(\cdot)$, such that the data becomes linearly separable. In this case, the dot product $(\vec{x}^{(i)T} \cdot \vec{x}^{(j)})$ is replaced with a kernel function $K(\vec{x}^{(i)}, \vec{x}^{(j)}) = \phi(\vec{x}^{(i)})^T \cdot \phi(\vec{x}^{(j)})$.

The algorithm searches for decision boundaries with the largest margin and solves for the hyperplane parameters. Once the optimal hyperplane is found, discrete class labels are assigned to make predictions on the new points.

5.2 Dataset

The data used are obtained from the Baryon Oscillation Spectroscopic Survey (Dawson et al. 2013) of the SDSS-III (Eisenstein et al. 2011) Data Release 12 Quasar (DR12Q; Pâris et al. 2017) catalogue. The SDSS DR12Q catalogue is retrieved through the VizieR catalogue access tool[1] (Ochsenbein et al. 2000), which is publicly available online. The details of the estimation of the global redshift, emission line redshift, and subsequently the widths and the rest frame EW for each line, are described in Sect. 4 of Pâris et al. (2012). We will briefly summarise them here.

[1] http://vizier.u-strasbg.fr/viz-bin/VizieR

Pâris et al. (2017) first estimated the overall redshift via visual inspection, $z_{\rm vi}$. The spectra are then fitted using a linear combination of four principal components constructed from a high quality subset of SDSS DR7Q (Schneider et al. 2010) spectra that do not exhibit BAL features. The redshifts are adjusted until the best fit is found, which yields the principal component analysis (PCA) redshift, $z_{\rm PCA}$. The individual emission lines are then fitted by a set of five principal components. The redshift of an emission line is estimated from the peak amplitude of the fitted line. The velocity offset between the lines is computed as the difference in the individual emission line redshifts. The symmetry of the line is defined as the ratio of the blue to red half width at half maximum (HWHM), which are evaluated bluewards and redwards of the emission line peak, respectively. The FWHM is then the sum of both HWHM values.

We adopt the convention that a blueshifted line has a negative velocity and will peak towards the bluer end of the wavelength (see Fig. 2.3). Conversely, the peak of a redshifted line has a positive value and tends towards longer wavelengths. A blue/red HWHM ratio of < 1 or blueward asymmetric line will have more flux on the blue wing, while a blue/red HWHM ratio of > 1 or redward asymmetric line will have a broader red wing (see Fig. 2.4).

Pâris et al. (2017) implemented the BALQ definition from Weymann et al. (1991) to identify BAL feature in C IV line. For a line to be considered as a BAL, the BI needs to be larger than $0\,{\rm km\,s^{-1}}$, have an absorption trough width of $\geq 2000\,{\rm km\,s^{-1}}$ at 10% depth below the continuum, and be blueshifted $\geq 3000\,{\rm km\,s^{-1}}$ from the emission line. The C IV BAL troughs are automatically detected for quasars with $z_{\rm vi} \geq 1.57$ to ensure that the region from S IV to C IV is included. The continuum is estimated using a linear combination of four principal components fit to the spectra iteratively to mask any absorption in the spectrum (see examples in Fig. 15 of Pâris et al. 2012). Based on the constructed continuum, the BI in the blue side of C IV emission line is calculated.

The flux density of the continuum can be represented by a power law, given by $f_{\rm cont} \propto \nu^{\alpha_\nu}$, where ν is the frequency. The spectral index, α_ν, is retrieved by applying this approximation to fit over regions with rest wavelength of 1450–1500, 1700–1850, and 1950–2750 Å. These regions are selected as they are free from emission lines. Based on the SDSS primary photometry, the i-band absolute magnitude at redshift $z = 2$, $M_i(z = 2)$, is computed assuming $\alpha_\nu = -0.5$ and K-correction from Table 4 in Richards et al. (2006).

We select a subsample of the SDSS DR12Q catalogue for this analysis such that both C IV and Mg II emission lines, and C IV BAL features, are present in the spectrum. For this purpose, the redshift is bounded for $z_{\rm vi}$ and $z_{\rm PCA} \geq 1.57$. The sample was also chosen to ensure that all measurements had high signal-to-noise (S/N), so that results are not biased by poor statistics. Thus, the sample is further constrained to ensure that the spectra have prominent emission lines: (i) median S/N per pixel over the whole spectrum ≥ 15, (ii) C IV and Mg II FWHMs $> 0\,{\rm km\,s^{-1}}$, and (iii) C IV amplitude ≥ 10 and Mg II amplitude ≥ 5 median root-mean-square pixel noise. Although the C III] line

is also included in this wavelength range, the uncertain contributions of Al III and Si III] emissions to the wings of the line means that an analysis including this line may not be as robust unless the Al III and Si III] emissions are deconvolved.

We remove the data with missing or undefined α_ν values from the raw data. Three outliers are also taken out from the sample. One has $M_i(z = 2) \sim -45$, much brighter than the rest of the samples which have $M_i(z = 2) < -35$. Upon visual inspection, we found that the other two with either EW(Mg II) < 0 or blue/red HWHM(Mg II) $> 10\,000$, have inaccurate measurements. The final sample consists of 2773 spectra and among those 313 show a BAL feature for the C IV line. This corresponds to a BAL quasar fraction of $\sim 11.29\%$. Hereafter, a BALQ refers to a quasar with the presence of a C IV line HiBAL feature only, unless mentioned otherwise. LoBALs might be present but are not identified in the dataset.

5.3 Methodology

Using the dataset presented in the previous section, we conduct several tests to find out whether the BALQ and non-BALQ populations belong to the same parent population using continuum and BEL properties. The two approaches employed are based on statistics and machine learning techniques, which will be described in § 5.3.1 and § 5.3.2 respectively. A total of 12 features are investigated in this work, as listed in Table 5.1.

Table 5.1: List of investigated features using continuum and broad emission line properties.

Property	Feature	Description	Notation
Continuum	`imag`	Absolute magnitude in i-band at $z = 2$	$M_i(z = 2)$
	`z.pca`	PCA redshift	$z_{\rm PCA}$
	`alphanu`	Spectral index	α_ν
BEL	`fw(civ)`	FWHM of C IV	FWHM(C IV)
	`civ_ratioskew`*	Asymmetry of C IV	Blue/red HWHM(C IV)
	`w(civ)`	EW of C IV	EW(C IV)
	`fw(mgii)`	FWHM of Mg II	FWHM(Mg II)
	`mgii_ratioskew`*	Asymmetry of Mg II	Blue/red HWHM(Mg II)
	`w(mgii)`	EW of Mg II	EW(Mg II)
	`civmgii_diffv`*	Velocity offsets of C IV and Mg II	Δv(C IV-Mg II)
	`civmgii_ratiofwhm`*	FWHM ratio of C IV and Mg II	FWHM(C IV/Mg II)
	`civmgii_ratioew`*	EW ratio of C IV and Mg II	EW(C IV/Mg II)

Note: Features are as those defined in VizieR access tool, except stated otherwise.
*User defined features from SDSS measurements.

5.3.1 Statistical Tests

For the K–S test, a two-tailed p-value is evaluated. We describe the statistics as highly significant at $< 0.1\%$, significant at $< 5\%$, and not significant at $> 5\%$. The p-value

can be interpreted as follows. If the p-value is $\leq 5\%$, there is sufficient evidence to reject the null hypothesis, suggesting that the two samples are not chosen from the same distribution. On the other hand, if the p-value is $> 5\%$, there is not enough evidence to reject the null hypothesis.

The 2s A–D test is estimated from the midrank EDF. The calculated significance level, α, is the probability of the null hypothesis being rejected when it is true. If the returned test statistic is greater than the critical value for a given significance level, then the null hypothesis is rejected at that level. The corresponding boundary for the critical value is the critical or rejection region. Since the interpretations for p-value and α are similar, we adopt the same statistical significance cut-off for both. For example, α of 4.9% implies a 4.9% chance that the null hypothesis is incorrectly rejected. The null hypothesis can be rejected at 5% level since α falls within the 5% critical region, but fails to reject for critical region of 2.5%.

The 2s statistical tests are computed using an open source scientific tools for Python, `scipy`[2] (Jones et al. 2001). The tests are calculated for one-dimensional (1d) case between BALQ and non-BALQ datasets.

5.3.2 Building ML Classifiers

The goal of using ML is to find the parameter space that plays the biggest role in separating the BALQ and non-BALQ populations without human intervention, providing us some clues to the dynamics and origins of the BLR. For the purposes of this study, we use supervised ML for binary classification problems and only review these methods. Following the "No Free Lunch" theorems, different supervised ML classifiers are investigated. The choice of ML algorithms is restricted to those that return feature importance or weighting such that the influence of each features can be quantified. We start with four basic supervised ML classification algorithms for interpretability, namely: decision tree, random forest, logistic regression, and support vector machine (see § 5.1.5).

We attempt to construct a supervised binary classification algorithm that can differentiate between the two populations, using a set of continuum and emission line properties. We examine if there is any one of them that outperforms in dividing the samples into their respective classes. The analyses use `scikit-learn`[3] (Pedregosa et al. 2011), an open source ML package in Python. Each of the algorithms utilised in this analysis requires tuning via hyperparameters. For example, the number of decision tree splits for a given decision tree, the number of decision trees used in the random forest algorithm, or the regularisation of the logistic regression algorithm that controls the complexity versus fit balance when finding the optimal weight vector. An outline of the steps performed is as following:

[2] `https://scipy.org/`
[3] `http://scikit-learn.org/`

1. Data preprocessing (see § 5.3.2.1)
    - Load raw data and remove those with missing values and bad measurements. Separate the data into binary classes of BALQ and non-BALQ populations based on BI values, where BALs are those with BI $> 0\,\mathrm{km\,s^{-1}}$ in C IV line.
    - Split data into 80% training and 20% test samples.
    - Apply feature scaling to dataset.
2. Tuning the models (see § 5.3.2.3)
    - Conduct coarse grid searches on algorithm hyperparameters with stratified 10-folds cross-validation (CV) using training set and evaluate the performance using scoring metrics (see § 5.3.2.2).
    - Conduct fine grid search and randomised search on algorithm hyperparameters with stratified 10-folds CV.
3. Model evaluation (see § 5.3.2.4)
    - Obtain the best estimator with the highest validation score.
    - Compare the performance of the different models using various scoring metrics (see § 5.3.2.2).
    - Predict the classes of the test set. Extract the feature importances and compare their significance in other models.

5.3.2.1 Data Preprocessing

After the samples have been refined (see § 5.2), the dataset is partitioned into 80% training and 20% test samples. This step enables the model to be generalised not only for the training set, but also on new samples. The training set consists of quasars from SDSS DR12Q catalogue, with known classes. It is used to learn a model and make a prediction on the new data. The performance of the model is then assessed using the test set.

Logistic regression and SVM algorithms require the data to be scaled, while tree-based estimators are scale-invariant. If a feature has a large variance, it causes the estimator to undermine other features with smaller variance. This problem can be avoided by scaling the features. Since there are possibly some outliers, a robust scaler is used to centre the median to zero and scale the input parameters by the interquartile range, which is the difference between the upper (75th) and lower (25th) quartiles. A pipeline is also applied to chain the scaler transformation and the classifier to avoid information leakage. This ensures that the scaling is done for each split during the CV.

An imbalanced dataset may render model predictions inaccurate towards the more common class. In the dataset, non-BALQs are more abundant and the estimator will attempt to maximise the prediction for this class and overlook the BALQ sample. To account for the imbalanced population, the weighting for each class is set to be the same. As a consequence, the cost of misclassifying the minority class is increased and the

classifier will assign equal emphasis to predicting both classes correctly. A scoring metric that is sensitive to imbalanced classes is employed to alleviate this issue as described next.

5.3.2.2 Scoring Metrics

One way to illustrate the number of samples that are correctly predicted in each class is with a contingency table or confusion matrix. Here, the binary classes can be denoted as non-BALQ (negative) and BALQ (positive). The resulting confusion matrix for binary classification is displayed in Table 5.2. A negative class sample that is correctly labelled is referred to as true negative (TN), while false positive (FP) if it is misclassified as positive. A sample in positive class that is predicted correctly is called true positive (TP), while false negative (FN) when it is wrongly identified as negative.

Table 5.2: Confusion matrix for binary classification.

		Actual	
	Class	non-BALQ	BALQ
Predicted	non-BALQ	True negative (TN)	False negative (FN)
	BALQ	False positive (FP)	True positive (TP)

The true and false positive and negative rates are given by

- True positive rate (TPR) or sensitivity or recall: The probability of detecting positive instances.

$$\text{TPR} = \frac{\text{TP}}{\text{TP+FN}}.$$

- True negative rate (TNR) or specificity: The probability of detecting negative conditions.

$$\text{TNR} = \frac{\text{TN}}{\text{FP+TN}}.$$

- False positive rate (FPR) or fall-out: The probability of misclassified points as positive among negative instances.

$$\text{FPR} = \frac{\text{FP}}{\text{FP+TN}} = 1 - \text{TNR}.$$

- False negative rate (FNR) or miss rate: The probability of misclassified points as negative among positive instances.

$$\text{FNR} = \frac{\text{FN}}{\text{TP+FN}} = 1 - \text{TPR}.$$

A scoring metric is assigned to quantify the efficacy of the model predictions. Model evaluations that use accuracy are unreliable in the presence of imbalanced dataset. Instead, a F1 score is used as the scoring parameter as it is slightly more sensitive to class imbalanced data. Several other relevant metrics are also computed in the following analysis for comparison. All metrics adopt the convention that a higher score signify a better estimator.

- F1 score: Represents the balance between precision and recall.

$$\text{F1} = 2\left(\frac{1}{\text{precision}} + \frac{1}{\text{recall}}\right),$$

  where precision=TP/(TP+FP) is the probability of predicting positive instances. The score ranges between 0 and 1, with 1 indicating perfect precision and recall.
- Area under the receiver operation characteristic (AUROC): Computes AUROC curve, which is the TPR against FPR at various discriminatory threshold, using trapezoidal rule. It provides an estimate of how good is the model in differentiating positive and negative results. The score ranges between 0 and 1, with 0.5 indicating random prediction.
- Balanced accuracy (BACC): Average of the true positive and negative rates.

$$\text{BACC} = \frac{1}{2}(\text{TPR} + \text{TNR}).$$

  The score ranges between 0 and 1.
- Cohen's kappa, κ: Measures the inter-rater agreement between two classifications. In this case, the two raters are the predictions by the ML classifier and the true classes.

$$\kappa = \frac{p_o - p_e}{1 - p_e},$$

  where p_o is the observed probability in agreement and p_e is the expected probability in agreement due to chance. The score ranges between -1 and 1, with ≤ 0 indicating poor agreement.
- Matthew's correlation coefficient (MCC): Measures the quality of binary classification and is a balanced representative statistic of the confusion matrix since it considers the true/false positives/negatives.

$$\text{MCC} = \frac{\text{TP} \times \text{TN} - \text{FP} \times \text{FN}}{\sqrt{(\text{TP} + \text{FP})(\text{TP} + \text{FN})(\text{TN} + \text{FP})(\text{TN} + \text{FN})}}.$$

The score ranges between -1 and 1, with ≤ 0 indicating random prediction.

5.3.2.3 Tuning the Models

Subsets of the training dataset can be further split using CV technique to tune the variables. One of CV strategies is a stratified k-fold CV, which is a sampling method that retains the initial fraction of each class. This method has been shown to reduce the bias and variance estimation in imbalanced data (Kohavi 1995). The strategy is as follows. The training set is randomly partitioned into k folds without replacement, i.e., each sample will be selected exactly once. Then, $k-1$ subsets are used to train the data and one subset for testing the performance. The one remaining fold is called the holdout or validation set. The preceding step is repeated k times. Lastly, all the model performances are averaged.

Before initialising a ML algorithm, there are a few variables that need to be specified. These variables are termed the hyperparameters and require tuning by exploring the parameter space. To calibrate the hyperparameters for a particular algorithm, parameter space searches are performed with stratified 10-folds CV. In general, there are two strategies to conduct a parameter search: grid and randomised search. Grid search CV explores a set of predefined parameter ranges. Randomised search CV probes parameters sampled from a prescribed distribution for a specified number of candidates. We perform both strategies to check the consistencies of the searches.

As outlined earlier, a coarse grid search with stratified 10-folds CV is first executed to find an appropriate range of hyperparameter values. If there are more than two hyperparameters to examine, a set of two values are varied while the rest are fixed in the hyperparameter search, such that the trends can be easily identified. The performance of the models is evaluated using a F1 score (see § 5.3.2.2). From this investigation, a set of parameter ranges is assembled for a fine grid search. Using the same range of parameter space, a randomised search is also sampled for 1000 iterations. The details on setting the parameter space for individual algorithm are summarised here.

The three hyperparameters that are tuned in decision tree classifier are as follows:

- `max_depth`: Maximum depth of tree.
- `max_features`: Maximum features considered in search for the best split.
- `min_samples_leaf`: Minimum number of samples in a leaf node.

Although there are other hyperparamters that can be calibrated, they are of secondary importance, and hence are omitted to save computational time. The splitting criteria is by Gini impurity defined earlier. At each node, the best split that maximised the purity of the children sample given the parent sample, is chosen.

The test scores computed using F1 score for a decision tree model tuned with rough grid search of two hyperparameters are shown in Fig. 5.2. The first pair of hyperparameters calibrated are `max_depth` $\in \{1, 6, \ldots, 26\}$ and `min_samples_leaf` $\in \{1, 11, \ldots, 101\}$, as presented in Fig. 5.2a. The test scores are lower if the maximum tree depth is less than 6 or minimum samples in a leaf is less than 51.

Figure 5.2b shows the tuning for `max_features` $\in \{3\,..\,12\}$ and `min_samples_leaf` $\in \{1, 11, \ldots, 101\}$. Although one of the model test scores is high using the parameters maximum features of 4 and minimum samples in a leaf of 31, the model shows signs of overfitting when the training and test scores are compared. This suggests that the lower the minimum number of samples at a leaf node, the more prone the model is to overfitting, as expected. A minimum number of one sample at a leaf node is also insufficient to properly classify the model as indicated by the low test scores.

The last pair of hyperparameters are `max_depth` $\in \{1, 6, \ldots, 26\}$ and `max_features` $\in \{3\,..\,12\}$ with constant `min_samples_leaf` of 80 to prevent overfitting. The test scores are roughly similar for maximum depth $\gtrsim 6$ regardless of the number of features. Notably, a few models have high test scores even with maximum tree depth of 6. Higher values for both parameters would imply a more complex model and are likely to overfit the samples. Hence, the maximum depth is restricted to below 15 in the fine grid search.

Since a random forest classifier is a collection of decision trees, the hyperparameters are the same as those used in the decision tree analysis. Following the procedure in the previous section, `max_depth`, `max_features`, and `min_samples_leaf` are tuned by grid search. An additional hyperparameter, which is the number of trees, `n_estimators`, can also be adjusted. A higher number of trees reduces the variance in the model but with the cost of increasing computational time. Due to this, the number of trees is fixed to be 100.

To ensure that this chosen parameter value would not considerably change the scores, a grid search is carried out for `n_estimators` $\in \{50, 70, \ldots, 510\}$ using the classifier with the best parameters from the search earlier, which are `max_depth`=9, `max_features`=7, and `min_samples_leaf`=53 (Table 5.3). For the given model, the test scores slightly decrease with increasing number of trees above 110, which is illustrated in Fig. 5.3. This justifies our choice of `n_estimators`.

The logistic regression algorithm is implemented using a library for large linear classification (LIBLINEAR)[4]. The grid searches on the hyperparameter C, which controls the regularisation, are done in a sequence of 100 evenly spaced samples in logarithmic scale. First, a broad range of parameter values is investigated using `C` $\in 2^{\{-10, -9.82, \ldots, 8\}}$. As shown in Fig. 5.4a, the test scores are slightly higher for smaller values of C. Next, the parameter space is further narrowed to `C` $\in 2^{\{-8, -7.92, \ldots, 0\}}$. The results are displayed in Fig. 5.4b, which hint that the test scores peak when $C < 0.3$.

The internal computation for SVM in `scikit-learn` is integrated with a library

[4] https://www.csie.ntu.edu.tw/~cjlin/liblinear/

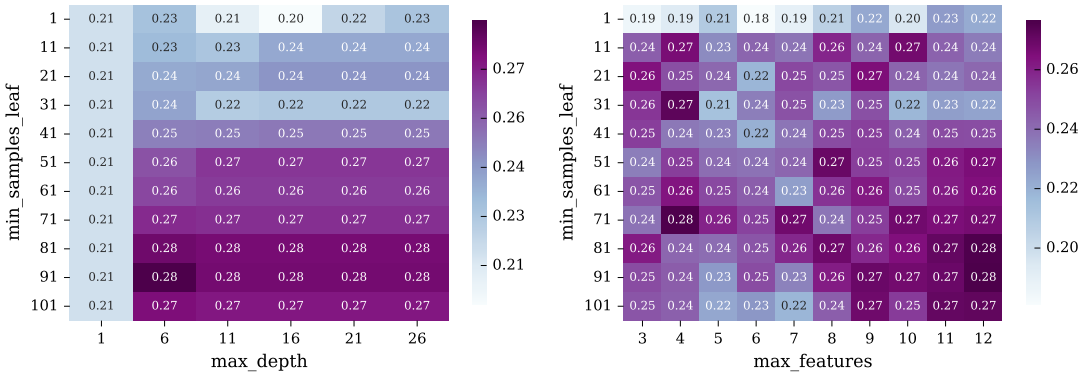

(a) Maximum tree depth and minimum sample size at leaf node

(b) Maximum number of features and minimum sample size at leaf node

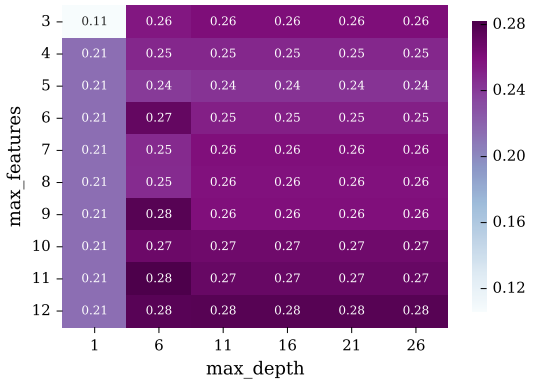

(c) Maximum tree depth and maximum number of features

Figure 5.2: Hyperparameter tuning using course grid search for decision tree. The test score is evaluated using F1 score as annotated in each cell. A better estimator has a higher F1 score, which is indicated by the progressively darker colour.

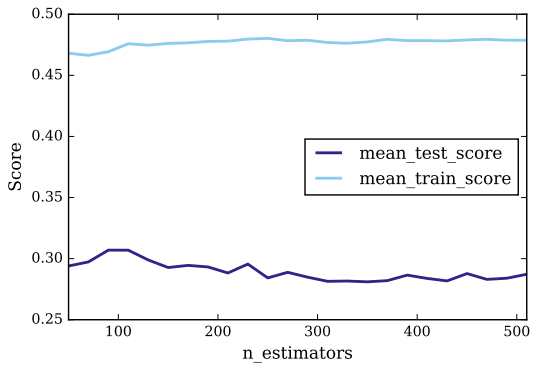

Figure 5.3: F1 test score as a function of number of estimators for random forest model with `max_depth`=9, `max_features`=7, and `min_samples_leaf`=53.

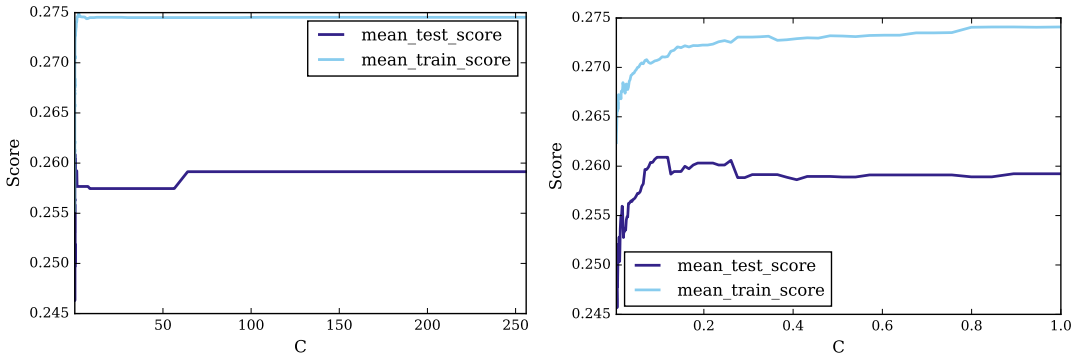

(a) $C \in 2^{\{-10,-9.82,\ldots,8\}}$ (b) $C \in 2^{\{-8,-7.92,\ldots,0\}}$

Figure 5.4: Hyperparameter tuning of C using course grid search evaluated with F1 score for logistic regression.

for SVM (LIBSVM)[5]. The hyperparameter and the tuning steps for SVM are essentially the same as for logistic regression. The prediction capabilities of SVM algorithm can be expanded by applying kernel tricks with high-dimensional kernels, such as radial basis function and polynomial. However, since the features coefficients can only be calculated if the separating plane and the input features are in the same dimension, the kernel type of the SVM algorithm is restricted to a linear function.

Based on the analyses from the coarse parameter space, an exhaustive fine grid search and a randomised search are conducted for each algorithm. The range of values explored are presented in Table 5.3. The best hyperparameter values found for the given classifiers are also provided. Generally, both grid and randomised searches for almost all algorithms yield consistent best estimators, except decision tree.

Table 5.3: Exploration of fine parameter space by the algorithms.

Algorithm	Hyperparameter	Grid Search		Randomised Search	
		Values	Best	Values	Best
Decision tree	`max_depth`	3..15	6	3..15	5
	`max_features`	4..12	9	4..12	11
	`min_samples_leaf`	50..100	74	50..100	66
Random forest	`max_depth`	4..9	9	4..9	9
	`max_features`	4..10	7	4..10	7
	`min_samples_leaf`	50..90	53	50..90	54
Logistic regression	`C`	$2^{\{-5,-4.96,\ldots,-1\}}$	{0.093, 0.120}*	$2^{\{-5,-1\}}$	{0.093, 0.120}*
SVM	`C`	$2^{\{-10,-9.95,\ldots,-5\}}$	0.002	$2^{\{-10,-5\}}$	0.002

* Multiple hyperparameter values with the same test scores and are stated within the range.

[5] https://www.csie.ntu.edu.tw/~cjlin/libsvm/

5.3.2.4 Model Evaluation

Based on the fine grid and randomised searches, the final best estimator is acquired from the model with the highest validation F1 score. Additional scoring metrics that are sensitive to imbalanced classes (see § 5.3.2.2) are also computed to diagnose the general performance of each algorithm. The higher the scores, the better the estimator.

The classes of the test dataset are predicted using the best model. The classifier also returns the feature of importance for the decision tree and random forest, while feature weighting for logistic regression and SVM (see § 5.1.5). The feature importance for tree-based estimators is computed using Gini index as the impurity function. For logistic regression and SVM, the contribution of a feature is taken to be the absolute value of the weight or coefficient.

5.4 Result

5.4.1 1d2s Statistical Tests

Two-sample A–D and two-tailed K–S tests between BALQ and non-BALQ samples are performed on each parameter independently. The statistics are presented in Table 5.4. Only those that are highly significant at $< 0.1\%$ are marked by an asterisk, while we also considered those that are $< 5\%$ as significantly different.

Table 5.4: One-dimensional two-sample A–D and K–S tests between BAL and non-BAL quasars.

Parameter	A–D Stats	A–D α (%)	K–S Stats	K–S p-value (%)
`alphanu`	32.94	0.04^*	0.19	$3.05 \times 10^{-7*}$
`civmgii_ratioew`	7.97	0.04^*	0.12	0.09^*
`civmgii_ratiofwhm`	7.47	0.06^*	0.09	2.06
`civ_ratioskew`	7.06	0.08^*	0.11	0.21
`w(civ)`	5.67	0.21	0.10	0.43
`fw(mgii)`	3.50	1.24	0.11	0.17
`mgii_ratioskew`	3.35	1.42	0.09	3.22
`z.pca`	3.15	1.69	0.09	3.04
`civmgii_diffv`	3.10	1.77	0.08	4.39
`fw(civ)`	1.87	5.42	0.07	13.70
`w(mgii)`	1.08	11.60	0.07	8.99
`imag`	-0.10	38.76	0.07	17.18

Note: The results are sorted in descending order of significance based on A–D significance level, α.
*Highly significant at $< 0.1\%$.

Based on the results, both statistical tests tend to be fairly consistent at 5% level. The parameters that are significant at the $< 5\%$ in the A–D test also manifest in the K–S test. The spectral index, α_ν, shows high significance level of 0.04% and p-value of $\ll 0.01\%$. This might imply that the BALQs and non-BALQs are physically different in some way.

The EW of C IV is significant at $< 1\%$, while the Mg II EW shows no statistical difference between the populations. The ratio of C IV and Mg II EW is even more significantly different, with A–D α of 0.04 and K–S p-value of $< 0.1\%$. Using the K–S test, Gibson et al. (2009) also obtained a comparably high significant difference of $p < 0.01\%$ for the EW of C IV between the BAL and non-BAL quasars. They applied an additional condition in their sample requiring the BAL minimum outflow velocity, $v_{\rm min}$, to be less than $-10\,000\,{\rm km\,s^{-1}}$, such that the C IV absorption trough is clearly separated and less affected by the line emission.

The FWHM ratios between the two emission lines are highly significantly different between the two samples using A–D statistics with α of 0.06 while the K–S p-value is $< 5\%$. The FWHM of Mg II is also significant at $< 5\%$ level. Conversely, the FWHM of C IV is not significantly different between the two samples. This is in agreement with Gibson et al. (2009), who found no difference in the FWHM of C IV distributions between BALQ and non-BALQ populations using samples from the SDSS DR5Q (Schneider et al. 2007) catalogue. In our result, there is statistical evidence that the asymmetry ratios of individual emission lines are different for the two populations, though α and p-value are slightly higher but still below 5% level for Mg II line.

The PCA redshift and the velocity offsets of the high-ionisation C IV line relative to the low-ionisation Mg II line are marginally significant at $< 5\%$. There appears to be no significant difference in the absolute i-band magnitude distribution between the two samples.

5.4.2 Spearman's Correlation Coefficient

To measure the strength of monotonic correlation between the two variables, a nonparametric statistical method using the Spearman's correlation coefficient (Spearman 1904), r_s, is conducted. A perfect positive or negative correlation between two variables will have r_s value of $+1$ or -1 respectively, while 0 indicates no correlation. Those that have $0.00 \geq |r_s| < 0.29$ show negligible or no correlation and $0.30 \geq |r_s| < 0.49$ show low or weak correlation. The threshold of $|r_s| \geq 0.50$ is considered significant correlation, either moderate or stronger correlation, and is commonly applied in many science fields (e.g., Cohen 1988; Mukaka 2012).

The error of the Spearman's correlation coefficient is also estimated. One method is using Monte-Carlo bootstrapping or resampling method (Curran 2014). Bootstrapping (Efron 1979) is done by generating 1000 iterations of subsample consisting of pair of parameters from the original dataset. Each sample is randomly selected with replacement, in a sense that the same point can appear multiple times and is independent to one other with equal chance of choosing any points. The Spearman's correlation coefficient is then computed for each iteration. The final value is quoted as the mean and the associated error as the standard deviation. This technique only accounts for the error in the population associated with lack of data and not error in each individual data point. The data uncertainties are not considered since they are not provided for some variables.

Additionally, the two-tailed p-value for r_s or the correlation probability of being drawn from a random sample, p_s, is also measured, with null hypothesis that a given pair of variable is uncorrelated. Similar to the criterion for p-value used in the previous statistical tests, $< 5\%$ is marginally significant and $< 0.1\%$ is highly significant, implying that the null hypothesis can be rejected.

The correlation coefficients among all the features examined are portrayed in Fig. 5.5a for all quasars and in Fig. 5.5b by considering BALQs (*lower triangle*) and non-BALQs (*upper triangle*) separately. Even though the coefficient is computed for every feature, only meaningful correlations will be interpreted. The rest are provided for completeness.

There is a moderate anti-correlation between C IV FWHM and EW at a highly statistical significance of $p_s = \ll 0.1\%$ for non-BAL samples ($r_s = -0.50^{+0.02}_{-0.02}$), while the negative correlation is weak for BAL samples ($r_s = -0.30^{+0.05}_{-0.06}$) and when considering both populations ($r_s = -0.47^{+0.02}_{-0.02}$). This negative relationship is also identified by Wills et al. (1993) in 123 high-luminosity quasars with r_s of -0.46 ($p_s < 10^{-4}\%$). Brotherton et al. (1994) performed a similar analysis and found r_s of -0.33 at p_s of 3% by using a portion of Wills et al. (1993) dataset within their total sample. Additionally, the line width of C IV is also positively related to that of Mg II line, with weaker relation in the BALQs compared to non-BALQs.

The FWHM and EW of Mg II are moderately correlated with $r_s \sim 0.50$ and $p_s \ll 0.1\%$. A weaker correlation is reported by Brotherton et al. (1994) with r_s and p_s of 0.21 and 10% respectively. Puchnarewicz et al. (1997) measured a higher positive correlation $r_s = 0.60$ with $< 1\%$ significance level in their sample of 160 X-ray selected Seyferts and quasars from ROSAT International X-ray/Optical Survey.

The velocity offset between C IV and Mg II exhibits weak to moderate correlations with nearly half of features inspected. It is moderately anti-correlated ($r_s \sim -0.50, p_s \ll 0.1\%$) with the FWHM of C IV and asymmetry of Mg II for all quasars and non-BALQs. A weak decreasing correlation of $r_s \sim -0.40$ at $p_s \ll 0.1\%$ is seen with the FWHM ratio of the two lines. There is a weak increasing relationship between the velocity offsets and EW of C IV, and consequently the two lines EW ratio using non-BALQs and all samples. In contrast, these trends are negligible in the BALQs. Interestingly, the velocity shift and

C IV asymmetry correlation coefficient is negligibly negative for non-BAL samples with $r_s = -0.15^{+0.02}_{-0.02}$ ($p_s \ll 0.1\%$) but is positive for BAL samples $r_s = 0.24^{+0.07}_{-0.07}$ ($p_s < 1\%$).

The negative correlation between the spectral index and the EW ratio of the lines is moderate, and correspondingly a slightly weaker relation with C IV EW. The Spearman's coefficient correlation between α_ν and C IV FWHM is low positive $r_s \sim 0.30$. Meanwhile, $z_{\rm PCA}$ and $M_i(z = 2)$ show negligible correlations with other features, except for the weakly negative relation between $z_{\rm PCA}$ and EW of Mg II ($r_s = -0.31^{+0.05}_{-0.04}, p_s \ll 0.1\%$).

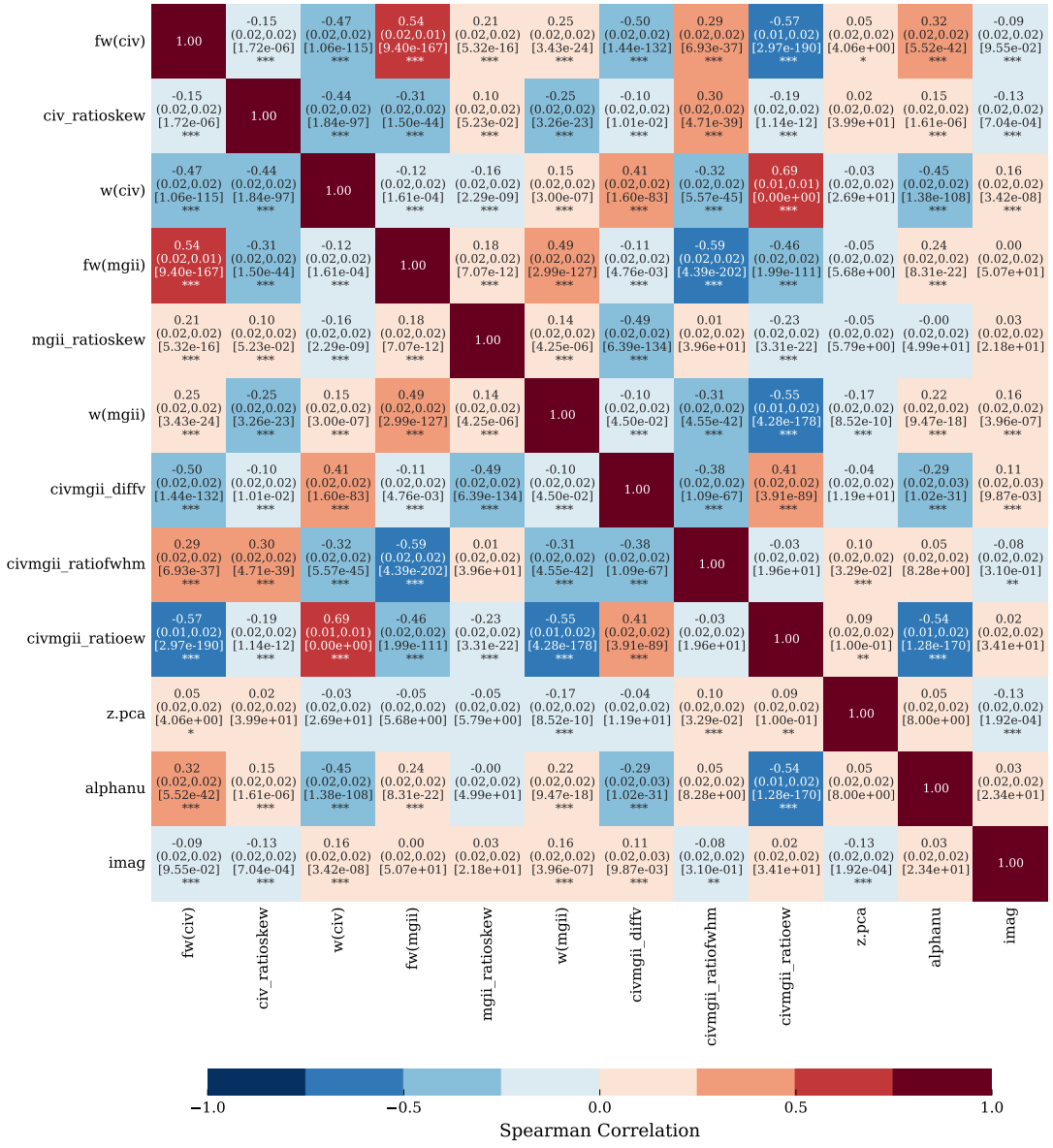

(a) For all quasar population

Figure 5.5: Spearman's correlation coefficient of all the features. In each panel, the first and second lines are the mean Spearman's correlation coefficient, r_s, and the associated uncertainty within one sigma using bootstrap method in parentheses, $(-\sigma, +\sigma)$. The third and fourth lines are the p-value in brackets, [p_s %], and the significant level in asterisk, where $< 5\%$ as $*$, $< 1\%$ as $**$, and $< 0.1\%$ as $***$.

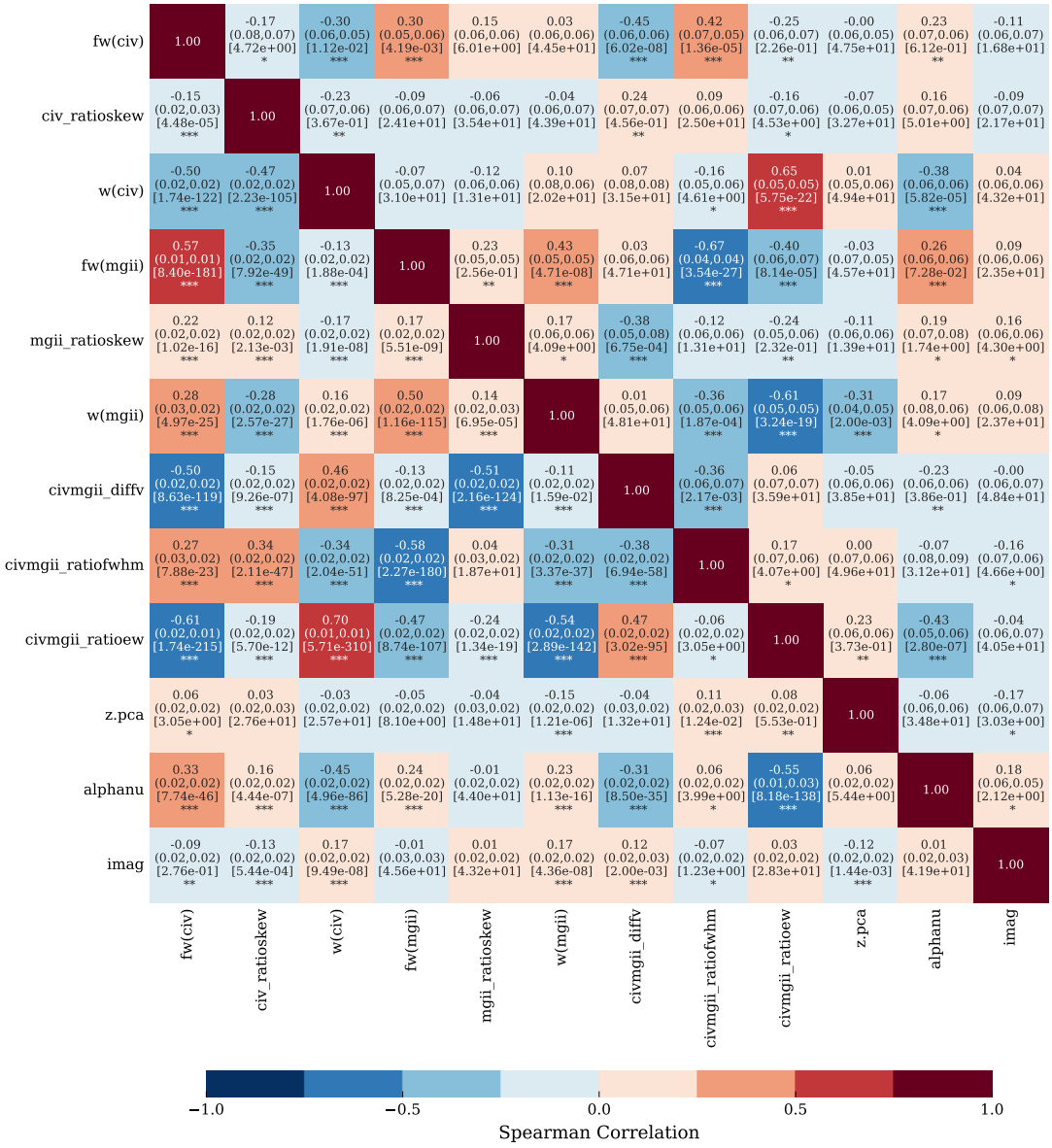

(b) *Lower triangle* for non-BAL population and *upper triangle* for BAL population

Figure 5.5: — Continued

5.4.3 Predictions with ML Classifiers

Table 5.5 presents the confusion matrix for the test dataset after the algorithms have been trained using the training dataset with the best estimators. The true and false positive and negative rates are also supplied. The complementary of true positive rate is the false negative rate. Similarly, the complementary of true negative rate is the false positive rate. Objects that are correctly labelled, i.e., the true positives and negatives, are highlighted in bold. The performances of different algorithms evaluated using various scoring metrics are shown in Fig. 5.6.

Table 5.5: Prediction results of the best estimators from each algorithm for the test dataset using grid and randomised searches.

	Algorithm	Decision Tree		Random Forest		Logistic Regression*		SVM	
	Class	non-BAL	BAL	non-BAL	BAL	non-BAL	BAL	non-BAL	BAL
Grid Search	non-BAL	**356**	34	**386**	29	**323**	22	**342**	24
	Rate (%)	**73.40**	48.57	**79.59**	41.43	**66.60**	31.43	**70.52**	34.29
	BAL	129	**36**	99	**41**	162	**48**	143	**46**
	Rate (%)	26.60	**51.43**	20.41	**58.57**	33.40	**68.57**	29.48	**65.71**
	F1 score	0.306		0.391		0.343		0.355	
Randomized Search	non-BAL	**362**	32	**385**	29	**323**	22	**342**	24
	Rate (%)	**74.64**	45.71	**79.38**	41.43	**66.60**	31.43	**70.52**	34.29
	BAL	123	**38**	100	**41**	162	**48**	143	**46**
	Rate (%)	25.36	**54.29**	20.62	**58.57**	33.40	**68.57**	29.48	**65.71**
	F1 score	0.329		0.389		0.343		0.355	

Note: Columns represent the actual non-BALQ and BALQ classes, while rows represent the predicted classes. Rates are the true and false positive and negative rates in percentage. The true positives and negatives are highlighted in bold.
*Multiple best estimators are present but only one is shown here.

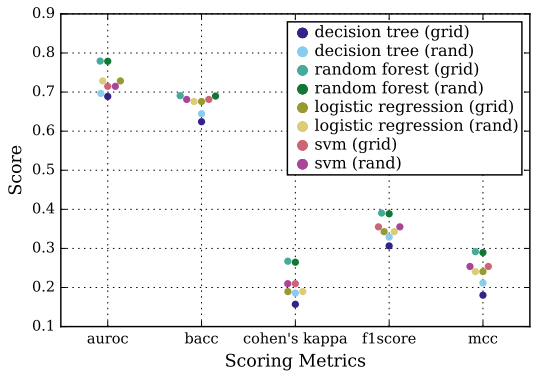

Figure 5.6: Scoring metrics for different algorithms.

Overall, random forest classifiers have the highest test scores. However, this model might suffer from high variance (overfitting), as will be discussed in § 5.5.2.2. Logistic regression and SVM models tend to perform similarly. Single decision tree models have lower test scores compared to the others, which is likely due to their simplistic nature. A small variation in the test scores is also observed in the decision tree classifier when using either the fine grid or randomised parameter space exploration methods, with poorer scoring metrics found for a grid search. As for the rest of the algorithms, the outputs are rather consistent between the two strategies. Indeed, they are exactly the same for logistic regression and SVM.

In general, the predictive power of the estimators are mediocre for the given imbalanced dataset. Tree-based estimators appear to place greater weight in capturing non-BALQ sample correctly, while logistic regression and SVM treat both equally. These can be seen by the percentage rate and number of accurately identified objects for the

individual algorithms. In fact, logistic regression models appears to assign slightly more emphasis on the minority class.

Most of the test scores evaluated using a variety of metrics perform moderately. The AUROC quantifies the ability of the classifier to distinguish between the two quasar population. It indicates that the probabilities of a randomly chosen BAL point is ranked higher than a randomly chosen non-BAL point are between 0.65 and 0.80. The mean of true positive rate and true negative rate described by the balanced accuracy is within 0.60–0.70. Based on the range of Cohen's kappa scores of 0.15–0.30, the level of agreement between the labels assigned by ML algorithms and the actual is poor to fair agreement. A qualitative measure of the precision and robustness of the algorithms indicated by the F1 scores are rather low with values span from 0.30 to 0.40. The assessment of the models using Matthew's correlation coefficient are only marginally better than random predictions with scores of 0.15–0.30.

5.4.4 Feature Importance and Weighting

The feature importance and absolute weighting are computed to identify the contributions of each feature in discriminating between the BALQ and non-BALQ groups. The results are depicted in Fig. 5.7 and the corresponding values are listed in Table 5.6. Higher values correspond to a greater deciding factor in the class separation. The three most influential features for each individual estimator are highlighted in bold in Table 5.6. To compare with the results from 1d2s EDF statistical tests, features that are highly significant at $< 0.1\%$ level and not significant at 5% level are also indicated with symbols.

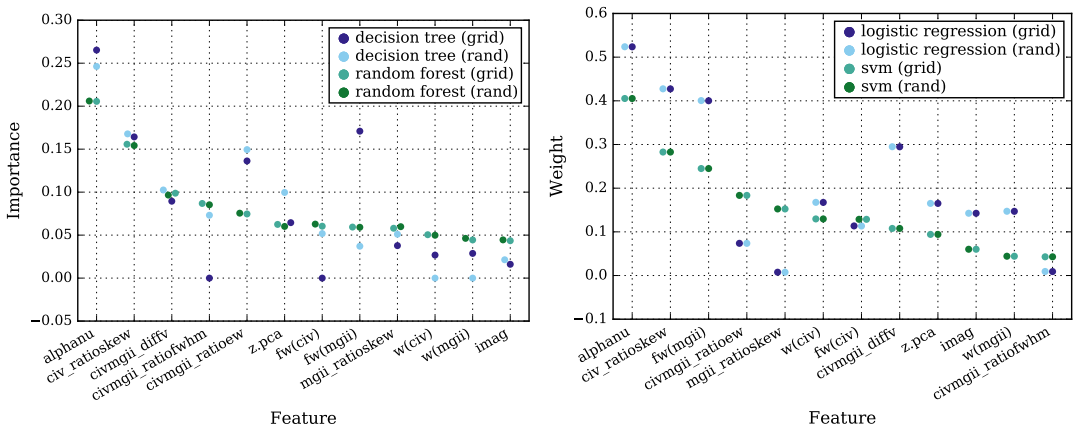

(a) For decision tree and random forest (b) For logistic regression and SVM

Figure 5.7: Feature importance and weighting. Using the best estimator with the highest test scores, the features are sorted in descending order of (a) importance based on random forest (grid) (b) weighting based on SVM (grid).

Table 5.6: Feature importance and weighting for all algorithms.

Feature	Importance				Weight			
	Decision Tree		Random Forest		Logistic Regression		SVM	
	Grid	Rand	Grid	Rand	Grid	Rand	Grid	Rand
alphanu*†	**0.265**	**0.246**	**0.206**	**0.206**	**0.524**	**0.524**	**0.405**	**0.405**
civ_ratioskew*	**0.164**	**0.168**	**0.156**	**0.154**	**0.427**	**0.427**	**0.283**	**0.283**
civmgii_diffv	0.089	0.103	**0.099**	**0.097**	0.295	0.295	0.108	0.108
civmgii_ratiofwhm*	0.000	0.073	0.087	0.085	0.009	0.009	0.043	0.043
civmgii_ratioew*†	0.136	**0.149**	0.075	0.076	0.074	0.074	0.183	0.183
z.pca	0.065	0.100	0.062	0.060	0.165	0.165	0.094	0.094
fw(civ)‡	0.000	0.052	0.060	0.063	0.114	0.113	0.129	0.129
fw(mgii)	**0.171**	0.037	0.059	0.059	**0.400**	**0.401**	**0.245**	**0.245**
mgii_ratioskew	0.038	0.051	0.058	0.060	0.008	0.008	0.152	0.152
w(civ)	0.027	0.000	0.050	0.050	0.167	0.168	0.130	0.130
w(mgii)‡	0.029	0.000	0.044	0.046	0.147	0.147	0.044	0.044
imag‡	0.016	0.021	0.043	0.044	0.143	0.143	0.060	0.060

Note: The features are sorted in descending order of importance based on random forest (grid), which is the best estimator with the highest test score. The top three highest values are highlighted in bold.
*A–D significance level of $< 0.1\%$.
†K–S p-value of $< 0.1\%$.
‡Not significant at 5% level.

Notably, every classifier is unanimous in determining the two of the features in the top three ranking, namely the spectral index and asymmetry of C IV line. These two features are also highly significant in the A–D tests, while only the spectral index is found to be significant in the K–S test. The FWHM of Mg II and the velocity shift between C IV and Mg II that fall into the three most important features in the ML algorithms, are just marginally significant in the statistical test with p-value of $< 5\%$.

Another parameter that is highly significant in both statistical tests is the EW ratio of C IV and Mg II lines. However, it can be seen that this feature is not substantial in splitting the populations with importance values below 0.1 for random forest and logistic regression. Even though the FWHM ratio of the two lines is significantly different between the samples at $< 0.1\%$ in the A–D test, the importance is below 0.1 and even equals zero for decision tree using grid search.

The distributions for three of the dominant features from each ML estimator are plotted in histograms and scatter plots, shown in Fig. 5.8. The spectral index distribution for the BALQ group appears to be shifted towards lower values with respect to that of non-BALQ group. BALs also show more extreme blue HWHM of C IV line, though the two histograms are comparatively alike on the lower end. There is a relatively higher number of BALQs with blueshifted C IV line from Mg II line. In principal, the velocity shifts between the two lines show the C IV to be predominantly blueshifted compared to Mg II line, in agreement with previous studies (e.g., Gaskell 1982). The EW ratio of the two BELs for the BALQ sample tends to be marginally larger than for non-BALQ sample. The BALQ population also exhibits a higher median in the Mg II FWHM distribution.

However, in all cases, the shape of the distributions is fairly similar. Based on the scatter plots, there seems to be no obvious trends that can possibly distinguish between the BALQ and non-BALQ classes. Clearly, it is insufficient to isolate the classes using only one or two features. The similarities in the BALQ and non-BALQ optical/UV emission line and continuum properties, apart from the excess N V emission and redder continua in BALQs, are well established and have been shown in several comparative studies (e.g., Weymann et al. 1991; Reichard et al. 2003).

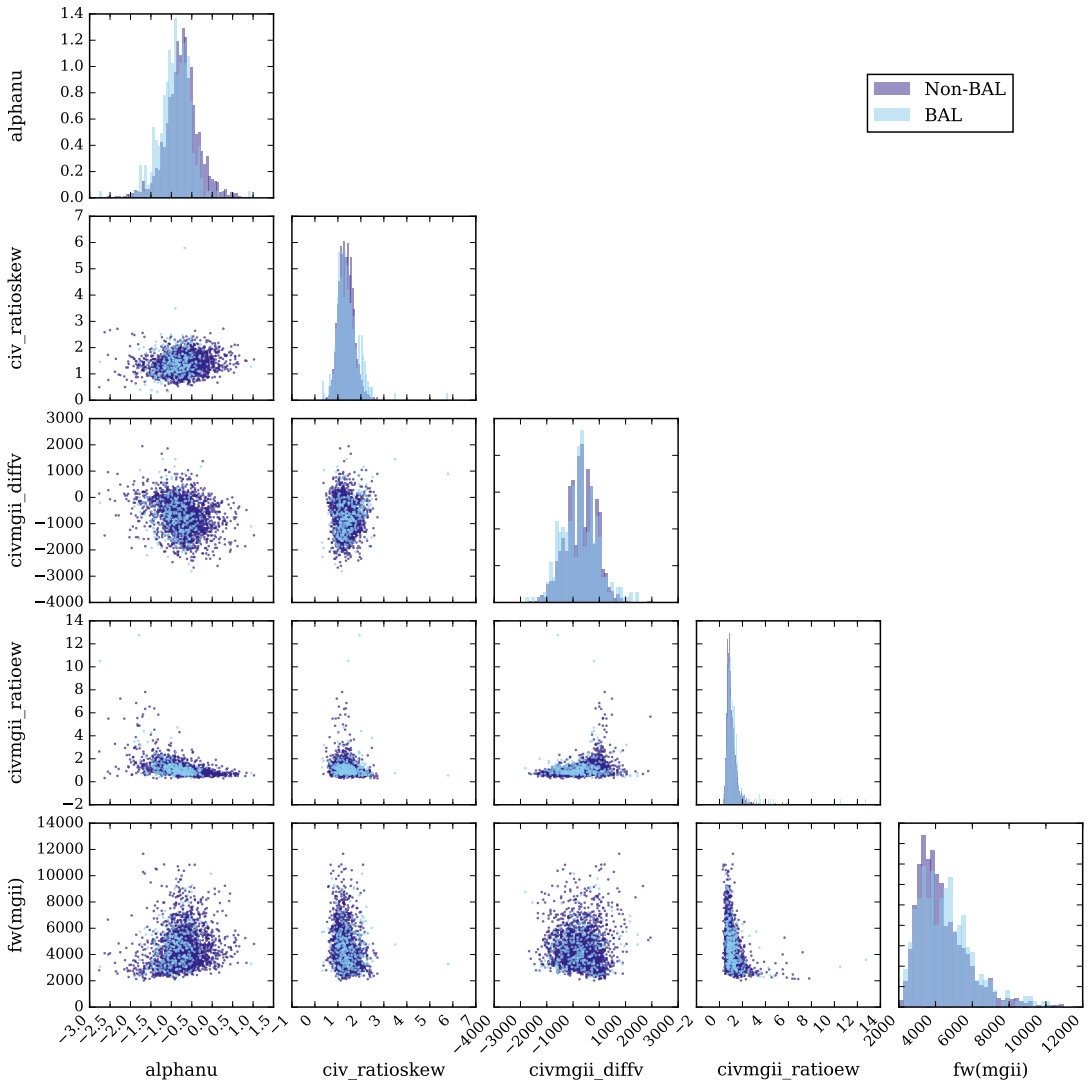

Figure 5.8: Pairwise correlation plot of top three features from each model. The histograms are normalised with the area underneath equals unity.

The results from the 1d2s EDF tests yield three parameters that are not significant at 5%, which are FWHM of C IV, EW of Mg II, and absolute magnitude in i-band. All of these features are also regarded as low importance by the ML classifiers. Two of these features, Mg II EW and absolute magnitude in i-band, received importance values of ≤ 0.060 from most models and ~ 0.145 for logistic regression. Meanwhile, C IV FWHM

importances are < 0.070 for tree-based estimators, while they are ~ 0.120 for logistic regression and SVM.

Generally, there appears to be some degree of consistency between the different ML classifiers employed. In particular, the features that are ranked prominently such as the spectral index and C IV line asymmetry by the tree-based estimators, also persist in logistic regression and SVM estimators. Most models are coherent in assigning low values to features that have minimal contribution, such as FWHM ratio of C IV and Mg II, FWHM C IV, Mg II line asymmetry, EW C IV, EW Mg II, and i-band absolute magnitude.

5.5 Discussion

As discussed in § 5.1, there are some pieces of evidence that support the disk-wind model. However, the dynamics and photoionisation structure of the wind are still uncertain. Several aspects of the wind kinematics appear to be well established. First, gas leaving the accretion disk should retain the angular momentum of the disk in line-driven winds or conserve gas angular velocity if the winds can co-rotate, at least close to the disk, as in magnetocentrifugally driven winds (Proga 2007). Thus, an outflowing wind would have a helical structure. In addition, there is strong evidence for a dominant outflowing component in at least some parts of the broad emission line region due to the observed blueshift between C IV and Mg II lines. And finally, only the near side of the disk-wind will be seen due to the opacity of the disk. Larger scale emission, such as the narrow line region would be much less obscured.

An outflowing helical wind, viewed along different lines-of-sight will appear to have different measured physical characteristics, for example the FWHM of the BELs. The effect of orientation, particularly for winds with relatively narrow opening angles, is explored in Chapter 4. It establishes two important results. Firstly, angle of viewing has a significant impact on the measured physical parameters of the BELs. If an emission line is located in a region of the wind with a non-negligible poloidal velocity, then from some angles of viewing, the velocity offset of the line from the systemic velocity will be large. Conversely, if the line is emitted from gas that has primarily rotational kinematics, then its peak velocity will largely reflect the systemic velocity of the quasar. Additionally, the FWHM of the line will vary with the angle of viewing, with the exact relationships dependent on the contributions of poloidal, rotational, and wind opening angle to the relevant part of the wind. Secondly, the observed BEL properties depend on the location of the emission region within the wind.

Clearly, the similarities and differences in the properties of the emission lines between BALQ and non-BALQ populations provide crucial information on the geometry and physics of the BLR. In a disk-wind model, the common hypothesis is that orientation effects determine whether a BAL or a non-BAL is detected (Murray et al. 1995; Elvis

2000, 2004). In these models, a BAL is predicted to be seen if the narrow outflowing wind falls within the line-of-sight of the observer. Though other quasar parameters, such as the black hole mass and mass accretion rate, might be important, they do not mitigate the effect of the AGN's orientation on the line shape. The scatter from the black hole mass and accretion rate will essentially contribute to the spread in the width of the distributions of BEL properties. However, the underlying trends will remain the same, and therefore differences between them can be differentiated by statistical tests. As noted in § 4.4.6, varying the black hole mass mainly affects the line width, as predicted from the virial motion, while the degree of ionisation is affected by the mass accretion rate. Generally, the trends in the line profiles, like blueshifting and line asymmetry, still persist. Hence, in a representative population of quasars, BALQs and non-BALQs will appear significantly different in a narrow disk-wind model, as viewed from varying range of angle, despite the expected variation in black hole masses and accretion rate. The differences in the emission line shapes should also be indicative of the structure of the associated wind region. Therefore, any observed difference between the two samples should enable us to deduce the spatial origin of a particular emission or absorption line.

5.5.1 Orientation vs. Evolutionary Models

It remains unclear from the literature which model, the orientation or evolutionary, can provide a definite explanation on the presence of BALs or whether a combination of both model is required. When considering the orientation model, most authors have assumed the BEL disk-wind to have a structure similar to Elvis (2004), with a fairly narrow wind opening angle. The similarity between the two samples in this analysis is in conflict with this model. Also, models that invoke a narrow wind, do not all agree on the orientation of the wind. In fact, there are several pieces of evidence that appear inconsistent with regards to the launching angle of the wind. Evidence of an equatorial wind launched from the accretion disk are supported by spectropolarimetry observations (Goodrich & Miller 1995; Cohen et al. 1995; Ogle et al. 1999; Lamy & Hutsemékers 2004; Brotherton et al. 2006; Young et al. 2007). Detailed models incorporating both hydrodynamical wind and photoionisation from radiation field also favour this idea (Proga et al. 2000; Proga & Kallman 2004). However, this is complicated by the discovery of RL BALQs with polar outflows, implying that they are seen near parallel to the relativistic radio jet (Zhou et al. 2006; Ghosh & Punsly 2007). This hints that BAL outflows can span a broad range of viewing angle.

Suppose the sole factor that governs the intrinsic BALQ fraction is the viewing angle along the narrow wind opening angle. Then, it is predicted that the fraction should remain the same over time, and therefore be redshift independent. However, Allen et al. (2011) found that the intrinsic fraction of C IV BALQs changes with redshift, which they argue contradicts the orientation only explanation. Additionally, Becker et al.

(2000), Montenegro-Montes et al. (2008), and Fine et al. (2011) demonstrated that the radio spectral index distributions in a small sample of BAL and non-BAL quasars are comparable, indicating no preference in orientation. Using a larger sample consisting of 74 BALQs, DiPompeo et al. (2011) discovered that there are more radio core sources in BALQs, associated with a face-on inclination, but with both BALQ and non-BALQ populations having the same spectral index range. DiPompeo et al. (2012) also found no relationship between the radio spectral index and BAL outflow properties. Each of these lines of evidence, argue against a limited angle of viewing for BALQs.

There are also some inconsistencies between the observations and the predictions of the evolutionary model. In the optical/UV wavelength regime, BALQs exhibit higher reddening than non-BALQs, which could indicate that a quasar with BALs is younger and dwells in a dustier environment (e.g., Weymann et al. 1991; Sprayberry & Foltz 1992). Our results in the previous section also show that there is a distinct difference in the spectral indices between BALQ and non-BALQ samples, which might be due to dust extinction. The distribution of the spectral index for BALQ sample tends to be smaller than that of non-BALQ sample. This difference in spectral indices between the two populations is also detected by the ML algorithms, which yields the spectral index as the dominant feature that distinguish the two groups. A quasar with a higher covering fraction, as deduced in the evolutionary model, is expected to exhibit relatively more emission in the longer wavelengths, where less dust is being absorbed. However, studies in the mid-infrared (Gallagher et al. 2007), far-infrared (Cao Orjales et al. 2012), and submillimetre (Willott et al. 2003) show that the SEDs are the same for a small sample of BAL and non-BAL quasars with similar luminosity. When using a larger sample of 72 RL BAL objects from DiPompeo et al. (2011), DiPompeo et al. (2013) discovered that there is indeed more radiation in the mid-infrared in the BALQ sample. Hence, a mixture of both the orientation and evolutionary models has been suggested (Gallagher et al. 2007; Allen et al. 2011; DiPompeo et al. 2013). Lawther et al. (2018) found close companion galaxies to a subset of observed FeLoBALs supporting a merger-induced young quasar scenario.

If the orientation model were valid, the observed emission line properties of the BAL and non-BAL quasars are predicted to be distinct in a narrow wind disk-wind model. We can rule out BALs arising from specific fixed narrow wind opening angle if the BEL properties are statistically indistinguishable. This is because the resulting BALQs and non-BALQs will populate different extremes of the BEL property distributions depending on the angle the wind is located. For BALs viewed through a polar narrow wind, the line profile will be narrower and more blueshifted compared to those for non-BALQs that are seen at non-polar angles. The opposite is true for equatorial BAL wind. Additionally, if the narrow wind lay in the middle of these extremes, we expect that the non-BALQs to show both the most narrow, blueshifted and the most wide, symmetric BEL profiles, while the BALQs would not. This would manifest as a difference between the BEL properties of BALQs and non-BALQs, and can be identified by statistical tests.

For a rotationally dominated structure, the FWHMs should increase significantly with inclination angles toward edge-on, as a higher portion of the velocity aligns with the line-of-sight (see Chapter 4). In this case, a systemic shift to larger FWHM values should be detectable by the statistical tests and machine learning. If the evolutionary model were valid, we could expect that there would be no difference in most of the emission line features for the two groups, assuming the only difference between the two groups is the shrouding of the AGN by a dust and gas cocoon. However, it is possible that we are looking at very different AGN states due to different accretion rates and less relaxed systems, and hence differences in emission properties may arise.

In our analysis, the BAL and non-BAL characteristics are found to be very much alike, which argues against the idea that a BAL is formed when the projected line-of-sight intercepts an equatorial outflowing wind with narrow opening angle. Although we assume that the BELs are formed in the BAL wind, our argument holds as long as the BEL emitting region has a realistically flattened axisymmetric geometry. In fact, only a few attributes of the BELs are highly significantly different at $< 0.1\%$ level. The outcomes from ML also support the difficulty in discriminating the BALQs from the non-BALQs. We found that with only the observed continuum and BEL features, the two populations cannot be clearly distinguished. Even the features that demonstrated significant differences still show strong similarities in the overall distributions. This suggests that a revision in the commonly used paradigms is required to describe the observed trends.

5.5.2 Caveats

5.5.2.1 Dataset

It is noteworthy to mention a few caveats that would affect our results. As datasets are normally heterogenous, they are prone to suffer from selection bias. This might shift the significance of the results and the observed trends, but it should not substantially alter our major conclusion.

The true BALQ fraction is still poorly established. In our sample, the percentage of quasars with BALs is $\sim 11.3\%$ within redshift of $1.57 \leq z \leq 2.42$, which is slightly lower than other published results. The observed fraction has been found to be $15 \pm 3\%$ for $1.5 \leq z \leq 3.0$ (Hewett & Foltz 2003), $14.0 \pm 1.0\%$ for $1.7 \leq z \leq 4.2$ (Reichard et al. 2003), $13.3 \pm 0.6\%$ for $1.68 \leq 2.3$ (Gibson et al. 2009), and $8.0 \pm 0.1\%$ for $1.6 \leq z \leq 5$ (Allen et al. 2011). After taking into account certain selection effects, the intrinsic fraction of BALQs are generally found to be larger, for example, about $22 \pm 4\%$ (Hewett & Foltz 2003), $15.9 \pm 1.4\%$ for $1.70 \leq z \leq 3.45$ (Reichard et al. 2003), $16.4 \pm 0.6\%$ (Gibson et al. 2009), and $40.7 \pm 5.4\%$ (Allen et al. 2011).

The number of BALQs in any given sample is dependent on the choice of constraints applied to classify BALQs and non-BALQs. Different S/N cuts affect the BALQ detection rate. There is a higher chance of identifying a BALQ in spectra with high S/N (Allen et al. 2011). In addition, the BI measure used to determine a BAL might underestimate the total BALQs as it rejects those with weak absorption troughs.

The measure of absorption trough relies on the method of line fitting applied on the quasar samples (Pâris et al. 2017). The emission lines in SDSS DR12Q are fitted using PCA components created using a sample of non-BALQ spectra. Each line is fitted with five PCA components and the continuum is fitted as a power-law using the best fit PCA component around the emission line. Pâris et al. (2017) reported that the PCA method produces a similar BI distribution to that of Allen et al. (2011) using non-negative matrix factorisation, but differs slightly from Gibson et al. (2009), which shows more objects with low BI values. Gibson et al. (2009) modelled the emission lines using a power-law continuum and a Voigt profile. Therefore, some BALQs may have been misidentified as non-BALQs or vice versa.

We did not inspect every spectra on the accuracy of each parameter value extracted from SDSS DR12Q (Pâris et al. 2017) catalogue. It is possible that some spectra, especially the BALQ sample, are not fitted accurately since the fitting procedure is done automatically and is based on a sample without broad absorption features. Consequently, the results could be biased towards the properties of the non-BALQs. Additionally, the measurement uncertainties for each property are not accounted for.

5.5.2.2 Bias-variance Trade-off in ML Algorithms

To determine if increasing the size of the training dataset will help to boost the score, we examine the learning curves with stratified 10-folds CV of every algorithm, as visualised in Fig. 5.9. The learning curve also serves to identify situations where ML models suffer from under or overfitting. The training and validation scores are evaluated using F1 score.

We found that no matter the size of the training sample, the properties used could not provide a good fit, in the sense that the training and validation scores are low. Using a more complex ML model, such as multi-layer perceptron and incorporating boosting methods, might marginally increase the scores. However, given the input features, the prediction capabilities using different ML classifiers is not expected to significantly boost the test scores. This is shown by the fairly similar test scores of the four different ML algorithms. An alternative method of improving the classification algorithm is to add more features. However, this requires some insight into which features are actually substantial in differentiating the BALQ from the non-BALQ group, which is not obvious at present.

Additionally, the random forest algorithms show signs of high variance, with a huge gap between the training and validation scores. A slight indication of this problem is also seen in decision tree algorithms. This means that the training dataset is overfit, and therefore gives poorer results when the algorithm is applied to the test set. To counteract this dilemma, increasing the training samples and reducing the complexity of the model might remove this gap. In contrast, logistic regression and linear SVM are free from this issue. The learning curves of both scores have somewhat converged. In this case, adding data will not further improve the results.

5.6 Proposed BLR Disk-wind Model

In general, there is a large diversity in line widths and line shifts between the different BELs in a single object. When this information is combined with the line strengths, this variety can be utilised to infer the ionisation potential and dynamics of the gas. The different properties of the high-ionisation C IV line and low-ionisation Mg II line suggest these two lines are emitted in distinct regions.

It is still unknown whether BELs and BALs originate from the same region or structure, or the nature of this region. As mentioned previously, some of the observed trends are inconsistent with the published disk-wind models, incorporating a narrow outflowing wind angled close to equatorial and emanating from an opaque accretion disk. This hints that other BLR outflow geometries are needed to understand the observations.

To address this situation, we present a potential disk-wind model of BLR with the assumption that the BLR is directly associated with the BAL wind. The highlights of our model include the following important additional features:

- The wind spans a wide range of angles between the torus and an axial ionised cone.
- Within that wind, there are multiple radial streams of higher density, clumpy material.
- BAL troughs are detected if an observer's line-of-sight intersects any of these streams, while non-BALQs are seen for other lines of sight through the wind.

The model is illustrated in Fig. 5.10 and the specifications of the features are elaborated as follows:

- **The BLR comprises a disk-wind with a rotational velocity component reflecting the angular momentum of its origin in the accretion disk, and a poloidal component resulting from an acceleration mechanism. The emission line flux produced at each region of the wind is expected to reflect the local density and ionisation state.**
  The main acceleration mechanism is not known but could be due to a gradient in gas pressure or thermal expansion (Weymann et al. 1982; Begelman et al. 1991),

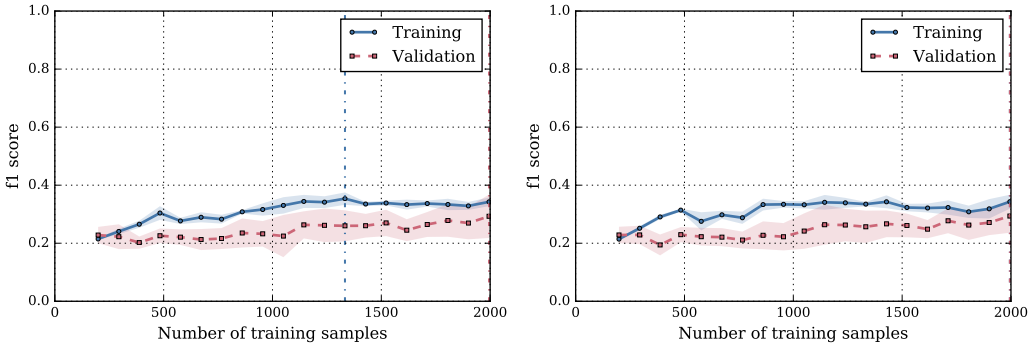

(a) Decision tree (grid search)

(b) Decision tree (randomised search)

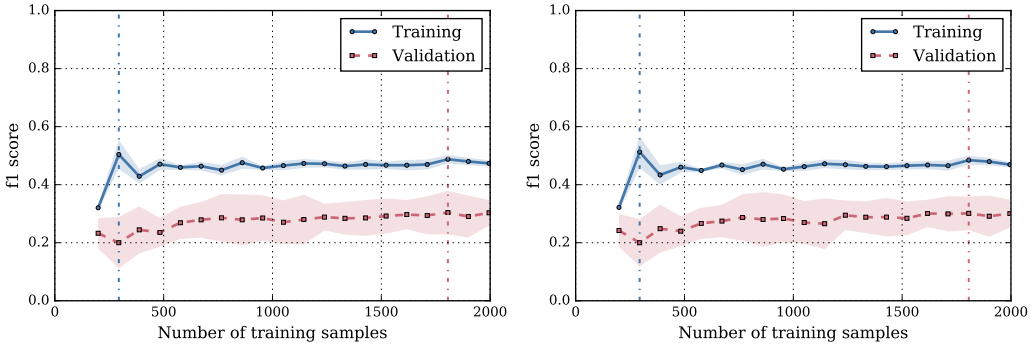

(c) Random forest (grid search)

(d) Random forest (randomised search)

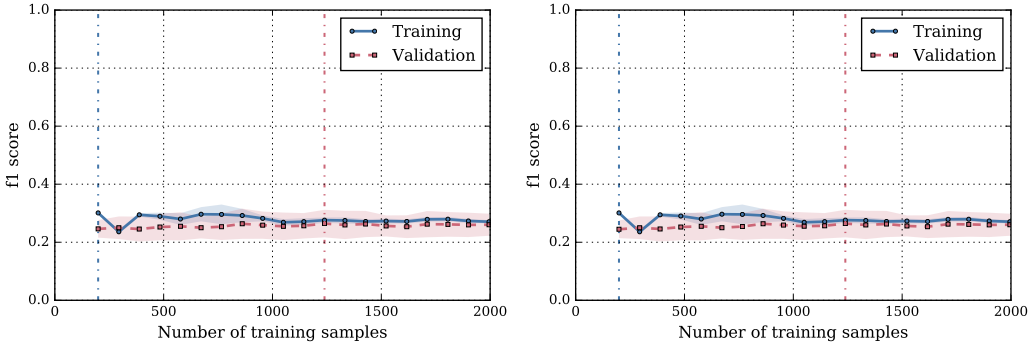

(e) Logistic regression (grid search)

(f) Logistic regression (randomised search)

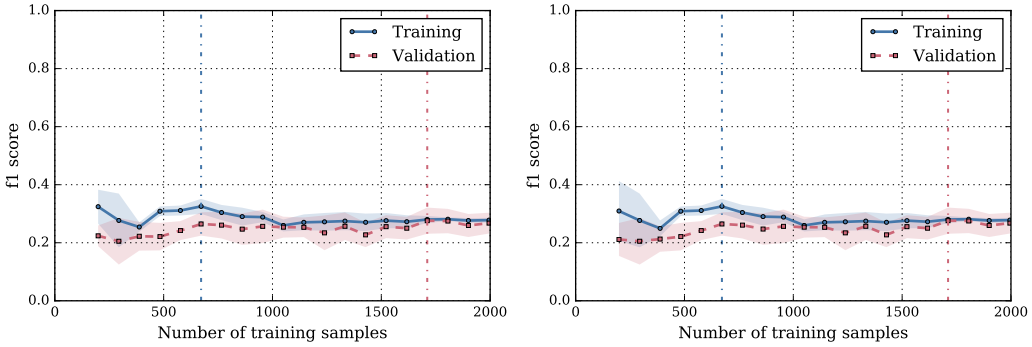

(g) SVM (grid search)

(h) SVM (randomised search)

Figure 5.9: Learning curves with stratified 10-folds CV for every algorithm. The dash-dotted vertical lines represent the maximum score.

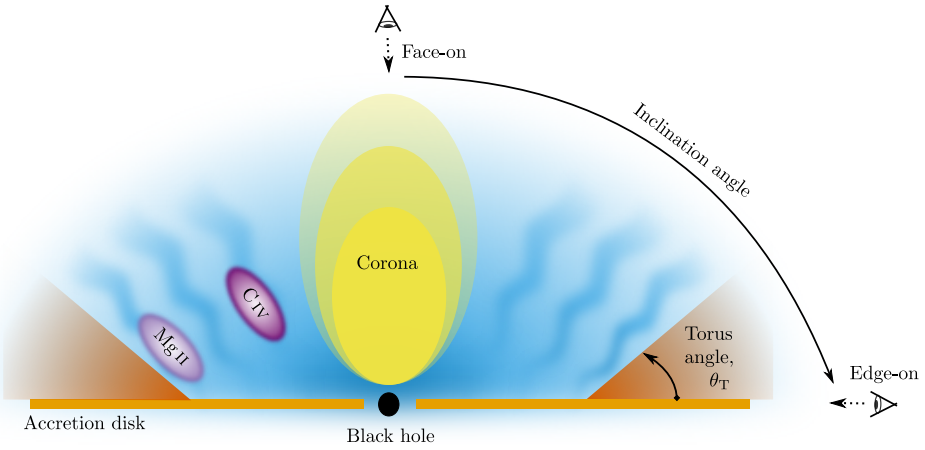

Figure 5.10: The proposed BLR disk-wind model with the following features: black hole (black), optically thick accretion disk (orange), dusty torus (vermillion), ionisation cone or corona (yellow), and wind that spans a wide range of angles (sky blue). The wind is driven by some acceleration mechanism, forming radial streams of regions with denser gas (curl lines in the wind). These regions can be transient in nature and occur at different angles in each quasar. BALs are seen when the line-of-sight intersects these regions. The bulk of the high-ionisation C IV line emission (dark purple) is emitted close to the black hole, while the bulk of the low-ionisation Mg II line emission (light purple) is emitted near the base of the wind and further from the centre of the ionising source. The region in the ionisation cone is completely ionised. The view of the inner regions will be obstructed by the dusty torus when seen with an angle θ_T of edge-on.

radiation pressure or line driving (Shlosman et al. 1985; Arav et al. 1994; Murray et al. 1995), or it could be a magnetically driven wind (Blandford & Payne 1982; Emmering et al. 1992; Konigl & Kartje 1994). The presence of the BALs strongly indicates that substantial momentum is transferred from a powerful radiation field to the gas. The preferred driving mechanisms for a disk-wind are often a combination of line-driven and magnetic field (Konigl & Kartje 1994; de Kool & Begelman 1995; Proga 2003; Everett 2005).

Our understanding on how line driving can produce powerful, high velocity winds is based on studies of winds in hot stars (Castor et al. 1975). Luminous and massive hot stars possess fast winds that are radiatively line-driven due to the intense radiation of the star (Castor et al. 1975; Pauldrach et al. 1986; Friend & Abbott 1986). Subsequently, line driving mechanisms has been adapted in other accreting systems, such as cataclysmic variables, quasars, and young stellar objects. Hydrodynamical models of AGN using line driving have successfully created winds of the observed dynamics (Proga et al. 2000; Proga & Kallman 2004). However, the efficiency of line driving is highly dependent on the ionisation state of the outflow. Due to the strong X-ray emission of AGN, without a layer of 'hitchhiking' gas (Murray et al. 1995) or a small filling factor (we will discuss this further), the gas will be too ionised to drive the wind.

Further evidence for the role of radiation in driving the wind is the blueshift

of emission lines. Richards et al. (2011) conducted a comprehensive investigation on the correlation of C IV blueshift with quasar properties and showed that the trends can be explained within the framework of disk and wind components. They suggested that weak C IV with large blueshift is indicative of a wind-dominated system with relatively low X-ray luminosity that allows strong winds to be driven via radiative pressure. In a disk-dominated system, the relatively high X-rays will over-ionise the wind and suppress line-driving mechanism. Shen et al. (2016) found that the blueshift of He II, C IV, and Si IV have strong luminosity dependence. Their average blueshift relative to LILs such as [O II] or Mg II increases with luminosity, consistent with previous findings (e.g., Hewett & Wild 2010; Richards et al. 2011; Shen et al. 2011; Shen & Liu 2012).

We expect that magnetic fields may be important in driving or confining the ionised outflowing wind. Magnetic fields are essential to the existence and evolution of accretion disks as magnetorotational instability is almost certainly responsible for local angular momentum transport in accretion disks (Balbus & Hawley 1991). Therefore, it is likely that the magnetic fields play a role in the wind. Magnetocentrifugal wind models are able to predict the geometry and kinematics of a wind, but considerable assumptions must be made on the mass-loss rate, making a magnetocentrifugal wind less robust to observational testing.

- **Only the near side of the BLR disk-wind is observed due to the opacity of the accretion disk.**
  This is a commonly accepted argument due to the high column density of the accretion disk. However, the assumption does depend on the opacity remaining high out beyond the self gravitation radius.

- **A region or cone around the accretion axis may be completely ionised, and therefore not contribute to the BELs.**
  Due to the strong X-ray component of the AGN emission, the gas close to the central source is expected to be over-ionised. Proga et al. (2000) and Proga & Kallman (2004) found a region consistent with this in their line driving simulations.

- **The BLR will be obscured for viewing angles close to edge-on (i.e., the plane of the accretion axis). Thus, the BLR will be observed in AGN viewed from a range of angles, significantly less than a solid angle covering of 4π.**
  This assumption is based on the general unification model of AGN, where the obscuration comes from a type of dusty torus, thickened accretion disk, or dusty outflow (e.g., Antonucci 1993). The existence of dust on scales just beyond the BLR is well established (Jaffe et al. 2004; Kishimoto et al. 2009, 2011; Hönig et al. 2012; Kishimoto et al. 2013), and can explain the observed broad line emission in the polarised spectra of some type 2 quasars (e.g., Antonucci & Miller 1985; Miller & Goodrich 1990; Tran et al. 1992; Heisler et al. 1997; Zakamska et al. 2005).

- **Within the wind, the ionisation (and density) will vary depending on the angle from the accretion axis and radial distance from central source. In particular, HILs such as C IV will be preferentially emitted closer to the accretion axis, while LILs such as Mg II and Hα will be emitted from regions closer to the accretion disk.**
  This assumption is based on the line profiles of the associated lines. LILs tend to be more symmetric, having little or no velocity shift from the systematic redshift of the object. Their line widths are consistent with their motions being dominated by Keplerian motion, and hence are often used to estimate the black hole masses (McLure & Jarvis 2002; Shen et al. 2008; Wang et al. 2009; Rafiee & Hall 2011; Trakhtenbrot & Netzer 2012; Mejía-Restrepo et al. 2016). In contrast, HILs are commonly blueshifted with respect to the systematic redshift and show significant asymmetry. Shape corrections are required to recover black hole masses consistent with those found with LILs (Collin et al. 2006; Shen & Liu 2012; Denney 2012; Park et al. 2013; Runnoe et al. 2013a; Coatman et al. 2017; Park et al. 2017). This may suggest another velocity component is playing a significant role in the motion of the HIL emitting gas. The small scatter in the broad line widths for more luminous objects also hints the presence of non-virial velocity component (Fine et al. 2008). The models presented in Chapter 4 show that emission lines emitted from close in a disk-wind are more symmetric and unshifted from the systematic redshift, while lines emitted from regions close to the central source with a larger angular offset from the disk show significant blueshifts for most inclinations, and have a substantial poloidal velocity component causing line asymmetries.

- **The BAL wind is co-spatial with the BLR or at least part of the same extended geometry.**
  As the BELs are often absorbed, the BAL wind must be either outside or co-spatial with the BLR. We expect that the BEL and BAL regions originate from the same continuous geometry in the BLR, driven by same mechanism, and not from distinct regions. This is due to the similar ionisation states required to emit and absorb the observed lines. Additionally, some connections have been found between BALs and BELs, such as correlations between the minimum outflow velocity (detachment) of the BAL troughs and the width or the strength of the BELs (Turnshek 1984; Lee & Turnshek 1995) and the BEL blueshifts are particularly large in BALQ composite spectra (Richards et al. 2002).

- **BALs will be observed when the angle of viewing intersects a region of denser gas. This suggests that these regions occur throughout the wind, not in a preferred direction.**
  The similarity between the BAL and non-BAL quasar FWHM distributions suggest that there is not a significant inclination difference between the two samples, as discussed in § 5.5.1. This means that BALQs are viewed from similar angles to

non-BALQs and a flattened or narrow disk-wind model, such as that proposed by Murray et al. (1995) and Elvis (2000, 2004), is inconsistent with our finding. Instead we propose a wind covering a large angular range that is intrinsically clumpy in nature. These clumps are embedded along streams and are regions of high column density. Multiple radial streams may be present, presumably with an integrated covering factor of $< 20\%$ to account for the observed fraction of BALQs to non-BALQs (assuming a non-evolutionary argument). BALs are observed when our line-of-sight passes through these streams. Some BELs are also produced in these streams. The regions are radially extended, spanning the wide velocity range observed in BAL troughs, whereas they can have orientations anywhere in the viewing angle range of non-BALQs. They are temporary with differing launching angles in individual quasars as this randomness works well with the observed timescale of variability in the BALs (Hamann et al. 2013). These regions can be thought of as radial streams of clumps with a range of optical depths. While they are expected to be mostly optically thick, overall these regions will have different density and optical thickness that give rise to the distinct emission and absorption lines in the spectrum.

The idea of small-scale dense substructure has already been well established in hot stars. Line-driven winds in stellar winds can be unstable and are affected by line-deshadowing instability (LDI; Lucy & Solomon 1970; MacGregor et al. 1979; Abbott 1980; Carlberg 1980; Lucy & White 1980; Owocki & Rybicki 1984). Time dependent numerical simulations have shown that LDI is able to create strong wind shocks, which leads to the compression of materials in the star atmosphere and the formation of a highly inhomogeneous dense clumped structure (e.g., Owocki et al. 1988; Feldmeier et al. 1997). The existence of clumped winds in massive stars is also confirmed by observations (see reviews by e.g., Hamann et al. 2008; Sundqvist et al. 2012). Additionally, the numerical studies on cataclysmic variable stars demonstrate that the clumps in the line-driven winds are time dependent (Proga et al. 1998; Dyda & Proga 2018).

In AGN models, a clumpy wind is naturally produced in both a magneto-centrifugal outflowing wind (Emmering et al. 1992) and a line-driven wind (Proga & Kallman 2004), or may represent transient density enhancements formed due to turbulence or shocks in radiatively driven wind (Arav et al. 1994). A clumpy wind is also one of the two main mechanisms proposed to resolve the over-ionisation problem found for all wind models regardless of driving mechanism. A sufficiently low filling factor increases the electron number density and lowers the ionisation parameter enough to prevent over-ionisation (e.g., de Kool 1997; Hamann et al. 2013; Baskin et al. 2014).

Sim et al. (2010) and Higginbottom et al. (2013, 2014) performed a Monte Carlo radiative transfer simulation of a line-driven disk-wind and managed to produce synthetic spectra of AGN. However, they noted that the wind in high

luminosity X-ray sources tends to over-ionised and consequently inhibits the production of UV absorption lines. An extension to their work by Matthews et al. (2016) found that a clumpy wind was required to moderate the ionisation state of the gas and allow the formation of BAL features at realistic X-ray luminosities. It also allowed the formation of strong emission lines, although their simulations were still not able to recreate all the emission lines seen in quasar spectra with the correct EW ratios. Everett et al. (2002) also found that a clumpy, multi-phase outflowing gas could explain the observed BAL spectra well, and models without clumping fail to explain how different ionisation absorption lines are found to have similar velocity structures.

There is also further evidence of dense substructures in AGN winds from BALQ absorption line profiles. BALQs show complex absorption line profiles, commonly consisting of a number of distinct troughs, each only a few $1000\,\mathrm{km\,s^{-1}}$ broad (e.g., Korista et al. 1992; Hamann 1998; Arav et al. 2001; Trump et al. 2006; Ganguly et al. 2006; Gibson et al. 2009; Simon & Hamann 2010) and exhibit variability in these profile shapes (e.g., Barlow 1994; Gibson et al. 2008; Capellupo et al. 2011, 2012, 2013; Grier et al. 2015), which suggests motion of absorbing gas transverse to our line-of-sight (Hamann et al. 2013). In addition, BALs display a wide range of ionisation levels, which is inconsistent with a single uniform-density absorber (Turnshek et al. 1996; Hamann 1997).

- **The covering fraction of the clumps and streams of dense clumps may vary as a function of age of the quasar or accretion rate.**
  In this case, the probability of seeing BALs in any particular quasar is still a function of the covering fraction of the absorbing material, but the coverage itself is a function of time or accretion rate. This helps explain the observed redshift evolution of the two populations found in Allen et al. (2011) and could be related to the difference in spectral index that we see.

We also attempt to explain some aspects of the observed phenomena:

- **LoBALs are HiBALs.**
  Quasars with LoBALs also have HiBALs, but not the opposite. Within our model, the presence of LoBALs and FeLoBALs is due to the enhanced covering fraction, enhanced Hydrogen column density, and to a lesser degree a smaller ionisation parameter. The generally weak [O III] emission and strong reddening of LoBALs suggest that LoBAL quasars tend to be surrounded by dust and gas that has a larger global covering factor compared to HiBALs (e.g., Boroson & Meyers 1992; Turnshek et al. 1994; Zhang et al. 2010). Additionally, Liu et al. (2015) found using photoionisation modelling that the column density of the respective ion species, N_{ion}, and thus the absorption strength depends on the ionisation parameter, U, and the cloud/outflow thickness (described by the cloud's Hydrogen column density, N_{H}). They found that the C IV column density, $N_{\mathrm{C\,IV}}$, was several

orders of magnitude larger than that of Mg II at small $N_{\rm H}$, but $N_{\rm Mg\,II}$ increased significantly to become comparable with C IV at a sufficiently large $N_{\rm H}$. $N_{\rm Mg\,II}$ is also dependent on U and a larger $N_{\rm H}$ is required for a system with a larger U to obtain the same $N_{\rm Mg\,II}$ value. If the cloud's $N_{\rm H}$ is sufficiently large, both high- and low-ionisation absorption lines will be detected. Baskin et al. (2014) also found LoBALs present in a high $N_{\rm H}$ radiation pressure confined gas slab, and that the corresponding absorption of the higher ionisation lines (e.g., C IV) was significantly more complete.

In addition, LoBAL quasars have been found to display typically larger HiBAL BI values compared to systems with only HiBALs (Allen et al. 2011). A higher BI value plausibly indicates that the range of velocities that are absorbed and the absorption depth are large. In the context of our model, this phenomenon is likely to occur when the absorption happens over a large region that contains a myriad of outflow velocities. The gas will have a larger covering fraction, and hence more clumps intercept with our line-of-sight, building up the column density and LoBAL quasars can be detected.

- **The trend between FWHM and EW of C IV and Mg II lines.**
The relationship between the FWHM and EW for the different quasar populations should then reveal details on the structure, kinematics, and dynamics of the BLR. There is an anti-correlation between FWHM and EW for HIL C IV (Francis et al. 1992; Wills et al. 1993; Brotherton et al. 1994), while a positive correlation is identified for LIL Mg II (Brotherton et al. 1994; Puchnarewicz et al. 1997).

  To explain the trend seen in HILs, Francis et al. (1992) and Wills et al. (1993) proposed that the BLR comprises a two line-emitting region: a very broad line region (VBLR) and an intermediate line region (ILR). The components of a BEL include a line core and broad line wings, which are emitted from the VBLR and ILR respectively. Since the spherical VBLR is located closer to the central ionising source, it has a higher velocity and density compared to the disk-like ILR. With increasing line core relative to the line wings of the HIL, the EW increases while the FWHM decreases since the peak is narrower and sharper. Meanwhile, the LIL has relatively weak core but strong line wings, which implies that it might originate within the ILR where the velocity is lower (Puchnarewicz et al. 1997).

  In our model, this trend is explained in combination with the Baldwin effect (Baldwin 1977). As the continuum luminosity increases and likely the SED softens, the EW of C IV and Mg II decreases. In a lower luminosity quasar, the observed emission is likely to be emitted closer to the central black hole based on the observed radius–luminosity (R–L) relationship (e.g., Kaspi et al. 2007; Bentz et al. 2009). To explain the trend found for C IV, we require the wind to be radiation driven or at least the strength of the wind to be positively correlated with the luminosity. In this case, the increase in FWHM for decreasing EW is due to an increase in outflow

velocity with increasing luminosity. Additionally, C IV FWHM is found to correlate with velocity shift, suggesting stronger outflows for these objects. This supports our interpretation. For a line profile dominated by Keplerian motion, expected for Mg II, things get more complicated. If a constant black hole mass is assumed, the FWHM should increase as the luminosity decreases with FWHM $\propto L^{-1/4}$, which fits the observed trend. However, the opposite trend is expected if the black hole mass is varied and the relative accretion rate (Eddington fraction) is kept fixed. In this case, the FWHM should decrease as the luminosity decreases with FWHM $\propto L^{1/4}$, that is the FWHM should decrease with increasing EW, assuming that the luminosity is proportional to black hole mass. This is in contradiction to the observed trend. Therefore, the Mg II EW vs. FWHM trend is not easily resolved in our model using a dynamically driven argument.

- **Variability in the line profile.**
  Based on reverberation mapping, it has been found that the response in the red side of most lines is faster than the blue side (e.g., Gaskell 1988; Koratkar & Gaskell 1989; Crenshaw & Blackwell 1990; Korista et al. 1995; Ulrich & Horne 1996; Kollatschny 2003; Bentz et al. 2010; Grier et al. 2013). Though, a leading blue side has been observed in some sources (e.g., Denney et al. 2009). In the simplest outflowing disk-wind model, it is expected that there will be little lag in the blue line wing compared to the variation in the continuum, while the red wing experiences up to twice the delay (Gaskell 2009). Gaskell & Goosmann (2016) suggested that the shorter response in the red wing is an evidence of inflow motion, and hence disfavouring the outflowing wind model.

  However, Mangham et al. (2017) using detailed radiative transfer and ionisation treatment of a disk-wind simulation argued that the classical indicator of Keplerian rotation, inflow, or outflow is not always denoted by the symmetric, red wing leading blue wing, or blue wing leading red wing line profile signature. Even for flows dominated by a rotational velocity component (Chiang & Murray 1996; Kashi et al. 2013; Waters et al. 2016; Mangham et al. 2017), a faster response in the red wing, which is often considered as a signature of inflow, can be produced in moderate luminosity objects (Mangham et al. 2017). An outflow signature is only apparent in high luminosity objects (Mangham et al. 2017).

  Chiang & Murray (1996) demonstrated that an earlier time delay of the red wing can be achieved in their outflowing spherical wind model due to the contributions of radial and rotational velocity components from the radiative transfer effects. By modelling a narrow outflowing wind model, a quicker response in the red side of the line profile in some regions of the wind especially for face-on inclination angle is found (see § 4.3.2). Furthermore, the dusty failed wind of Czerny & Hryniewicz (2011) and quasar rain model of Elvis (2017) suggest that both infall and outflow are present in the wind. This is consistent with the

observations from dynamical modelling of the BLR (Pancoast et al. 2014) and velocity-resolved reverberation mapping (Grier et al. 2013).

- **Radio loudness and BAL.**
  The presence of both BALs and radio jets in a quasar was initially believed to be impossible (e.g., Stocke et al. 1992). However, numerous RL BALQs now have been detected (e.g., Becker et al. 1997; Brotherton et al. 1998). Yet, only $\sim 5\%$ of RL quasars are BALQs (e.g., Becker et al. 2001; Menou et al. 2001), compared to the $\sim 15\%$ of the entire quasar population being BALQs (e.g., Kellermann et al. 1989; Ivezić et al. 2002; Baloković et al. 2012). BALQs with high radio power and radio luminosity are even rarer (Gregg et al. 2006; Shankar et al. 2008). This discrepancy can be explained in the context of the orientation scenario, due to relativistic beaming of the radio jets along the observer's line-of-sight. In this case, a fraction of RQ quasars will be relativistically beamed towards the observer and boosted to higher radio luminosities. These beamed radio sources become a disproportionate fraction of the bright radio source. This reasoning is discussed in Shankar et al. (2008), though they also pointed out that other mechanisms are necessary to accelerate the BAL winds in polar RL quasars.

    In our model, we have an ionisation cone or corona that is aligned with the radio jet. An observer looking down this ionisation cone will not observe BALs. Therefore, BALQs will generally be non-beamed sources, and even when BALQs are a fixed fraction of radio quasars, the observed fraction of BALQs seen will decrease with radio power due to the apparent increase in RL quasars numbers due to beaming.

    Using samples in the optical domain, Bruni et al. (2014) reported that the BALQs have similar geometries, black hole masses, and accretion rates, regardless of their radio properties. DiPompeo et al. (2012) and Rochais et al. (2014) also found no statistical difference in the BAL features between RL and RQ ultraviolet BALQ spectra. This hints that the radio loudness might be independent of the BAL characteristics. Thus, the findings can be generalised to both radio phases of BALQs Rochais et al. (2014).

    Our model allows a wide range of BAL viewing angles, and therefore a range of observed radio properties. We also do not expect the radio loudness of the AGN to affect the BLR properties, hence we expect the observed similarities between the RL and RQ samples.

- **X-ray observational features.**
  X-ray spectra of AGN have revealed the presence of ionised absorption, which is often considered to be indicative of outflowing photoionised material along the line-of-sight (Halpern 1984). The WAs or X-ray blueshifted absorption lines are associated to highly ionised gas with velocity of order 100–1000 $\mathrm{km\,s^{-1}}$ (e.g., Kaastra et al. 2000; Kaspi et al. 2002; McKernan et al. 2007). WAs are also

common and present in about half of Seyfert 1 galaxies (e.g., Reynolds & Fabian 1995; Reynolds 1997; George et al. 1998). Although less is known about the exact nature and origin of the WAs (see review by e.g., Crenshaw et al. 2003), several suggestions on their nature include evaporating clouds in the BLR (e.g., Netzer 1996), scattering gas through the obscuring torus (e.g., Krolik & Kriss 1995), two-component WA regions (e.g., Otani et al. 1996), and accretion disk wind (e.g., Konigl & Kartje 1994; Elvis 2000; Bottorff et al. 2000). There is also an extreme class of absorbers, called ultra-fast outflows (UFOs), with velocity $\gtrsim 10^3\,\mathrm{km\,s^{-1}}$ and even extending up to $\sim 0.4\,c$, where c is the speed of light (e.g., Chartas et al. 2002; Reeves et al. 2003; Chartas et al. 2003; Pounds et al. 2003). It has been suggested that the UFOs and WAs belong to the same single large-scale stratified wind, with WAs located further away from the black hole than the UFOs (e.g., Tombesi et al. 2013, but see also Laha et al. 2014). We do not attempt to explain these phenomena in our model.

- **Unification of AGN.**
  The basis of our proposed BLR disk-wind model is based on the study of BAL features from quasar samples. However, to a certain degree, we believe that our model could be extended to other types of AGN, such as Seyfert galaxies. Although, the strength of the outflow is likely to be dependent on the properties of the AGN, in a sense that more luminous systems are associated with stronger BAL winds while narrower absorptions occur in less luminous systems (Laor & Brandt 2002; Ganguly et al. 2007). Since Seyferts are low or moderate luminosity counterparts of quasars, those with BALs are scarce and only a transient BAL outflow, for example in the narrow-line Seyfert 1 galaxy WPVS 007 (Leighly et al. 2009), is found. In this case, we expect Seyferts to fit into our model but with wind power scaled to its luminosity and black hole mass.

Our model differs from the majority of disk-wind models as it does not have a narrow opening angle for the wind. Additionally, the wind is stratified in both ionisation and probably density by angle from the axis of accretion and distance from the central accretion disk. The model quite naturally accounts for the substantial observed similarities between BALQs and non-BALQs, while retaining some of the key elements of the models of Murray et al. (1995) and Elvis (2000, 2004).

5.7 Summary

Using quasar samples from the SDSS DR12Q, we have investigated the various characteristics of the continuum and BELs, namely the absolute magnitude, redshift spectral index, FWHM, asymmetry, EW, and velocity shifts for HIL C IV and LIL Mg II. We have applied statistical tests and supervised machine learning for classification to examine

whether the attributes for BALQ and non-BALQ populations originate from the same parent population.

Although a few parameters have shown statistical differences between the BALQ and non-BALQ samples, the overriding result is that the two populations have largely similar properties. The shape of the distributions is highly similar in most cases. Analysis from machine learning also points out the complexity in separating the two classes as all the algorithms employed only performed marginally in the classification tasks. These observed trends appear to be inconsistent with predictions from a purely orientation explanation based on a narrow disk-wind for explaining the BALQ population. We have no evidence against an evolutionary model.

Under the assumption that the BAL and BEL regions are co-spatial, our analysis can be used to infer something about the structure of the BLR. BELs are standard features of quasars from almost all lines-of-sight that are not obscured by a dusty torus. In the orientation explanation, the BLR is described as a traditional disk-wind model that is constrained within a narrow angular range. This means that the covering factor of the absorbing part of the wind is reflected by the proportion of BALQs. Importantly, the measured profiles of BELs will vary significantly with line-of-sight. Since we do not observe any significant difference between the properties of the BALQs and non-BALQs, BALs must not have a preferred direction. This argues against a disk-wind of small opening angle, and instead favours a clumpy wind covering a wide range of angles.

A modified model for the disk-wind is required and proposed, retaining key features of the traditional models:

- The clumpy wind is stratified and covers a wide range of angles.
- The wind consists of multiple radial streams of high density gas and BALs are seen when the viewing angle intersects with these streams in the wind.
- The high-ionisation lines, such as C IV, lie close to the ionising source, while low-ionisation lines, such as Mg II, lie further from the source but close to the accretion disk.

This model appears to consistently explain a lot of the observed features in BAL and non-BAL quasars.

CHAPTER 6

Quasar Orientation

This chapter is based on the publication:

- *Yong, S. Y., Webster, R. L., King, A. L., Bate, N. F., Labrie, K., & O'Dowd, M. J. (2020). Determining quasar orientation.* MNRAS, *491(1), 1320–1334. ADS: 2020MNRAS.491.1320Y. doi: 10.1093/mnras/stz3074*

Abstract

Since the discovery of AGN and their subclasses, a unification scheme of AGN has been long sought. Orientation-based unified models predict that some of the diversity within AGN subclasses can be explained by the different viewing angles of the observer. Several orientation categorisations have been suggested, but a widely applicable measure has yet to be found.

Using the properties of the ultraviolet and optical broad emission lines of quasars, in particular the velocity offsets and line widths of high-ionisation C IV and low-ionisation Mg II lines, a correlation has been measured. It is postulated that this correlation is due to the viewing angle of the observer. Comparison with other orientation tracers shows consistency with this interpretation. Using a simulation of a wide angle disk-wind model for the broad emission line region, we successfully replicate the observed correlation with inclination. Future more detailed modelling will not only enable improved accuracy in the determination of the viewing angle to individual AGN, but will also substantially increase our understanding of the emitting regions of AGN.

6.1 Background

There has been a long-held belief that there should be a simple unifying physical model for quasars, similar to the primary characterisation of stars by their mass. However its form and shape has proven elusive. Quasars are seen as the unresolved cores of distant galaxies, powered by accreting supermassive black holes. It has been difficult to disentangle the geometry of the emitting regions as there seems to be a degeneracy between orientation and at least three, and possibly more, parameters, such as the black hole mass, accretion rate, embodied in the Eddington ratio, and luminosity (e.g., Laor 2000). The geometry of some of the inner components can depend on the listed parameters, for example, the possible dependence of the thickness of the accretion disk and the characteristics of the emitting region on the accretion rate and luminosity of the objects (e.g., Collin & Huré 2001). The similarities between individual quasars also suggests possible unification, providing the motivation to search for a simple physical model. The classic Urry & Padovani (1995) model of AGN is axisymmetric, powered by an accretion disk surrounding a black hole. Thus orientation is expected to affect the measurement of observables at all wavelengths.

Despite extensive studies of many observable parameters, a clean measurement of the orientation of the accretion disk rotational axis to the line-of-sight has proven elusive. We describe a simple correlation that measures the angle-of-viewing to a quasar, unlocking one of the systematic variables to understanding the complexities of observed quasar properties. We propose an orientation indicator based on the velocity shifts and line width ratio of high-ionisation C IV and low-ionisation Mg II lines. We interpret the correlation with inclination in the context of the quasar disk-wind model. The outline is as follows. § 6.1 discusses some of the potential orientation proxies available. § 6.2 describes the quasar sample employed. Our proposed quasar orientation indicator is presented in § 6.3. Comparison with other orientation tracers and simulation are examined in § 6.4 and § 6.5, respectively. Further discussion on our inclination mapping is in § 6.6. Lastly, § 6.7 provides the summary.

6.1.1 Obscuration, Orientation, and Unification

The opening angle of the torus measured from the axis of accretion disk, $\theta_{\rm T}$, reflects the covering factor of the absorbing material in the torus. In particular, it describes the degree of obscuration whereby photons coming from the BLR are blocked by the circumnuclear dusty torus when viewed at certain inclination, and thus the object lacks broad lines and is identified as type 2. This aspect is what distinguishes type 1 and type 2 AGN in the unification scheme (Antonucci 1993). Earlier studies have also envisaged the idea of two AGN populations between quasars and radio galaxies (Scheuer 1987; Barthel 1989), in which the latter lacks BELs as their BLRs are hidden by the torus.

Estimation of the torus opening angle can be made based on the fraction of the two AGN types (e.g., Osterbrock & Shaw 1988; Huchra & Burg 1992; Maiolino & Rieke 1995). Sampling of the AGN is performed in various wavebands as the amount of obscuration due to dust and gas differs depending on the wavelength of the observations. Radio-selected data at low frequency has the advantage of being an unbiased orientation sample. Early findings using low frequency radio samples from the Revised Third Cambridge catalogue of radio sources found that the boundary that separates quasars and radio galaxies to be around 45° (Barthel 1989). Subsequent studies using the revised version of the catalogue also obtain similar results with unobscured opening angle of $\sim$ 50–60°, implying $\theta_{\rm T} \sim$ 30–40° (Willott et al. 2000; Wilkes et al. 2013; Baldi et al. 2013; Marin & Antonucci 2016).

Meanwhile, dust obscuration can be detected in the infrared, while in the hard X-ray, it is mainly associated with dust-free gas (see review by Ramos Almeida & Ricci 2017). By modelling the SEDs of the torus emission in the infrared, the dust covering factor is inferred to be about 0.6–0.7 with plausible torus half-opening angle of $\sim 30°$ (Stalevski et al. 2016). Findings from low redshift hard X-ray selected Seyferts and spectral X-ray modelling recovered the intrinsic obscured AGN fraction of $\lesssim 0.6$ and $\theta_{\rm T} \lesssim 45°$ in high luminosity sample, but can be as large as ~ 0.85 with $\theta_{\rm T} \gtrsim 60°$ in low luminosity sample (Sazonov et al. 2015).

The torus structure dependence on luminosity has also been noted by other works (e.g., Lawrence 1991; Willott et al. 2000; Arshakian 2005; Simpson 2005, but see also Lawrence & Elvis 2010; Mateos et al. 2016; Stalevski et al. 2016; Mateos et al. 2017). In brighter AGN, the higher ionising radiation from the central engine gradually evaporates more of the obscuring material. Consequently, the inner dust sublimation radius of the torus extends further out and the torus appears to recede, which is aptly named the receding torus model (Lawrence 1991). This is also in accordance with observations from RM time lags, whereby the dust sublimation radius is related to the square root of AGN luminosity (Suganuma et al. 2006). Assuming a fixed torus height, this leads to a decrease in dust covering fraction and a smaller torus opening angle with increasing luminosity. Thus, the fraction of obscured type 2 AGN is expected to be smaller while the chance of detecting unobscured type 1 AGN is higher in brighter AGN.

6.1.2 Quasar Diversity in Eigenvector 1

For the past years, the idea of attaining an analogous metric to the stellar Hertzsprung-Russell (H-R) diagram to classify the diverse spectral properties of quasars, has always been appealing. The search came to fruition when Boroson & Green (1992) applied principal component analysis to a sample of 87 low redshift $z < 0.5$ Palomar-Green quasars and subsequently identified a set of measurable parameters with meaningful correlations. They found that the largest source of dispersion, referred to as the

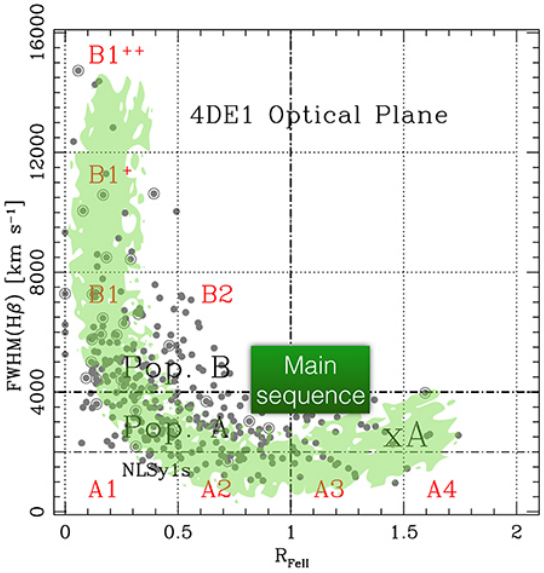

Figure 6.1: Quasar main sequence in Eigenvector 1 optical plane given by Hβ FWHM vs. $R_{\rm Fe\,II}$ from Marziani et al. (2018). The shaded region shows an indication of a quasar main sequence using Zamfir et al. (2010) quasar sample.

Eigenvector 1 (E1), is attributed to the strong anti-correlation between the strength of Fe II and [O III] λ5007. Additionally, E1 is also related to FWHM and asymmetry of Hβ line. These trends have been verified in other studies (e.g., Sulentic et al. 2000; Marziani et al. 2001; Shen & Ho 2014). It is speculated that the Eddington ratio is mainly responsible for driving the observed E1 pattern, but other physical drivers, such as black hole mass, spin, and orientation, might also contribute (Boroson & Green 1992; Marziani et al. 2001; Boroson 2002; Shen & Ho 2014; Marziani et al. 2018). The secondary source of dispersion or Eigenvector 2 is described by the inverse relationship between strength of He II λ4686 and optical luminosity.

This breakthrough has provided a foundation to construct a potential H-R diagram for AGN with broad lines. In particular, there appears to be a systematic pattern in the optical plane of E1 parameters Hβ FWHM and $R_{\rm Fe\,II}$ =EW(Fe II λ4570/Hβ) (e.g., Sulentic et al. 2000; Marziani et al. 2001; Sulentic et al. 2003; Zamfir et al. 2008, 2010), dubbed the main sequence of quasars (Marziani et al. 2001). Figure 6.1 shows the plot of E1 parameters from Marziani et al. (2018), with possible indication of quasar main sequence using Zamfir et al. (2010) quasar sample shaded in green (see review by e.g., Marziani et al. 2018). The main sequence of quasars resembles a wedge-shaped, compared to that of stellar H-R diagram. The difference is primarily because quasars do not radiate isotropically unlike stars, which hints to additional dimensions in the parameter space required to reflect the complexity.

The four dimensional Eigenvector 1 (4DE1) parameter space is introduced as complimentary to E1. It contains E1 parameters (Sulentic et al. 2000) plus 2 extras, the soft X-ray photon index, $\Gamma_{\rm soft}$ (Wang et al. 1996), and C IV λ1549 broad line centroid shift

at half maximum, $c\left(\frac{1}{2}\right)$ (Sulentic et al. 2007). Basically, two populations can be identified within the 4DE1 formalism for low redshift quasars, population A and B. Population A has FWHM(Hβ)$\lesssim 4000\,\mathrm{km\,s^{-1}}$, strong $R_{\mathrm{Fe\,II}} \approx 0.7$, blueshifted C IV $c\left(\frac{1}{2}\right) \approx -800\,\mathrm{km\,s^{-1}}$, and large $\Gamma_{\mathrm{soft}} > 2$. In contrast, population B has FWHM(Hβ)$> 4000\,\mathrm{km\,s^{-1}}$, weak $R_{\mathrm{Fe\,II}} \approx 0.3$, no blueshift C IV $c\left(\frac{1}{2}\right)$, and $\Gamma_{\mathrm{soft}} \approx 2$. Several other physical properties that are associated with each population have also been found (see Table 1 of Sulentic et al. 2011; Fraix-Burnet et al. 2017).

The pursuit for a quasar H-R diagram and main sequence have been built upon the context of E1 parameter space. Although a precise H-R diagram for quasars has yet to be established, the E1 provides a useful framework to distinguish the majority of low redshift broad line sources according to their spectral types. As will be discussed in the next section, hints of orientation indicator have also been proposed in the E1 plane.

6.1.2.1 [O III] EW as Orientation Tracer

The [O III] λ5007 is a prominent NEL in the optical spectrum. The line, originating from the NLR, emits isotropically (Mulchaey et al. 1994, but see also di Serego Alighieri et al. 1997), while the continuum is often assumed to exhibit anisotropic emission from the optically thick and geometrically thin accretion disk (Shakura & Sunyaev 1973). Hence, the flux of the optical continuum from the disk is expected to decrease with increasing angle from face-on to edge-on, while the variation in the line intensity is insignificant.

By inspecting the distribution of [O III] EW for $\sim$ 6000 SDSS quasar spectra, Risaliti et al. (2011) demonstrated that the [O III] EW parameter plays a part in orientation effect. A follow-up study with twice the sample size also supports the idea (Bisogni et al. 2017). These studies argued that the power-law tail slope of -3.5 of the EW distribution above 30 Å is a strong signature of orientation and indicates near edge-on quasar. Values below this may be due to the intrinsic variance due to factors such as the continuum properties and narrow line region structure. In relation to E1 parameter space, the Hβ width is also expected to be broad in this case due to the contribution from the virial component. As the orientation moves towards pole-on, the EW of [O III] decreases by a factor of cosine angle, between the disk and line-of-sight, along with narrower Hβ width. Their analyses also favoured a disk-like BLR geometry, which has been reported by several authors (e.g., Netzer 1987; Collin-Souffrin & Dumont 1990; Wanders et al. 1995; McLure & Dunlop 2002; Jarvis & McLure 2006).

6.1.2.2 Fe II Strength and Hβ FWHM as Eddington Ratio and Orientation Tracer

As aforementioned, the Eddington ratio is thought to be the primary driver of E1 (e.g., Boroson & Green 1992). Shen & Ho (2014) took a step further by developing a unification scheme solely defined by the Eddington ratio and orientation. Using 20 000 quasars at low redshift $0.1 \leq z \leq 0.9$ from the SDSS, they mapped the quasar distribution in the E1 optical parameter space, as shown in Fig. 6.2a.

The FWHM of Hβ is plotted against the EW ratio of Fe II line and broad Hβ line, denoted by $R_{\mathrm{Fe\,II}}$. With stronger $R_{\mathrm{Fe\,II}}$ and weaker EW [O III], the Eddington ratio is higher. Information on orientation is provided at any constant value of $R_{\mathrm{Fe\,II}}$. At pole-on, the FWHM of Hβ is narrow and becomes broader as the inclination angle increases approaching edge-on (e.g., Wills & Browne 1986; Boroson & Green 1992; Shen & Ho 2014).

The radio morphologies and orientation relationships are also demonstrated in Fig. 6.2b. Their findings are consistent with the prediction that core-dominated objects are mainly viewed pole-on, and hence a less broad FWHM of Hβ than lobe-dominated objects. Furthermore, the RL sample dwells in region with larger Hβ FWHM and smaller range of $R_{\mathrm{Fe\,II}}$ compared to the RQ sample. This suggests that RL AGN are likely to harbour massive black holes, accreting at lower Eddington ratio, as has been determined in earlier studies (e.g., Laor 2000; Ho 2002).

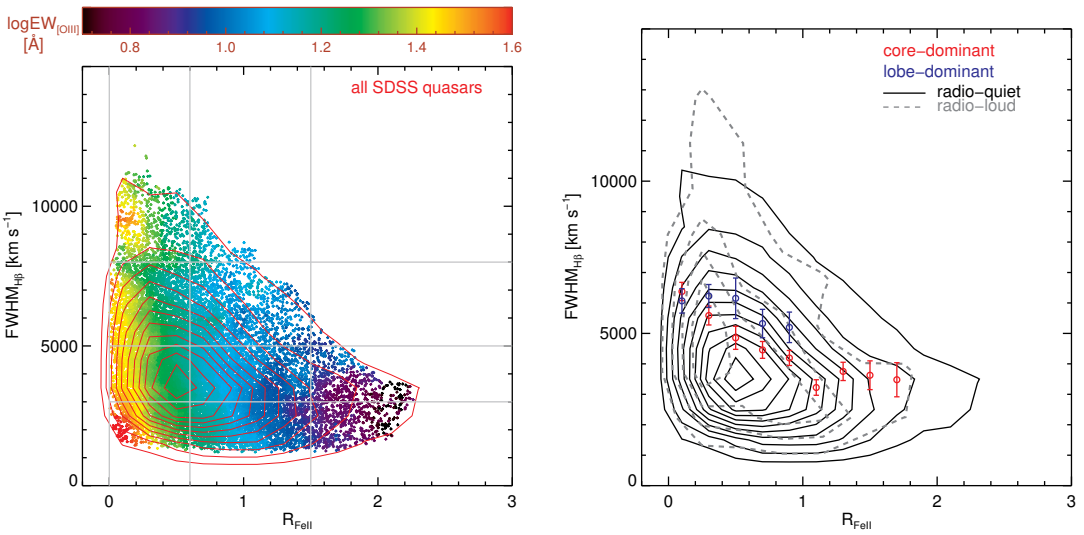

(a) Quasar distribution

(b) Radio-quiet and radio-loud quasars distributions. The points with error bar indicate the median FWHM Hβ at constant $R_{\mathrm{Fe\,II}}$ for core- and lobe-dominated radio quasars

Figure 6.2: Eigenvector 1 for quasars from Shen & Ho (2014).

6.1.3 Radio Core Dominance

Although RQ AGN make up the majority of AGN population, compared to their counterpart the RL AGN, orientation effects are harder to establish in these objects. Most orientation tracers have been applied to RL sources, although their effectiveness have been debated (e.g., Van Gorkom et al. 2015). The presence of a relativistic jet in RL AGN enables the determination of their inclination angle based on the jet alignment and radio properties (e.g., Orr & Browne 1982; Ghisellini et al. 1993; Wills & Brotherton 1995). One such dichotomy for radio quasars is flat-/steep-spectrum division. Viewing close to pole-on along the jet axis provides a direct view of the relativistic jet associated with non-thermal emission. The object will appear as a BL Lac object or FSRLQ, both of which are blazars. BL Lac objects are distinguished by their optically featureless continua with almost no emission lines. As the viewing angle moves away from the jet, the Doppler-boosted component of the jet is weaker and the object is seen as a SSRLQ. FSRLQs tend to be core-dominated with flat radio spectra, while SSRLQs are mainly lobe-dominated and exhibit steep radio spectra (Orr & Browne 1982).

Several orientation indicators have been proposed for RL sources, though which is the best measure of orientation is still inconclusive. The core dominance of RL sources reflects the strength of the Doppler-boosted jet. As the angle between the jet and line-of-sight decreases (towards pole-on), the emission from the core increases (Padovani & Urry 1992; Ghisellini et al. 1993), and hence higher core dominance will be detected. This is also related to the radio jet morphology between core- and lobe-dominated RL quasars. Sources that are near pole-on have high optical depth due to the relativistic beaming from the core and their spectra tend to be flat, whereas near edge-on sources are dominated by the optically thin lobe radio emission and have steeper spectra. However, the true radio morphological type of RL objects can be hard to resolve. Their ranges of inclination often overlap at intermediate angles. In practice, this approach is merely suggestive of the inclination position of the object and by no means a definitive orientation indicator.

A few quantitative measures of radio core dominance have been introduced, where the sole difference is the normalisation, i.e., the denominator used to define the parameter. The numerator is specified by the radio core luminosity, often taken at 5 GHz rest frequency. Assuming that the extended lobe emission is isotropic, the core flux density reflects the Doppler boosting of the beamed jet, and thus inducing orientation dependence. Subsequently, the best orientation proxy should perfectly account for the intrinsic central engine power (see Van Gorkom et al. 2015).

Two notable radio core dominance parameters are prescribed by the quantities R and R_V. The pioneer paper by Orr & Browne (1982) suggested using R with the radio lobe luminosity as the denominator. Wills & Brotherton (1995) provided an alternative expression of the radio core dominance, R_V, which is normalised by the optical continuum luminosity at 2500 Å. Though it is shown that there is a correlation between the radio

core dominance and angle, there appears to have a large scatter for small radio core dominance values (Orr & Browne 1982; Wills & Brotherton 1995). There are some authors who prefer one over the other, albeit which is superior remains debatable (see e.g., Van Gorkom et al. 2015; Marin & Antonucci 2016). Other normalisations include using the NLR luminosity (Rawlings & Saunders 1991) and 151 MHz radio luminosity (Willott et al. 1999).

There are several studies to investigate whether there is a correlation between radio core dominance and line width of BELs. It was found that the core dominance is inversely related to the line widths of Hβ (Wills & Browne 1986; Baker & Hunstead 1995; Runnoe et al. 2013b, 2014; Brotherton et al. 2015b) and Mg II (Baker & Hunstead 1995; Runnoe et al. 2013b). The broad FWHM corresponds to low radio core dominance, which is predicted to be seen at high inclination angle with respect to the jet axis. Though the FWHM of C IV shows no dependence, there appears to be anti-correlation when using the line width measured close to the base of the line, around one-quarter of maximum C IV emission line peak (Vestergaard et al. 2000; Runnoe et al. 2014).

The radio spectral index, which describes the steepness of a radio spectrum, has also been demonstrated to agree closely with R, and subsequently with the FWHM of Hβ (e.g., Brotherton 1996; Jarvis & McLure 2006; Runnoe et al. 2013b). However, there is a weaker orientation dependence when Mg II line is used instead (e.g., Jarvis & McLure 2006; Fine et al. 2011; Runnoe et al. 2013b). In contrast, the C IV line width shows a negligible relation with the radio spectral index (e.g., Fine et al. 2011). This evidence implies that orientation matters in at least part of the BLR where LILs are situated. It is also vital to point out these proxies are not a perfect measure of orientation as they are often subject to scatter, and hence difficult to measure. Nevertheless, they act as reasonable indicators for source orientation.

6.1.4 Orientation Indicator for Radio-quiet

The inclination of RQ sources is harder to estimate as these sources show no relativistic beaming from the jet. Though a few methods of orientation specific for RQ AGN have been suggested, their reliability is still controversial. Boroson (2011) proposed that the presence of [O III] blueshift and Fe II redshift in a spectrum, along with the strength of Eddington ratio, determine the viewing angle of RQ quasars. However, this technique is questionable as Sulentic et al. (2012) found no evidence of Fe II line redshift with respect to broad Hβ line.

In Marin (2016), four measures of nuclear inclination for RQ targets, specifically Seyferts, are examined. Each of these methods is limited to different regions of the AGN. In order of increasing radial scale from the black hole: X-ray reflection spectroscopy for inner section of the disk (Nandra et al. 1997, 2007), empirical $M_{\rm BH}$–σ relation for BLR (Wu & Han 2001; Zhang & Wu 2002), infrared modelling for torus (Mor et al.

2009; Alonso-Herrero et al. 2011; Sales et al. 2011; Ruschel-Dutra et al. 2014), and [O III] mapping for NLR (Crenshaw et al. 2000; Fischer et al. 2013).

The first method is utilised to detect iron fluorescence emission from near-neutral material at 6.4 keV, in which the line width is associated with the inclination of the accretion disk. The X-ray spectra is then fitted with accretion disk reflection models in special and general relativity spacetimes to retrieve the orientation. The second approach is based on the assumption that the LIL gas in the BLR is mainly in Keplerian motion. Using the $M_{\rm BH}$–σ relation, the measured black hole mass and FWHM are used to provide an estimate of the BLR inclination. The third method extracts the torus orientation by fitting the spectral properties of infrared spectra with clumpy torus models. The fourth technique, that is [O III] λ5007 mapping, involves inferring the NLR inclination from kinematic modelling of the extended NLR with a radial outflow resembling a biconical funnel. Their analyses suggested that all other techniques are less effective compared to NLR [O III] fitting, though this method is also not foolproof as it might be affected in the presence of a warped disk at close radial distance < 0.01 pc of the black hole.

6.1.5 Orientation Indicator in BALQs

A subpopulation of quasars that display BALs bluewards of the main UV broad emission lines (Weymann et al. 1991), such as C IV, also seems to provide clues to orientation. BALs exhibit a broad absorption trough, which is often blueshifted with respect to the emission line, that hints to evidence of outflowing material. One interpretation of the BAL phenomenon is in the context of orientation model, whereby BAL quasars are detected when the line-of-sight and outflow intersects a disk-wind within a narrow range of angle to account for the low fraction of BAL population (e.g., Murray et al. 1995; Elvis 2004). The constraint on the outflow angle is not yet well-determined. Findings from spectropolarimetric observations favour an equatorial outflow geometry (Goodrich & Miller 1995; Cohen et al. 1995; Ogle et al. 1999). This is challenged by the existence of RL BAL quasars, including those with LoBALs, that possess a large brightness temperature (Zhou et al. 2006; Ghosh & Punsly 2007). From radio variability reasoning, they argued that the observer's sightline is closely aligned with the radio emission from the relativistic jet in the polar direction about $\sim 10°$–$35°$. However, this trait also is manifested in RQ quasars with weak radio emission, which could be explained by an optically thin free-free (bremsstrahlung) emission from the accretion disk wind model (Blundell & Kuncic 2007). Other evidence that prefers a polar BAL wind is the excess narrow Hβ line width in LoBAL quasars since a large width would indicate an equatorial view using the assumption of Hβ line width as orientation tracer (Punsly & Zhang 2010).

6.2 Dataset

We select quasar data set using two releases of the SDSS from the DR7 (Shen et al. 2011) and DR12 (Pâris et al. 2017) quasar catalogues. The data are publicly accessible online through the VizieR catalogue access tool[1] (Ochsenbein et al. 2000).

The catalogue of quasar properties (Shen et al. 2011) is derived from the SDSS DR7Q (Schneider et al. 2010). The specifications on the sample and spectral line measurements for SDSS DR7Q (Shen et al. 2011) catalogue are described in Sect. 2 and Sect. 3 of their paper. The broad emission lines are modelled using at least one Gaussian profile and are separated into their corresponding broad and narrow line components, except for C IV which retains both components. The FWHMs are also computed in the process. The velocity shifts with respect to the systemic redshift for Mg II broad line component and C IV line are estimated from the fitted model emission line peak. They evaluated the uncertainties in the spectral line measurements using a Monte Carlo approach. From the flux density errors, Gaussian noise is introduced to the original spectrum by generating 50 random mock spectra fitted by the same fitting procedure to yield distribution of individual spectral quantity. The measurement errors are calculated from the 68% range at the median of the distribution.

We further limit our sample to spectra with C IV and Mg II FWHM and velocity shift measurements available, and median S/N per pixel of ≥ 15 in Mg II region at 2700–2900 Å and C IV region at 1500–1600 Å. To minimise the induced scatter in the observed correlation, we further constrain our sample as follows. Due to the presence of broad absorption features in quasars with BALs, the FWHM measurements of these objects might be imprecise. Therefore, we limit our sample to be non-BAL quasars. Furthermore, we also remove anomalous values, which are plausibly outliers, using the interquartile range (IQR) method (Tukey 1977) for outlier detection. The IQR represents the dispersion of a data set and is given by the difference between upper (third or 75^{th} percentile) and lower (first or 25^{th} percentile) quartiles, IQR=Q_3-Q_1. Measurements outside of 1.5 times the IQR are considered outliers and are omitted. The implications of excluding these points will be discussed later. This reduces our quasar sample to 1835, with redshifts $1.50 \leq z \leq 2.25$, excluding BAL quasars (228) and outliers (98).

The quasar sample from SDSS DR12Q is the same as described in § 5.2. Additionally, those with BALs (313) and plausible outliers (31) are also taken out, yielding 2429 quasars at redshift $1.57 \leq z \leq 2.42$.

[1] http://vizier.u-strasbg.fr/viz-bin/VizieR

6.3 Velocity Shifts and Ratio Line Width as Orientation Indicator

The quest to acquire an accurate proxy of orientation has proven to be a challenging task. Most proxies are either ineffective or restricted to certain criteria, as discussed in § 6.1. For example, the E1 scheme seems promising but it is exclusive for low redshift AGN in optical regime. The radio core dominance depends on the presence of beamed jet, and thus impractical for the majority of AGN that are RQ. Among the four inclination methods for RQ targets investigated in Marin (2016) (see § 6.1.4), the best is [O III] λ5007 mapping, is only applicable in the NLR domain. At present, there is no reliable orientation indicator in the UV-optical plane for the BLR component. In this domain, the only indicator using $M_{\rm BH}$–σ relation has been argued to be unsuitable (Marin 2016). We propose a simple and robust way to estimate inclination angle using the observable characteristic of the UV-optical emission lines.

Qualitatively, we expect that a number of the physical characteristics of line shape will result from differences in the angle-of-viewing to the quasar: line velocity-offsets, line widths and line asymmetries. In order to test these ideas, we concentrate on the emission lines that are observed in the optical, but are emitted at UV wavelengths. Two broad emission lines with little contamination from other emission lines close by, originating from the BLR, are compared: the high-ionisation C IV and low-ionisation Mg II lines. Although the Fe II multiplets can contaminate the Mg II line, the Fe II emissions do not significantly affect the peak or FWHM of the Mg II line. The C IV and Mg II lines are emitted at rest wavelengths 1549 Å and 2798 Å respectively with ionisation potentials of 64.49 eV and 15.04 eV. Typically, the emission lines in quasars are broadened, with FWHM velocities ranging from $\sim$ 2000–10 000 km s^{-1}. Physical constraints on the state of the emitting regions implies that these velocities must result from bulk motions of the emitting ions.

To examine trends in observable parameters, we use the quasar sample from SDSS DR7Q (Shen et al. 2011) and DR12Q (Pâris et al. 2017) described in § 6.2. Figure 6.3 shows an anti-correlation between the velocity offset[2] of the C IV line with respect to the Mg II line, Δv(C IV-Mg II), and the ratio of the FWHM of the two emission lines, FWHM(C IV/Mg II). Based on a kinematical argument, we propose that the correlation is attributed to angle-of-viewing.

To measure the orientation of the quasar axis to the line-of-sight, a suitable model within which to interpret the key observables is required. In the UV/optical region of the spectrum, the broad emission lines are easily observable, with the broadening attributed to the velocity of the emitting ions projected onto the line-of-sight. To model the BLR, a kinematic disk-wind model is explored Chapter 5, based on previous quasar models (Murray et al. 1995; Elvis 2004) but with some key differences. Importantly, a disk-wind

[2]Negative velocity indicates blueshift and positive velocity indicates redshift (see Fig. 2.3).

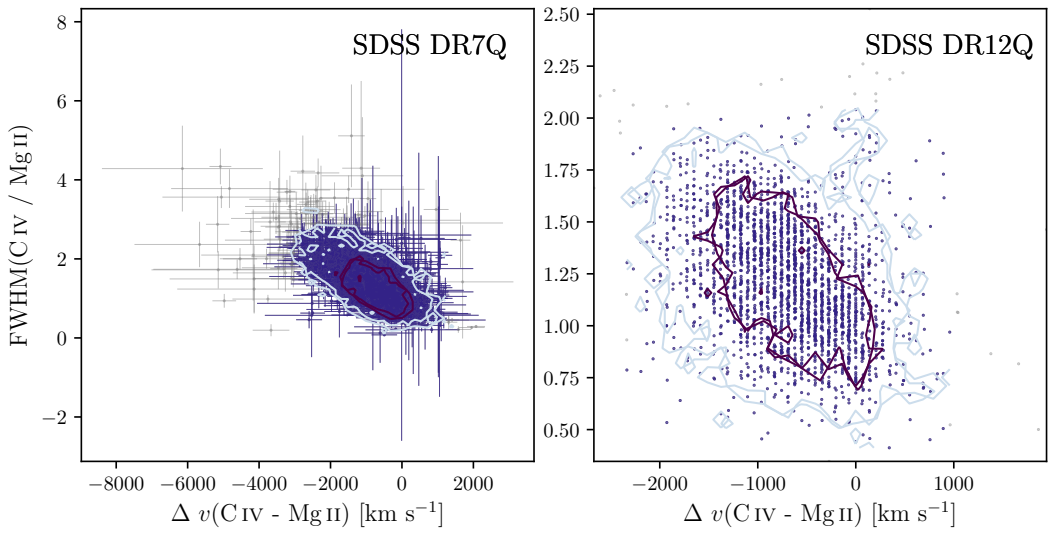

Figure 6.3: Ratio of full width at half maximum, FWHM, against velocity shift, Δv, between C IV and Mg II. We interpret the correlation to be attributed to inclination angle, with the upper left corner towards the lower right of the correlation indicating face-on to edge-on. The contours show the density of the sample at one- and two-sigma confidence levels. For comparison, the removed outliers are superimposed in small grey symbols.

covering a wide angle is required since there are similarities in emission line shapes between BAL and non-BAL quasars, which contradicts the wind arising from a narrow opening angle. The features that differentiate our disk-wind model from others are as elaborated in § 5.6 and shown in Fig. 5.10. In this model, ions leave the accretion disk at some radius, retaining the angular momentum associated with that radius (a rotational velocity), and then experience an outward acceleration due to radiation pressure or a similar mechanism (a poloidal velocity). Thus, the trajectories of these ions will be outward spiralling paths, with different mixes of the two velocity components. Note that the effect of likely magnetic fields is ignored in this simple model. The opacity of the accretion disk, combined with a putative dusty torus will obscure the far-side of the BLR. Thus, only the forward-facing hemisphere of the quasar would be observed. Continuum emission is observed either directly from the accretion disk or re-processed emission from an atmosphere. It is expected that in the region close to the rotational axis, the ions will be completely ionised and so will not contribute to the emission line flux. This will be called the ionisation cone or corona. As the angle from the rotational axis increases, the density of the atmosphere or gas above the disk will increase, providing regions where the dominant emission will be from ions of decreasing ionisation. This is also a direct consequence of BLR stratification with different ionisation potential. Since the wind is likely to be launched in the proximity of the central ionising source, we expect high-ionisation lines such as the C IV line to have a significant poloidal component, while retaining the velocity component from its rotational footprint. As the angle from the

axis approaches the disk, emission from low-ionisation ions such as Mg II and Hβ will be observed, largely reflecting the rotational velocity of their footprint. These outflowing components are termed the disk-wind, but the geometric location and kinematics of different ionic species will vary within the wind. Regions of higher density within the wind will be responsible for the absorption observed in BAL quasars. In particular, LoBALs should appear to be viewed from a preferential direction closer to the plane of the quasar. HiBAL quasars are still seen when the viewing angle intersects these streams, but they are not restricted to any preferential line-of-sight.

It is well-known that the C IV line is mostly blueshifted with respect to other lines (e.g., Gaskell 1982; Wilkes 1986; Espey et al. 1989; Tytler & Fan 1992; McIntosh et al. 1999; Vanden Berk et al. 2001; Shen et al. 2016). The Mg II emission is observed to be close to the systemic velocity of the quasar (Hewett & Wild 2010). Within the model described above, the Mg II line is expected to be emitted close to the disk and have only a small poloidal velocity component, while the C IV line is emitted closer to rotational axis. Therefore, C IV will reflect the projection of the poloidal or outflowing velocity along the line-of-sight, while Mg II will show predominantly the rotational velocity. The FWHM of each line will measure the projection of the bulk motion of the wind onto the line-of-sight. If these two ions are emitted in different parts of the wind, then the ratio of the FWHM of the two lines will reflect the different contributions to the two velocity components, projected along the line-of-sight. Thus, this ratio provides some constraints on the magnitude of the outflowing velocity, with respect to the rotational component at this particular angle of viewing.

The relation shown in Fig. 6.3 then reflects the strength of the poloidal and rotational velocity component, which can be used as a proxy to determine the inclination angle. Quasars viewed at face-on will be populating the top left-hand corner of the correlation and those views edge-on, towards the bottom right. Other physical parameters such as black hole mass and accretion rate, might determine the scatter in this relationship. Thus, due to the intrinsic properties of the sources, the correlation might be expected to have a significant but natural dispersion. It is not a trivial matter to extract information on these intrinsic properties and is beyond the scope of the current work.

6.3.1 Methodology

We conduct statistical analysis and linear regression techniques in order to investigate this relationship. Before fitting the correlation, we first rescale the data since the two variables have different magnitude which would result in a biased fit. This is done via z-score normalisation or standardisation, by centring the variable values at zero with a unit variance. In any case, rescaling data will not alter the general trend. Note that the original scales are used to produce the plots to illustrate the actual values.

6.3. VELOCITY SHIFTS AND RATIO LINE WIDTH AS ORIENTATION INDICATOR

Regression analysis is a valuable statistical tool for representing and examining the relationship between two or more variables. A simple linear regression model is when a linear relationship is considered with one dependent variable, x, and another independent variable, y, which gives the standard function $y = mx + c$, where m and c is the slope and intercept respectively. In linear regression technique, models with measurement errors attempt to minimise the variance along the fitted line. One measurement error model is the orthogonal regression model or also known as total least squares (Adcock 1878; Golub & van Loan 1980), which assumes uncertainties in the two-dimensional data and minimises the squared orthogonal distance. This method treats the two variables symmetrically rather than depending on one another. For this reason, we choose to fit a linear line using orthogonal regression to the FWHM(C IV/Mg II) versus Δv(C IV-Mg II) correlation.

There are several sources of uncertainty that can be considered in our inclination estimation. One plausible source is from the fitted line. The error on the orthogonal fit can be directly determined by including the errors for each data point. To account for the measurement errors and intrinsic scatter in both velocity shifts and FWHM ratios, we perform the linear regression using bivariate correlated errors and intrinsic scatter (BCES; Akritas & Bershady 1996) method based on the publicly available Python module (Nemmen et al. 2012)[3]. The BCES is only applied on the SDSS DR7Q sample as measurement errors are not given in DR12Q. To estimate the error in the orthogonal fit for the SDSS DR12Q sample, we fit the correlation using a different linear regression method. Another measurement error model is the ordinary least squares (Legendre 1805; Gauss 1809), which only treats error in the dependent variable. The ordinary least squares of y on x assumes y as dependent variable and minimises the squared vertical distance, while the x on y assumes x dependence and minimises the squared horizontal distance. The shallow and steep slopes from these methods allow us to retrieve the extremes at both ends of the lines. This provides an estimate of the error in the projected inclinations. We compute these linear regression models for the SDSS DR12Q.

To assess the reliability of the fitted line if the same observation is done repeatedly, a bootstrap resampling method of the correlation is conducted. Random pairs of correlation are sampled with replacement from the original data set to assemble a new sample of the same size. The new sample is fitted with a linear regression model yielding its corresponding slope and intercept, and the whole process is iterated 1000 times. The median of the bootstrapped slopes and intercepts are taken as the best fit line. The 99.7% confidence interval at the three standard deviation level of the slope and intercept are also computed. To quantify the fit, we calculate the residuals, which is distance between the observed and predicted values, and the corresponding mean squared error, where the error in this case is the residuals.

Determining the angle-of-viewing is clearly model dependent. We start by assuming a simplest possible mapping. For each quasar, the FWHM(C IV/Mg II) and Δv(C IV-

[3] https://github.com/rsnemmen/BCES

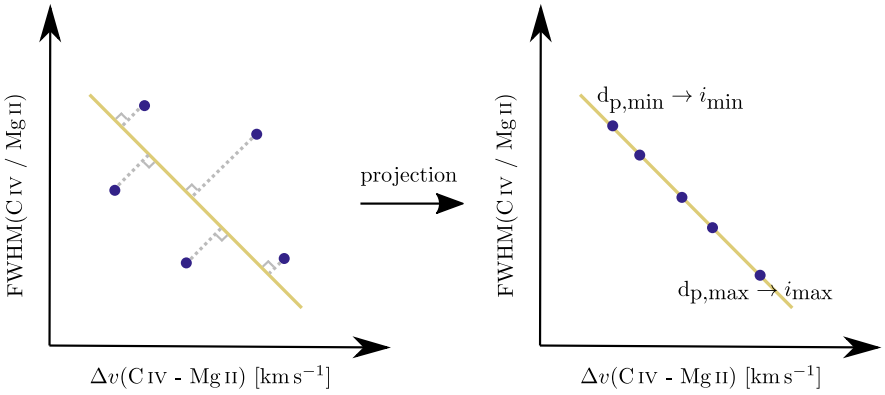

Figure 6.4: Sketch of our proposed inclination mapping using the relationship between the velocity shift, Δv, and ratio full width at half maximum, FWHM, of C IV and Mg II. The upper left corner towards the lower right of the correlation corresponds to face-on to edge-on viewing angle. *Left*: Each point is projected onto the best fit line as the projected distance, $d_{\rm p}$. The projection is performed in the perpendicular direction for orthogonal regression model, as shown by the dashed line. Whereas for ordinary least squares regression models, the projection is in the vertical direction for y on x and horizontal direction for x on y. *Right*: The $d_{\rm p}$ is then mapped to inclination angle, i, using Eq. (6.1).

Mg II) values are mapped to a projected distance along the best fit line. Based on the linear regression models, the mapping is performed in the perpendicular direction for orthogonal, vertical direction for y on x, and horizontal direction for x on y regression. A distribution is generated from the projection. Assuming that the projected distance, $d_{\rm p}$, scales linearly with the inclination angle, i, the mapping is performed using

$$i = 90^{\circ} \left[\frac{d_{\rm p} - d_{\rm p,min}}{d_{\rm p,max} - d_{\rm p,min}} \right], \tag{6.1}$$

where $d_{\rm p,min}$ and $d_{\rm p,max}$ are the minimum and maximum limits of $d_{\rm p}$. A sketch of our proposed inclination angle mapping for orthogonal projection is portrayed in Fig. 6.4. Indeed, the choice of projected scaling factor also contributes to the error in the inclination angle estimate. It is worth mentioning that the given prescription here is by no means univocal, but merely serves as a guide to whether it is viewed from polar, intermediate, or equatorial viewing angle. We further comment on the effects of our mapping procedure on the estimated viewing angle in § 6.3.3.

The expected differential probability of observing a quasar at a particular inclination angle, i, defined from the rotation axis of the accretion disk, is given by $P(i) = \sin i$ with $0^{\circ} \leq i \leq 90^{\circ}$. The mapped inclination angle distribution is then normalised by the relative area on the sky to generate the 'transparency distribution' as a function of inclination, i.e., the fraction of quasars whose inner regions are visible to the observer, given the orientation of the source and the presence of possible obscuring components, such as the torus.

6.3.2 Results and Discussion

The linear regression models fitting onto the Δv(C IV-Mg II) and FWHM(C IV/Mg II) correlation, accounting for measurement errors in SDSS DR7Q and without in DR12Q, are displayed in Fig. 6.5 along with the residuals in Fig. 6.6. The samples from SDSS DR7Q and DR12Q catalogues before (grey) and after (blue) removing the outliers are also shown. The fitted line parameters and their corresponding errors at 99.7% confidence interval are presented in Table 6.1. The Spearman's correlation coefficient, r_S, (Spearman 1904) between Δv(C IV-Mg II) and FWHM(C IV/Mg II) and its corresponding correlation probability, p_S, are statistically significant in both samples, with ($r_S = -0.580, p_S \ll 0.01\%$) using SDSS DR7Q and ($r_S = -0.387, p_S \ll 0.01\%$) using SDSS DR12Q.

The distribution of our simple mapping from Δv(C IV-Mg II) and FWHM(C IV/Mg II) plane to inclination angle are demonstrated in Fig. 6.7. The transparency plot that indicates the fraction of quasars that is not obstructing our line-of-sight is displayed in Fig. 6.8. For SDSS DR12Q, the variation in the fitted slopes using different regression models are portrayed by the error bars.

The transparency is fairly constant at low inclination and peaks at intermediate angle, implying that most objects are seen at this range of direction. The scarcity of equatorial objects suggests an increase in obscuring material between the emitting region and the observer, which is possibly due to the presence of a torus. The dust distribution of the torus is supposedly clumpy, rather than smooth (e.g., Krolik & Begelman 1988; Nenkova et al. 2002, 2008; Elitzur & Shlosman 2006), such that emission from the ionising source is only partially blocked by the torus. This aspect is what distinguishes type 1 and 2 AGN, as have been established in the classic unification scheme of AGN (Antonucci 1993; Urry & Padovani 1995). Obscured AGN lack broad emission lines and are classified as type 2 AGN.

The boundary where there is a higher amount of obscuration along the line-of-sight is demonstrated by the drop-off in the distribution. This suggests that the angle of torus is $\theta_{\rm T} \sim 25°$–$35°$ from the accretion disk plane using the samples without outliers (Fig. 6.8, thick blue). Other findings based on the fraction of two AGN types found the torus angle to be $\theta_{\rm T} \sim 30°$–$40°$ (Willott et al. 2000; Wilkes et al. 2013; Baldi et al. 2013; Marin & Antonucci 2016) and extend to 45° (Barthel 1989). These ranges of torus angle are consistent with our estimation.

However, the distribution of orientation angles obtained depends on the quality of the dataset analysed. This also affects the fitted regression, as illustrated by the underlying grey data points in Fig. 6.7 and Fig. 6.8 when outliers are retained in the sample. In the SDSS DR7Q sample with outliers included, the underlying shape of both distributions are more negatively skewed compared to those when outliers are excluded. There are lower number of quasars at low inclination angles, and hence the transparency

distribution is much flatter at low ends. The suggested torus angle is also smaller, about $\theta_{\rm T} \sim 20°$ for SDSS DR7Q and $\theta_{\rm T} \sim 35°$ for SDSS DR12Q.

Table 6.1: Velocity shift and ratio full width at half maximum of C IV and Mg II correlation fitting using linear regression models. The linear fits of the expression FWHM(C IV/Mg II)= $m\Delta v$(C IV-Mg II)+c, where m is the slope and c is the intercept. The uncertainties in the fitted lines at 99.7% confidence interval are computed using bootstrapping of 1000 samples.

Catalogue	Regression Model	Slope	Intercept	Mean Squared Error
S11	BCES orthogonal	$(-6.906^{+1.838}_{-1.901}) \times 10^{-4}$	$0.798^{+0.168}_{-0.173}$	0.396
S11 [-O]	BCES orthogonal	$(-6.918^{+1.999}_{-2.418}) \times 10^{-4}$	$0.790^{+0.165}_{-0.200}$	0.420
P17	Orthogonal	$(-5.039^{+0.362}_{-0.589}) \times 10^{-4}$	$0.877^{+0.025}_{-0.041}$	0.662
	yx	$(-1.711^{+0.175}_{-0.156}) \times 10^{-4}$	$1.107^{+0.012}_{-0.011}$	0.886
	xy	$(-1.495^{+0.142}_{-0.205}) \times 10^{-3}$	$0.192^{+0.098}_{-0.142}$	0.886
P17 [-O]	Orthogonal	$(-5.062^{+0.407}_{-0.525}) \times 10^{-4}$	$0.868^{+0.028}_{-0.036}$	0.648
	yx	$(-1.778^{+0.177}_{-0.161}) \times 10^{-4}$	$1.096^{+0.012}_{-0.011}$	0.876
	xy	$(-1.436^{+0.116}_{-0.173}) \times 10^{-3}$	$0.222^{+0.081}_{-0.120}$	0.876

Note: The quasar properties SDSS DR7Q catalogue (Shen et al. 2011) as S11 and SDSS DR12Q catalogue as P17 (Pâris et al. 2017). Sample with outliers removed is indicated with [-O].

6.3.3 Error in Fits

Several aspects of the data can affect the mapping of inclination angle to the fitted line. There is a subtle difference in the emission line modelling method adopted by different catalogues. In general, the trend in Δv(C IV-Mg II) and FWHM(C IV/Mg II) correlation remains regardless of the different dataset employed. The line profiles in SDSS DR7Q catalogue are fitted with combination of Gaussian functions and yield wider ranges of FWHM and velocity shift values than those in SDSS DR12Q using principal component analysis.

For this purpose, we visually inspect samples with high velocity offsets of C IV and Mg II, those that are $\leq -4000\,{\rm km\,s^{-1}}$ or $\geq 1500\,{\rm km\,s^{-1}}$ in SDSS DR7Q and $\leq -2000\,{\rm km\,s^{-1}}$ or $\geq 1000\,{\rm km\,s^{-1}}$ in SDSS DR12Q. Selected examples of high blueward and redward velocity offsets quasars are shown in Fig. 6.9 from SDSS DR7Q and Fig. 6.10 from SDSS DR12Q, with the corresponding measurements in Table 6.2. In general, the reported measurements from the catalogue are mostly overestimated, especially those that are claimed to have redward offsets. In almost all cases, the redward shifts of these objects are measured to be $< 1000\,{\rm km\,s^{-1}}$, contrary to the given measurements. We found that objects with measured offsets of $\geq 1000\,{\rm km\,s^{-1}}$ are due to the broad and redward asymmetric Mg II line, with peak shifted towards the lower wavelength. Indeed,

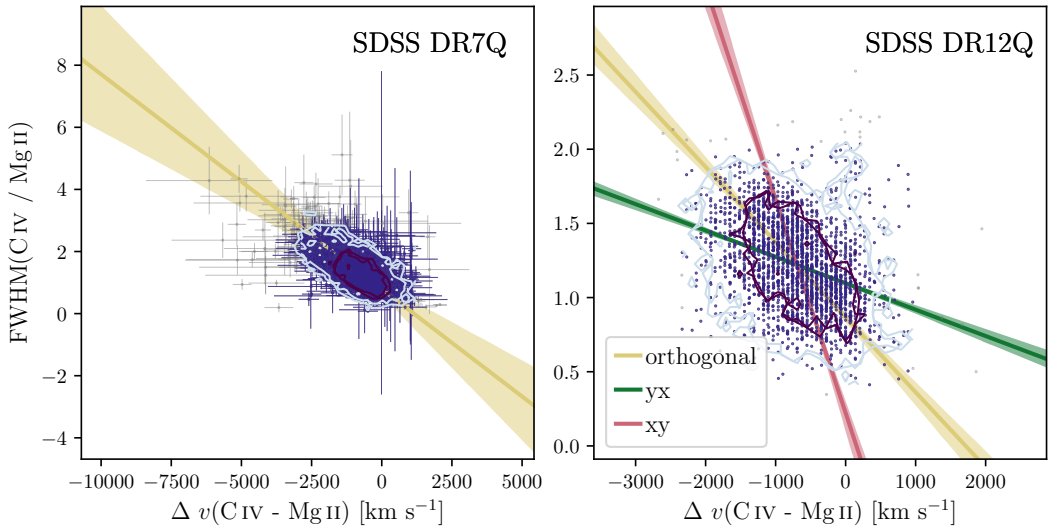

Figure 6.5: Ratio of full width at half maximum, FWHM, against velocity shift, Δv, between C IV and Mg II fitted using linear regression models. The fitted line is given in solid line with shaded region indicating the 99.7% confidence interval. The contours show the density of the sample at one- and two-sigma confidence levels. *Left*: The SDSS DR7Q sample with measurement errors is fitted using bivariate correlated errors and intrinsic scatter. *Right*: The SDSS DR12Q sample is fitted without accounting for measurement error. For comparison, the removed outliers are superimposed in small grey symbols.

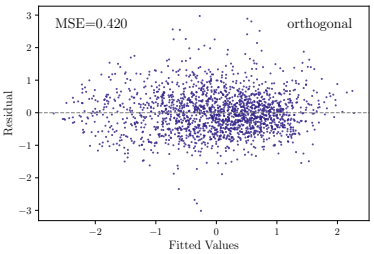

(a) SDSS DR7Q sample

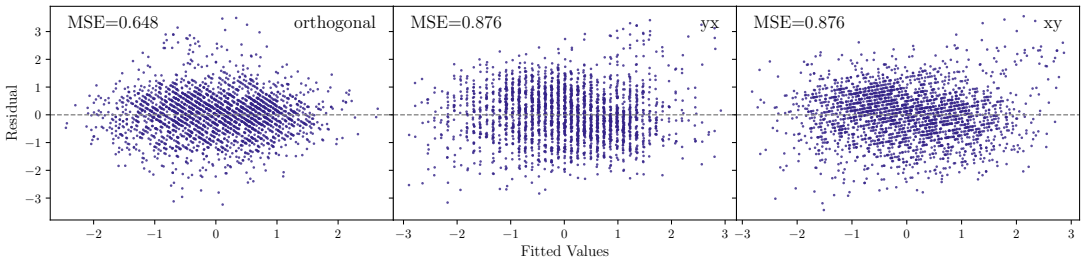

(b) SDSS DR12Q sample

Figure 6.6: Standardised residuals plot of the relation between ratio full width at half maximum and velocity shift of C IV and Mg II. The mean squared error (MSE) and linear regression model are listed on the upper left and right of each panel, respectively. The fitted lines are shown in Fig. 6.5.

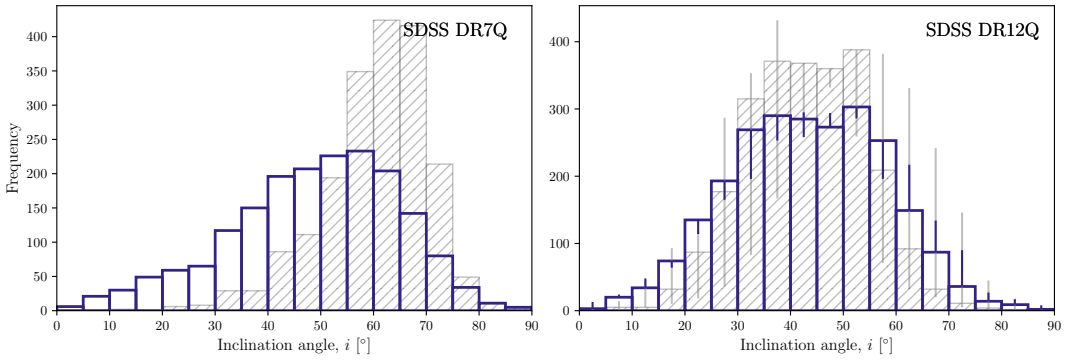

Figure 6.7: Histograms of mapped velocity shift and ratio full width at half maximum of C IV and Mg II plane onto inclination angle. The distribution of inclination angles is a linear projection of distance along the best fit line using orthogonal regression. For SDSS DR12Q, the error bars are estimated from ordinary least squares fitted lines. The fitted lines are shown in Fig. 6.5. For comparison, the distribution using samples including outliers is superimposed in hatch grey.

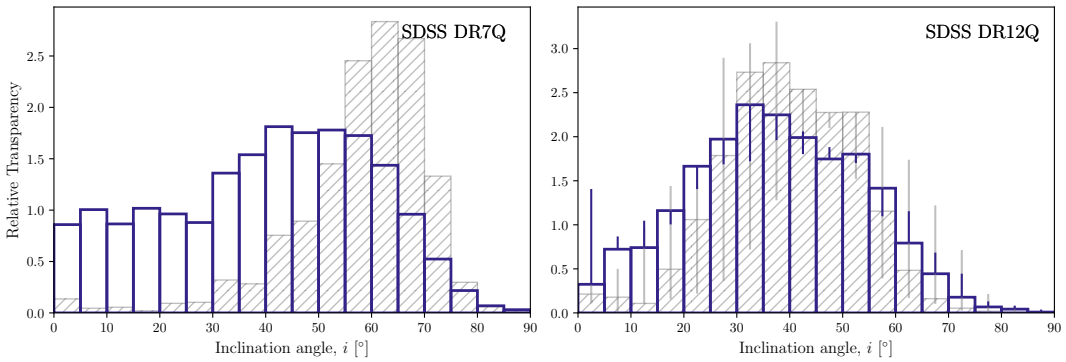

Figure 6.8: Fraction of quasars along the line-of-sight normalised to area on the sky using velocity shift and ratio full width at half maximum of C IV and Mg II mapping. The distributions of the projected distance mapped onto inclination are shown in Fig. 6.7. For comparison, the distribution using samples including outliers is superimposed in hatch grey.

a careful inspection of the spectral measurements will better constrain the model.

The differences between the measurements from the two catalogues are shown in Fig. 6.11 for 273 samples with same object name. It is clear that most of them are on the one-to-one relationship. The dispersion in the distribution is evident for large FWHM values. The FWHMs from SDSS DR7Q for both C IV and Mg II lines tend to be larger than those from SDSS DR12Q, which can be up to ~ 1.6 times broader or more in the case of Mg II. The scatter in the velocity shifts range between $\pm \sim 1500\,\mathrm{km\,s^{-1}}$.

Although we opt for high S/N quasar spectra, uncertainties in the spectral line measurements are inevitable. This can be due to systematic errors since the measurements from the catalogue are collected automatically, which might also be the cause of the redshifted velocity offsets seen. Additionally, erroneous parameter values or outliers might be present as we did not manually check the accuracy of the automated measurements. This effectively results in a mapped inclination angle distribution with long tails, particularly on both ends at low and high inclinations. The data rescaling that we did, is an attempt to mitigate the contributions from the outliers.

Another key question that needs to be considered is the method for mapping from the data points to the regression line. For example, instead of using orthogonal regression model with projected points along the perpendicular direction, it could be projected along the vertical direction. The different gradients and projections produce different distributions of mapped projected distance to viewing angle. At low inclination angles, the transparency is higher when using ordinary least squares projections onto the fitted lines (Fig. 6.8, *right*). The torus angle is also wider $\theta_{\mathrm{T}} \sim 30°$–$35°$ with quicker falloff in the distribution.

As given by Eq. (6.1), the normalisation for the histogram of mapped inclination is over 0°–90°. A different normalisation can be applied, for example 0°–80° to account for the obscuration by the torus, although this would not significantly alter the distribution. The linear scaling between the projected distance and inclination might also be a simplification as the exact scaling is still unclear. Deducing a proper mapping will requires a thorough investigation and more insight on the physical properties and the relationship between them.

6.4 Other Proposed Measurements of Inclination

In the standard unified AGN scheme (Urry & Padovani 1995), the diversity of AGN classes is partly attributed to orientation. Various orientation indicators have been introduced in the literature, though most often accompanied by some limitations. We compare our proposed measurement of inclination with specific examples from the literature. We utilise the VizieR catalogue access tool to retrieve the data. Our choice of catalogues are limited to non-BAL objects within the SDSS coverage, unless mentioned

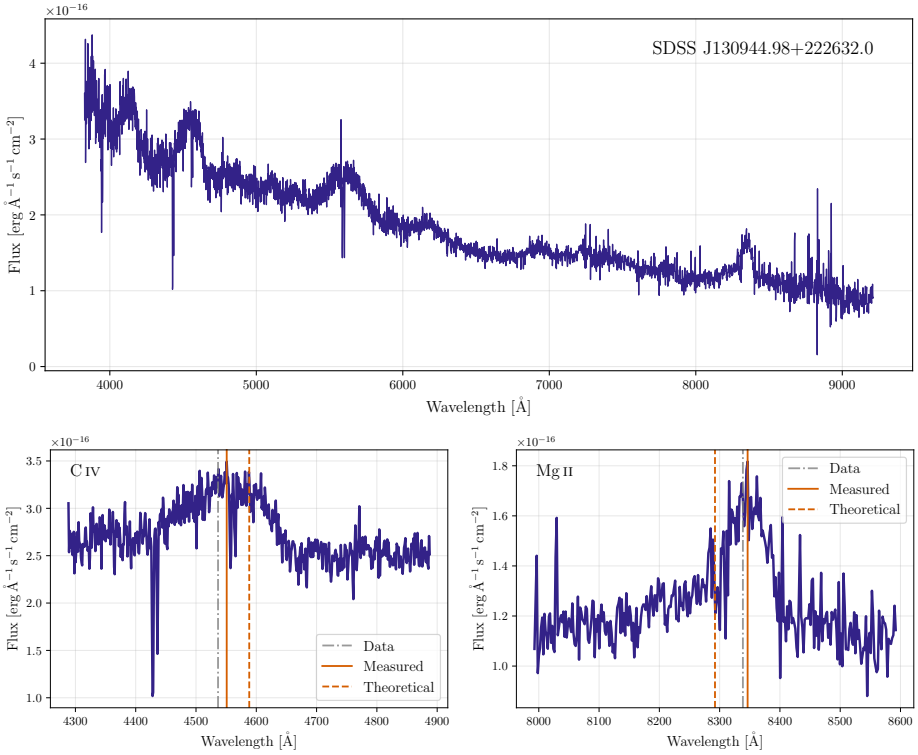

(a) Negative Δv(C IV-Mg II)

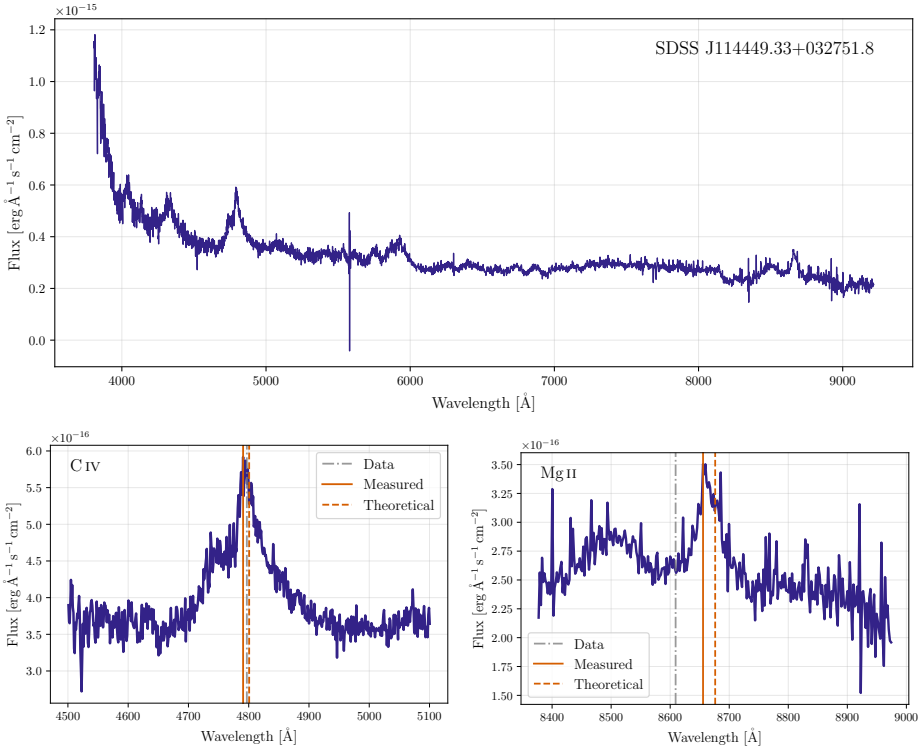

(b) Positive Δv(C IV-Mg II)

Figure 6.9: Example of spectra and emission line measurements of high velocity offsets, Δv(C IV-Mg II), outliers from SDSS DR7Q. The dash-dotted line indicates the data measurement from the catalogue, the solid line for the measured maximum peak, and the dashed line for the theoretical value based on the quasar redshift. The measurements are given in Table 6.2.

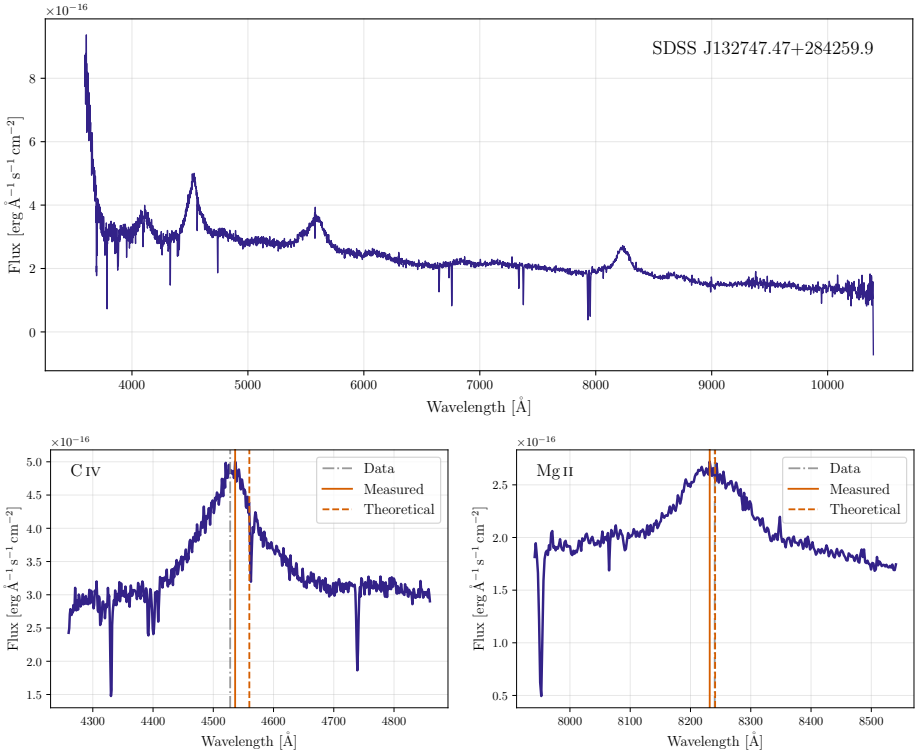

(a) Negative Δv(C IV-Mg II)

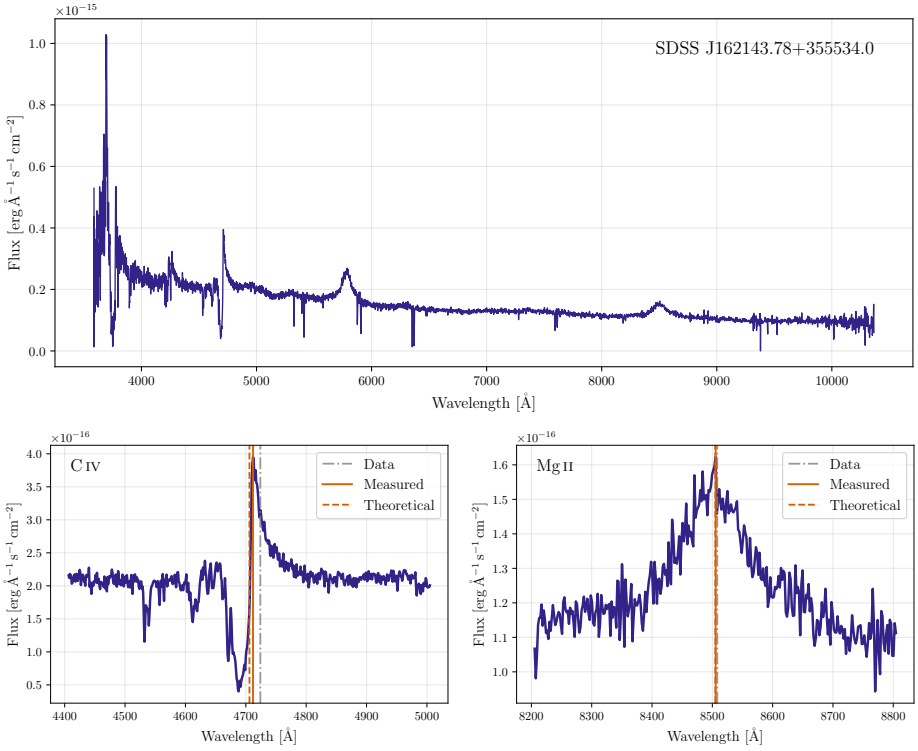

(b) Positive Δv(C IV-Mg II)

Figure 6.10: Example of spectra and emission line measurements of high velocity offsets, Δv(C IV-Mg II), outliers from SDSS DR12Q. The dash-dotted line indicates the data measurement from the catalogue, the solid line for the measured maximum peak, and the dashed line for the theoretical value based on the quasar redshift. The measurements are given in Table 6.2.

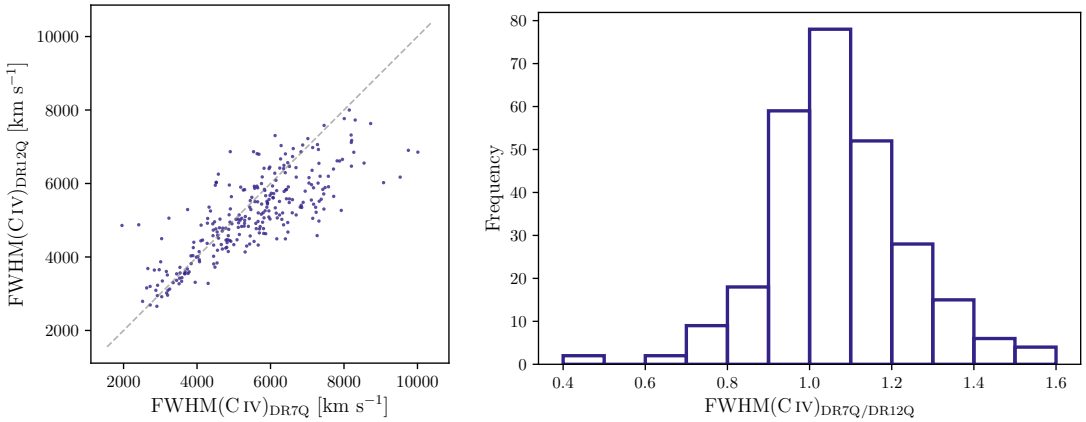

(a) Full width at half maximum of C IV

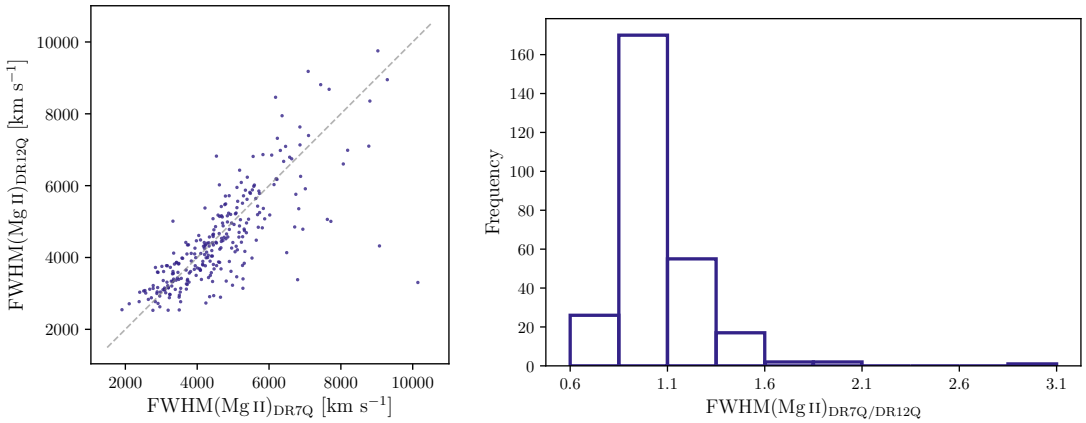

(b) Full width at half maximum of Mg II

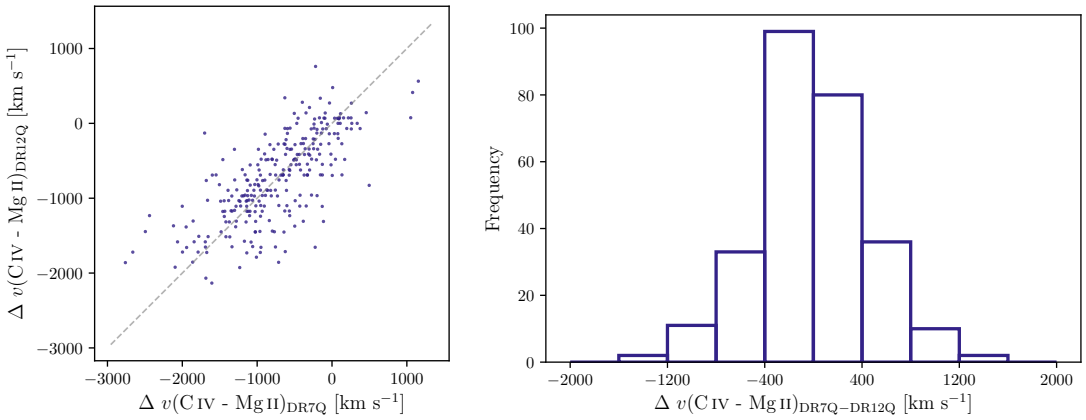

(c) Velocity shift of C IV and Mg II

Figure 6.11: Comparison between SDSS DR7Q and DR12Q parameter measurements. The distributions are on the *left* panels with one-to-one relationship in dashed grey line. The histograms on the *right* panels, where the full with at half maximum (FWHM) values between the two catalogue are compared using the ratios and the Δv using the differences.

Table 6.2: Velocity shift measurements for examples of high velocity offsets outliers shown in Fig. 6.9 and Fig. 6.10.

Name (SDSS J)	z	$v_{\mathrm{C\,IV}}$[a] (km s^{-1}), $z_{\mathrm{C\,IV}}$[b]		$v_{\mathrm{Mg\,II}}$[a] (km s^{-1}), $z_{\mathrm{Mg\,II}}$[b]		Δv(C IV-Mg II) (km s^{-1})	
		Data	Measured	Data	Measured	Data	Measured
Quasars from SDSS DR7Q[a]							
130944.98+222632.0	1.961	-3382.300	-2443.186	1673.500	1956.670	-5055.800	-4371.325
114449.33+032751.8	2.098	-241.500	-627.212	-2315.500	-710.461	2074.000	83.446
Quasars from SDSS DR12Q[b]							
132747.47+284259.9	1.943	1.922	1.928	1.943	1.940	-2068.167	-1225.583
162143.78+355534.0	2.037	2.049	2.041	2.038	2.037	1036.047	359.808

[a] The offsets in the emission lines are given in velocity shifts relative to the quasar redshifts in SDSS DR7Q.
[b] The offsets in the emission lines are given in line redshifts in SDSS DR12Q.

otherwise, so that they can be cross-matched with the parent dataset from SDSS DR7Q properties catalogue (Shen et al. 2011) and SDSS DR12Q (Pâris et al. 2017) that contain measurements of the spectral lines. This ensures a sufficient sample is acquired, though it does not guarantee that the spectra are of high S/N.

How can we compare the utility of our correlation to measure orientation with other indicators in the literature? We have not measured orientation, and so cannot make a direct comparison with metrics that measure a specific angle. However we can compare with correlations that claim to reflect orientation. We measure the Spearman's correlation coefficient, r_S, of our proposed correlation with other measures of inclination. The corresponding probability that two parameters are unrelated, p_S, is also measured. We use the cross-matched samples with the SDSS DR7Q properties catalogue as they yield a larger sample and a stronger Spearman's correlation coefficient. The Spearman's correlation coefficients and the corresponding probability for the investigated parameters are listed in Table 6.3. In almost all the sub-samples resulting from the cross-match with data in other bands, the FWHM(C IV/Mg II) and Δv(C IV − Mg II) correlation is significant at $p_S < 5\%$, except one which is due to the small sample size.

6.4.1 Radio Morphology

We use catalogues of quasar properties (Shen et al. 2011), radio properties of quasars (Kimball et al. 2011), and Radio Optical X-ray Italian Space Agency Science Data Center (ROXA; Turriziani et al. 2007), that includes the radio morphology classification. The SDSS DR7Q properties catalogue (Shen et al. 2011) contains radio properties obtained by matching the DR7Q catalogue to the Faint Images of the Radio Sky at Twenty cm (FIRST; White et al. 1997) catalogue using a 30" matching radius. Radio quasars with single FIRST source within 30" matching radius are rematched with higher matching radius of 5" and are categorised into core-dominant radio quasars. Whereas, those with multiple FIRST sources within 5" matching radius are lobe-dominant radio quasars. The rest are either undetected or outside FIRST area coverage.

Table 6.3: Spearman's correlation coefficient for the investigated parameters.

Sample	Parameter	Δv(C IV − Mg II)	R	FWHM Hβ	EW [O III]
S11 [1933]	FWHM(C IV/Mg II)	-0.608 ($6.039 \times 10^{-194}\%$)*			
S11 [-O: 1835]	FWHM(C IV/Mg II)	-0.580 ($2.946 \times 10^{-163}\%$)*			
S11 [Cd+Ld: 231]	FWHM(C IV/Mg II)	-0.454 ($3.841 \times 10^{-11}\%$)*			
P17 [2460]	FWHM(C IV/Mg II)	-0.380 ($3.005 \times 10^{-83}\%$)*			
P17 [-O: 2429]	FWHM(C IV/Mg II)	-0.387 ($7.597 \times 10^{-86}\%$)*			
T06 x S11 [B: 72]	FWHM(C IV/Mg II)	-0.264 (2.491%)			
K11 x S11 [1122]	FWHM(C IV/Mg II)	-0.185 ($4.217 \times 10^{-8}\%$)*			
K11 x S11 [L+T: 203]	FWHM(C IV/Mg II)	-0.186 (0.781%)	0.145 (3.870%)		
	R	-0.222 (0.144%)			
T07 x S11 [47]	FWHM(C IV/Mg II)	-0.425 (0.290%)			
K12 x S11 [15]	FWHM(C IV/Mg II)	0.196 (48.290%)			
T12 [70]	FWHM(C IV/Mg II)	-0.271 (2.338%)		-0.711 ($5.086 \times 10^{-10}\%$)*	-0.411 ($4.036 \times 10^{-2}\%$)*
	FWHM Hβ	0.203 (9.209%)			0.534 ($1.915 \times 10^{-4}\%$)*
	EW [O III]	0.194 (10.763%)		0.534 ($1.915 \times 10^{-4}\%$)*	
S12 x S16 [60]	FWHM(C IV/Mg II)	-0.457 ($2.418 \times 10^{-2}\%$)*		-0.513 ($2.722 \times 10^{-3}\%$)*	-0.210 (10.682%)
	FWHM Hβ	0.320 (1.263%)			0.333 (0.930%)
	EW [O III]	0.091 (48.925%)		0.333 (0.930%)	
T12, S12 x S16 [130]	FWHM(C IV/Mg II)	-0.460 ($3.780 \times 10^{-6}\%$)*		-0.556 ($6.551 \times 10^{-10}\%$)*	-0.399 ($2.637 \times 10^{-2}\%$)*
	FWHM Hβ	0.196 (2.548%)			0.375 ($1.078 \times 10^{-3}\%$)*
	EW [O III]	0.304 ($4.458 \times 10^{-2}\%$)*		0.375 ($1.078 \times 10^{-3}\%$)*	

Note: The catalogues are S11 for Shen et al. (2011), P17 for Pâris et al. (2017), T06 for Trump et al. (2006), K11 for Kimball et al. (2011), T07 for Turriziani et al. (2007), K12 for Kuźmicz & Jamrozy (2012), T12 for Tang et al. (2012), S12 for Shen & Liu (2012), and S16 for Shen (2016), with the character x indicates cross-match. The number of samples is in square brackets, with selected samples without outliers as -O, BAL as B, core- or lobe-dominated as Cd+Ld, and lobe or triple classes as L+T. The p_S value is given in round brackets.
*Highly significant at $p_S < 0.1\%$.

The radio properties catalogue (Kimball et al. 2011) has also utilised optical quasar spectra from SDSS and line measurements from SDSS DR7Q (Shen et al. 2011) (see Sect. 2 of their paper). Their sub-sample of radio quasars are then classified via visual inspection using FIRST (Becker et al. 1995) $2' \times 2'$ images and $4' \times 4'$ if the image has radio emission relative to the optical position of $\gtrsim 1'$. Depending on the location of the radio emission (see Sect. 3 of their paper), radio quasars are primarily sorted into core if emission is at optical position, jet if emission is from core and jet components, lobe if emission is from core and single lobe, and triple if emission from core and double lobe. The core and lobe 20 cm flux densities of lobe and triple class are also provided. We then cross-match with the full sample from the quasar properties SDSS DR7Q catalogue (Shen et al. 2011) to obtain the broad emission line FWHM and velocity shifts. We also select only those with clear identifiable morphology classification where two examiners concur with each other on the designation, as flagged in the catalogue. Additionally, we remove 3 points with extreme ratio FWHM of > 8. The number of object in the sample is then 1122.

The ROXA catalogue (Turriziani et al. 2007) includes identifications of blazars and FSRLQs. The selection and classification process are elaborated in Sect. 2 and Sect. 3 of their paper. Their sample is built based on multi-frequency approach using radio and X-ray surveys to attain the spectral slopes, through which possible candidates are identified. They then distinguished the radio sources by analysing the spectral energy distributions and optical spectra from the SDSS and 2dF surveys. We obtain 47 radio quasars with FSRLQ, BL Lac, or SSRLQ category after cross-matching their catalogue with SDSS DR7Q properties catalogue (Shen et al. 2011).

In Figs. 6.12 to 6.14, we present the radio morphology overlaid onto the FWHM (C IV/Mg II) versus Δv(C IV-Mg II) distribution. Most data points are situated towards the lower right, which would signify intermediate to edge-on viewing angle in our simple inclination angle mapping. However, if we disregard the large dispersion in the relation at high FWHM(C IV/Mg II) and blueshifts, and concentrate on the bulk of the dispersion, the difference between radio classes with inclination can be clearly identified. Core-dominated radio quasars are shifted towards the negative velocity shifts and higher FWHM ratio compared to those of lobe-dominated (Figs. 6.12 and 6.13). Similarly, most SSRLQs have the same trend as lobe-dominant radio quasars, while their counterpart FSRLQs as core-dominant (Fig. 6.14). There is one BL Lac that seems to contradict with our assumption, though we are unable to statistically infer its true effect with only a data point. The jet and lobe classes in Fig. 6.13 are also clustered around the bottom right end of the trend.

Although the radio morphology classification provides a crude way to deduce the orientation of radio sources, generally they are in agreement with our simple approach of inferring the orientation. In our scheme, objects viewed along the line-of-sight approaching edge-on tend to have emission line properties that are less blueshifted with FWHM C IV roughly equal or smaller than FWHM Mg II, which match with what we

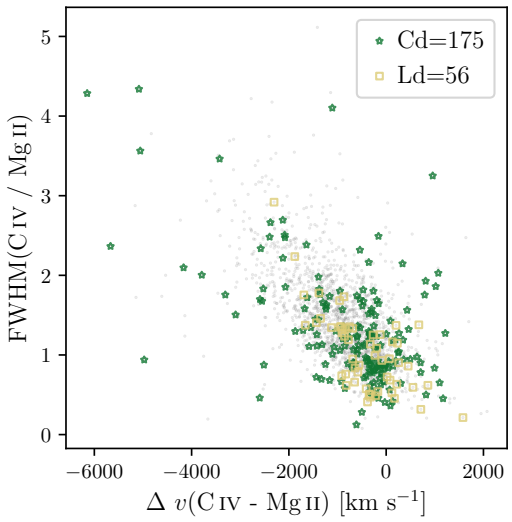

Figure 6.12: Ratio of full width at half maximum, FWHM, against velocity shift, Δv, between C IV and Mg II, with radio morphology. The quasar sample is obtained from Shen et al. (2011) SDSS DR7Q. Quasars classified as core-dominated (Cd) are indicated with green stars and lobe-dominated (Ld) with yellow squares. For comparison, their high spectral quality (high S/N) samples are superimposed in small grey symbols.

found for lobe-dominated SSRLQs. Meanwhile, core-dominated FSRLQs cover a wide range of FWHM ratios and velocity shifts, but mostly are blueshifted and at higher FWHM ratios.

6.4.2 Radio Core Dominance

We examine the trend in core dominance with our suggested model using the cross-matched sample between radio properties catalogue (Kimball et al. 2011) and quasar properties SDSS DR7Q catalogue (Shen et al. 2011) mentioned in the previous section. The core dominance in terms of ratio of core to lobe flux density at 20 cm, K-corrected to its rest frame, is calculated for lobe and triple class radio quasars (Kimball et al. 2011):

$$R = \frac{S_{\rm core}}{S_{\rm lobe}}(1+z)^{\alpha_{\rm lobe}-\alpha_{\rm core}}, \tag{6.2}$$

where $S_{\rm core}$ and $S_{\rm lobe}$ are the observed 20 cm core and lobe flux densities, and $\alpha_{\rm core} = 0$ and $\alpha_{\rm lobe} = -0.8$ are the core and lobe spectral indexes.

Figure 6.15 shows the core dominance in R for the radio sources. The values of R seem to be increasing, from the lower right to upper left of the ratio FWHM versus the velocity shift relation. This is also identified using the Spearman correlation coefficient (Table 6.3). The parameter is significantly anti-correlated with Δv(C IV-Mg II) at ($r_S = -0.222, p_S < 1\%$) and correlated with FWHM(C IV/Mg II) at ($r_S = 0.145, p_S < 5\%$).

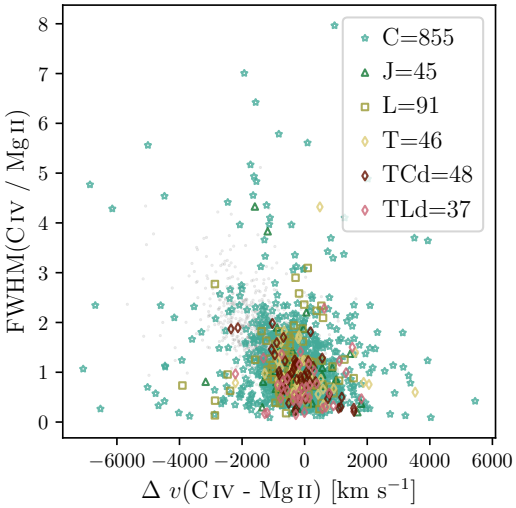

Figure 6.13: Ratio of full width at half maximum, FWHM, against velocity shift, Δv, between C IV and Mg II, with radio morphology. The radio morphology classifications are obtained from Kimball et al. (2011). Quasars classified as core (C) are indicated with stars, jet (J) with triangles, lobe (L) with squares, and triple (T) with diamonds. Triple class quasars are subdivided into core-dominated triple (TCd) and lobe-dominated triple (TLd), denoted in different colours. The emission lines measurements are obtained from Shen et al. (2011) SDSS DR7Q catalogue. For comparison, their high spectral quality (high S/N) samples are superimposed in small grey symbols.

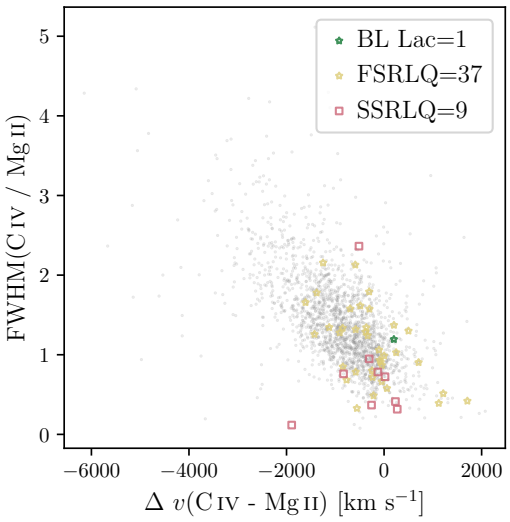

Figure 6.14: Ratio of full width at half maximum, FWHM, against velocity shift, Δv, between C IV and Mg II, with radio morphology. The radio morphology classifications are obtained from Turriziani et al. (2007). Quasars classified as blazars are indicated with stars, including BL Lacertae (BL Lacs) in green and flat-spectrum radio-loud quasar (FSRLQ) in yellow, while steep-spectrum radio-loud quasars (SSRLQs) with pink squares. The emission lines measurements are obtained from Shen et al. (2011) SDSS DR7Q catalogue. For comparison, their high spectral quality (high S/N) samples are superimposed in small grey symbols.

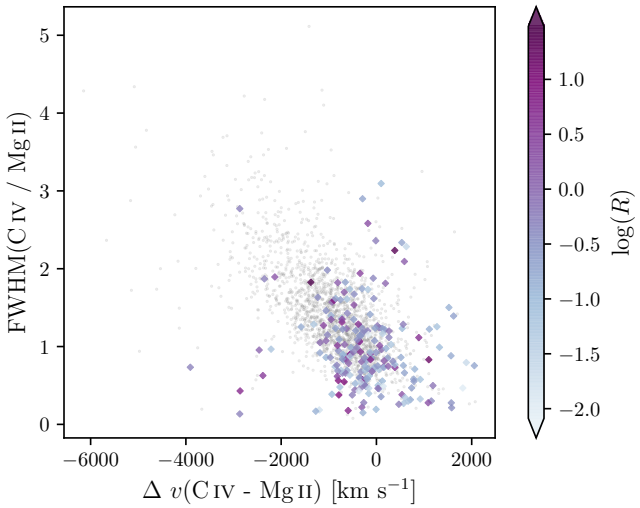

Figure 6.15: Ratio of full width at half maximum, FWHM, against velocity shift, Δv, between C IV and Mg II, with core dominance, R. The distribution is colour-coded by increasing colour gradient with R using quasars sample of Kimball et al. (2011). The emission lines measurements are obtained from Shen et al. (2011) SDSS DR7Q catalogue. For comparison, their high spectral quality (high S/N) samples are superimposed in small grey symbols.

Although it has been argued that radio lobe flux density is not the best normalisation for radio core dominance (Wills & Brotherton 1995), our results are consistent with edge-on objects having lower R.

6.4.3 Inclination Angle from Radio

In radio-loud quasars, the strength of the Doppler boosted jet component can be used to infer the orientation of the source. Kuźmicz & Jamrozy (2012) have assembled a sample of 43 giant- and 49 smaller-sized lobe-dominated radio quasars at redshift range $0.4 \lesssim z \lesssim 2$, with inclination angle measurements from radio data. The giant radio sources are those with radio structure > 0.72 Mpc, assuming the cosmological parameters from Spergel et al. (2003). The selection method and possible biases in the sample are described in Sect. 2 and Sect. 3 of their paper. Kuźmicz & Jamrozy (2012) shown that the two populations are rather similar in their properties, such as black hole mass and accretion rate, and hence we consider both as one sample.

They measured the viewing angle, defined from the jet axis to the line-of-sight, with the assumption that the asymmetries of an object is due to the Doppler beaming of the jet:

$$i = \arccos\left[\frac{1}{\beta_j}\frac{s-1}{s+1}\right], \tag{6.3}$$

where $s = (S_j/S_{cj})^{1/(2-\alpha)}$, S_j and S_{cj} are the peak flux density of the lobe nearer to and father from the core respectively. The jet velocity, β_j, is taken to be 0.6 of speed of light (Wardle & Aaron 1997; Arshakian & Longair 2004) and the spectral index, α, is -0.6 (Wardle & Aaron 1997).

Since the velocity shifts of the lines are not provided, we cross-match their sample with $z \geq 1.5$, with those in the parent sample of SDSS DR12Q (Pâris et al. 2017) and SDSS DR7Q (Shen et al. 2011) catalogues. 15 sources found in SDSS DR7Q and 8 in SDSS DR12Q, with 7 of them are also in SDSS DR7Q. Thus, our analysis can only exploit the 15 objects from SDSS DR7Q along with their corresponding values of broad emission lines properties for consistency.

We show the distribution of ratio FWHM and velocity shifts with inclination angle in Fig. 6.16. Similarly, the samples from Shen et al. (2011) SDSS DR7Q catalogue are also plotted for representation of the actual trend. The small sample of radio quasars mostly have high inclination angle (near edge-on) located at low FWHM ratio and high velocity shift of the distribution, while the only object with near pole-on viewing angle of 13° is situated at higher FWHM ratio and lower velocity shift. However, there is also a mixture of intermediate inclination angles, between $\sim 40°$ and $\sim 60°$, in the lower right end of the sequence. Some of the associated errors in the FWHM ratio and velocity offsets are also large.

It has been noted that the majority of radio quasars consist of close to edge-on objects of $i > 60°$ (Kuźmicz & Jamrozy 2012). Although seems to contradict the traditional unified AGN picture, this can be related to the clumpy (Nenkova et al. 2008) or receding torus model (Lawrence 1991). The nearly pole-on angle object also might be a possible BL Lac source (Kuźmicz & Jamrozy 2012).

6.4.4 Line Width of Hβ

We use two samples from the literature that provide emission line measurements covering the UV and optical regime. The first sample (Tang et al. 2012, hereafter T12) contains bright quasars with redshift $z < 1.4$, including radio-loud and radio-quiet, compiled from three subsamples, namely selected UV-excess Palomar-Green quasars, spectra with far-UV from Far Ultraviolet Spectroscopic Explorer and Hubble Space Telescope, and radio-loud quasars. Sect. 2 of their paper outlines the sample selection and spectral fitting procedure. They modelled the regions in the vicinity of C IV, Mg II, and Hβ with a power-law continuum. Two Gaussian components are applied to fit individual broad emission lines, except for Hβ which requires an extra Gaussian to reflect the narrow line region emission. Using the fitted model, they calculated the properties of the emission lines. They also evaluated the velocity shifts between the fitted peak of the line and the systemic redshift. The spectral line measurements are listed in Table 3 and Table 4 of

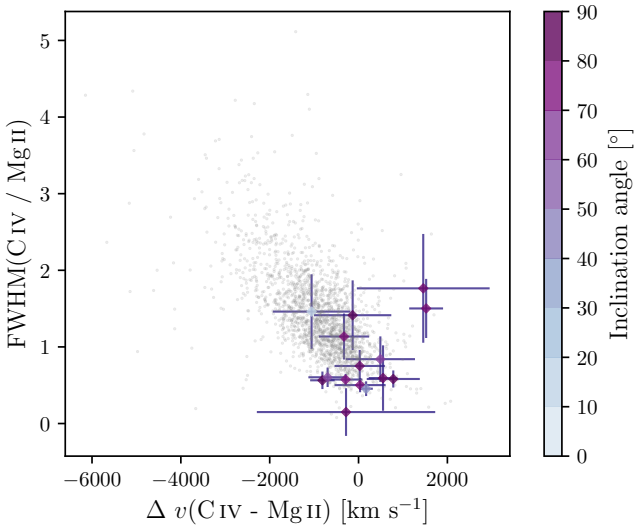

Figure 6.16: Ratio of full width at half maximum, FWHM, against velocity shift, Δv, between C IV and Mg II, with inclination. The distribution is colour-coded by increasing colour gradient with inclination from 0° (pole-on) to 90° (edge-on) using radio quasars sample of Kuźmicz & Jamrozy (2012). The emission lines measurements and errors are obtained from Shen et al. (2011) SDSS DR7Q catalogue. For comparison, their high spectral quality (high S/N) samples are superimposed in small grey symbols.

their paper. For our sample, we use 70 out of 85 objects that have complete emission line measurements for C IV, Mg II, Hβ, and [O III].

The second sample consists of 60 luminous quasars at intermediate redshift of $z \sim 1.5$–2.2 that cover the C IV to Hβ region (Shen & Liu 2012) and a subsequent follow-up survey that extends to cover [O III] region (Shen 2016). The selection of sample and spectral measurements are specified in Sect. 2 (Shen 2016) and Sect. 3 (Shen & Liu 2012) of their paper. They applied spectral fitting to the optical and near-infrared spectra to extract the continuum and line features. A pseudo-continuum is created by fitting a power-law continuum using UV and optical line templates, depending on the wavelength region. It is then subtracted from the original spectrum to yield the spectrum of emission lines. They fitted Gaussian profiles in logarithmic wavelength to model the broad and narrow components of the emission line. Using the fitted model, the emission line properties are derived, including the FWHMs of the broad line component. The relative velocity shifts are measured at the centroid of the narrow [O III], broad C IV, Mg II, and Hβ. Since [O III] is not within the coverage in Shen & Liu (2012), in our analysis, the Hβ and [O III] line measurements are taken from Shen (2016), while the C IV and Mg II line properties are from Shen & Liu (2012) to be consistent. Hereafter, this cross-matched sample is the S12xS16 sample.

The distribution of Hβ FWHM onto the Δv(C IV-Mg II) and FWHM(C IV/Mg II) relation is illustrated in Fig. 6.17. The Δv(C IV-Mg II) and FWHM Hβ are positively correlated, while the opposite correlation between FWHM(C IV/Mg II) and FWHM Hβ is

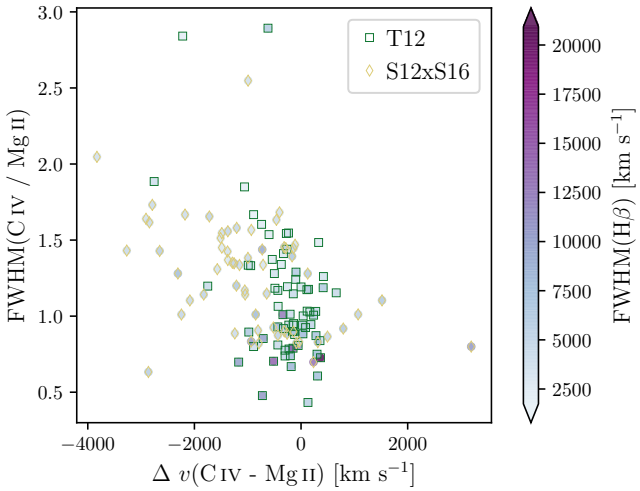

Figure 6.17: Ratio of full width at half maximum, FWHM, against velocity shift, Δv, between C IV and Mg II, with FWHM Hβ. The distribution is colour-coded by increasing colour gradient with FWHM Hβ using quasars sample of T12 (Tang et al. 2012) in green squares and S12xS16 (Shen & Liu 2012; Shen 2016) in yellow diamonds.

seen (Table 6.3). This finding agrees with the expectation from the orientation indicator using Hβ line width, whereby the FWHM of Hβ is broader for high inclination, less blueshifted, and small FWHM(C IV/Mg II) ratio objects.

Using T12 sample, the Δv(C IV-Mg II) and FWHM(C IV/Mg II) correlation is weaker compared to that using S12xS16 sample, though both are significant at $p_S < 5\%$. The anti-correlation between the line width ratio and Hβ is highly significant with $p_S \ll 0.01\%$ in both samples. Meanwhile, the relationship between the velocity shift and Hβ is not statistically significant in T12 sample but significant at $p_S < 5\%$ in S12xS16 sample. Combining both samples yields a significant p_S value between the parameters.

6.4.5 Line Strength of [O III]

We use the bright quasar samples (Tang et al. 2012) and the SDSS DR7Q optical and near-infrared spectral measurements (Shen & Liu 2012; Shen 2016) described in the previous section. The behaviour of EW [O III] on the FWHM(C IV/Mg II) versus Δv(C IV-Mg II) map, shown in Fig. 6.18, seems to be consistent with high EW [O III] objects situated at lower right end of the map for viewing angle close to the accretion disk. When considering both samples from T12 and S12xS16, the Spearman rank correlation coefficients of velocity shifts and FWHM ratio with EW [O III] are highly significant ($p_S < 0.1\%$) with $r_S = 0.304$ and $r_S = -0.399$, respectively (Table 6.3).

However, examining the samples separately, the EW [O III] with Δv(C IV-Mg II) and FWHM(C IV/Mg II) relations in S12xS16 sample are not significant. This inconsistency is probably due to the lack of high EW [O III] quasars in S12xS16 sample to be considered

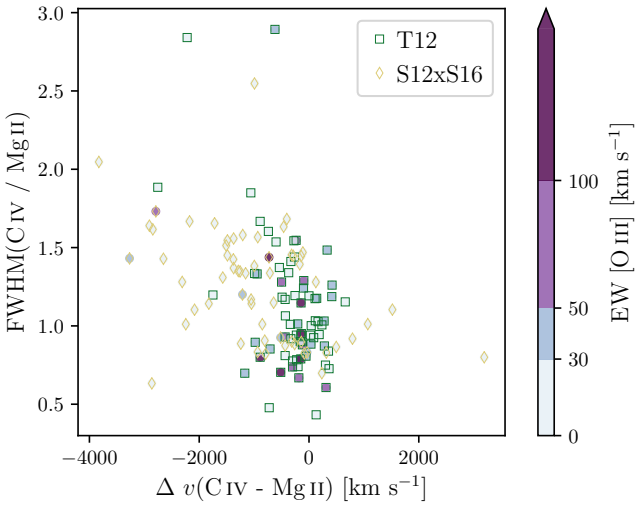

Figure 6.18: Ratio of full width at half maximum, FWHM, against velocity shift, Δv, between C IV and Mg II, with equivalent width (EW) [O III]. The distribution is colour-coded by increasing colour gradient with EW [O III] using quasars sample of T12 (Tang et al. 2012) in green squares and S12xS16 (Shen & Liu 2012; Shen 2016) in yellow diamonds.

as near edge-on orientation objects, whereby only 6 quasars have EW [O III] ≥ 30 Å, with 4 of them range $\sim$ 30–40 Å. This is portrayed in Fig. 6.18, where it is colour-coded into a different range of EW for distinction. The sample in T12 contains more objects with high EW, with almost half or 30 of them that display high EW [O III] of ≥ 30 Å. There is a highly significant anti-correlation between the EW [O III] and FWHM(C IV/Mg II) at $p_S < 0.1\%$, though EW [O III] and Δv(C IV-Mg II) show non-significant correlation. This might be also because of the weak negative relation between Δv(C IV-Mg II) and FWHM(C IV/Mg II) with $r_S = -0.271$ and lower significance at $p_S < 5\%$.

Assuming that the line width of Hβ and the line strength of [O III] are both inclination diagnostics, the Spearman correlation coefficients are highly significant at $p_S \ll 0.01\%$ when using T12 sample and with S12xS16 merged. The r_S and p_S values are weaker in S12xS16 sample.

6.4.6 Low-ionisation Broad Absorption Line Quasars

To examine the emission line properties of LoBAL quasars, we use the catalogue of BAL quasars from the SDSS DR3 (Trump et al. 2006). The descriptions on the construction of the spectra and selection of BAL quasars are given in Sect. 3 and Sect. 4 of their paper. They identified $0.5 \leq z \leq 2.15$ quasars with LoBAL features in Mg II line that satisfy a less stricter measure of BAL, the absorption index (AI; Hall et al. 2002). They adopted a modified version of AI such that it measures the true EW and the whole absorption up to 29 000 km s^{-1} through an automated pipeline. Their parent sample consists of about

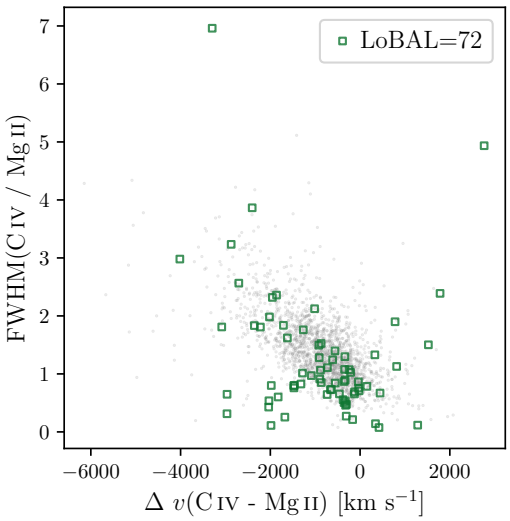

Figure 6.19: Ratio of full width at half maximum, FWHM, against velocity shift, Δv, between C IV and Mg II, with low-ionisation broad absorption line (LoBAL) quasars. The LoBAL classification is obtained from Trump et al. (2006). The emission lines measurements are obtained from Shen et al. (2011) SDSS DR7Q catalogue. For comparison, their high spectral quality (high S/N) samples are superimposed in small grey symbols.

1.31% LoBAL quasars. By cross-matching their catalogue with the quasar properties SDSS DR7Q catalogue (Shen et al. 2011), we obtain 72 LoBAL quasars.

Figure 6.19 shows the sample of LoBAL quasars on the ratio FWHM and velocity shift relation. They seem to be preferentially clustered towards the lower right of the distribution, implying mid to high inclination angles. This supports our viewpoint that LoBALs are seen preferentially near equatorial angle, though about 20% appears on the opposite end with more blueshifted and higher C IV FWHM than Mg II. It is crucial to point out that BALs might inherently have large blueshift, which reflects the wind outflow. Additionally, the absorption trough might affect the line width measurement.

6.4.7 Summary of Comparison with Other Inclination Measurements

The presented statistics and analyses demonstrate that our proposed correlation using the ratio of FWHM and the velocity shift of C IV and Mg II is generally consistent with other inclination angle measurements from the literature. Inclinations of radio sources can be loosely inferred from the radio morphology and radio core dominance. These measurements of inclination are also roughly consistent when projected onto our proposed indicator.

Since Hβ and Mg II are both low-ionisation lines, they are expected to be emitted at similar locations in the BLR, close to the disk with a dominant rotational component. Hence the strong correlation between the FWHM(Hβ) and ratio FWHM(C IV/Mg II).

The strength of [O III] provides an indication of the geometry of the emitting region, which also reflects orientation. This metric is weakly correlated when compared to the FWHM ratio and velocity shifts. The distribution of LoBAL quasars on our proposed inclination indicator also agrees with the prediction that these population being observed close to equatorial plane.

6.5 Comparison with Simulations

Since our proposed inclination indicator is derived mainly based on the kinematics of the wind, we can test whether our simple kinematical BLR disk-wind model is able to predict a similar trend as seen in observation. Detailed descriptions on the wind kinematics and modelling are mentioned in § 3.2. The BLR disk-wind is modelled with a wide wind opening angle and the choices of our input parameters are mentioned next.

6.5.1 Modelling the Wind Kinematics

A sketch of the wide disk-wind model is presented in Fig. 6.20. The main parameter values adopted are shown on the left side of Fig. 6.20 and the full list in Table 6.4. To create our fiducial model, we utilise constraints from observations and theory. The black hole mass is estimated based on the virial black hole mass measurements from the SDSS DR7Q quasar properties catalogue (Shen et al. 2011). Assuming that it scales with the continuum luminosity, λL_λ, and the broad emission line width, the virial black hole mass, $M_{\rm BH,vir}$, is expressed as

$$\log M_{\rm BH,vir} = a \log \left(\frac{\lambda L_\lambda}{10^{44}\,{\rm erg\,s^{-1}}} \right) + 2 \log {\rm FWHM} + b, \tag{6.4}$$

where $(a, b) = (0.62, 0.74)$ calibrated based on Mg II line for $0.7 \leq z < 1.9$ (Shen et al. 2011) and $(a, b) = (0.53, 0.66)$ calibrated based on C IV line for $z \geq 1.9$ (Vestergaard & Peterson 2006). The mean of $M_{\rm BH,vir}$ in our SDSS DR7Q sample is $10^{9.49}\,M_\odot$ ($3.07 \times 10^9\,M_\odot$), and we set $M_{\rm BH} = 10^9\,M_\odot$ in our model.

The mass accretion rate onto the black hole is determined by the accretion parameters. The radiative efficiency at which mass is converted to radiation is given by $\eta = L_{\rm bol}/\dot{M}_{\rm acc}c^2$, where $L_{\rm bol}$ is the bolometric luminosity and $\dot{M}_{\rm acc}$ is the total mass accretion rate. For luminous sources at intermediate redshift, η is found to be > 0.2 (Davis & Laor 2011; Trakhtenbrot 2014). Since our sample consists of high bolometric luminosity quasars with mean $L_{\rm bol} \approx 1.23 \times 10^{47}\,{\rm erg\,s^{-1}}$, we use $\eta = 0.2$. The accretion rate is then $\dot{M}_{\rm acc} \sim 10\,M_\odot\,{\rm yr^{-1}}$ and the total mass-loss rate of the wind, $\dot{M}_{\rm wind}$, is also set to this value.

The wind has a wide range of angles from 15° to 60°. For this model, the wind is also optically thick and is bounded within radius from 5×10^{17} cm to 4×10^{18} cm. To justify our selected parameters, these values are chosen using the well-known BLR radius–luminosity (r–L) relation (Kaspi et al. 2007; Bentz et al. 2009) from RM studies as a baseline. The BLR radius in units of light days is given by

$$r_{\rm BLR} = c \left(\frac{\lambda L_\lambda}{10^{44}\,{\rm erg\,s^{-1}}} \right)^d , \tag{6.5}$$

where $(c, d) = (19.1, 0.56)$ derived at 1350 Å using the average of fitted slopes from mean time lags of Balmer lines for all dataset per object (Kaspi et al. 2005) and $(c, d) = (18.5, 0.62)$ derived at 3000 Å (McLure & Dunlop 2004). Using these relations, the mean radii of the BLR are 1.39×10^{18} cm for 1350 Å and 1.50×10^{18} cm for 3000 Å, which provide an estimate of the emitting region for C IV and Mg II lines in the wind. These values are within the bounds of the BLR wind in our model. The size of BLR using Hβ of reverberation-mapped samples is also found to be $\sim$ 2–3 times larger than that using C IV (Peterson et al. 2004). Subsequently, we fix the BLR radius to be $r_{\rm BLR} = 5 \times 10^{18}$ cm.

For C IV to be blueshifted and broader than Mg II, the wind poloidal velocity has to be boosted enough to overcome the rotational component. There are couple of free parameters that regulate the poloidal velocity, two of which are R_v and α. The acceleration scale height, R_v, of the poloidal velocity determines the stage where the wind attains half of its terminal velocity. The acceleration of the poloidal wind is dictated by the power law index, α. The quantities R_v and α are set to be 1×10^{18} cm and 3.5 respectively such that the poloidal velocity near the wind base accelerates slowly but quickly gains speed with higher poloidal distance.

The wind is partitioned into 4 by 4 'wind zones' to emulate the stratification in the BLR wind, as illustrated on the right side of Fig. 6.20. We explore a set of zone pairs for Mg II and C IV emission lines. Wind zones [0, 1]–[0, 3] are chosen as plausible line emitting region for Mg II line, and zones [2, 0]–[2, 1] for C IV.

Once the wind kinematics are set up, a Monte Carlo simulation is employed to generate large number of random particles within each zone. The projected line-of-sight velocity as a function of inclination angle between 10° and 80° is computed for each particle, which is binned to create a histogram, and finally considered in the production of the total line profile. Within each specified bins, the counts are weighted according to the density and radiative transfer intensity. The contribution of every particle at its given velocity is then the total emission line profile. A smooth emission line profile is produced by convolving with a Gaussian kernel. The line width of the smoothed line is evaluated at its FWHM. The velocity shift of individual emission line is estimated from the median of the line to the axis centre. The median is used instead of the line peak due to the shape of the generated line profile. The velocity shift of C IV with respect to Mg II is then the difference between the two shifts.

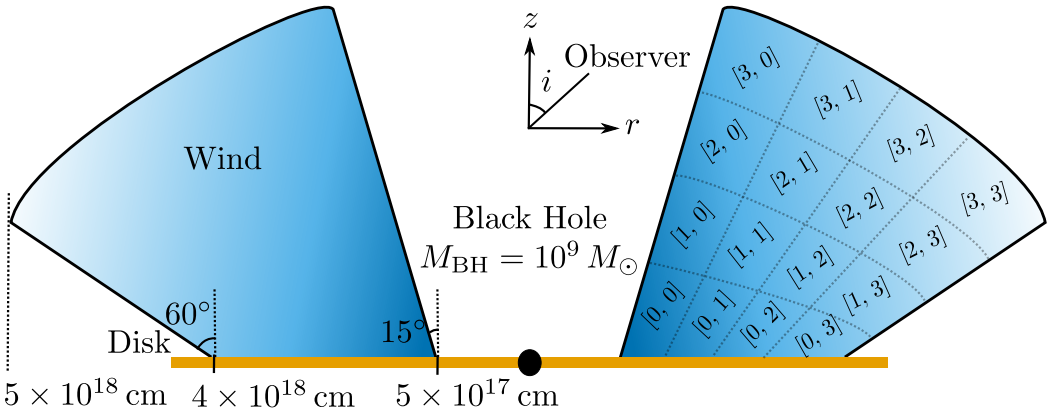

Figure 6.20: A sketch of the disk-wind model with wide opening wind. *Left*: Adopted fiducial parameters values. *Right*: Wind zones indicated by rows and column, from bottom to top and left to right.

Table 6.4: Adopted parameter values in the fiducial wide wind model.

Parameter	Notation	Value
Black hole mass	$M_{\rm BH}$ ($10^9\,M_\odot$)	1.0
BLR size	$r_{\rm BLR}$ (10^{17} cm)	50.0
	$r_{\rm BLR}$ (light-days)	1930.3
	$r_{\rm BLR}$ ($r_{\rm g}$)	33 852.5
Wind radius	$r_{\rm min}$; $r_{\rm max}$ (10^{17} cm)	5.0; 40.0
	$r_{\rm min}$; $r_{\rm max}$ (light-days)	193.0; 1544.3
	$r_{\rm min}$; $r_{\rm max}$ ($r_{\rm g}$)	3385.2; 27 082.0
Wind opening angle	$\theta_{\rm min}$; $\theta_{\rm max}$	15.0°; 60.0°
Scale height	R_v (10^{17} cm)	10.0
	R_v (light-days)	386.1
	R_v ($r_{\rm g}$)	6770.5
Acceleration power law index	α	3.5
Total mass-loss rate	$\dot{M}_{\rm wind}$ ($M_\odot\,{\rm yr}^{-1}$)	10.0

6.5.2 Predictions with Simulation

The predicted emission line profile properties with inclination angle are shown in Fig. 6.21. Additionally, Fig. 6.22 depicts the shape of the line profiles in each zone. As expected, the line profiles closest to the base of the wind streamline at zones [0, b] are less blueshifted and broader due to the stronger contribution from the Keplerian rotational velocity. Meanwhile, emission lines situated at zones further above the disk have larger wind poloidal velocity wind and lesser from the rotational component, which are reflected by the more blueward shifts away from the line centroid and reduced FWHMs. The line shifts and FWHMs in zones [2, b] and [3, b] are also fairly similar.

The blueshift is the most prominent at low inclination angle (Fig. 6.21a). Subsequently, it becomes smaller with increasing viewing angle since the line-of-sight is moving away relative to the wind. At small inclination angle, the line-of-sight velocity is also less affected by the rotational component, and hence the smaller FWHM (Fig. 6.21b). The line width peaks as the angle of inclination approaches equatorial view.

Figure 6.23 presents the ratio FWHM versus the velocity shifts of the line profiles emitted from zones [2, 0]–[2, 1] and [0, 1]–[0, 3]. As explained in the previous section, [2, 0]–[2, 1] is the zone of the wind emitting C IV, while [0, 1]–[0, 3] is emitting Mg II. Figure 6.23 therefore examine how the ratio of the FWHM and the velocity shifts between the two lines vary when comparing different regions of the wind. As the relative distance between the two emitting regions increases, the velocity shift decreases while the FWHM ratio increases. This is demonstrated in, for example, the line profiles in zone pairs [2, 0] and [0, 2] have higher blueshift and FWHM ratio than those in zones [2, 1] and [0, 2].

As a comparison, the fitted linear regression models using observational data are also overlaid in Fig. 6.24. The prediction from our simple kinematical model matches well with the fitted slopes, with the scales of the parameter within those from observations. In general, the model is able to qualitatively reproduce the negative relationship between the ratio FWHM and velocity shift with higher inclination angle (near edge-on), consistent with our proposition.

6.6 Potential of the Orientation Indicator

Using two easily measured characteristics of emission line in the UV-optical, we demonstrate that the correlation between the velocity difference and FWHM ratio of C IV and Mg II lines is due to angle-of-viewing. We argued that the relation can be explained in a simple physical model of the disk-wind. We have tested the predictions of our diagnostic against other tests which claim to indicate orientation. The results shown indicate broad consistency with our indicator. The analytic disk-wind modelling performed has also successfully reproduced the range of velocity difference and FWHM ratio.

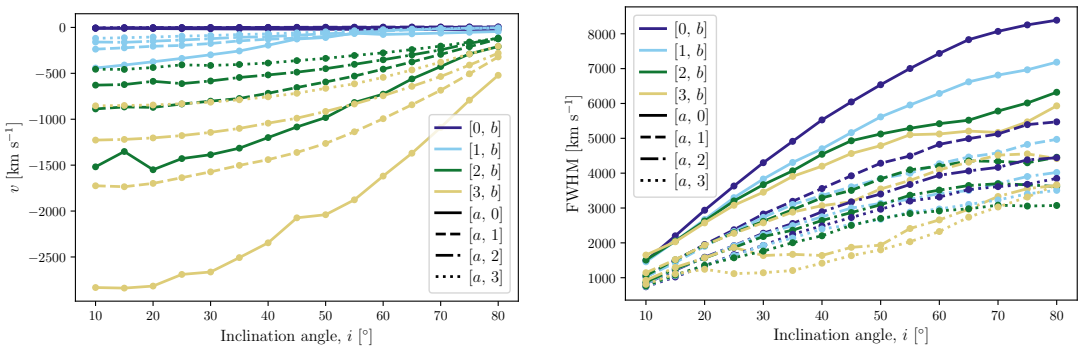

(a) Velocity shift relative to the line profile centroid, v, against i

(b) Full width at half maximum, FWHM, against i

Figure 6.21: Simulated emission line properties as a function of inclination angle i. The different colours and line-styles represent distinct rows and columns in the wind zones.

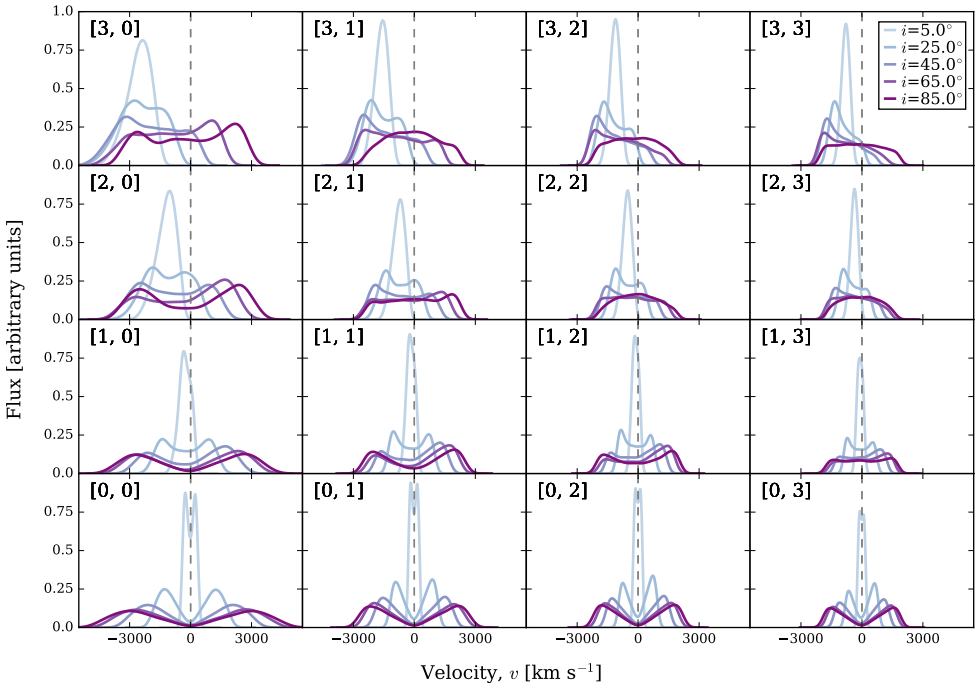

Figure 6.22: Simulated emission line profiles as a function of inclination angle for wide wind model model. The position of the 'wind zone' $[a, b]$ is indicated on the top left of each panel. The dashed line shows the systemic centroid of the line.

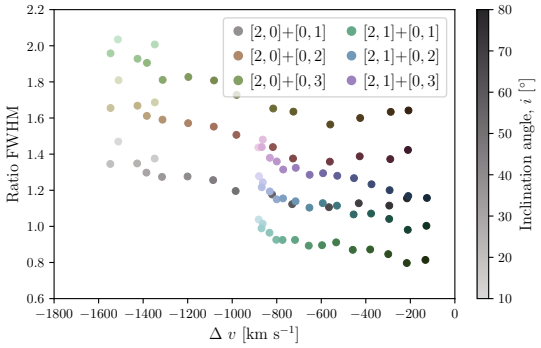

Figure 6.23: Simulated ratio of full width at half maximum, FWHM, against velocity shift, Δv, between two emission lines in distinct wind zones. The different colours represent different pairs of wind zones [2, 0]–[2, 1] relative to [0, 1]–[0, 3]. The increasing colour gradient indicates the inclination, i, from low at 10° (near pole-on) to high at 80° (near edge-on).

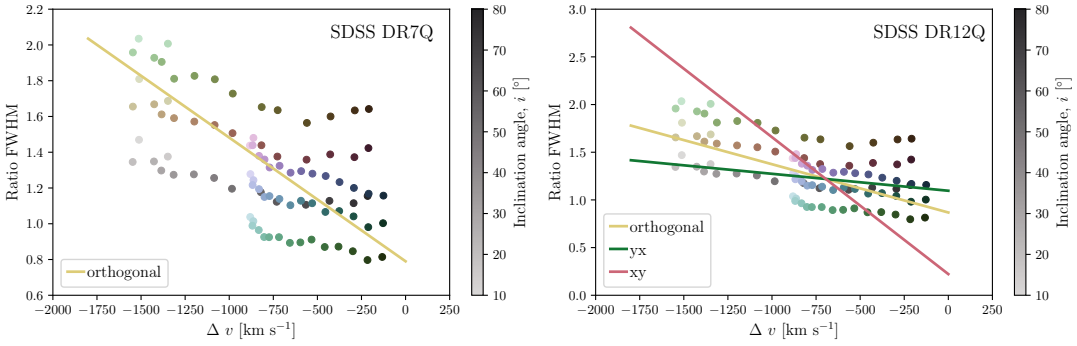

Figure 6.24: Comparison between simulation and observation. Figure 6.23 with superimposed fitted lines from observation, shown in Fig. 6.5. The representation of the different colours is as detailed in Fig. 6.23 caption.

All evidence that has been presented favours a disk-wind model similar to the one presented. However, as mentioned in § 6.3.3, there are a few caveats in our approach that are worth reiterating. The dataset used to test the model has been derived from automated algorithms of the very large SDSS dataset. Thus, it is expected that some individual data points will be revised with more careful individual analysis. However, this will not void the basic trend. The chosen linearity between the projected distance and the inclination angle and the range of this mapping is also not entirely justified, however, this choice leads to a physically sensible interpretation and fits our simple model. Ultimately, further modelling, including the choice of the C IV and Mg II emission regions and photoionisation effects, will be needed to better establish this mapping.

In our modelling, the acceleration power law index of 3.5 is chosen as it fits the model with the observations. The α parameter provides a sense of the rate of increase in the poloidal velocity component as the wind travels further out. For $\alpha = 1$, this implies a slow increase in the wind acceleration with increasing distance (see Fig. 4.10). The high α value in our model suggests that a significant boost in the poloidal velocity is needed to be able to reproduce the observed non-virial broadening in high-ionisation emission lines, like C IV. Understanding the behaviour of the wind will allows us to make predictions on the physics of the BLR.

The expected variation in physical properties due to the angle-of-viewing provides a strong motivation to develop this model and improve the estimation. Future detailed analysis of the datasets, combined with optimisation of model parameters and properly account for other intrinsic properties of the source such as the accretion state and luminosity, will enable the angle-of-viewing to be well-determined. Once the effects of orientation are accounted for, more robust determinations of other physical parameters are possible, providing a natural framework for unravelling a detailed physical model for quasars. If the physics of these highly luminous sources can be unravelled, they potentially provide a standard candle, with which to map the structure of the distant universe (Marziani & Sulentic 2014; Risaliti & Lusso 2015, 2019; Lusso et al. 2019).

The measured characteristics of the high and low ionisation lines differ, providing clear evidence that they arise in different geometric and kinematic locations of the disk-wind. Interpreted in the correct model, this data can be used to measure angle-of-viewing to the quasar. If the angle-of-viewing can be robustly measured, then finally a key observational parameter in the physical model of the emitting regions of a quasar can be determined, significantly helping the mapping, both geometrically and kinematically, of those regions. Also, emission line widths are used to estimate black hole masses, and the orientation may introduce up to an order of magnitude variation (see Chapter 7). Thus, determination of the angle-of-viewing will significantly improve black hole estimates.

6.7 Summary

The scales of AGN emission regions are small enough that the detailed structure is unlikely to be directly resolved at wavelengths shorter than infrared in the foreseeable future. Thus, the challenge of understanding their complex physical structure must rely on observational proxies and physically motivated modelling. Since AGN are powered by gravitational accretion, the emission regions are expected to be axisymmetric. This also suggests that the accretion disk will be opaque in the inner regions, and therefore only the forward side of the emission region will be observed. Therefore, unravelling the detailed physics will be greatly simplified if an accurate measure of the viewing angle of the observer can be determined.

In this work, we have made significant progress in determining the viewing angle to individual AGN. We have:

- Found a strong correlation between two easily measurable parameters in the ultraviolet emission spectrum of AGN. Specifically, we have chosen a high ionisation line, C IV, and a lower ionisation line, Mg II, and shown that they must be emitted in different parts of a disk-wind. The measured physical parameters are the velocity shifts and line widths, both of which might be expected to depend on orientation.
- Established that qualitatively, the correlation is consistent with an explanation due to orientation angle. Quasars viewed at close to face-on angle are predicted to exhibit large blueshifts and line width ratio of C IV and Mg II. In contrast, the blueshifts and relative ratio of the line widths decrease as the inclination is towards edge-on.
- Compared this measurement with a few known orientation indicators in the literature. In particular, the results for LoBALs is strongly consistent, but other indicators are broadly consistent with our predictions.
- Modelled the correlation using a simple disk-wind, suggesting that a detailed exploration of the model parameters will further refine the structure of the physical models for the broad emission line regions of AGN.

AGN, particularly at high redshift, have a profound impact on galaxy evolution and as tracers of cosmography. If a standard physical model for the observables of an AGN can be determined, then these objects might realise their potential for cosmological studies.

CHAPTER 7

Black Hole Mass Estimation

This chapter is based on the publications:

- *Yong, S. Y., Webster, R. L., & King, A. L. (2016). Black Hole Mass Estimation: How Good is the Virial Estimate?* PASA, *33, e009. ADS: 2016PASA...33...9Y. doi: 10.1017/pasa.2016.8*
- *Yong, S. Y. & Webster, R. L. (2019). Black hole mass estimation: Modelling the biases. In* 2019 6th International Conference on Space Science and Communication (IconSpace) *(pp. 139–143). doi: 10.1109/IconSpace.2019.8905923*

Abstract

Black hole mass is a key factor in determining how a black hole interacts with its environment. However, the determination of black hole masses at high redshifts depends on secondary mass estimators, which are based on empirical relationships and broad approximations. A dynamical disk wind BLR model of AGN is built in order to test the impact of different BLR geometries and inclination angles on the black hole mass estimation. Monte Carlo simulations of the disk wind model are constructed to recover the virial scale factor, f, at various inclination angles. The resulting f values strongly correlate with inclination angle, with large f values associated with small inclination angles (close to face-on) and small f values with large inclination angles (close to edge-on).

The recovered f factors are consistent with previously determined f values, found from empirical relationships. Setting f as a constant may introduce a bias into virial black hole mass estimates for a large sample of AGN. However, the extent of the bias depends on the line width characterisation (e.g., FWHM or line dispersion). Masses estimated using f_{FWHM} tend to be biased towards larger masses, but this can generally be corrected by calibrating for the width or shape of the emission line.

7.1 Background

BHs are widely believed to be located at the centre of most galaxies, both active and quiescent galaxies (Kormendy & Richstone 1995; Richstone 1998; Ferrarese & Ford 2005; Kormendy & Ho 2013). Relationships have long been observed between the mass of the black hole and the properties of the host-galaxy, namely stellar velocity dispersion (the $M_{\rm BH}$–σ_* relation; Ferrarese & Merritt 2000; Gültekin et al. 2009; McConnell & Ma 2013), light concentration (the $M_{\rm BH}$–C_{r_c} relation; Graham et al. 2001), bulge luminosity and bulge stellar mass (the $M_{\rm BH}$–$L_{\rm bulge}$ and $M_{\rm BH}$–$M_{\rm bulge}$ relations; Magorrian et al. 1998; Marconi & Hunt 2003; McConnell & Ma 2013). Despite this, the origin of these correlations and the role of the central BH in galaxy evolution, are still not well understood (Silk & Rees 1998; King 2003, 2005; Di Matteo et al. 2005; Murray et al. 2005; Di Matteo et al. 2008; Park et al. 2015). The properties of a BH can be related to its mass, $M_{\rm BH}$, and to understand the interplay between the BH and its host galaxy, we require precise and accurate $M_{\rm BH}$ measurements over a broad range of galaxy properties and cosmic time.

We attempt to recover a theoretical prediction of the f factor in the BH mass estimation based on a dynamical disk wind model of the BLR and investigate the impact of orientation on the value of f. The overview of this chapter is as follows. The different methods used to measure the BH mass and the associated uncertainty are reviewed in § 7.1. In § 7.2, we describe our approach in modelling the disk wind. The results of the simulations are presented in § 7.3. In § 7.4, we discuss our findings and compare them to previous studies. The conclusions are given in § 7.5.

7.1.1 Methods of BH Mass Measurement

There are two methods of BH mass measurement. The BH masses estimated using the aforementioned relations between the $M_{\rm BH}$ and host-galaxy attributes are examples of indirect method. In general, an indirect method is based on established observables related to the mass of the BH. Other examples are fundamental plane and AGN scaling correlations, e.g., between the size of BLR and luminosity of AGN, which will be discussed later. The main advantage of this method is that it can be applied to large samples, albeit less accurately for individual sources. On the other hand, the direct method measures the value of $M_{\rm BH}$ directly using the dynamics of stars or gas in close proximity to the BH (Ferrarese & Ford 2005; McConnell & Ma 2013). However, this method is limited to the local universe due to the high spatial resolution required. Examples of this method are stellar and gas dynamics, megamasers, and RM.

Additionally, depending on the number of assumptions and model involved, the methods are categorised into primary, secondary, and tertiary, where the primary estimator contains the fewest assumptions. Stellar dynamics, gas dynamics, and megamasers are grouped under primary method since they are not based on other results. The RM technique is currently a secondary direct method as it requires another primary method for calibration. This will be reviewed in the next section. A flowchart of different BH mass calibration methods from Peterson (2010) is displayed in Fig. 7.1.

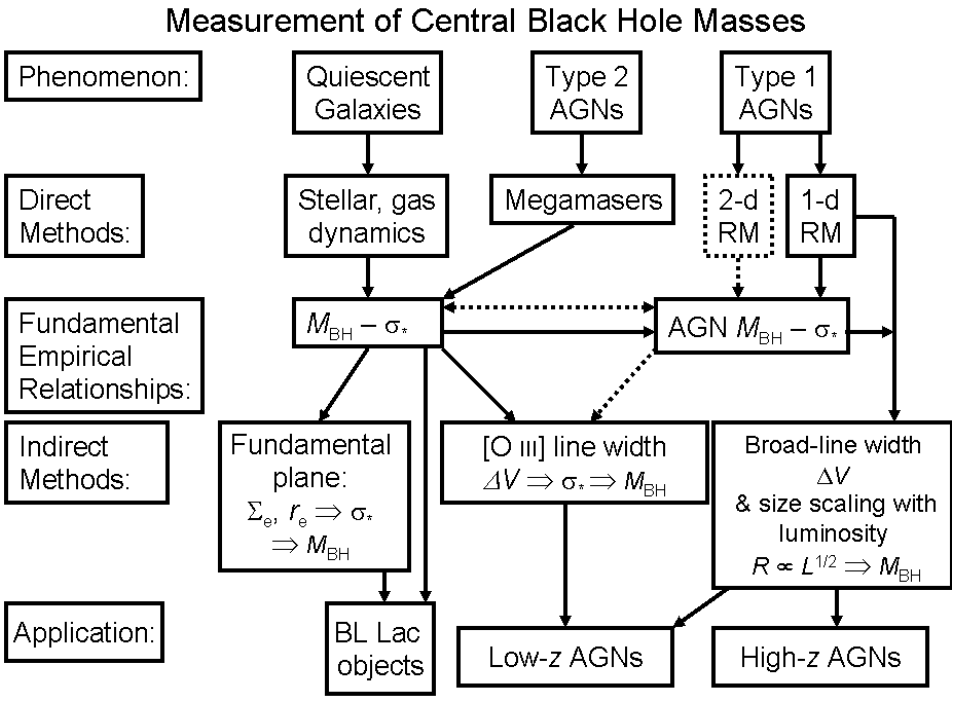

Figure 7.1: Flow chart of black hole mass measurements methods from Peterson (2010).

7.1.1.1 Reverberation Mapping BH Mass

RM of AGN provide an alternative method of BH estimation at high cosmological distance, with calibration via $M_{\rm BH}$–σ_* relation. Variable continuum emission originating from the accretion disk is absorbed by nearby gas deep within the gravitational potential of the BH (broad line region). The BLR gas reprocesses this radiation and emits Doppler broadened emission-lines. The corresponding emission-line flux is observed to vary in response to the continuum flux in a roughly linear fashion with a time delay, τ. This time delay corresponds to the light travel time to the mean responsivity-weighted distance to the BLR from the accretion disk. RM is based on the assumption that there is a simple, though not necessarily linear, relationship between the observed continuum and the ionising continuum (Peterson 1993). In general, the emission line response has been

found to be approximately linear in fashion; however, non-linear responses have been observed in NGC7469 (Peterson et al. 2014), NGC5548 (De Rosa et al. 2015) during the second half of the campaign, and J080131 (Du et al. 2015). The mechanism causing the observed non-linear response in these objects is not well understood.

Under the assumption that the gas in the BLR is virialised and its motion is dominated by the gravitational field of the central BH, the mass of the BH is (Peterson & Wandel 1999)

$$M_{\rm BH} = f\left(\frac{\Delta V^2 R}{G}\right) = f M_{\rm vir}, \tag{7.1}$$

where $R = c\tau$ is the radius of the emitting line, c is the speed of light, and G is the gravitational constant. The velocity dispersion, denoted by ΔV, is determined from the width of an individual broad emission line by measuring the FWHM or the line dispersion, $\sigma_{\rm line}$, and f is the virial factor that links the line-of-sight virial product, $M_{\rm vir}$, to the true BH mass.

7.1.1.2 Radius–Luminosity Relation

RM has yielded masses for approximately ~ 50 AGN (Bentz & Katz 2015) and the values of R have been found to exhibit a power law relationship with the AGN continuum luminosity, λL_λ (Kaspi et al. 2000; Bentz et al. 2009, 2013), as predicted from simple photoionisation physics (Davidson 1972; Krolik & McKee 1978). The empirical relation has the form of $R \propto L^a$ with different value of a depending on which emission line is used. It is formally known as the BLR radius–luminosity (R–L) relationship (e.g., Kaspi et al. 2007; Bentz et al. 2009).

Assuming that the SEDs and BLR density distribution are independent of the luminosity, the value of $a = 0.5$ is expected based on photoionisation calculation. The ionisation parameter, U, can be expressed as (Osterbrock & Ferland 2006):

$$U = \frac{1}{4\pi R^2 c n_{\rm H}} \int_{\nu_0}^{\infty} \frac{L_\nu}{h\nu}\,{\rm d}\nu = \frac{Q({\rm H})}{4\pi R^2 c n_{\rm H}}, \tag{7.2}$$

where R is the distance from the central source, $n_{\rm H}$ is hydrogen number density, ν_0 is the threshold frequency for ionisation of hydrogen, L_ν is the source luminosity per unit frequency interval, and $Q({\rm H}) \propto L$ is the number of ionising photons for hydrogen. Then, the radius of the BLR follows the square root of the ionising luminosity, $R \propto L^{0.5}$ (e.g., Netzer 1990). This is also anticipated if the BLR size is reflected by the dust sublimation radius (Netzer & Laor 1993). However, there have been observational indications of the SED dependency on the luminosity, and hence one assumption is not validated (e.g., Mushotzky & Wandel 1989; Zheng & Malkan 1993; Puchnarewicz et al. 1996).

7.1.1.3 Single-Epoch Virial BH Mass Estimator

The strong R–L correlation is the basis of single-epoch virial BH mass estimators ('virial BH mass estimators' for short), which estimate the mass of the BH using a single-epoch of spectroscopy (e.g., Laor 1998; Wandel et al. 1999; McLure & Jarvis 2002; Vestergaard & Peterson 2006). The single-epoch mass estimation method is routinely used to estimate BH masses (e.g., Vestergaard et al. 2008; Vestergaard & Osmer 2009; Willott et al. 2010; Schulze & Wisotzki 2010; Mortlock et al. 2011; Trump et al. 2011; Shen & Liu 2012; Kelly & Shen 2013), and allows the black hole–galaxy correlations to be studied using large samples of galaxies. Using FWHM as the velocity dispersion, the BH mass scaling is then $M_{\rm vir} = M_{\rm vir}(L, {\rm FWHM}) \propto L^a {\rm FWHM}^2$, which can be rewritten as (e.g., Vestergaard & Peterson 2006)

$$\log\left(\frac{M_{\rm vir}}{M_\odot}\right) = a\log\left(\frac{\lambda L_\lambda}{10^{44}\,{\rm erg\,s^{-1}}}\right) + 2\log\left(\frac{\rm FWHM}{\rm km\,s^{-1}}\right) + b, \tag{7.3}$$

where L_λ is the monochromatic luminosity at wavelength λ and (a, b) are the coefficients empirically estimated using local reverberation-mapped AGN. A list of commonly adopted cross-calibrated recipes is provided by McGill et al. (2008).

The Balmer line Hβ with the optical continuum luminosity at 5100 Å, L_{5100}, was originally used in the R–L relation and arguably the most reliable estimator of the BLR size and single-epoch BH mass (e.g., Kaspi et al. 2000; Bentz et al. 2009). Subsequently, other emission lines, including Mg II and C IV, and their corresponding continuum luminosities at 3000 Å and 1350 Å, can also be utilised in the calibration. Theoretically as derived previously, the quantity $a = 0.5$ will also recover the virial assumption. Some studies are able to obtain (a, b) of $(0.50, 0.910)$ for Hβ (Vestergaard & Peterson 2006) and $(0.50, 0.860)$ for Mg II (Vestergaard & Osmer 2009). Though, it often differs slightly from the ideal case, for example, $(0.61, 0.672)$ from McLure & Dunlop (2004) for Hβ, $(0.62, 0.505), (0.62, 0.740)$ from McLure & Dunlop (2004) and Shen et al. (2011) for Mg II, and $(0.53, 0.660)$ from Vestergaard & Peterson (2006) for C IV.

A number of studies has also considered alternative parameters to be used for the line width and luminosity in Eq. (7.3). Instead of the FWHM, it has been suggested that the line dispersion $\sigma_{\rm line}$ is more representative of the emission line width and yields a less biased estimate (e.g., Peterson et al. 2004; Collin et al. 2006). Another indicator for the line width, using the mean absolute deviation, has been found to be a better measure of the velocity width, especially if the quality of the data is poor, as it is less sensitive to the core component and the high velocity wings of the line profile (Denney et al. 2016; Park et al. 2017).

Sometimes using the continuum luminosity is not practical since the continuum might be too faint or contaminated by host galaxy starlight or relativistic jet emissions of RL AGN. In this case, the line luminosity of the BELs, such as those based on recombination line like Hβ (Osterbrock & Ferland 2006), can be employed to approximate

the BLR size and BH mass (e.g., Wu et al. 2004; Greene & Ho 2005; Shen et al. 2011; Shen & Liu 2012). Various studies have been conducted to examine the correlation between the luminosities of different lines and the continuum luminosity at 5100 Å. Using samples with minimal contamination from host galaxy light, Shen & Liu (2012) showed that $L_{\mathrm{H}\beta}$ and $L_{\mathrm{Mg\,II}}$ are comparable to that of L_{5100}, while $L_{\mathrm{C\,IV}}$ and $L_{\mathrm{C\,III]}}$ are poorly constrained with L_{5100}. One reason is due to the fact that HILs and LILs differ in ionisation potential and so we might expect them to exhibit dissimilar properties and behave differently (Sulentic et al. 2000). Alternatively, other proxies for ionising luminosity include those using fluxes at hard X-ray, narrow [O III] λ5007, and narrow [O IV] λ25.8 μm (Greene et al. 2010), though their reliabilities are still debatable due to lack of calibration.

7.1.2 Sources of Uncertainty

Despite the widespread use of the single-epoch method, it is not immune to random and systematic uncertainties (e.g., Vestergaard & Peterson 2006; Collin et al. 2006; McGill et al. 2008; Shen et al. 2008; Denney et al. 2009; Richards et al. 2011; Denney 2012; Park et al. 2012b). Some common sources of uncertainty are mentioned below.

Firstly, the dominant portion of error is due to the insufficient information about the BLR, which is integrated into the unknown virial factor f. The uncertainty in the single-epoch BH mass induced from the f factor is one of the main subjects of this chapter and will be discussed in detail in the next section. Secondly, the R–L relationship used to deduce the BLR size is prone to intrinsic scatter. Using reverberation-mapped AGN, the scatter in the slope of the R–L relation is approximated to be 34%–40% after accounting for the contribution from the host-galaxy starlight (Bentz et al. 2009).

Thirdly, there might be some systematic differences in the line width measurements between the single-epoch spectra and root-mean-square (rms) spectra used in RM studies. The widths of Hβ line profile computed in mean spectra for single-epoch mass estimates are often broader compared to those in rms spectra (e.g., Sergeev et al. 1999; Shapovalova et al. 2004; Collin et al. 2006; Denney et al. 2009; Park et al. 2012b). Fourthly, variability in the line profile due to the changes in continuum luminosity and line width can also induce a small scatter of roughly $\sim 25\%$ or ~ 0.1 dex to the single-epoch masses (e.g., Wilhite et al. 2007; Denney et al. 2009; Park et al. 2012b). This is because the luminosity variability amplitude only fluctuates slightly ~ 0.1–0.2 magnitude over an order of few years timescales (e.g., Sesar et al. 2007; MacLeod et al. 2010, 2012).

Lastly, the selected AGN samples in RM campaigns are likely to suffer from selection bias. The samples are usually heterogeneous and do not encompass the whole AGN population, whereby luminous and/or high redshift objects are under-sampled (e.g., Richards et al. 2011). Therefore, a proper calibration of the BH mass estimator for

single-epoch method is required to reduce the systematic and statistical errors. This will ensure that the mass estimated remains accurate and unbiased.

7.1.2.1 The Virial Factor f

Several different virial BH mass estimators have been developed in the last decade, based on different line width characterisations and different lines. The FWHM of the Hβ, Mg II, and C IV emission lines and a set value of f, are commonly used. Due to the widespread use of virial BH mass estimators, it is critical to fully understand the variation expected in f within the AGN population.

The value of the f factor depends on the structure, kinematics, dynamics, and orientation of the BLR with respect to the observer. Its value is expected to be different for every AGN. Nevertheless, it is a common practice to adopt a single f factor value for all AGN, calibrated from the local RM sample under the assumption that the $M_{\rm BH}$–σ_* relation is consistent between quiescent and active galaxies (Gebhardt et al. 2000; Ferrarese et al. 2001).

Since the primary assumption in the virial mass determination is that the dynamics of the BLR is regulated by the central BH gravity, other forces, like radiation pressure, are not taken into consideration. Marconi et al. (2008) accounted for the possible role of radiation pressure by including an additional term that depends on the source luminosity and column density into the classic virial calculation. They demonstrated that the scatter between virial BH mass for single-epoch spectra and RM samples is substantially reduced from 0.4 to 0.2 dex. They also stated that the failure to consider radiation pressure will consequently underestimate the BH mass, though this claim is challenged by Netzer & Marziani (2010).

It has been established that BLR is not isotropic, and hence the velocity distribution of the BEL is likely to be affected by orientation effects (e.g., Runnoe et al. 2013b; Shen & Ho 2014; Brotherton et al. 2015b). In particular, a flattened disk BLR geometry will induce an inclination dependence on the width of the line profile (e.g., Wills & Browne 1986; Jarvis & McLure 2006; Decarli et al. 2008). This interpretation is based on the Hβ line, where they reported possible correlation between Hβ FWHM and radio core dominance, R. The parameter R, defined as the rest frame ratio of 5 GHz radio core to extended flux density, is widely used as an orientation indicator (Orr & Browne 1982). Essentially, it is linked to the viewing angle of radio jet axis relative to the line-of-sight in relativistic beaming model for radio objects.

The value of f also depends on line width characterisation (e.g., FWHM or $\sigma_{\rm line}$) and whether the mean or rms spectrum is used for the line width measurement. Recent measurements of $\langle f \rangle$ based on rms spectra and $\sigma_{\rm line}$ vary between $\langle f_\sigma \rangle = 2.8^{+0.7}_{-0.5}$ (Graham et al. 2011) and $\langle f_\sigma \rangle = 5.5 \pm 1.8$ (Onken et al. 2004), with most $\langle f_\sigma \rangle$ values lying within the range of $\langle f_\sigma \rangle \sim$ 4–6 (Collin et al. 2006; Park et al. 2012a; Grier 2013; Woo et al.

2013; Pancoast et al. 2014; Woo et al. 2015). The $\langle f_\sigma \rangle$ obtained from mean spectra is 3.85 ± 1.15 (Collin et al. 2006). On the other hand, the mean $f_{\rm FWHM}$ measured using rms spectra were found to be $\langle f_{\rm FWHM} \rangle = 1.12^{+0.36}_{-0.27}$ by Woo et al. (2015) and $\langle f_{\rm FWHM} \rangle = 1.44 \pm 0.49$ by Collin et al. (2006). The $\langle f_{\rm FWHM} \rangle$ using mean spectra is 1.17 ± 0.50 (Collin et al. 2006). The calibration of the f factor makes RM a secondary mass estimation method. The typical uncertainties in reverberation masses resulting from the uncertainty in f is ~ 0.43 dex (Woo et al. 2010), due to the intrinsic scatter in the $M_{\rm BH}$–σ_* relation.

7.1.3 Bias in Emission Line Estimator

The underlying assumption for the virial mass estimation is that the significant contribution of the BEL width comes from the virialised bulk motion of the line emitting gas. In essence, LILs provide reasonable estimates as they are primarily dominated by the virial component. This is reflected by the roughly symmetric line profile shape with velocity shifts close to the systemic shift of quasars (e.g., Hewett & Wild 2010), indicating that the line is likely to be governed by gravity due to the virialised dynamics associated with the BH.

Generally, different emission lines are employed to derive the single-epoch BH mass depending on the range of wavelength regime. Since the BH scaling relationship is dependent on the broad line used, it is important to ensure consistent scaling formalisms and measurement procedures are applied throughout the calibration process (e.g., Shen et al. 2008; Assef et al. 2011; Denney 2012; Shen & Liu 2012). It has been noted that for low redshift of $z \sim 0.7$, single-epoch method using Hβ Balmer line is the standard line of choice and is currently the best approach in virial BH masses calibration, in a sense that extensive monitoring of RM samples is done based on this line (e.g., Kaspi et al. 2000, 2005; Bentz et al. 2009). In a situation where the Hβ line is inaccessible, another broad Balmer line, Hα, can serve as a substitute since its line measurements correlate well with the FWHM of Hβ and L_{5100} (Greene & Ho 2005).

On the other hand, the Mg II LIL has been used for intermediate redshift of $z \sim 1.9$ (McLure & Jarvis 2002). The comparison between the line width of Mg II and Hβ shows agreement, but the relationship is not directly one-to-one with shallower slope than unity relative to the Hβ line width (e.g., Salviander et al. 2007; McGill et al. 2008; Shen et al. 2008; Wang et al. 2009; Shen & Liu 2012). Although some discrepancies have been reported, possibly related to Eddington ratio (Kollmeier et al. 2006; Onken & Kollmeier 2008), most virial BH masses determined using Mg II line are found to be fairly consistent with those using Hβ line (e.g., McLure & Dunlop 2004; Shen et al. 2008; Wang et al. 2009; Rafiee & Hall 2011; Shen & Liu 2012; Marziani et al. 2013; Woo et al. 2018; Bahk et al. 2019).

Despite the usefulness of LILs to estimate BH masses, these lines are only measurable for low redshift. In contrast, using the C IV line has an advantage of being observable at even higher redshifts, $z \gtrsim 2$ (Vestergaard 2002). Yet, the accuracy of the BH mass scaling for this line has been questioned, as there are contradictions in the reported effectiveness of C IV-based BH estimator. While some studies claimed that the BH masses evaluated using C IV and Hβ are in agreement with one another (e.g., Warner et al. 2003; Vestergaard & Peterson 2006; Kelly & Bechtold 2007), others are more skeptical. Several studies found a weak relationship between C IV and Hβ line widths, and consequently a large scatter when comparing their estimated BH masses (e.g., Baskin & Laor 2005; Sulentic et al. 2007; Shen & Liu 2012; Trakhtenbrot & Netzer 2012).

The fact that HIL C IV line is typically asymmetric and blueshifted from the rest frame of the quasar (e.g., Gaskell 1982), may result in a poorer fit to the virial model. As the shift in C IV line is presumably linked to the non-virial component of the system probably due to non-gravitational force, such as from outflows (e.g., Leighly 2004; Shen et al. 2008; Richards et al. 2011; Denney 2012), the BH mass calibrated might be unreliable (e.g., Sulentic et al. 2007; Park et al. 2013; Mejía-Restrepo et al. 2016; Coatman et al. 2017; Marziani et al. 2019). There are also other aspects of the C IV line that raise concerns, such as the Baldwin effect, a possible narrow line component, and a strong broad absorption feature (see e.g., Denney 2012).

Several recommendations have been suggested for an unbiased C IV-based BH mass estimator. Using samples of lensed quasars, Assef et al. (2011) recommended a prescription to mitigate the BH mass residuals by correcting the ratio of UV to optical continuum luminosities (colour dependence). Additionally, Denney (2012) discovered that C IV emission line profiles from the C IV reverberation-mapped sources exhibit two components: the variable and non-variable parts. Denney (2012) deduced that the latter component is the main cause of the scatter in BH mass calibration and suggested an empirical correction with parameterisation given by the ratio of FWHM to line dispersion (shape parameter). Following Wang et al. (2009) approach for Mg II-based BH mass scaling, Park et al. (2013) treated the coefficient for the line width in the C IV-based mass calibration as a free parameter with best fit values of 1.74 using $\sigma_{\rm line}$ and 0.56 using FWHM. The fitted values are much lower than the conventional value of 2 and effectively lessen the scaling dependence of the BH mass on the line width. Runnoe et al. (2013a) and Brotherton et al. (2015a) applied the peak flux ratio of Si IV+O IV] at 1400 Å to C IV to account for the contribution from the non-virialised component of the C IV emission line. Shen & Liu (2012) and Coatman et al. (2016, 2017) corrected for the C IV bias caused by the C IV blueshift.

7.2 Methodology

Following the disk-wind modelling approach presented in § 3.2 with constraints on the input parameters for a wide wind opening angle as given in Table 6.4, an extension of our model into practical application is to retrieve the f factors and examine the bias on the BH mass estimation. We further incorporate this in our simulation.

For each 'wind zone' line profile, the FWHM and $\sigma_{\rm line}$ values are measured and the corresponding f factor is calculated using Eq. (7.1). As Hβ is typically used to calculate the BH mass in RM studies (Collin et al. 2006; Park et al. 2012b; Grier 2013; Woo et al. 2013; Pancoast et al. 2014; Woo et al. 2015), we concentrate our analysis on a wind zone close to the base of the wind and towards the outer edge of the BLR, corresponding to expectations for Hβ emission. Zone [0, 3] is chosen in this case. We also calculate the probability of measuring a given BH mass based on a fixed f value from the literature using the cumulative probability of viewing a quasar at any given inclination angle, i, of $F(i) = 1 - \cos(i)$, with $0° \leq i \leq 90°$.

The response of an individual emission line to changes in the continuum flux is expected to vary depending on where the line is emitted within the disk wind and the luminosity of the AGN (due to differences in density and ionising flux; Korista & Goad 2000, 2004). Without further assumptions about the degree of continuum variability and luminosity and further photoionisation modelling, it becomes impossible to model rms spectra. Therefore, we only compare our generated spectra with the f factors measured using the mean spectra.

7.3 Results

7.3.1 f Factor vs. Inclination for All Zones

The range of f factors found for the wide angle disk-wind model at various inclination angles and for each zone are presented in Table 7.1. The range of f factors found extend well beyond the spread prescribed in the empirically determined $\langle f \rangle$ values of Collin et al. (2006).

The f value as a function of inclination angle for every wind zone is illustrated in Fig. 7.2. The zones provide some indication of the f values for different emission lines expected to be emitted from different locations in the wind. The recovered values of f using FWHM and σ for each layer in the wind zones of roughly the same radius ([0, b]–[3, b]) are generally comparable. The wind is dominated by virialised rotational dynamics for wind zones close to the base of the wind. For wind zones at large r and small z (e.g., [0, 3]), f has a steeper trend with inclination and its value is slightly larger than the f factor obtained in wind zones closer to the ionisation source (e.g., [0, 0]).

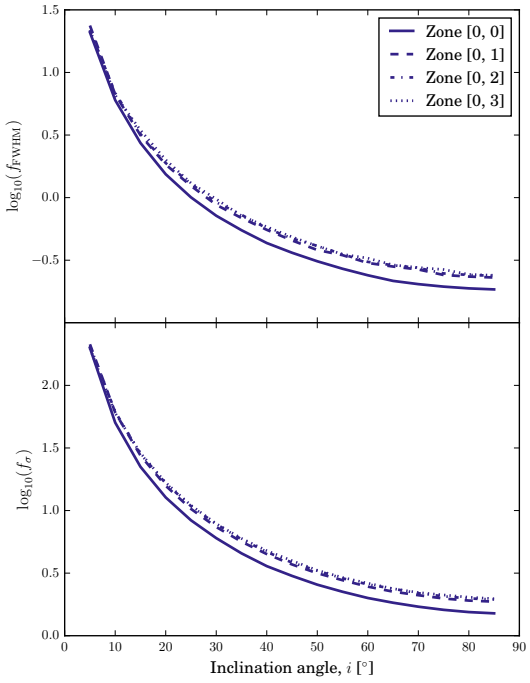

(a) Zones [0, b]

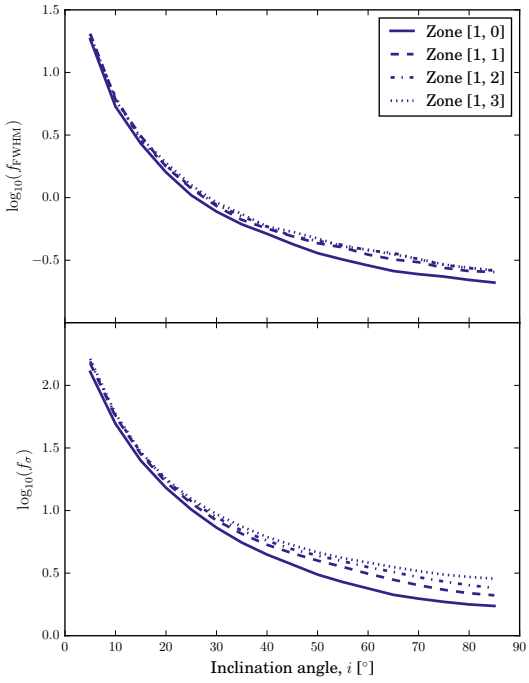

(b) Zones [1, b]

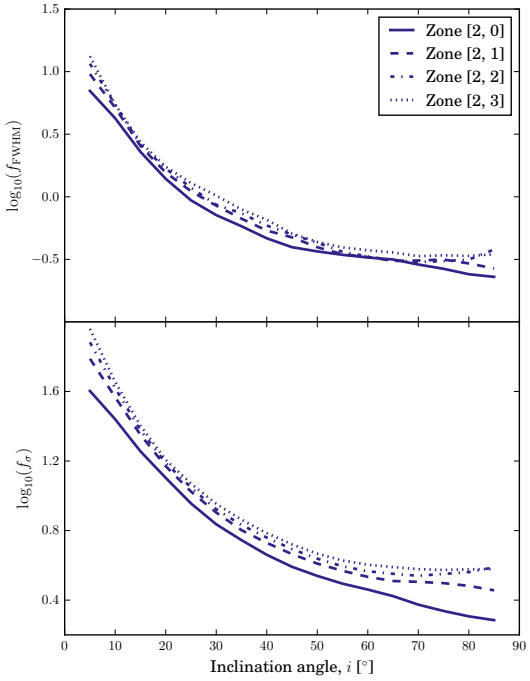

(c) Zones [2, b]

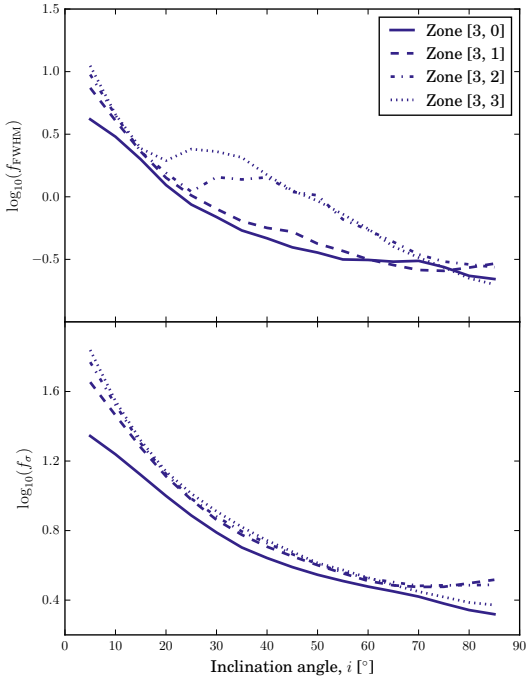

(d) Zones [3, b]

Figure 7.2: Plot of f factors against inclination angle for all wind zones.

Table 7.1: Values of f for all zones.

Zone	$f_{\rm FWHM}$			f_σ		
	$i = 5°$	$i = 45°$	$i = 85°$	$i = 5°$	$i = 45°$	$i = 85°$
[0, 0]	20.90	0.36	0.18	199.37	3.01	1.51
[1, 0]	18.48	0.43	0.21	128.39	3.70	1.73
[2, 0]	7.01	0.40	0.23	40.09	3.90	1.93
[3, 0]	4.16	0.39	0.22	22.09	3.89	2.08
[0, 1]	23.71	0.45	0.23	213.03	3.71	1.87
[1, 1]	20.41	0.49	0.25	149.81	4.56	2.10
[2, 1]	9.55	0.47	0.27	61.44	4.62	2.86
[3, 1]	7.42	0.53	0.29	45.05	4.49	3.29
[0, 2]	21.71	0.47	0.24	207.15	3.84	1.95
[1, 2]	18.54	0.49	0.26	155.31	4.91	2.41
[2, 2]	11.56	0.50	0.38	76.34	4.94	3.88
[3, 2]	9.47	1.10	0.27	58.74	4.62	3.08
[0, 3]	21.77	0.49	0.24[a]	197.69	3.98	1.97[b]
[1, 3]	20.06	0.53	0.26	162.87	5.30	2.86
[2, 3]	13.26	0.51	0.35	91.24	5.25	3.79
[3, 3]	11.15	1.13	0.20	68.96	4.77	2.35

[a] Compare with $\langle f_{\rm FWHM(H\beta)} \rangle = 1.17 \pm 0.50$ (or $\log_{10}\langle f_{\rm FWHM(H\beta)} \rangle = 0.07^{+0.15}_{-0.24}$) from Collin et al. (2006).
[b] Compare with $\langle f_{\sigma(\rm H\beta)} \rangle = 3.85 \pm 1.15$ (or $\log_{10}\langle f_{\sigma(\rm H\beta)} \rangle = 0.59^{+0.11}_{-0.15}$) from Collin et al. (2006).

Based on the Table 7.1, it can be seen that the f values in wind zones of the same radial streamline ([a, 0]–[a, 3]) have increasing and then decreasing trends as the zone increases radially outwards. Since the initial positions of the streamlines, r_0, are contained within zone [0, b], the rotational velocity in the outer zones (e.g., [1, b]) rapidly diverges from Keplerian motion and quickly becomes smaller with larger r, in accordance with the conservation of angular momentum (see Eq. (3.6)). This results in the much larger f values found in these zones compared with zone [0, b]. However, as the poloidal velocity gradually increases and becomes dominant with increasing poloidal distance (that is, large r and z; e.g., zone [3, 0]), the line width broadens and the true value of f decreases.

As the inclination angle is closer to edge-on, the line width is expected to be broader due to the increasing contribution from the Keplerian rotational velocity component to the projected line-of-sight velocity, which yields a lower f value. However, there are a few cases where the f measurements using FWHM increased drastically at some i and decreased unevenly later at high i, as shown in Fig. 7.2c and Fig. 7.2d. This unexpected trend arises as a result of the artifact created on the line profile, and subsequently the half maximum chosen. Further discussion on this issue is presented in § 7.4.3.2.

7.3.2 f Factor vs. Inclination for Hβ and Comparison with Literature

The distribution of f factors with inclination angle for the equivalent Hβ wind zone [0, 3], in both models, is shown in Fig. 7.3. The agreement between the empirically determined f value from Collin et al. (2006) and our predictions varies between the two velocity dispersion characterisations. The Collin et al. (2006) $f_{\rm FWHM}$ measurement coincides with the low range viewing angle (around 20° to 35°) predictions using our disk wind models. Meanwhile, the Collin et al. (2006) f_{σ} measurement was consistent with our prediction for a middle inclination angle (around 40° to 60°) disk wind model.

Our predictions for f were found to cover a similar range of values and fit closely with those found using direct modelling estimates of Pancoast et al. (2014). Pancoast et al. (2014) estimated the f factor via direct BLR modelling using RM mean spectra of five Seyfert galaxies. Our predicted $f_{\rm FWHM}$ values also follow the general trend with inclination of the Pancoast et al. (2014) results.

A comparison with the $f_{\rm FWHM}$ values from Mangham et al. (2017) is also displayed in Fig. 7.3. Using radiative transfer and reverberation modelling, Mangham et al. (2017) determined the Hβ line response function for a rotating and outflowing disk-wind BLR model of a $10^9\,M_{\odot}$ quasar with a narrow wind opening angle of 70° to 82°. They then computed the values of f from the FWHM and the centroid of the emission line time delay for mean spectra. The steepness of the slope is comparable to that of our predictions; however, their results exhibit a slight systematic shift towards larger f values. They also anticipated an increase in f factor value as the i passes through the wind, a trait that is not identified in our models. The reason is because our simulations only create emission lines, whereas their synthetic quasar spectra also simulate the absorption and emission spectral features at which BALQ spectrum is produced when the line-of-sight is viewed anywhere within the wind opening angle. The narrower line width in their spectra is then a consequence of the absorption feature, whereby the blue wing of the line profile is suppressed, resulting in a higher f factor.

If a fixed value of f is assumed, and the potential bias of orientation is ignored, then a large sample of quasars of the same mass will produce a broad distribution of BHs masses. To quantify the effect of the orientation dependence of f on the BH mass estimation for a large sample of AGN, we calculated the differential probability of estimating a given BH mass using the fixed mean f value from Collin et al. (2006). The results are shown in Fig. 7.4. Since the differential probability increases with increasing inclination angle, the possibility of seeing closer to edge-on is higher, $P(i) = \sin(i)$. Therefore, broader profiles are more likely to be observed as they become dominant in edge-on viewing angle, and BH masses will generally be overestimated.

Regardless of the line width characterisations of $\langle f \rangle$, the recovered median BH masses are biased towards larger values. This is more pronounced when using FWHM and in general, the masses determined from FWHM tend to be overestimated for both disk

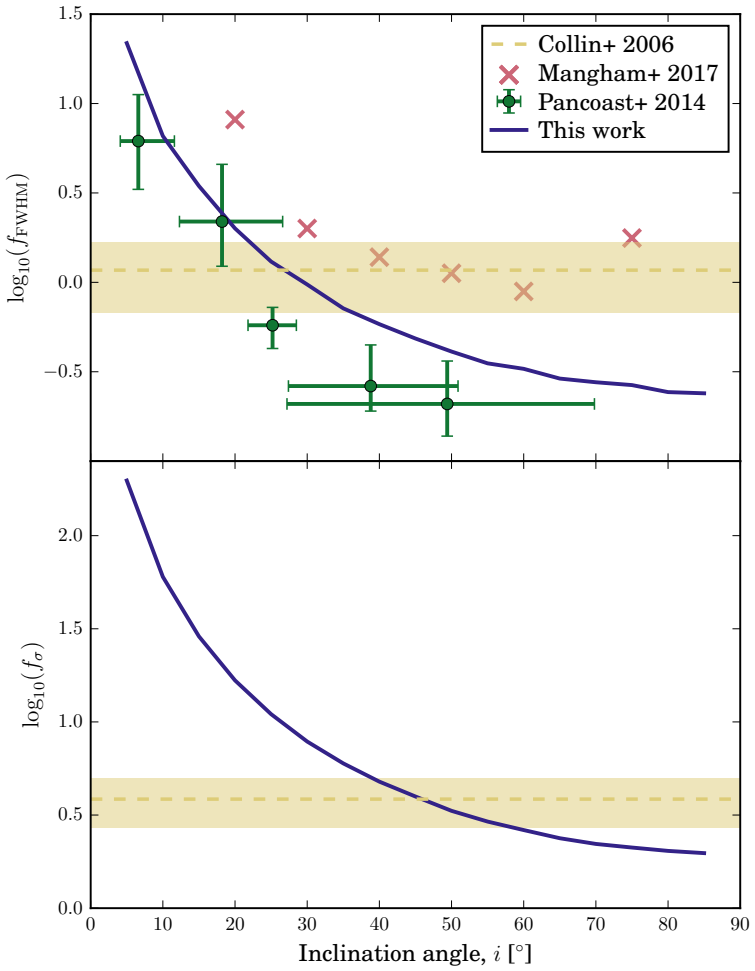

Figure 7.3: Plot of f factors against inclination angle for Hβ line characterised by emission from the [0, 3] location in the wind zone. *Upper*: Virial factor using FWHM, $f_{\rm FWHM}$. *Lower*: Virial factor using $\sigma_{\rm line}$, f_σ. The dashed lines are the mean f factor, $\langle f \rangle$, with uncertainties (shaded) from Collin et al. (2006). In the *upper* panel, the green circles with error bars show $f_{\rm FWHM(H\beta)}$ for individual quasars using direct modelling from Pancoast et al. (2014), while the red crosses show those from reverberation modelling of Hβ response function from Mangham et al. (2017).

wind geometries (Fig. 7.4, *left*). The median BH mass recovered is $3.56^{+0.45}_{-1.20} \times 10^9\,M_\odot$, approximately 3.5 times larger than the input BH mass of $10^9\,M_\odot$. The BH masses obtained from $\sigma_{\rm line}$ (Fig. 7.4, *right*) tend to be less biased and more accurate in general in comparison to those from FWHM. Despite that, the median recovered BH mass is $1.47^{+0.17}_{-0.49} \times 10^9\,M_\odot$, which is still bigger by a factor of about 1.5.

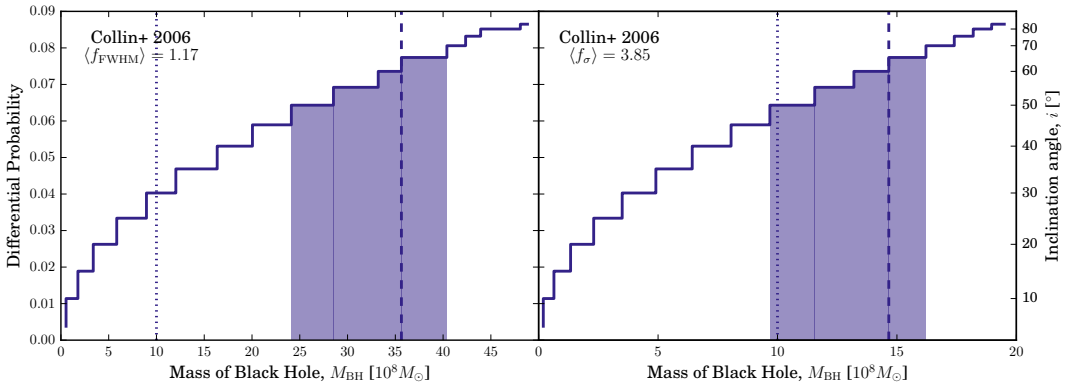

Figure 7.4: Differential probability associated with black hole mass for Hβ line characterised by emission from the [0, 3] location in the wind zone using $\langle f \rangle$ values for mean spectrum from Collin et al. (2006). In these models, the true black hole mass is $10^9\,M_\odot$ (dotted vertical line). The shaded region represents the $M_{\rm BH}$ within one sigma range of the median (dashed vertical line). *Left*: Mean f factor using FWHM of $\langle f_{\rm FWHM(H\beta)} \rangle = 1.17$. *Right*: Mean f factor using $\sigma_{\rm line}$ of $\langle f_{\sigma(\rm H\beta)} \rangle = 3.85$.

7.4 Discussion

Obtaining accurate BH mass measurements is crucial for understanding the role of BH growth in galaxy evolution. Therefore, it is important to understand how the geometry and inclination of the BLR, and the chosen line width measurement affect the accuracy in our mass estimation.

7.4.1 BLR Geometry and Inclination Dependence

The range of f values can be much greater than the prescribed spread in the literature value. Therefore, we need to be cautious when using a single value of f as it may bias mass estimates especially when the inclination angle of the AGN is low. The disk-wind model with wide wind opening angle establishes a relationship between the f factor and inclination angle (Fig. 7.3, *upper*), in agreement with Pancoast et al. (2014) and Mangham et al. (2017) despite a different modelling approach.

The BLR geometry, kinematics and the origin of the emission line also affects the true f value for individual AGN. This is evident from the differences in the f values calculated for the different disk wind models, the offset between the disk wind models, the differences in the f values for the different wind zones, the dynamical modelling results of Pancoast et al. (2014), and the reverberation modelling results of Mangham et al. (2017). The true nature of the BLR is unknown, and although some consistency is expected in the BLR, we currently cannot characterise the intrinsic distribution of f values for the whole AGN population. However, the differences in f due to the geometry and kinematics appears to be small compared to the effects of inclination angle. Also, our model assumes that the BLR is visible for all inclination angles. However, in the standard model of AGN, the BLR is believed to be obscured by a dusty torus. When this is taken into consideration, the estimate of the median BH mass (Fig. 7.4) is lowered as the probability of observing a closer to face-on AGN is increased.

Several studies have also investigated the scaling relationship between the f factor and inclination angle (Decarli et al. 2008; Kashi et al. 2013). Our predicted range of $f_{\rm FWHM}$ value is close to the analytical prediction of f from Decarli et al. (2008) for a geometrically thin disk model given by $f \approx 1/(2\sin i)^{1/2}$, although their slope is much flatter than those in our models. The Kashi et al. (2013) theoretical predictions based on a axisymmetric time dependent numerical simulation for a virialised line-driven disk wind model with $f \approx 1.32/\sin^2 i$, better matches our findings for f_σ.

7.4.2 Line Width Characterisation Dependence

The line widths are typically measured using the FWHM or $\sigma_{\rm line}$. As the FWHM is a zeroth moment of the line profile, the sensitivity to the line core is higher than it is in the line wings. In contrast, $\sigma_{\rm line}$ is a second moment of the line and is less affected by the line core. The $\sigma_{\rm line}$ from rms spectra is commonly employed as a proxy in calculating the BH mass since it has been argued that this provides a smaller bias and a better fit to the virial relation (Peterson et al. 2004; Collin et al. 2006; Peterson 2011; Denney et al. 2013).

We found that the BH mass estimated using the $\langle f_{\sigma({\rm H}\beta)}\rangle$ is closer to the input BH mass, in a sense that it is less overestimated, compared to $\langle f_{\rm FWHM({\rm H}\beta)}\rangle$ value from Collin et al. (2006) (Fig. 7.4). However, this discrepancy can be reduced when the shape corrections for $\langle f_{\rm FWHM({\rm H}\beta)}\rangle$, suggested by Collin et al. (2006), are taken into consideration. The median BH mass is $1.52^{+0.19}_{-0.51} \times 10^9\,M_\odot$ after the $\langle f_{\rm FWHM({\rm H}\beta)}\rangle$ shape correction (Equation 5; Collin et al. 2006), which is marginally consistent with the true mass and the mass estimate found using $\langle f_{\sigma({\rm H}\beta)}\rangle$.

However, there appears to be no significant change in the recovered median BH mass of $3.57^{+0.25}_{-1.19} \times 10^9\,M_\odot$ using the FWHM width correction (Equation 7; Collin et al. 2006). The reason is because the FWHMs of the generated line profiles are all less than

4000 km s^{-1}. Then according to the correction scheme (Collin et al. 2006), the corrected f values are always ≥ 1, with most of them larger than $\langle f_{\mathrm{FWHM(H}\beta)} \rangle = 1.17$ of (Collin et al. 2006). Essentially, those with broad FWHM need to be corrected to a small f to lessen the overestimated virial BH mass, and vice versa for narrow FWHM. Hence, the corrected median BH mass is still overestimated.

The implementation of the Collin et al. (2006) shape correction on the f_{FWHM} has effectively minimised the overestimation of the BH masses by more than half. Although the BH masses predicted are now comparable to those using $\langle f_{\sigma(\mathrm{H}\beta)} \rangle$, the recovered masses are still significantly larger the initial true mass. Hence, extensive care should be practiced whenever f is assumed to be a constant as this inevitably leads to a biased BH mass.

7.4.3 Caveats

7.4.3.1 Assumptions

It is worth mentioning several caveats in our modelling approach. The disk wind model simulations presented are simplifications of the complex BLR. The line driving mechanisms of the wind or photoionisation physics are not included in this model. We have also made major assumptions about the wind dynamics in our models, such as the local mass loss rate and the wind acceleration profile. The poloidal component might be random and will affect the HIL C IV more significantly than the LILs. The effects of these assumptions have not been investigated in this work. Future work will systematically search the parameter space in order to refine the models and to obtain a better fit with observations, and therefore predictions of BH mass.

7.4.3.2 Accuracy of the FWHM Measurements

Several examples of the FWHM line width measurements from generalised line profiles are illustrated in Fig. 7.5. It performs reasonably well in locating both ends of the line profile at half maximum. However, as can be seen, some of the FWHMs (orange) are not perfectly horizontal from the left to the right edge at half maximum. This slight imprecision is due to the algorithm selecting the nearest index of the half maximum. The FWHM calculated will be overestimated, inducing in a smaller f value. Despite the small offset, generally the algorithm is robust in a sense that it does well in detecting the maximum peak even in the presence of multiple peaks.

Clearly, the offset problem can be easily rectified by increasing number of points assigned to plot the convolved Gaussian line profile. As these points are used to locate the half maximums and the peak, these locations can be pinpointed more accurately. However, this solution is not without a flaw. The line profile will also be afflicted by more random noise, consequently needing a larger smoothing parameter for the Gaussian kernel width (see § 3.2.4). Hence, this idea is not implemented.

The shape of the line profiles affects the FWHM line width measurement. This is evident especially for emitting regions further out in wind zones [3, *b*] (see Fig. 7.2d *upper* panels). Due to the artifact of the line profile generated, there seems to be an increase in the recovered f factor for certain increases in i, instead of a smooth decrease in f with increasing i as shown in other zones. While the emission line profiles are single peaked, there appears to be a bump on either the red or blue side of the line profile particularly for low and mid angle range inclination angles as shown in Fig. 7.6. Consequently, the FWHM measurements are dependent on the positions of the half maximum and the bump. For example in Fig. 7.6a–Fig. 7.6b, the spurious increment in f at $i \approx 25°$ is because the right half maximum detected is slightly narrower compared to the previous iteration of inclination angle. Another defect is the sudden decrement in f with wider FWHM in some high inclinations. An example of this case is portrayed in Fig. 7.6c–Fig. 7.6d. In Fig. 7.6c, the bump is almost inconspicuous, however, in the subsequent i shown in Fig. 7.6d, the FWHM extends to the edge of the bump, which leads to the abrupt broadening of FWHM.

7.5 Summary

In this work, we have implemented a dynamical disk wind prescription to explore the influence of BLR orientation on the recovered black hole mass. The virial factor, f, which scales the line-of-sight virial product to the true black hole mass, is calculated using the disk wind model and compared to f values from the literature. It is evident that the black hole masses recovered depend on several factors: the BLR geometry and dynamics, the origin of the emission line, and the inclination angle. The observed trend with inclination angle agrees with the results of Pancoast et al. (2014) despite the different models investigated. Additionally, the spread in the model predicted f values significantly exceeds the spread prescribed for the empirically determined values of f from the literature. Therefore, using a single average value of f may bias the mass estimate for large AGN samples.

We also computed the black hole mass using literature values of f_σ and $f_{\rm FWHM}$ from Collin et al. (2006). The black hole mass is closer to the true mass if the velocity dispersion is measured using the $\sigma_{\rm line}$. Nevertheless, as suggested by Collin et al. (2006), the $f_{\rm FWHM}$ can be corrected to improve the mass estimate.

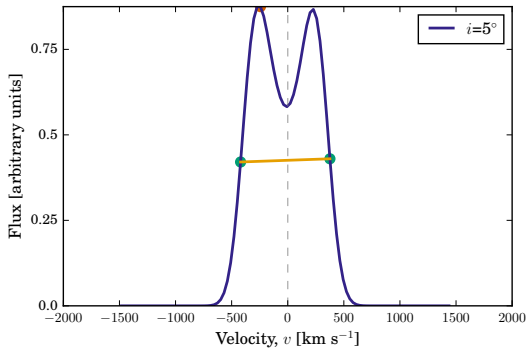

(a) Zone [0, 0]; $i = 5°$

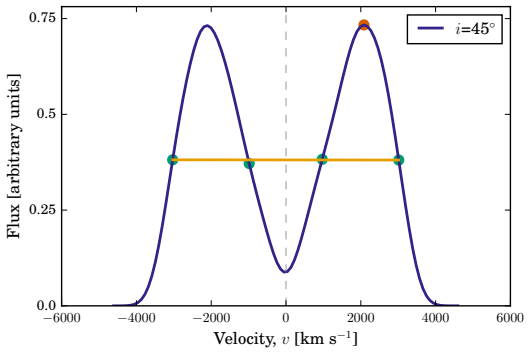

(b) Zone [0, 0]; $i = 45°$

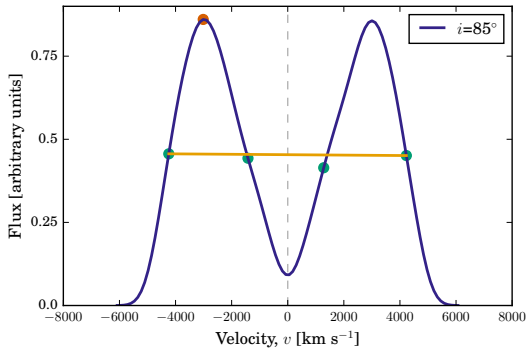

(c) Zone [0, 0]; $i = 85°$

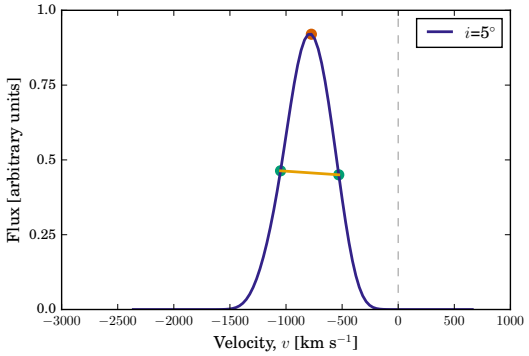

(d) Zone [3, 3]; $i = 5°$

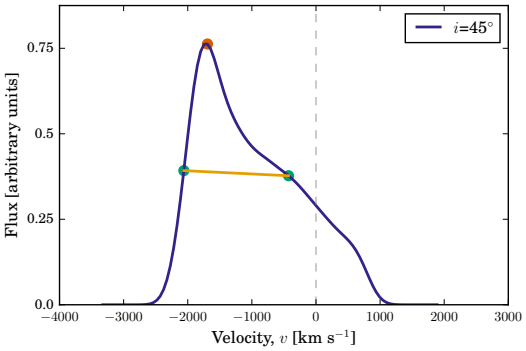

(e) Zone [3, 3]; $i = 45°$

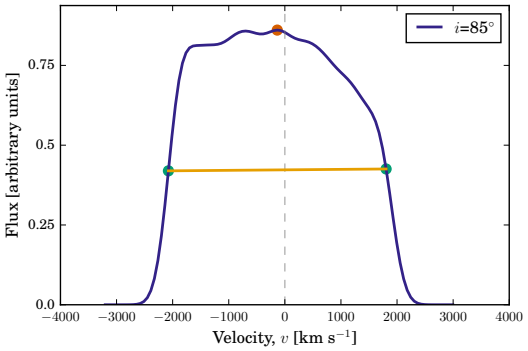

(f) Zone [3, 3]; $i = 85°$

Figure 7.5: Examples of line profile measurements using FWHM. The detected maximum and half maximum points are indicated by the vermillion and green dots respectively. The orange horizontal line is the FWHM measurement. The dashed grey vertical line shows the systemic centroid of the line.

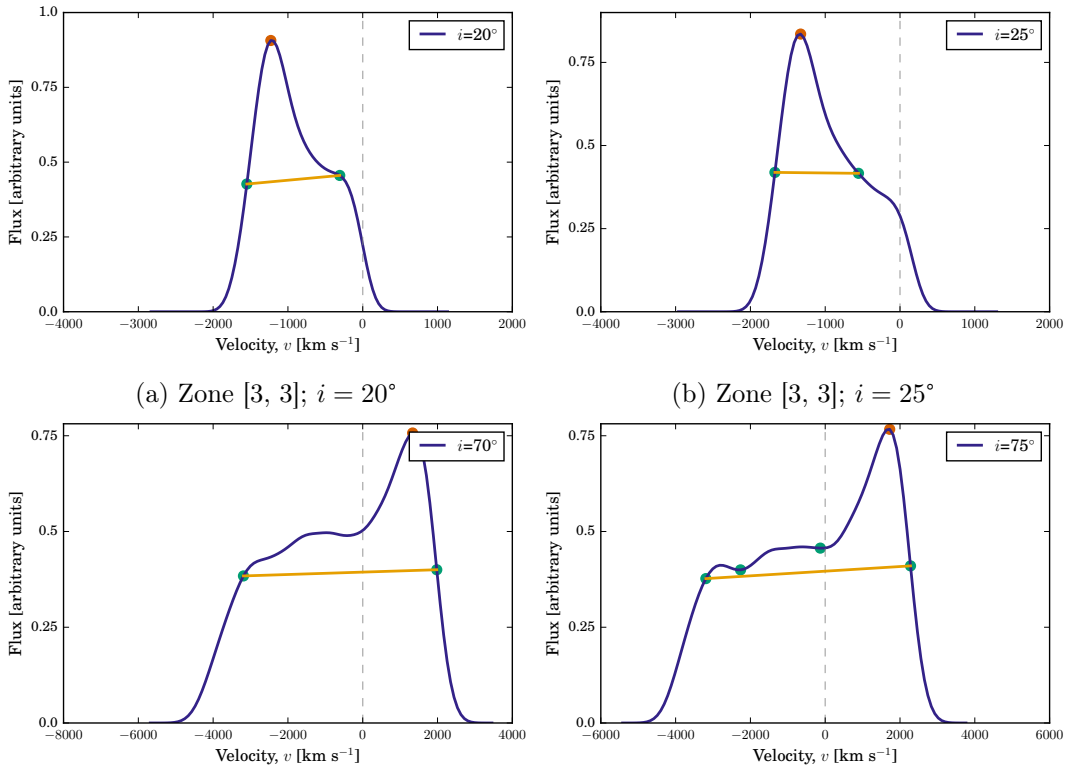

(a) Zone [3, 3]; $i = 20°$

(b) Zone [3, 3]; $i = 25°$

(c) Zone [3, 0]; $i = 70°$

(d) Zone [3, 0]; $i = 75°$

Figure 7.6: Examples of artifacts of line profile measurements using FWHM. The detected maximum and half maximum points are indicated by the vermillion and green dots respectively. The orange horizontal line is the FWHM measurement. The dashed grey vertical line shows the systemic centroid of the line. For a–b, the FWHM slightly decreases with increasing inclination from a to b. For c–d, the FWHM increased irregularly from c to d.

CHAPTER 8

Conclusion

8.1 Summary

Among the various subclassifications of AGN, quasars are the brightest sources in the universe, even outshining whole galaxies. A key to unlock their structure is through spectral analysis. The unique broad spectral lines in a quasar spectrum reveal information on the geometry and kinematics of the emitting region, that is the BLR. These lines are effectively produced in the wind that is emitted off the accretion disk, which is the so-called disk-wind model. The notion that the BLR is in general not spherically symmetric, implies that there is some interplay with the angle of viewing. Orientation unites the different AGN classes in the basic AGN unification paradigm, however, a reliable orientation indicator has yet been found. The recurring motifs of this thesis entail exploring the spectral line characteristics, a disk-wind model, and the viewing angle.

In Chapter 3, we constructed a simple kinematical disk-wind BLR model with radiative transfer in the high velocity limit. The outflow of the wind accounts for both the poloidal and rotational velocity components, where the former is mainly contributed by the acceleration of the wind, while the latter is due to the Keplerian motion of the emitting ions. The model provided the necessary groundwork and enabled qualitative analysis into the key properties of the observed spectral lines.

In Chapter 4, we presented a detailed analysis of the disk-wind in the form of a narrow outflowing wind, as has been suggested by several disk-wind models in the literature. Essentially, we considered whether a narrow wind model can replicate the observed trends in the line widths and velocity shifts. The work focused on gaining insight into the diverse shape of the emission lines and their dependence on three factors, namely orientation, angle of the wind, and emitting region. Correction to the optical depth is also applied to examine whether single-peaked line profiles can be recovered. One of the flaws in an outflowing disk-wind model is that observations have indicated that

the red side of the line displays shorter time delay than the blue side. We investigated this issue by considering the time delay in our model. Our major findings are as follow:

- At pole-on inclination angles, the emission line is narrow, asymmetric, and blueshifted. When the line-of-sight intersects the wind, the blueshift is larger. The emission line profile is broad, symmetric, and less shifted relative to the centroid for edge-on inclinations.
- A narrow polar wind model yields greater blueshifts than those of intermediate and equatorial winds.
- For a wind emitting region near the base of the accretion disk, the emission line is broad and symmetric, reflecting the dominant Keplerian motion. The poloidal velocity dominates as the line is emitted further away from the source of ionisation.
- Single-peaked emission lines are retrieved for optically thick winds, while the lines mostly remained double-peaked for the optically thin case.
- A quicker time lag in the red or blue side of the line can be reproduced in an outflowing wind model.

In Chapter 5, we undertook statistical and machine learning approaches to determine whether the given quasar properties are able to differentiate between BAL and non-BAL populations. An explanation for the rarity of these objects is associated with the geometric unification model in the context of a narrow disk-wind. In such cases, the intersection between the line-of-sight and the wind will define the presence of BAL. Using a quasar dataset from the SDSS, we analysed the continuum and emission properties of the two populations. We found that their underlying distributions are similar with respect to one another, contradicting the expectation from an orientation based narrow disk-wind model. Thus, we suggested an alternative disk-wind model with the following key traits:

- The angle of the wind covers a wide range.
- The wind is filled by multiple radial streams embedded with dense clumps, such that BAL occurs when the sightline and the streams overlap.

In Chapter 6, we introduced a robust mapping to inclination angle based on the observables of emission lines. To examine its reliability, we conducted simulations and several tests against other orientation indicators. The main highlights are as follows:

- A UV-optical orientation indicator using the relation between the velocity shift and line width ratio of high-ionisation C IV and low-ionisation Mg II emission lines is suggested.
- Quasars with large blueshifts and line width ratios are expected to be face-on, while those with small velocity shifts and line width ratio correspond to edge-on view.
- The predictions are qualitatively consistent with other orientation tracers and with simulations.

In Chapter 7, we implemented our modelling to determine the biases induced by the scale factor, f, on the virial black hole mass estimation. Our key results are listed below:

- The f factor is subjected to orientation effects. As the inclination angle changes from face-on to edge-on, the f value decreases.
- The f factor is affected by the line width characterisation. The recovered masses are relatively larger using FWHM than those using line dispersion.
- The f factor is dependent on the position of the emitting region in the wind.
- The estimated black hole mass will be biased if a fixed value of f is applied.

8.2 Future Prospect

8.2.1 Exploring the Parameter Space

A set of reasonable parameters is vital to create a physically realistic disk-wind model of the BLR. One option is to obtain estimates of the parameters through observational efforts. With improved time delay measurements from reverberation mapping campaigns, a tighter limit on the BLR radius can be established. Alternatively, microlensing of lensed quasars also provides information on the size of the emitting region and can be used even for bright distant quasars. Subsequently, the black hole mass can be derived from the BLR radius.

Although most parameter values are either based on the disk-wind model from literature or measurements from observations, a number of free parameters are arbitrarily set to some fixed value. In order to find the best value for the free parameters, a full exploration of the parameter space using, e.g., a grid search combined with Markov chain Monte Carlo and maximum likelihood, is crucial. This would lead to proper constraints on the model and would effectively better match the predictions from simulations to those of observations.

Exhaustive modelling will also help in deciphering the exact contribution of the different velocity components on the line broadening. The role of the poloidal component is particularly significant in HILs as they are located at region further away from the disk, while the rotational component dominates in LILs. A thorough investigation of the wind kinematics, especially the relationship between the rotational and poloidal velocity component, will boost our insight of the distinct broad spectral line shapes. Understanding the physical meaning and refining each model parameter will greatly aid the current view of the BLR structure.

8.2.2 Improving the Modelling

A substantial improvement to the modelling can be performed with the inclusion of the following elements. This is done by incorporating the dynamics into the model, such as photoionisation and full radiative transfer. An example of publicly available photoionisation code is `CLOUDY`[1], which has been intensively developed and tested. Consequently, the line profiles generated will account for both the emission and absorption features, which better represent the actual spectra of quasars. Through photoionisation modelling, the density and ionising flux of individual emission lines can be calculated, and therefore provide an estimate of the line location in the BLR.

Instead of a straight-edged wind in our model assumption, it is plausible that the wind contains a certain degree of curvature, in which case this feature can be included to determine the difference it will make to the emission line profiles. Clumps can be added to emulate the clumpy torus so that some photons are able to pass through and the torus is not completely opaque. `CLUMPY`[2] is one such example of publicly accessible code for modelling the clumpiness of the torus emission. There is also the possibility that the accretion disk is warped (e.g., Sanders et al. 1989; Pringle 1996; Nayakshin 2005; Tremaine & Davis 2014) and not entirely flat (e.g., Collin et al. 2006). Some fraction of the central engine will be obscured due to the misalignment of the disk (Lawrence & Elvis 2010). The wind might also be influenced by the presence of magnetic field (e.g., Blandford & Payne 1982; Emmering et al. 1992; Konigl & Kartje 1994). These modifications reflect the complexity of the BLR and will create a physically more realistic model of the emitting region.

8.2.3 Extending to Application

The potential and robustness of our simple kinematical modelling approach can be extended to numerous practical applications. We have applied our model to recover the time delay of the emission lines and to examine the effects of f factors on the virial black hole mass estimation. The model can be adapted and modified to make predictions for reverberation mapping and microlensing data.

For example, using our wide disk-wind model shown in Fig. 6.20 and the corresponding parameters in Table 6.4, a velocity-delay map can be constructed as demonstrated in Fig. 8.1, similar to those from Horne et al. (e.g., 2004) and Grier et al. (2013). The three scenarios of the fiducial model correspond to signatures of inflow, outflow, and rotation, respectively. A roughly symmetric velocity profile with shorter/longer time delay at the wing/core of the line indicates Keplerian rotation dominated. On the other hand, an asymmetric velocity profile with quicker time delay in the red/blue wing of

[1] https://www.nublado.org/
[2] https://www.clumpy.org/

the line suggests inflow/outflow. These maps convey information of the BLR geometry, through which the behaviour of the wind can be deduced.

Additionally, line profile modelling can be conducted to study microlensing by accommodating the distortions of the emission line due to microlensing effect. Such work has been done by Braibant et al. (e.g., 2017). A comparative study with those will further help in assessing the influence of microlensing on the emission lines.

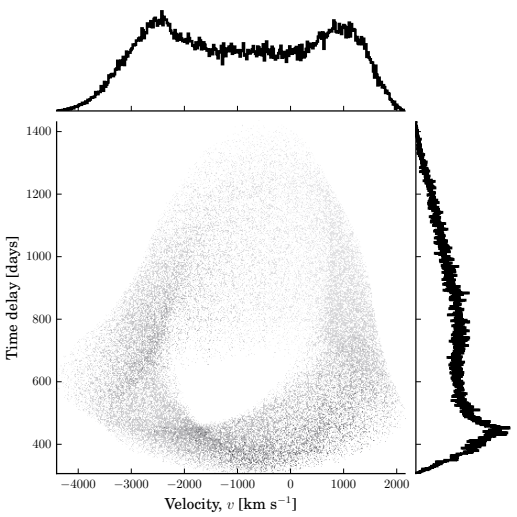

(a) Inflow in zone [2, 0]

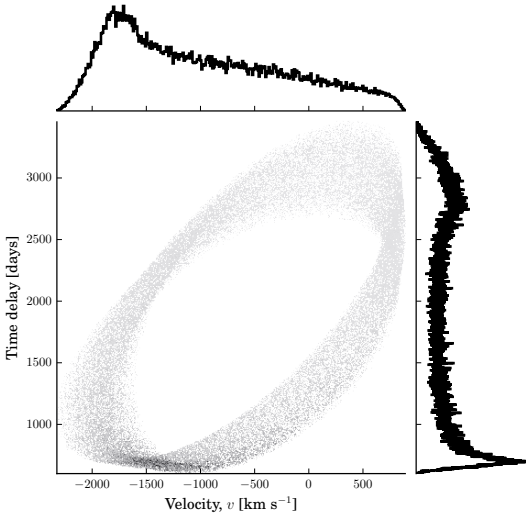

(b) Outflow in zone [3, 3]

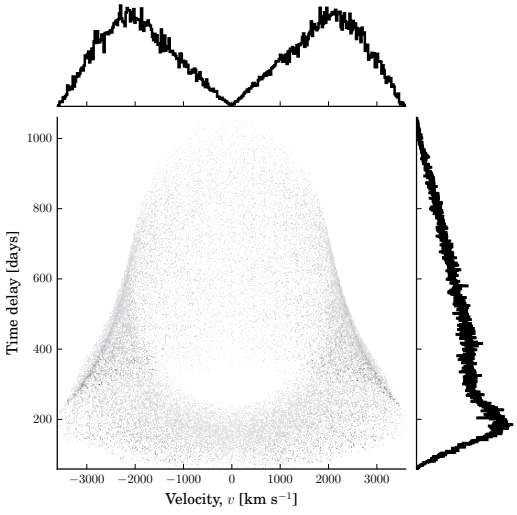

(c) Rotation in zone [0, 0]

Figure 8.1: Velocity-delay maps representing different kinematical signatures for fiducial wide disk-wind model at inclination angle of 45°. The input parameters for our model are listed in Table 6.4.

8.2.4 Utilising Big Data and Artificial Intelligence

In recent years, incredible progress has been made in the fields of machine learning and artificial intelligence, creating advanced mathematical and statistical methods to learn from data. These techniques, coupled with the availability and sheer volume of astronomical datasets, enable more information to be extracted and analysed. The ability of technology to efficiently process the data has also made this task effortless.

With the upcoming next generation of telescopes, the volume of data collected will increase exponentially and limited samples will no longer be a major issue. In the near future, wide-field surveys, such as the ground-based Large Scale Synoptic Telescope (LSST)[3], will produce terabytes of data per night. The LSST, which is scheduled to be operational in 2023, is also determined to make data publicly accessible, allowing scientific discoveries to be conducted in many areas of astronomy. The large data exploration will enhance the chances of finding elusive AGN with exotic features, among which are LoBALs, FeLoBALs, changing-look AGN, UFOs, and others. By piecing together the information from different AGN subclasses, a more comprehensive picture of AGN as a whole can be inferred.

A variety of data analytical methods is required to accommodate and process the massive dataset. Statistical tests and machine learning techniques are invaluable tools to investigate the relationship between the observed properties and subpopulation of quasars. We have used these methods on the BAL population. The same analyses can be extended to different datasets, for example, using a slightly lower S/N cut or a less restrictive BAL definition. We can investigate how these selection choices affect the findings. This can be used to evaluate the reliability and robustness of the classification algorithms on the new dataset. If there is a change in the statistical difference or/and features of importance from machine learning, this will further reinforce the difficulty in segregating the BAL and non-BAL quasars.

The employment of a more complex learning algorithm, such as neural networks, might be able to accurately differentiate the quasar subgroups. A further extension is to apply them to learn about other subclasses of AGN, such as type 1 versus type 2 AGN and RL versus RQ. These resources have proven to be indispensable, bringing a better understanding of the data and gaining a broader perspective on various aspects of the BLR.

8.2.5 Probing the Orientation

The proposed orientation indicator based on the velocity shifts and line width relation is indeed enticing and survived several tests. Nevertheless, the choice of mapping the

[3] https://www.lsst.org

orientation to the regression line is still unclear, and so is the orientation range of the sample. More work needs to be done, including inspecting and assessing various tests to determine whether the proposed model still holds. Datasets with clean measurements will be beneficial to avoid biases in the presence of limited samples. The need for quality data and refined individual measurements will also form tighter constraints on the correlation. Observational constraints combined with detailed modelling will assist in fully resolving the mapping.

If our proposed orientation indicator is proven to be valid, this will open up new realms of application. This is extremely useful, notably in the black hole mass estimation. By knowing the inclination of a system, the bias in the virial black hole mass due to orientation can corrected.

8.3 Final Remarks

There are endless mysteries lurking in the depths of the universe. One such source, quasars, is the most luminous and energetic star-like active galactic nuclei harbouring a supermassive black hole at their core. The disk-wind seems to be ubiquitous in these systems as an efficient mechanism to transport radiation off the accretion disk, giving rise to the observed spectral features of the line profiles.

Our simple kinematical disk-wind model offers a promising avenue to probe the shape of the quasar spectral lines with respect to the different geometry and orientation of the BLR. The findings in this thesis have quantified several key attributes of the disk-wind as well as seeking an orientation tracer of quasars in the UV-optical, leading to potential unification. Although significant advancements have been made in understanding the quasar structure, some questions remain unanswered. With the breakthrough of machine learning and artificial intelligence in the astronomy community, it is possible to unravel information, which then helps to disentangle existing problems and even sparks new ideas. The abundance of high quality data from next generation telescopes and surveys also allows meaningful statistical analysis to be conducted. Ultimately, the accumulated knowledge will bring a step closer towards unveiling the true nature of the AGN.

APPENDIX A

Emission Line Features

Table A.1 presents selected emission line identifications, laboratory rest wavelengths, velocity shifts, skewness, EWs, and ionisation potentials from Vanden Berk et al. (2001). The various properties of the emission lines are measured by using a median composite spectrum (see Fig. 2.2). The composite is generated by compiling more than 2200 quasar spectra with redshift range between 0.04 and 4.79 from the SDSS catalogue. Note that the relative EWs do not represent the physics of a single object but median values.

Table A.1: Selected emission line features from Vanden Berk et al. (2001).

Ion	Wavelength (Å)	Velocity Shifts[a] ($km\,s^{-1}$)	Skew[b]	EW (Å)	Ionisation Potential (eV)
Lyα	1215.67	143	0.40	92.91	13.60
C IV	1549.06	-70	-0.04	23.78	97.89
He II	1640.42	-471	-0.22	0.51	54.42
C III]	1908.73	-224	-0.27	21.19	47.89
Mg II	2798.75	161	-0.06	32.28	15.04
[O II]	3728.48	94	-0.24	1.56	35.12
[Ne III]	3869.85	-6	-0.50	1.38	63.46
Hγ	4341.68	23	0.12	12.62	13.60
Hβ	4862.68	-1	0.61	46.21	13.60
[O III]	4960.30	3	-0.22	3.50	54.94
[O III]	5008.24	-1	-0.22	13.23	54.94
He I	5877.29	-27	0.26	4.94	24.59
[O I]	6302.05	47	-0.64	1.15	13.62
Hα	6564.61	27	0.35	194.52	13.60

[a] Measured relative to the forbidden [O III] λ5007 line.
[b] Measured using the Pearson's coefficient of skewness given by $3(\text{mean} - \text{median})/\sigma_\lambda$, where σ_λ is the root mean square wavelength dispersion.

Bibliography

Abbott, D. C. (1980). The theory of radiatively driven stellar winds. I - A physical interpretation. *ApJ*, 242, 1183–1207. ADS: 1980ApJ...242.1183A. doi: 10.1086/158550.

Abbott, D. C. (1982). The theory of radiatively driven stellar winds. II - The line acceleration. *ApJ*, 259, 282–301. ADS: 1982ApJ...259..282A. doi: 10.1086/160166.

Ackermann, M., Ajello, M., Allafort, A., Baldini, L., Ballet, J., Barbiellini, G., Bastieri, D., Bechtol, K., Bellazzini, R., Berenji, B., Bloom, E. D., Bonamente, E., Borgland, A. W., Bregeon, J., Brigida, M., Bruel, P., Buehler, R., Buson, S., Caliandro, G. A., Cameron, R. A., Caraveo, P. A., Casandjian, J. M., Cavazzuti, E., Cecchi, C., Charles, E., Chekhtman, A., Cheung, C. C., Chiang, J., Ciprini, S., Claus, R., Cohen-Tanugi, J., Conrad, J., Cutini, S., D'Ammando, F., de Angelis, A., de Palma, F., Dermer, C. D., Silva, E. d. C. e., Drell, P. S., Drlica-Wagner, A., Enoto, T., Favuzzi, C., Fegan, S. J., Ferrara, E. C., Fortin, P., Fukazawa, Y., Fusco, P., Gargano, F., Gasparrini, D., Gehrels, N., Germani, S., Giglietto, N., Giommi, P., Giordano, F., Giroletti, M., Godfrey, G., Grove, J. E., Guiriec, S., Hadasch, D., Hayashida, M., Hays, E., Hughes, R. E., Jóhannesson, G., Johnson, A. S., Kamae, T., Katagiri, H., Kataoka, J., Knödlseder, J., Kuss, M., Lande, J., Llena Garde, M., Longo, F., Loparco, F., Lott, B., Lovellette, M. N., Lubrano, P., Madejski, G. M., Mazziotta, M. N., Michelson, P. F., Mizuno, T., Monte, C., Monzani, M. E., Morselli, A., Moskalenko, I. V., Murgia, S., Nishino, S., Norris, J. P., Nuss, E., Ohno, M., Ohsugi, T., Okumura, A., Orlando, E., Ozaki, M., Paneque, D., Pesce-Rollins, M., Pierbattista, M., Piron, F., Pivato, G., Porter, T. A., Rainò, S., Rando, R., Razzano, M., Reimer, A., Reimer, O., Ritz, S., Roth, M., Sanchez, D. A., Sbarra, C., Sgrò, C., Siskind, E. J., Spandre, G., Spinelli, P., Stawarz, Ł., Strong, A. W., Takahashi, H., Takahashi, T., Tanaka, T., Thayer, J. B., Thompson, D. J., Tibaldo, L., Tinivella, M., Torres, D. F., Tosti, G., Troja, E., Uchiyama, Y., Usher, T. L., Vandenbroucke, J., Vasileiou, V., Vianello, G., Vitale, V., Waite, A. P., Winer, B. L., Wood, K. S., Wood, M., Yang, Z., & Zimmer, S. (2012a). Search for Gamma-ray Emission from X-Ray-selected Seyfert Galaxies with Fermi-LAT. *ApJ*, 747, 104. ADS: 2012ApJ...747..104A. doi: 10.1088/0004-637X/747/2/104.

Ackermann, M., Ajello, M., Allafort, A., Baldini, L., Ballet, J., Bastieri, D., Bechtol, K., Bellazzini, R., Berenji, B., Bloom, E. D., Bonamente, E., Borgland, A. W., Bouvier, A., Bregeon, J., Brigida, M., Bruel, P., Buehler, R., Buson, S., Caliandro, G. A., Cameron, R. A., Caraveo, P. A., Casandjian, J. M., Cecchi, C., Charles, E., Chekhtman, A., Cheung, C. C., Chiang, J., Cillis, A. N., Ciprini, S., Claus, R., Cohen-Tanugi, J., Conrad, J., Cutini, S., de Palma, F., Dermer, C. D., Digel, S. W., Silva, E. d. C. e., Drell, P. S., Drlica-Wagner,

A., Favuzzi, C., Fegan, S. J., Fortin, P., Fukazawa, Y., Funk, S., Fusco, P., Gargano, F., Gasparrini, D., Germani, S., Giglietto, N., Giordano, F., Glanzman, T., Godfrey, G., Grenier, I. A., Guiriec, S., Gustafsson, M., Hadasch, D., Hayashida, M., Hays, E., Hughes, R. E., Jóhannesson, G., Johnson, A. S., Kamae, T., Katagiri, H., Kataoka, J., Knödlseder, J., Kuss, M., Lande, J., Longo, F., Loparco, F., Lott, B., Lovellette, M. N., Lubrano, P., Madejski, G. M., Martin, P., Mazziotta, M. N., McEnery, J. E., Michelson, P. F., Mizuno, T., Monte, C., Monzani, M. E., Morselli, A., Moskalenko, I. V., Murgia, S., Nishino, S., Norris, J. P., Nuss, E., Ohno, M., Ohsugi, T., Okumura, A., Omodei, N., Orlando, E., Ozaki, M., Parent, D., Persic, M., Pesce-Rollins, M., Petrosian, V., Pierbattista, M., Piron, F., Pivato, G., Porter, T. A., Rainò, S., Rando, R., Razzano, M., Reimer, A., Reimer, O., Ritz, S., Roth, M., Sbarra, C., Sgrò, C., Siskind, E. J., Spandre, G., Spinelli, P., Stawarz, Ł., Strong, A. W., Takahashi, H., Tanaka, T., Thayer, J. B., Tibaldo, L., Tinivella, M., Torres, D. F., Tosti, G., Troja, E., Uchiyama, Y., Vandenbroucke, J., Vianello, G., Vitale, V., Waite, A. P., Wood, M., & Yang, Z. (2012b). GeV Observations of Star-forming Galaxies with the Fermi Large Area Telescope. *ApJ*, 755, 164. ADS: 2012ApJ...755..164A. doi: 10.1088/0004-637X/755/2/164.

Adcock, R. J. (1878). A problem in least squares. *The Analyst*, 5(2), 53–54.

Akritas, M. G. & Bershady, M. A. (1996). Linear Regression for Astronomical Data with Measurement Errors and Intrinsic Scatter. *ApJ*, 470, 706. ADS: 1996ApJ...470..706A. doi: 10.1086/177901.

Alexander, D. M. (2001). The unified model and the Seyfert 2 infrared dichotomy. *MNRAS*, 320, L15–L19. ADS: 2001MNRAS.320L..15A. doi: 10.1046/j.1365-8711.2001.04131.x.

Alexandroff, R., Strauss, M. A., Greene, J. E., Zakamska, N. L., Ross, N. P., Brandt, W. N., Liu, G., Smith, P. S., Ge, J., Hamann, F., Myers, A. D., Petitjean, P., Schneider, D. P., Yesuf, H., & York, D. G. (2013). Candidate type II quasars at $2 < z < 4.3$ in the Sloan Digital Sky Survey III. *MNRAS*, 435, 3306–3325. ADS: 2013MNRAS.435.3306A. doi: 10.1093/mnras/stt1500.

Allen, J. T., Hewett, P. C., Maddox, N., Richards, G. T., & Belokurov, V. (2011). A strong redshift dependence of the broad absorption line quasar fraction. *MNRAS*, 410, 860–884. ADS: 2011MNRAS.410..860A. doi: 10.1111/j.1365-2966.2010.17489.x.

Alonso-Herrero, A., Ramos Almeida, C., Mason, R., Asensio Ramos, A., Roche, P. F., Levenson, N. A., Elitzur, M., Packham, C., Rodríguez Espinosa, J. M., Young, S., Díaz-Santos, T., & Pérez-García, A. M. (2011). Torus and Active Galactic Nucleus Properties of Nearby Seyfert Galaxies: Results from Fitting Infrared Spectral Energy Distributions and Spectroscopy. *ApJ*, 736, 82. ADS: 2011ApJ...736...82A. doi: 10.1088/0004-637X/736/2/82.

Anderson, T. W. & Darling, D. A. (1954). A test of goodness of fit. *Journal of the American statistical association*, 49(268), 765–769.

Antonucci, R. (1993). Unified models for active galactic nuclei and quasars. *ARA&A*, 31, 473–521. ADS: 1993ARA&A..31..473A. doi: 10.1146/annurev.aa.31.090193.002353.

Antonucci, R. R. J. & Miller, J. S. (1985). Spectropolarimetry and the nature of NGC 1068. *ApJ*, 297, 621–632. ADS: 1985ApJ...297..621A. doi: 10.1086/163559.

Arav, N. (1996). The “Ghost of LY alpha ” as Evidence for Radiative Acceleration in Quasars.

ApJ, 465, 617. ADS: 1996ApJ...465..617A. doi: 10.1086/177447.

Arav, N., de Kool, M., Korista, K. T., Crenshaw, D. M., van Breugel, W., Brotherton, M., Green, R. F., Pettini, M., Wills, B., de Vries, W., Becker, B., Brandt, W. N., Green, P., Junkkarinen, V. T., Koratkar, A., Laor, A., Laurent-Muehleisen, S. A., Mathur, S., & Murray, N. (2001). HST STIS Observations of PG 0946+301: The Highest Quality UV Spectrum of a BALQSO. *ApJ*, 561, 118–130. ADS: 2001ApJ...561..118A. doi: 10.1086/323369.

Arav, N., Korista, K. T., Barlow, T. A., & Begelman (1995). Radiative acceleration of gas in quasars. *Nature*, 376, 576–578. ADS: 1995Natur.376..576A. doi: 10.1038/376576a0.

Arav, N., Li, Z.-Y., & Begelman, M. C. (1994). Radiative acceleration in outflows from broad absorption line quasi-stellar objects. 2: Wind models. *ApJ*, 432, 62–74. ADS: 1994ApJ...432...62A. doi: 10.1086/174549.

Aretxaga, I., Joguet, B., Kunth, D., Melnick, J., & Terlevich, R. J. (1999). Seyfert 1 Mutation of the Classical Seyfert 2 Nucleus NGC 7582. *ApJ*, 519, L123–L126. ADS: 1999ApJ...519L.123A. doi: 10.1086/312114.

Arshakian, T. G. (2005). Direct evidence of the receding "torus" around central nuclei of powerful radio sources. *A&A*, 436, 817–824. ADS: 2005A&A...436..817A. doi: 10.1051/0004-6361:20042341.

Arshakian, T. G. & Longair, M. S. (2004). On the jet speeds of classical double radio sources. *MNRAS*, 351, 727–732. ADS: 2004MNRAS.351..727A. doi: 10.1111/j.1365-2966.2004.07823.x.

Assef, R. J., Denney, K. D., Kochanek, C. S., Peterson, B. M., Kozłowski, S., Ageorges, N., Barrows, R. S., Buschkamp, P., Dietrich, M., Falco, E., Feiz, C., Gemperlein, H., Germeroth, A., Grier, C. J., Hofmann, R., Juette, M., Khan, R., Kilic, M., Knierim, V., Laun, W., Lederer, R., Lehmitz, M., Lenzen, R., Mall, U., Madsen, K. K., Mandel, H., Martini, P., Mathur, S., Mogren, K., Mueller, P., Naranjo, V., Pasquali, A., Polsterer, K., Pogge, R. W., Quirrenbach, A., Seifert, W., Stern, D., Shappee, B., Storz, C., Van Saders, J., Weiser, P., & Zhang, D. (2011). Black Hole Mass Estimates Based on C IV are Consistent with Those Based on the Balmer Lines. *ApJ*, 742, 93. ADS: 2011ApJ...742...93A. doi: 10.1088/0004-637X/742/2/93.

Assef, R. J., Stern, D., Kochanek, C. S., Blain, A. W., Brodwin, M., Brown, M. J. I., Donoso, E., Eisenhardt, P. R. M., Jannuzi, B. T., Jarrett, T. H., Stanford, S. A., Tsai, C.-W., Wu, J., & Yan, L. (2013). Mid-infrared Selection of Active Galactic Nuclei with the Wide-field Infrared Survey Explorer. II. Properties of WISE-selected Active Galactic Nuclei in the NDWFS Boötes Field. *ApJ*, 772, 26. ADS: 2013ApJ...772...26A. doi: 10.1088/0004-637X/772/1/26.

Astropy Collaboration, Robitaille, T. P., Tollerud, E. J., Greenfield, P., Droettboom, M., Bray, E., Aldcroft, T., Davis, M., Ginsburg, A., Price-Whelan, A. M., Kerzendorf, W. E., Conley, A., Crighton, N., Barbary, K., Muna, D., Ferguson, H., Grollier, F., Parikh, M. M., Nair, P. H., Unther, H. M., Deil, C., Woillez, J., Conseil, S., Kramer, R., Turner, J. E. H., Singer, L., Fox, R., Weaver, B. A., Zabalza, V., Edwards, Z. I., Azalee Bostroem, K., Burke, D. J., Casey, A. R., Crawford, S. M., Dencheva, N., Ely, J., Jenness, T., Labrie, K., Lim, P. L., Pierfederici, F., Pontzen, A., Ptak, A., Refsdal, B., Servillat, M., & Streicher, O. (2013). Astropy: A community Python package for astronomy. *A&A*, 558, A33. ADS: 2013A&A...558A..33A.

doi: 10.1051/0004-6361/201322068.

Bañados, E., Venemans, B. P., Mazzucchelli, C., Farina, E. P., Walter, F., Wang, F., Decarli, R., Stern, D., Fan, X., Davies, F. B., Hennawi, J. F., Simcoe, R. A., Turner, M. L., Rix, H.-W., Yang, J., Kelson, D. D., Rudie, G. C., & Winters, J. M. (2018). An 800-million-solar-mass black hole in a significantly neutral Universe at a redshift of 7.5. *Nature*, 553, 473–476. ADS: 2018Natur.553..473B. doi: 10.1038/nature25180.

Bahcall, J. N., Kozlovsky, B.-Z., & Salpeter, E. E. (1972). On the Time Dependence of Emission-Line Strengths from a Photoionized Nebula. *ApJ*, 171, 467. ADS: 1972ApJ...171..467B. doi: 10.1086/151300.

Bahk, H., Woo, J.-H., & Park, D. (2019). Calibrating Mg II—based Black Hole Mass Estimators with Hβ Reverberation Measurements. *ApJ*, 875(1), 50. ADS: 2019ApJ...875...50B. doi: 10.3847/1538-4357/ab100d.

Baker, J. C. & Hunstead, R. W. (1995). Revealing the Effects of Orientation in Composite Quasar Spectra. *ApJ*, 452, L95. ADS: 1995ApJ...452L..95B. doi: 10.1086/309726.

Balbus, S. A. & Hawley, J. F. (1991). A powerful local shear instability in weakly magnetized disks. I - Linear analysis. II - Nonlinear evolution. *ApJ*, 376, 214–233. ADS: 1991ApJ...376..214B. doi: 10.1086/170270.

Baldi, R. D., Capetti, A., Buttiglione, S., Chiaberge, M., & Celotti, A. (2013). An optical spectroscopic survey of the 3CR sample of radio galaxies with z $<$ 0.3. V. Implications for the unified model for FR IIs. *A&A*, 560, A81. ADS: 2013A&A...560A..81B. doi: 10.1051/0004-6361/201322842.

Baldi, R. D., Capetti, A., & Giovannini, G. (2015). Pilot study of the radio-emitting AGN population: the emerging new class of FR 0 radio-galaxies. *A&A*, 576, A38. ADS: 2015A&A...576A..38B. doi: 10.1051/0004-6361/201425426.

Baldwin, J. A. (1977). Luminosity Indicators in the Spectra of Quasi-Stellar Objects. *ApJ*, 214, 679–684. ADS: 1977ApJ...214..679B. doi: 10.1086/155294.

Baloković, M., Smolčić, V., Ivezić, Ž., Zamorani, G., Schinnerer, E., & Kelly, B. C. (2012). Disclosing the Radio Loudness Distribution Dichotomy in Quasars: An Unbiased Monte Carlo Approach Applied to the SDSS-FIRST Quasar Sample. *ApJ*, 759, 30. ADS: 2012ApJ...759..30B. doi: 10.1088/0004-637X/759/1/30.

Barlow, T. A. (1994). Time Variability of Broad-Absorption-Line QSOs. *PASP*, 106, 548. ADS: 1994PASP..106..548B. doi: 10.1086/133411.

Barthel, P. D. (1989). Is every quasar beamed? *ApJ*, 336, 606–611. ADS: 1989ApJ...336..606B. doi: 10.1086/167038.

Baskin, A. & Laor, A. (2005). What controls the CIV line profile in active galactic nuclei? *MNRAS*, 356, 1029–1044. ADS: 2005MNRAS.356.1029B. doi: 10.1111/j.1365-2966.2004.08525.x.

Baskin, A., Laor, A., & Stern, J. (2014). Radiation pressure confinement - IV. Application

to broad absorption line outflows. *MNRAS*, 445, 3025–3038. ADS: 2014MNRAS.445.3025B. doi: 10.1093/mnras/stu1732.

Becker, R. H., Gregg, M. D., Hook, I. M., McMahon, R. G., White, R. L., & Helfand, D. J. (1997). The FIRST Radio-loud Broad Absorption Line QSO and Evidence for a Hidden Population of Quasars. *ApJ*, 479, L93–L96. ADS: 1997ApJ...479L..93B. doi: 10.1086/310594.

Becker, R. H., White, R. L., Gregg, M. D., Brotherton, M. S., Laurent-Muehleisen, S. A., & Arav, N. (2000). Properties of Radio-selected Broad Absorption Line Quasars from the First Bright Quasar Survey. *ApJ*, 538, 72–82. ADS: 2000ApJ...538...72B. doi: 10.1086/309099.

Becker, R. H., White, R. L., Gregg, M. D., Laurent-Muehleisen, S. A., Brotherton, M. S., Impey, C. D., Chaffee, F. H., Richards, G. T., Helfand, D. J., Lacy, M., Courbin, F., & Proctor, D. D. (2001). The FIRST Bright Quasar Survey. III. The South Galactic Cap. *ApJS*, 135, 227–262. ADS: 2001ApJS..135..227B. doi: 10.1086/321798.

Becker, R. H., White, R. L., & Helfand, D. J. (1995). The FIRST Survey: Faint Images of the Radio Sky at Twenty Centimeters. *ApJ*, 450, 559. ADS: 1995ApJ...450..559B. doi: 10.1086/176166.

Beckmann, V. & Shrader, C. R. (2012). *Active Galactic Nuclei*. ADS: 2012agn..book.....B.

Begelman, M., de Kool, M., & Sikora, M. (1991). Outflows driven by cosmic-ray pressure in broad absorption line QSOs. *ApJ*, 382, 416–432. ADS: 1991ApJ...382..416B. doi: 10.1086/170731.

Begelman, M. C., Blandford, R. D., & Rees, M. J. (1980). Massive black hole binaries in active galactic nuclei. *Nature*, 287, 307–309. ADS: 1980Natur.287..307B. doi: 10.1038/287307a0.

Bentz, M. C., Cackett, E. M., Crenshaw, D. M., Horne, K., Street, R., & Ou-Yang, B. (2016). A Reverberation-based Black Hole Mass for MCG-06-30-15. *ApJ*, 830, 136. ADS: 2016ApJ...830..136B. doi: 10.3847/0004-637X/830/2/136.

Bentz, M. C., Denney, K. D., Grier, C. J., Barth, A. J., Peterson, B. M., Vestergaard, M., Bennert, V. N., Canalizo, G., De Rosa, G., Filippenko, A. V., Gates, E. L., Greene, J. E., Li, W., Malkan, M. A., Pogge, R. W., Stern, D., Treu, T., & Woo, J.-H. (2013). The Low-luminosity End of the Radius-Luminosity Relationship for Active Galactic Nuclei. *ApJ*, 767, 149. ADS: 2013ApJ...767..149B. doi: 10.1088/0004-637X/767/2/149.

Bentz, M. C., Horne, K., Barth, A. J., Bennert, V. N., Canalizo, G., Filippenko, A. V., Gates, E. L., Malkan, M. A., Minezaki, T., Treu, T., Woo, J.-H., & Walsh, J. L. (2010). The Lick AGN Monitoring Project: Velocity-delay Maps from the Maximum-entropy Method for Arp 151. *ApJ*, 720, L46–L51. ADS: 2010ApJ...720L..46B. doi: 10.1088/2041-8205/720/1/L46.

Bentz, M. C. & Katz, S. (2015). The AGN Black Hole Mass Database. *PASP*, 127, 67–73. ADS: 2015PASP..127...67B. doi: 10.1086/679601.

Bentz, M. C., Peterson, B. M., Netzer, H., Pogge, R. W., & Vestergaard, M. (2009). The Radius-Luminosity Relationship for Active Galactic Nuclei: The Effect of Host-Galaxy Starlight on Luminosity Measurements. II. The Full Sample of Reverberation-Mapped AGNs. *ApJ*, 697, 160–181. ADS: 2009ApJ...697..160B. doi: 10.1088/0004-637X/697/1/160.

Best, P. N. & Heckman, T. M. (2012). On the fundamental dichotomy in the local radio-AGN population: accretion, evolution and host galaxy properties. *MNRAS*, 421, 1569–1582. ADS: 2012MNRAS.421.1569B. doi: 10.1111/j.1365-2966.2012.20414.x.

Bianchi, S., Guainazzi, M., Matt, G., Chiaberge, M., Iwasawa, K., Fiore, F., & Maiolino, R. (2005). A search for changing-look AGN in the Grossan catalog. *A&A*, 442, 185–194. ADS: 2005A&A...442..185B. doi: 10.1051/0004-6361:20053389.

Bisogni, S., Marconi, A., & Risaliti, G. (2017). Orientation effects on spectral emission features of quasars. *MNRAS*, 464, 385–397. ADS: 2017MNRAS.464..385B. doi: 10.1093/mnras/stw2324.

Blanchard, P. K., Nicholl, M., Berger, E., Guillochon, J., Margutti, R., Chornock, R., Alexander, K. D., Leja, J., & Drout, M. R. (2017). PS16dtm: A Tidal Disruption Event in a Narrow-line Seyfert 1 Galaxy. *ApJ*, 843, 106. ADS: 2017ApJ...843..106B. doi: 10.3847/1538-4357/aa77f7.

Blandford, R. D. & McKee, C. F. (1982). Reverberation mapping of the emission line regions of Seyfert galaxies and quasars. *ApJ*, 255, 419–439. ADS: 1982ApJ...255..419B. doi: 10.1086/159843.

Blandford, R. D. & Payne, D. G. (1982). Hydromagnetic flows from accretion discs and the production of radio jets. *MNRAS*, 199, 883–903. ADS: 1982MNRAS.199..883B.

Blundell, K. M. & Kuncic, Z. (2007). On the Origin of Radio Core Emission in Radio-quiet Quasars. *ApJ*, 668, L103–L106. ADS: 2007ApJ...668L.103B. doi: 10.1086/522695.

Boroson, T. A. (2002). Black Hole Mass and Eddington Ratio as Drivers for the Observable Properties of Radio-loud and Radio-quiet QSOs. *ApJ*, 565, 78–85. ADS: 2002ApJ...565...78B. doi: 10.1086/324486.

Boroson, T. A. (2011). A New Orientation Indicator for Radio-quiet Quasars. *ApJ*, 735, L14. ADS: 2011ApJ...735L..14B. doi: 10.1088/2041-8205/735/1/L14.

Boroson, T. A. & Green, R. F. (1992). The emission-line properties of low-redshift quasi-stellar objects. *ApJS*, 80, 109–135. ADS: 1992ApJS...80..109B. doi: 10.1086/191661.

Boroson, T. A. & Meyers, K. A. (1992). The optical properties of IR-selected and MG II broad absorption line quasars. *ApJ*, 397, 442–451. ADS: 1992ApJ...397..442B. doi: 10.1086/171800.

Boser, B. E., Guyon, I. M., & Vapnik, V. N. (1992). A training algorithm for optimal margin classifiers. In D. Haussler (Ed.), *Proceedings of the fifth annual workshop on Computational learning theory* (pp. 144–152).: ACM ACM Press.

Bottorff, M., Korista, K. T., Shlosman, I., & Blandford, R. D. (1997). Dynamics of Broad Emission-Line Region in NGC 5548: Hydromagnetic Wind Model versus Observations. *ApJ*, 479, 200–221. ADS: 1997ApJ...479..200B. doi: 10.1086/303867.

Bottorff, M. C., Korista, K. T., & Shlosman, I. (2000). Dynamics of Warm Absorbing Gas in Seyfert Galaxies: NGC 5548. *ApJ*, 537, 134–151. ADS: 2000ApJ...537..134B. doi: 10.1086/309006.

Braibant, L., Hutsemékers, D., Sluse, D., & Goosmann, R. (2017). Constraining the geometry and kinematics of the quasar broad emission line region using gravitational microlensing. I. Models and simulations. *A&A*, 607, A32. ADS: 2017A&A...607A..32B. doi: 10.1051/0004-6361/201731086.

Breiman, L. (2001). Random forests. *Machine Learning*, 45(1), 5–32. doi: 10.1023/A:1010933404324.

Breiman, L., Friedman, J., Stone, C. J., & Olshen, R. A. (1984). *Classification and regression trees*. CRC press.

Brotherton, M. S. (1996). The Profiles of H beta and [O iii] lambda 5007 in Radio-loud Quasars. *ApJS*, 102, 1. ADS: 1996ApJS..102....1B. doi: 10.1086/192249.

Brotherton, M. S., De Breuck, C., & Schaefer, J. J. (2006). Spectropolarimetry of PKS 0040-005 and the orientation of broad absorption line quasars. *MNRAS*, 372, L58–L62. ADS: 2006MNRAS.372L..58B. doi: 10.1111/j.1745-3933.2006.00226.x.

Brotherton, M. S., Runnoe, J. C., Shang, Z., & DiPompeo, M. A. (2015a). Bias in C IV-based quasar black hole mass scaling relationships from reverberation mapped samples. *MNRAS*, 451, 1290–1298. ADS: 2015MNRAS.451.1290B. doi: 10.1093/mnras/stv767.

Brotherton, M. S., Singh, V., & Runnoe, J. (2015b). Orientation and quasar black hole mass estimation. *MNRAS*, 454, 3864–3871. ADS: 2015MNRAS.454.3864B. doi: 10.1093/mnras/stv2186.

Brotherton, M. S., Tran, H. D., Becker, R. H., Gregg, M. D., Laurent-Muehleisen, S. A., & White, R. L. (2001). Composite Spectra from the FIRST Bright Quasar Survey. *ApJ*, 546, 775–781. ADS: 2001ApJ...546..775B. doi: 10.1086/318309.

Brotherton, M. S., van Breugel, W., Smith, R. J., Boyle, B. J., Shanks, T., Croom, S. M., Miller, L., & Becker, R. H. (1998). Discovery of Radio-Loud Broad Absorption Line Quasars Using Ultraviolet Excess and Deep Radio Selection. *ApJ*, 505, L7–L10. ADS: 1998ApJ...505L...7B. doi: 10.1086/311599.

Brotherton, M. S., Wills, B. J., Steidel, C. C., & Sargent, W. L. W. (1994). Statistics of QSO broad emission-line profiles. 2: The C IV wavelength 1549, C III) wavelength 1909, and MG II wavelength 2798 lines. *ApJ*, 423, 131–142. ADS: 1994ApJ...423..131B. doi: 10.1086/173794.

Bruni, G., González-Serrano, J. I., Pedani, M., Benn, C. R., Mack, K.-H., Holt, J., Montenegro-Montes, F. M., & Jiménez-Luján, F. (2014). Investigating the radio-loud phase of broad absorption line quasars. *A&A*, 569, A87. ADS: 2014A&A...569A..87B. doi: 10.1051/0004-6361/201424424.

Cao Orjales, J. M., Stevens, J. A., Jarvis, M. J., Smith, D. J. B., Hardcastle, M. J., Auld, R., Baes, M., Cava, A., Clements, D. L., Cooray, A., Coppin, K., Dariush, A., De Zotti, G., Dunne, L., Dye, S., Eales, S., Hopwood, R., Hoyos, C., Ibar, E., Ivison, R. J., Maddox, S., Page, M. J., & Valiante, E. (2012). Herschel-ATLAS: the far-infrared properties and star formation rates of broad absorption line quasi-stellar objects. *MNRAS*, 427, 1209–1218.

ADS: 2012MNRAS.427.1209C. doi: 10.1111/j.1365-2966.2012.22049.x.

Capellupo, D. M., Hamann, F., Shields, J. C., Halpern, J. P., & Barlow, T. A. (2013). Variability in quasar broad absorption line outflows - III. What happens on the shortest time-scales? *MNRAS*, 429, 1872–1886. ADS: 2013MNRAS.429.1872C. doi: 10.1093/mnras/sts427.

Capellupo, D. M., Hamann, F., Shields, J. C., Rodríguez Hidalgo, P., & Barlow, T. A. (2011). Variability in quasar broad absorption line outflows - I. Trends in the short-term versus long-term data. *MNRAS*, 413, 908–920. ADS: 2011MNRAS.413..908C. doi: 10.1111/j.1365-2966.2010.18185.x.

Capellupo, D. M., Hamann, F., Shields, J. C., Rodríguez Hidalgo, P., & Barlow, T. A. (2012). Variability in quasar broad absorption line outflows - II. Multi-epoch monitoring of Si IV and C IV broad absorption line variability. *MNRAS*, 422, 3249–3267. ADS: 2012MNRAS.422.3249C. doi: 10.1111/j.1365-2966.2012.20846.x.

Capriotti, E. R., Foltz, C. B., & Peterson, B. M. (1982). The time variation of broad emission-line profiles of Seyfert 1 galaxies. *ApJ*, 261, 35–41. ADS: 1982ApJ...261...35C. doi: 10.1086/160315.

Carlberg, R. G. (1980). The instability of radiation-driven stellar winds. *ApJ*, 241, 1131–1140. ADS: 1980ApJ...241.1131C. doi: 10.1086/158428.

Carswell, R. F., Mountain, C. M., Robertson, D. J., Beard, S. M., Glendinning, A. R., Laird, D. C., Lawrence, L. C., Montgomery, D., Pentland, G., Pickup, D. A., Smith, I. A., Bailey, J. A., Bridger, A., Casali, M. M., Geballe, T. R., Puxley, P., Smith, M. G., Wright, G. S., Ramsay, S. K., Baker, A. C., Espey, B. R., & Ward, M. J. (1991). The systemic redshift of the quasar 1331 + 170. *ApJ*, 381, L5–L8. ADS: 1991ApJ...381L...5C. doi: 10.1086/186183.

Castor, J. I., Abbott, D. C., & Klein, R. I. (1975). Radiation-driven winds in Of stars. *ApJ*, 195, 157–174. ADS: 1975ApJ...195..157C. doi: 10.1086/153315.

Chajet, L. S. & Hall, P. B. (2013). Magnetohydrodynamic disc winds and linewidth distributions. *MNRAS*, 429, 3214–3229. ADS: 2013MNRAS.429.3214C. doi: 10.1093/mnras/sts580.

Chajet, L. S. & Hall, P. B. (2017). Magnetohydrodynamic disc winds and line width distributions - II. *MNRAS*, 465, 1741–1756. ADS: 2017MNRAS.465.1741C. doi: 10.1093/mnras/stw2626.

Chambers, K. C., Miley, G. K., & van Breugel, W. J. M. (1988). 4C 40.36 - A radio galaxy at a redshift of 2.3. *ApJ*, 327, L47–L50. ADS: 1988ApJ...327L..47C. doi: 10.1086/185137.

Chartas, G., Brandt, W. N., & Gallagher, S. C. (2003). XMM-Newton Reveals the Quasar Outflow in PG 1115+080. *ApJ*, 595, 85–93. ADS: 2003ApJ...595...85C. doi: 10.1086/377299.

Chartas, G., Brandt, W. N., Gallagher, S. C., & Garmire, G. P. (2002). CHANDRA Detects Relativistic Broad Absorption Lines from APM 08279+5255. *ApJ*, 579, 169–175. ADS: 2002ApJ...579..169C. doi: 10.1086/342744.

Chartas, G., Charlton, J., Eracleous, M., Giustini, M., Hidalgo, P. R., Ganguly, R., Hamann, F., Misawa, T., & Tytler, D. (2009). High velocity outflows in narrow absorption line quasars. *NewAR*, 53, 128–132. ADS: 2009NewAR..53..128C. doi: 10.1016/j.newar.2009.07.010.

Chelouche, D. & Netzer, H. (2005). Dynamical and Spectral Modeling of the Ionized Gas and Nuclear Environment in NGC 3783. *ApJ*, 625, 95–107. ADS: 2005ApJ...625...95C. doi: 10.1086/429580.

Chen, K. & Halpern, J. P. (1989). Structure of line-emitting accretion disks in active galactic nuclei - ARP 102B. *ApJ*, 344, 115–124. ADS: 1989ApJ...344..115C. doi: 10.1086/167782.

Chen, K., Halpern, J. P., & Filippenko, A. V. (1989). Kinematic evidence for a relativistic Keplerian disk - ARP 102B. *ApJ*, 339, 742–751. ADS: 1989ApJ...339..742C. doi: 10.1086/167332.

Chiang, J. & Murray, N. (1996). Reverberation Mapping and the Disk-Wind Model of the Broad-Line Region. *ApJ*, 466, 704. ADS: 1996ApJ...466..704C. doi: 10.1086/177543.

Chiu, H.-Y. (1964). Gravitational Collapse. *Physics Today*, 17, 21. ADS: 1964PhT....17e..21C. doi: 10.1063/1.3051610.

Clavel, J., Reichert, G. A., Alloin, D., Crenshaw, D. M., Kriss, G., Krolik, J. H., Malkan, M. A., Netzer, H., Peterson, B. M., Wamsteker, W., Altamore, A., Baribaud, T., Barr, P., Beck, S., Binette, L., Bromage, G. E., Brosch, N., Diaz, A. I., Filippenko, A. V., Fricke, K., Gaskell, C. M., Giommi, P., Glass, I. S., Gondhalekar, P., Hackney, R. L., Halpern, J. P., Hutter, D. J., Joersaeter, S., Kinney, A. L., Kollatschny, W., Koratkar, A., Korista, K. T., Laor, A., Lasota, J.-P., Leibowitz, E., Maoz, D., Martin, P. G., Mazeh, T., Meurs, E. J. A., Nair, A. D., O'Brien, P., Pelat, D., Perez, E., Perola, G. C., Ptak, R. L., Rodriguez-Pascual, P., Rosenblatt, E. I., Sadun, A. C., Santos-Lleo, M., Shaw, R. A., Smith, P. S., Stirpe, G. M., Stoner, R., Sun, W. H., Ulrich, M.-H., van Groningen, E., & Zheng, W. (1991). Steps toward determination of the size and structure of the broad-line region in active galactic nuclei. I - an 8 month campaign of monitoring NGC 5548 with IUE. *ApJ*, 366, 64–81. ADS: 1991ApJ...366...64C. doi: 10.1086/169540.

Coatman, L., Hewett, P. C., Banerji, M., & Richards, G. T. (2016). C IV emission-line properties and systematic trends in quasar black hole mass estimates. *MNRAS*, 461, 647–665. ADS: 2016MNRAS.461..647C. doi: 10.1093/mnras/stw1360.

Coatman, L., Hewett, P. C., Banerji, M., Richards, G. T., Hennawi, J. F., & Prochaska, J. X. (2017). Correcting C IV-based virial black hole masses. *MNRAS*, 465, 2120–2142. ADS: 2017MNRAS.465.2120C. doi: 10.1093/mnras/stw2797.

Cohen, J. (1988). Statistical power analysis for the behavioral sciences. 2nd.

Cohen, M. H., Ogle, P. M., Tran, H. D., Vermeulen, R. C., Miller, J. S., Goodrich, R. W., & Martel, A. R. (1995). Spectropolarimetry of Two Broad Absorption Line Quasars with the W. M. Keck Telescope. *ApJ*, 448, L77. ADS: 1995ApJ...448L..77C. doi: 10.1086/309602.

Cohen, R. D., Puetter, R. C., Rudy, R. J., Ake, T. B., & Foltz, C. B. (1986). Variability of Markarian 1018 - Seyfert 1.9 to Seyfert 1. *ApJ*, 311, 135–141. ADS: 1986ApJ...311..135C. doi: 10.1086/164758.

Collin, S. & Huré, J. M. (2001). Size-mass-luminosity relations in AGN and the role of the accretion disc. *A&A*, 372, 50–58. ADS: 2001A&A...372...50C. doi: 10.1051/0004-6361:

20010475.

Collin, S., Kawaguchi, T., Peterson, B. M., & Vestergaard, M. (2006). Systematic effects in measurement of black hole masses by emission-line reverberation of active galactic nuclei: Eddington ratio and inclination. *A&A*, 456, 75–90. ADS: 2006A&A...456...75C. doi: 10.1051/0004-6361:20064878.

Collin-Souffrin, S., Alloin, D., & Andrillat, Y. (1973). A discussion of the new variations observed in the nucleus of the Seyfert galaxy NGC 3516. *A&A*, 22, 343–354. ADS: 1973A&A....22..343C.

Collin-Souffrin, S. & Dumont, A. M. (1990). Line and continuum emission from the outer regions of accretion discs in active galactic nuclei. II - Radial structure of the disc. *A&A*, 229, 292–328. ADS: 1990A&A...229..292C.

Corbin, M. R. (1990). New results on quasars emission-line redshift differences. *ApJ*, 357, 346–352. ADS: 1990ApJ...357..346C. doi: 10.1086/168925.

Corbin, M. R. (1995). QSO Broad Emission Line Asymmetries: Evidence of Gravitational Redshift? *ApJ*, 447, 496. ADS: 1995ApJ...447..496C. doi: 10.1086/175894.

Corbin, M. R. (1997). Relativistic Effects in the QSO Broad-Line Region. *ApJ*, 485, 517–522. ADS: 1997ApJ...485..517C.

Corbin, M. R. & Boroson, T. A. (1996). Combined Ultraviolet and Optical Spectra of 48 Low-Redshift QSOs and the Relation of the Continuum and Emission-Line Properties. *ApJS*, 107, 69. ADS: 1996ApJS..107...69C. doi: 10.1086/192355.

Corbin, M. R. & Francis, P. J. (1994). The emission-line properties of the QSO population at Z approximately 2. *AJ*, 108, 2016–2024. ADS: 1994AJ....108.2016C. doi: 10.1086/117214.

Cordova, F. A. & Mason, K. O. (1982). High-velocity winds from a dwarf nova during outburst. *ApJ*, 260, 716–721. ADS: 1982ApJ...260..716C. doi: 10.1086/160291.

Cortes, C. & Vapnik, V. (1995). Support-vector networks. *Machine learning*, 20(3), 273–297.

Cottis, C. E., Goad, M. R., Knigge, C., & Scaringi, S. (2010). Searching for the signature of radiative line driving: on the absence of Lyα-NV line-locking features in a large sample of BALQSOs. *MNRAS*, 406, 2094–2112. ADS: 2010MNRAS.406.2094C. doi: 10.1111/j.1365-2966.2010.16839.x.

Cox, D. R. (1958). The regression analysis of binary sequences. *Journal of the Royal Statistical Society. Series B (Methodological)*, 20(2), 215–242.

Crenshaw, D. M. & Blackwell, Jr., J. H. (1990). Evidence for a supermassive black hole in the nucleus of the Seyfert galaxy NGC 5548. *ApJ*, 358, L37–L40. ADS: 1990ApJ...358L..37C. doi: 10.1086/185774.

Crenshaw, D. M., Kraemer, S. B., & George, I. M. (2003). Mass Loss from the Nuclei of Active Galaxies. *A&A*, 41, 117–167. ADS: 2003ARA&A..41..117C. doi: 10.1146/annurev.astro.41.082801.100328.

Crenshaw, D. M., Kraemer, S. B., Hutchings, J. B., Bradley, II, L. D., Gull, T. R., Kaiser, M. E., Nelson, C. H., Ruiz, J. R., & Weistrop, D. (2000). A Kinematic Model for the Narrow-Line Region in NGC 4151. *AJ*, 120, 1731–1738. ADS: 2000AJ....120.1731C. doi: 10.1086/301574.

Curran, P. A. (2014). Monte Carlo error analyses of Spearman's rank test. *ArXiv e-prints*. ADS: 2014arXiv1411.3816C. arXiv: 1411.3816.

Czerny, B. & Hryniewicz, K. (2011). The origin of the broad line region in active galactic nuclei. *A&A*, 525, L8. ADS: 2011A&A...525L...8C. doi: 10.1051/0004-6361/201016025.

Darling, D. A. (1957). The kolmogorov-smirnov, cramer-von mises tests. *The Annals of Mathematical Statistics*, 28(4), 823–838.

Dasyra, K. M., Ho, L. C., Netzer, H., Combes, F., Trakhtenbrot, B., Sturm, E., Armus, L., & Elbaz, D. (2011). A View of the Narrow-line Region in the Infrared: Active Galactic Nuclei with Resolved Fine-structure Lines in the Spitzer Archive. *ApJ*, 740, 94. ADS: 2011ApJ...740...94D. doi: 10.1088/0004-637X/740/2/94.

Davidson, K. (1972). Photoionization and the Emission-Line Spectra of Quasi-Stellar Objects. *ApJ*, 171, 213. ADS: 1972ApJ...171..213D. doi: 10.1086/151274.

Davis, S. W. & Laor, A. (2011). The Radiative Efficiency of Accretion Flows in Individual Active Galactic Nuclei. *ApJ*, 728, 98. ADS: 2011ApJ...728...98D. doi: 10.1088/0004-637X/728/2/98.

Dawson, K. S., Schlegel, D. J., Ahn, C. P., Anderson, S. F., Aubourg, É., Bailey, S., Barkhouser, R. H., Bautista, J. E., Beifiori, A., Berlind, A. A., Bhardwaj, V., Bizyaev, D., Blake, C. H., Blanton, M. R., Blomqvist, M., Bolton, A. S., Borde, A., Bovy, J., Brandt, W. N., Brewington, H., Brinkmann, J., Brown, P. J., Brownstein, J. R., Bundy, K., Busca, N. G., Carithers, W., Carnero, A. R., Carr, M. A., Chen, Y., Comparat, J., Connolly, N., Cope, F., Croft, R. A. C., Cuesta, A. J., da Costa, L. N., Davenport, J. R. A., Delubac, T., de Putter, R., Dhital, S., Ealet, A., Ebelke, G. L., Eisenstein, D. J., Escoffier, S., Fan, X., Filiz Ak, N., Finley, H., Font-Ribera, A., Génova-Santos, R., Gunn, J. E., Guo, H., Haggard, D., Hall, P. B., Hamilton, J.-C., Harris, B., Harris, D. W., Ho, S., Hogg, D. W., Holder, D., Honscheid, K., Huehnerhoff, J., Jordan, B., Jordan, W. P., Kauffmann, G., Kazin, E. A., Kirkby, D., Klaene, M. A., Kneib, J.-P., Le Goff, J.-M., Lee, K.-G., Long, D. C., Loomis, C. P., Lundgren, B., Lupton, R. H., Maia, M. A. G., Makler, M., Malanushenko, E., Malanushenko, V., Mandelbaum, R., Manera, M., Maraston, C., Margala, D., Masters, K. L., McBride, C. K., McDonald, P., McGreer, I. D., McMahon, R. G., Mena, O., Miralda-Escudé, J., Montero-Dorta, A. D., Montesano, F., Muna, D., Myers, A. D., Naugle, T., Nichol, R. C., Noterdaeme, P., Nuza, S. E., Olmstead, M. D., Oravetz, A., Oravetz, D. J., Owen, R., Padmanabhan, N., Palanque-Delabrouille, N., Pan, K., Parejko, J. K., Pâris, I., Percival, W. J., Pérez-Fournon, I., Pérez-Ràfols, I., Petitjean, P., Pfaffenberger, R., Pforr, J., Pieri, M. M., Prada, F., Price-Whelan, A. M., Raddick, M. J., Rebolo, R., Rich, J., Richards, G. T., Rockosi, C. M., Roe, N. A., Ross, A. J., Ross, N. P., Rossi, G., Rubiño-Martin, J. A., Samushia, L., Sánchez, A. G., Sayres, C., Schmidt, S. J., Schneider, D. P., Scóccola, C. G., Seo, H.-J., Shelden, A., Sheldon, E., Shen, Y., Shu, Y., Slosar, A., Smee, S. A., Snedden, S. A., Stauffer, F., Steele, O., Strauss, M. A., Streblyanska, A., Suzuki, N., Swanson, M. E. C., Tal, T., Tanaka, M., Thomas, D., Tinker, J. L., Tojeiro, R.,

Tremonti, C. A., Vargas Magaña, M., Verde, L., Viel, M., Wake, D. A., Watson, M., Weaver, B. A., Weinberg, D. H., Weiner, B. J., West, A. A., White, M., Wood-Vasey, W. M., Yeche, C., Zehavi, I., Zhao, G.-B., & Zheng, Z. (2013). The Baryon Oscillation Spectroscopic Survey of SDSS-III. *AJ*, 145, 10. ADS: 2013AJ....145...10D. doi: 10.1088/0004-6256/145/1/10.

De Breuck, C., van Breugel, W., Röttgering, H., Stern, D., Miley, G., de Vries, W., Stanford, S. A., Kurk, J., & Overzier, R. (2001). Spectroscopy of Ultra-steep-Spectrum Radio Sources. *AJ*, 121, 1241–1265. ADS: 2001AJ....121.1241D. doi: 10.1086/319392.

de Kool, M. (1997). An Overview of Dynamical Models for Outflows in BAL QSOs and Seyferts. In N. Arav, I. Shlosman, & R. J. Weymann (Eds.), *Mass Ejection from Active Galactic Nuclei*, volume 128 of *Astronomical Society of the Pacific Conference Series* (pp. 233). ADS: 1997ASPC..128..233D.

de Kool, M. & Begelman, M. C. (1995). Radiation Pressure–driven Magnetic Disk Winds in Broad Absorption Line Quasi-stellar Objects. *ApJ*, 455, 448. ADS: 1995ApJ...455..448D. doi: 10.1086/176594.

De Rosa, G., Peterson, B. M., Ely, J., Kriss, G. A., Crenshaw, D. M., Horne, K., Korista, K. T., Netzer, H., Pogge, R. W., Arévalo, P., Barth, A. J., Bentz, M. C., Brandt, W. N., Breeveld, A. A., Brewer, B. J., Dalla Bontà, E., De Lorenzo-Cáceres, A., Denney, K. D., Dietrich, M., Edelson, R., Evans, P. A., Fausnaugh, M. M., Gehrels, N., Gelbord, J. M., Goad, M. R., Grier, C. J., Grupe, D., Hall, P. B., Kaastra, J., Kelly, B. C., Kennea, J. A., Kochanek, C. S., Lira, P., Mathur, S., McHardy, I. M., Nousek, J. A., Pancoast, A., Papadakis, I., Pei, L., Schimoia, J. S., Siegel, M., Starkey, D., Treu, T., Uttley, P., Vaughan, S., Vestergaard, M., Villforth, C., Yan, H., Young, S., & Zu, Y. (2015). Space Telescope and Optical Reverberation Mapping Project.I. Ultraviolet Observations of the Seyfert 1 Galaxy NGC 5548 with the Cosmic Origins Spectrograph on Hubble Space Telescope. *ApJ*, 806, 128. ADS: 2015ApJ...806..128D. doi: 10.1088/0004-637X/806/1/128.

Decarli, R., Labita, M., Treves, A., & Falomo, R. (2008). On the geometry of broad emission region in quasars. *MNRAS*, 387, 1237–1247. ADS: 2008MNRAS.387.1237D. doi: 10.1111/j.1365-2966.2008.13320.x.

Denney, K. D. (2012). Are Outflows Biasing Single-epoch C IV Black Hole Mass Estimates? *ApJ*, 759, 44. ADS: 2012ApJ...759...44D. doi: 10.1088/0004-637X/759/1/44.

Denney, K. D., De Rosa, G., Croxall, K., Gupta, A., Bentz, M. C., Fausnaugh, M. M., Grier, C. J., Martini, P., Mathur, S., Peterson, B. M., Pogge, R. W., & Shappee, B. J. (2014). The Typecasting of Active Galactic Nuclei: Mrk 590 no Longer Fits the Role. *ApJ*, 796, 134. ADS: 2014ApJ...796..134D. doi: 10.1088/0004-637X/796/2/134.

Denney, K. D., Horne, K., Shen, Y., Brandt, W. N., Ho, L. C., Peterson, B. M., Richards, G. T., Trump, J. R., & Ge, J. (2016). The Sloan Digital Sky Survey Reverberation Mapping Project: An Investigation of Biases in C IV Emission Line Properties. *ApJS*, 224, 14. ADS: 2016ApJS..224...14D. doi: 10.3847/0067-0049/224/2/14.

Denney, K. D., Peterson, B. M., Pogge, R. W., Adair, A., Atlee, D. W., Au-Yong, K., Bentz, M. C., Bird, J. C., Brokofsky, D. J., Chisholm, E., Comins, M. L., Dietrich, M., Doroshenko, V. T., Eastman, J. D., Efimov, Y. S., Ewald, S., Ferbey, S., Gaskell, C. M., Hedrick, C. H.,

Jackson, K., Klimanov, S. A., Klimek, E. S., Kruse, A. K., Ladéroute, A., Lamb, J. B., Leighly, K., Minezaki, T., Nazarov, S. V., Onken, C. A., Petersen, E. A., Peterson, P., Poindexter, S., Sakata, Y., Schlesinger, K. J., Sergeev, S. G., Skolski, N., Stieglitz, L., Tobin, J. J., Unterborn, C., Vestergaard, M., Watkins, A. E., Watson, L. C., & Yoshii, Y. (2009). Diverse Kinematic Signatures from Reverberation Mapping of the Broad-Line Region in AGNs. *ApJ*, 704, L80–L84. ADS: 2009ApJ...704L..80D. doi: 10.1088/0004-637X/704/2/L80.

Denney, K. D., Pogge, R. W., Assef, R. J., Kochanek, C. S., Peterson, B. M., & Vestergaard, M. (2013). C IV Line-width Anomalies: The Perils of Low Signal-to-noise Spectra. *ApJ*, 775, 60. ADS: 2013ApJ...775...60D. doi: 10.1088/0004-637X/775/1/60.

Di Matteo, T., Colberg, J., Springel, V., Hernquist, L., & Sijacki, D. (2008). Direct Cosmological Simulations of the Growth of Black Holes and Galaxies. *ApJ*, 676, 33–53. ADS: 2008ApJ...676...33D. doi: 10.1086/524921.

Di Matteo, T., Springel, V., & Hernquist, L. (2005). Energy input from quasars regulates the growth and activity of black holes and their host galaxies. *Nature*, 433, 604–607. ADS: 2005Natur.433..604D. doi: 10.1038/nature03335.

di Serego Alighieri, S., Cimatti, A., Fosbury, R. A. E., & Hes, R. (1997). Anisotropic [OIII] emission in radio loud AGN. *A&A*, 328, 510–516. ADS: 1997A&A...328..510D.

DiPompeo, M. A., Brotherton, M. S., Cales, S. L., & Runnoe, J. C. (2012). The rest-frame ultraviolet properties of radio-loud broad absorption line quasars. *MNRAS*, 427, 1135–1152. ADS: 2012MNRAS.427.1135D. doi: 10.1111/j.1365-2966.2012.21971.x.

DiPompeo, M. A., Brotherton, M. S., De Breuck, C., & Laurent-Muehleisen, S. (2011). A Very Large Array Survey of Radio-selected SDSS Broad Absorption Line Quasars. *ApJ*, 743, 71. ADS: 2011ApJ...743...71D. doi: 10.1088/0004-637X/743/1/71.

DiPompeo, M. A., Hickox, R. C., Eftekharzadeh, S., & Myers, A. D. (2017). The characteristic halo masses of half-a-million WISE-selected quasars. *MNRAS*, 469, 4630–4643. ADS: 2017MNRAS.469.4630D. doi: 10.1093/mnras/stx1215.

DiPompeo, M. A., Runnoe, J. C., Brotherton, M. S., & Myers, A. D. (2013). An Infrared Excess Identified in Radio-loud Broad Absorption Line Quasars. *ApJ*, 762, 111. ADS: 2013ApJ...762..111D. doi: 10.1088/0004-637X/762/2/111.

Du, P., Hu, C., Lu, K.-X., Huang, Y.-K., Cheng, C., Qiu, J., Li, Y.-R., Zhang, Y.-W., Fan, X.-L., Bai, J.-M., Bian, W.-H., Yuan, Y.-F., Kaspi, S., Ho, L. C., Netzer, H., Wang, J.-M., & SEAMBH Collaboration (2015). Supermassive Black Holes with High Accretion Rates in Active Galactic Nuclei. IV. Hβ Time Lags and Implications for Super-Eddington Accretion. *ApJ*, 806, 22. ADS: 2015ApJ...806...22D. doi: 10.1088/0004-637X/806/1/22.

Dullemond, C. P. & van Bemmel, I. M. (2005). Clumpy tori around active galactic nuclei. *A&A*, 436, 47–56. ADS: 2005A&A...436...47D. doi: 10.1051/0004-6361:20041763.

Dumont, A. M. & Collin-Souffrin, S. (1990). Line and Continuum Emission from the Outer Regions of Accretion Discs in Active Galactic Nuclei - Part IV - Line Emission. *A&A*, 229, 313. ADS: 1990A&A...229..313D.

Dyda, S. & Proga, D. (2018). Non-axisymmetric line-driven disc winds - I. Disc perturbations. *MNRAS*, 475, 3786–3796. ADS: 2018MNRAS.475.3786D. doi: 10.1093/mnras/sty030.

Efron, B. (1979). Bootstrap methods: Another look at the jackknife. *The Annals of Statistics*, 7(1), 1–26. doi: 10.1214/aos/1176344552.

Eisenstein, D. J., Weinberg, D. H., Agol, E., Aihara, H., Allende Prieto, C., Anderson, S. F., Arns, J. A., Aubourg, É., Bailey, S., Balbinot, E., & et al. (2011). SDSS-III: Massive Spectroscopic Surveys of the Distant Universe, the Milky Way, and Extra-Solar Planetary Systems. *AJ*, 142, 72. ADS: 2011AJ....142...72E. doi: 10.1088/0004-6256/142/3/72.

Elitzur, M. (2012). On the Unification of Active Galactic Nuclei. *ApJ*, 747, L33. ADS: 2012ApJ...747L..33E. doi: 10.1088/2041-8205/747/2/L33.

Elitzur, M. & Ho, L. C. (2009). On the Disappearance of the Broad-Line Region in Low-Luminosity Active Galactic Nuclei. *ApJ*, 701, L91–L94. ADS: 2009ApJ...701L..91E. doi: 10.1088/0004-637X/701/2/L91.

Elitzur, M., Ho, L. C., & Trump, J. R. (2014). Evolution of broad-line emission from active galactic nuclei. *MNRAS*, 438, 3340–3351. ADS: 2014MNRAS.438.3340E. doi: 10.1093/mnras/stt2445.

Elitzur, M. & Shlosman, I. (2006). The AGN-obscuring Torus: The End of the "Doughnut" Paradigm? *ApJ*, 648, L101–L104. ADS: 2006ApJ...648L.101E. doi: 10.1086/508158.

Elvis, M. (2000). A Structure for Quasars. *ApJ*, 545, 63–76. ADS: 2000ApJ...545...63E. doi: 10.1086/317778.

Elvis, M. (2004). Quasar Atmospheres: Toward a 'Low' Theory for Quasars. In G. T. Richards & P. B. Hall (Eds.), *AGN Physics with the Sloan Digital Sky Survey*, volume 311 of *Astronomical Society of the Pacific Conference Series* (pp. 109). ADS: 2004ASPC..311..109E.

Elvis, M. (2017). Quasar Rain: The Broad Emission Line Region as Condensations in the Warm Accretion Disk Wind. *ApJ*, 847, 56. ADS: 2017ApJ...847...56E. doi: 10.3847/1538-4357/aa82b6.

Emmering, R. T., Blandford, R. D., & Shlosman, I. (1992). Magnetic acceleration of broad emission-line clouds in active galactic nuclei. *ApJ*, 385, 460–477. ADS: 1992ApJ...385..460E. doi: 10.1086/170955.

Engmann, S. & Cousineau, D. (2011). Comparing distributions: the two-sample anderson–darling test as an alternative to the kolmogorov–smirnov test. 6, 1–17.

Eracleous, M. (2006). Accretion Disks and the Broad-Line Regions of Active Galactic Nuclei. In C. M. Gaskell, I. M. McHardy, B. M. Peterson, & S. G. Sergeev (Eds.), *Astronomical Society of the Pacific Conference Series*, volume 360 of *Astronomical Society of the Pacific Conference Series* (pp. 217). ADS: 2006ASPC..360..217E.

Eracleous, M. & Halpern, J. P. (1994). Doubled-peaked emission lines in active galactic nuclei. *ApJS*, 90, 1–30. ADS: 1994ApJS...90....1E. doi: 10.1086/191856.

Eracleous, M. & Halpern, J. P. (2003). Completion of a Survey and Detailed Study of Double-

peaked Emission Lines in Radio-loud Active Galactic Nuclei. *ApJ*, 599, 886–908. ADS: 2003ApJ...599..886E. doi: 10.1086/379540.

Eracleous, M., Lewis, K. T., & Flohic, H. M. L. G. (2009). Double-peaked emission lines as a probe of the broad-line regions of active galactic nuclei. *NewAR*, 53, 133–139. ADS: 2009NewAR..53..133E. doi: 10.1016/j.newar.2009.07.005.

Eracleous, M., Livio, M., Halpern, J. P., & Storchi-Bergmann, T. (1995). Elliptical accretion disks in active galactic nuclei. *ApJ*, 438, 610–622. ADS: 1995ApJ...438..610E. doi: 10.1086/175104.

Espey, B. R., Carswell, R. F., Bailey, J. A., Smith, M. G., & Ward, M. J. (1989). H-alpha emission lines in high-redshift quasars. *ApJ*, 342, 666–676. ADS: 1989ApJ...342..666E. doi: 10.1086/167627.

Everett, J., Königl, A., & Arav, N. (2002). Observational Evidence for a Multiphase Outflow in Quasar FIRST J1044+3656. *ApJ*, 569, 671–675. ADS: 2002ApJ...569..671E. doi: 10.1086/339346.

Everett, J. E. (2005). Radiative Transfer and Acceleration in Magnetocentrifugal Winds. *ApJ*, 631, 689–706. ADS: 2005ApJ...631..689E. doi: 10.1086/432678.

Everett, J. E. & Murray, N. (2007). Large-Scale Parker Winds in Active Galactic Nuclei. *ApJ*, 656, 93–104. ADS: 2007ApJ...656...93E. doi: 10.1086/510324.

Fabian, A. C. (2012). Observational Evidence of Active Galactic Nuclei Feedback. *ARA&A*, 50, 455–489. ADS: 2012ARA&A..50..455F. doi: 10.1146/annurev-astro-081811-125521.

Fanaroff, B. L. & Riley, J. M. (1974). The morphology of extragalactic radio sources of high and low luminosity. *MNRAS*, 167, 31P–36P. ADS: 1974MNRAS.167P..31F. doi: 10.1093/mnras/167.1.31P.

Fanti, C., Fanti, R., Lari, C., Padrielli, L., van der Laan, H., & de Ruiter, H. (1977). A search for radio emission from a sample of optically selected quasars. *A&A*, 61, 487–491. ADS: 1977A&A....61..487F.

Feldmeier, A., Puls, J., & Pauldrach, A. W. A. (1997). A possible origin for X-rays from O stars. *A&A*, 322, 878–895. ADS: 1997A&A...322..878F.

Fernandes, C. A. C., Jarvis, M. J., Martínez-Sansigre, A., Rawlings, S., Afonso, J., Hardcastle, M. J., Lacy, M., Stevens, J. A., & Vardoulaki, E. (2015). Black hole masses, accretion rates and hot- and cold-mode accretion in radio galaxies at z $\sim$ 1. *MNRAS*, 447, 1184–1203. ADS: 2015MNRAS.447.1184F. doi: 10.1093/mnras/stu2517.

Ferrarese, L. & Ford, H. (2005). Supermassive Black Holes in Galactic Nuclei: Past, Present and Future Research. *SSRv*, 116, 523–624. ADS: 2005SSRv..116..523F. doi: 10.1007/s11214-005-3947-6.

Ferrarese, L. & Merritt, D. (2000). A Fundamental Relation between Supermassive Black Holes and Their Host Galaxies. *ApJ*, 539, L9–L12. ADS: 2000ApJ...539L...9F. doi: 10.1086/312838.

Ferrarese, L., Pogge, R. W., Peterson, B. M., Merritt, D., Wandel, A., & Joseph, C. L. (2001). Supermassive Black Holes in Active Galactic Nuclei. I. The Consistency of Black Hole Masses in Quiescent and Active Galaxies. *ApJ*, 555, L79–L82. ADS: 2001ApJ...555L..79F. doi: 10.1086/322528.

Ferrucci, D., Brown, E., Chu-Carroll, J., Fan, J., Gondek, D., Kalyanpur, A. A., Lally, A., Murdock, J. W., Nyberg, E., Prager, J., et al. (2010). Building watson: An overview of the deepqa project. *AI magazine*, 31(3), 59–79.

Fine, S., Croom, S. M., Hopkins, P. F., Hernquist, L., Bland-Hawthorn, J., Colless, M., Hall, P. B., Miller, L., Myers, A. D., Nichol, R., Pimbblet, K. A., Ross, N. P., Schneider, D. P., Shanks, T., & Sharp, R. G. (2008). Constraining the quasar population with the broad-line width distribution. *MNRAS*, 390, 1413–1429. ADS: 2008MNRAS.390.1413F. doi: 10.1111/j.1365-2966.2008.13691.x.

Fine, S., Jarvis, M. J., & Mauch, T. (2011). Orientation effects in quasar spectra: the broad- and narrow-line regions. *MNRAS*, 412, 213–222. ADS: 2011MNRAS.412..213F. doi: 10.1111/j.1365-2966.2010.17898.x.

Fischer, T. C., Crenshaw, D. M., Kraemer, S. B., & Schmitt, H. R. (2013). Determining Inclinations of Active Galactic Nuclei via their Narrow-line Region Kinematics. I. Observational Results. *ApJS*, 209, 1. ADS: 2013ApJS..209....1F. doi: 10.1088/0067-0049/209/1/1.

Flohic, H. M. L. G., Eracleous, M., & Bogdanović, T. (2012). Effects of an Accretion Disk Wind on the Profile of the Balmer Emission Lines from Active Galactic Nuclei. *ApJ*, 753, 133. ADS: 2012ApJ...753..133F. doi: 10.1088/0004-637X/753/2/133.

Foltz, C. B., Weymann, R. J., Morris, S. L., & Turnshek, D. A. (1987). The complex absorption spectrum of the broad absorption line QSO 1303 + 308. *ApJ*, 317, 450–459. ADS: 1987ApJ...317..450F. doi: 10.1086/165290.

Foltz, C. B., Weymann, R. J., Peterson, B. M., Sun, L., Malkan, M. A., & Chaffee, Jr., F. H. (1986). C IV absorption systems in QSO spectra - Is the character of systems with Z(abs) = about Z(em) different from those with Z(abs) much less than Z(em)? *ApJ*, 307, 504–534. ADS: 1986ApJ...307..504F. doi: 10.1086/164440.

Fraix-Burnet, D., Marziani, P., D'Onofrio, M., & Dultzin, D. (2017). The phylogeny of quasars and the ontogeny of their central black holes. *Frontiers in Astronomy and Space Sciences*, 4, 1. ADS: 2017FrASS...4....1F. doi: 10.3389/fspas.2017.00001.

Francis, P. J., Hewett, P. C., Foltz, C. B., & Chaffee, F. H. (1992). An objective classification scheme for QSO spectra. *ApJ*, 398, 476–490. ADS: 1992ApJ...398..476F. doi: 10.1086/171870.

Friend, D. B. & Abbott, D. C. (1986). The theory of radiatively driven stellar winds. III - Wind models with finite disk correction and rotation. *ApJ*, 311, 701–707. ADS: 1986ApJ...311..701F. doi: 10.1086/164809.

Gallagher, S. C. & Everett, J. E. (2007). Stratified Quasar Winds: Integrating X-ray and Infrared Views of Broad Absorption-line Quasars. In L. C. Ho & J.-W. Wang (Eds.), *The*

Central Engine of Active Galactic Nuclei, volume 373 of *Astronomical Society of the Pacific Conference Series* (pp. 305). ADS: 2007ASPC..373..305G.

Gallagher, S. C., Everett, J. E., Abado, M. M., & Keating, S. K. (2015). Investigating the structure of the windy torus in quasars. *MNRAS*, 451, 2991–3000. ADS: 2015MNRAS.451.2991G. doi: 10.1093/mnras/stv1126.

Gallagher, S. C., Hines, D. C., Blaylock, M., Priddey, R. S., Brandt, W. N., & Egami, E. E. (2007). Radio through X-Ray Spectral Energy Distributions of 38 Broad Absorption Line Quasars. *ApJ*, 665, 157–173. ADS: 2007ApJ...665..157G. doi: 10.1086/519438.

Ganguly, R. & Brotherton, M. S. (2008). On the Fraction of Quasars with Outflows. *ApJ*, 672, 102–107. ADS: 2008ApJ...672..102G. doi: 10.1086/524106.

Ganguly, R., Brotherton, M. S., Cales, S., Scoggins, B., Shang, Z., & Vestergaard, M. (2007). Outflows and the Physical Properties of Quasars. *ApJ*, 665, 990–1003. ADS: 2007ApJ...665..990G. doi: 10.1086/519759.

Ganguly, R., Sembach, K. R., Tripp, T. M., Savage, B. D., & Wakker, B. P. (2006). High-Resolution Absorption Spectroscopy of Multiphase, High-Metallicity Gas Associated with the Luminous Quasar HE 0226-4110. *ApJ*, 645, 868–889. ADS: 2006ApJ...645..868G. doi: 10.1086/504395.

Gaskell, C. M. (1982). A redshift difference between high and low ionization emission-line regions in QSOs - Evidence for radial motions. *ApJ*, 263, 79–86. ADS: 1982ApJ...263...79G. doi: 10.1086/160481.

Gaskell, C. M. (1983). Quasars as supermassive binaries. In J.-P. Swings (Ed.), *Liege International Astrophysical Colloquia*, volume 24 of *Liege International Astrophysical Colloquia* (pp. 473–477). ADS: 1983LIACo..24..473G.

Gaskell, C. M. (1988). Direct evidence for gravitational domination of the motion of gas within one light-week of the central object in NGC 4151 and the determination of the mass of the probable black hole. *ApJ*, 325, 114–118. ADS: 1988ApJ...325..114G. doi: 10.1086/165986.

Gaskell, C. M. (2009). What broad emission lines tell us about how active galactic nuclei work. *NewAR*, 53, 140–148. ADS: 2009NewAR..53..140G. doi: 10.1016/j.newar.2009.09.006.

Gaskell, C. M. & Goosmann, R. W. (2016). The case for inflow of the broad-line region of active galactic nuclei. *Ap&SS*, 361, 67. ADS: 2016Ap&SS.361...67G. doi: 10.1007/s10509-015-2648-1.

Gaskell, C. M. & Sparke, L. S. (1986). Line variations in quasars and Seyfert galaxies. *ApJ*, 305, 175–186. ADS: 1986ApJ...305..175G. doi: 10.1086/164238.

Gauss, C. (1809). *Theoria motus corporum coelestium in sectionibus conicis solem ambientium*. Carl Friedrich Gauss Werke. sumtibus F. Perthes et I. H. Besser. https://books.google.com.au/books?id=ORUOAAAAQAAJ.

Gayley, K. G. (1995). An Improved Line-Strength Parameterization in Hot-Star Winds. *ApJ*, 454, 410. ADS: 1995ApJ...454..410G. doi: 10.1086/176492.

Gebhardt, K., Kormendy, J., Ho, L. C., Bender, R., Bower, G., Dressler, A., Faber, S. M., Filippenko, A. V., Green, R., Grillmair, C., Lauer, T. R., Magorrian, J., Pinkney, J., Richstone, D., & Tremaine, S. (2000). Black Hole Mass Estimates from Reverberation Mapping and from Spatially Resolved Kinematics. *ApJ*, 543, L5–L8. ADS: 2000ApJ...543L...5G. doi: 10.1086/318174.

George, I. M., Turner, T. J., Netzer, H., Nandra, K., Mushotzky, R. F., & Yaqoob, T. (1998). ASCA Observations of Seyfert 1 Galaxies. III. The Evidence for Absorption and Emission Due to Photoionized Gas. *ApJS*, 114, 73–120. ADS: 1998ApJS..114...73G. doi: 10.1086/313067.

Gezari, S., Halpern, J. P., & Eracleous, M. (2007). Long-Term Profile Variability of Double-peaked Emission Lines in Active Galactic Nuclei. *ApJS*, 169, 167–212. ADS: 2007ApJS..169..167G. doi: 10.1086/511032.

Gezari, S., Hung, T., Cenko, S. B., Blagorodnova, N., Yan, L., Kulkarni, S. R., Mooley, K., Kong, A. K. H., Cantwell, T. M., Yu, P. C., Cao, Y., Fremling, C., Neill, J. D., Ngeow, C.-C., Nugent, P. E., & Wozniak, P. (2017). iPTF Discovery of the Rapid "Turn-on" of a Luminous Quasar. *ApJ*, 835, 144. ADS: 2017ApJ...835..144G. doi: 10.3847/1538-4357/835/2/144.

Ghisellini, G., Padovani, P., Celotti, A., & Maraschi, L. (1993). Relativistic bulk motion in active galactic nuclei. *ApJ*, 407, 65–82. ADS: 1993ApJ...407...65G. doi: 10.1086/172493.

Ghosh, K. K. & Punsly, B. (2007). The Physical Nature of Polar Broad Absorption Line Quasars. *ApJ*, 661, L139–L142. ADS: 2007ApJ...661L.139G. doi: 10.1086/518859.

Gibson, R. R., Brandt, W. N., Schneider, D. P., & Gallagher, S. C. (2008). Quasar Broad Absorption Line Variability on Multiyear Timescales. *ApJ*, 675, 985–1001. ADS: 2008ApJ...675..985G. doi: 10.1086/527462.

Gibson, R. R., Jiang, L., Brandt, W. N., Hall, P. B., Shen, Y., Wu, J., Anderson, S. F., Schneider, D. P., Vanden Berk, D., Gallagher, S. C., Fan, X., & York, D. G. (2009). A Catalog of Broad Absorption Line Quasars in Sloan Digital Sky Survey Data Release 5. *ApJ*, 692, 758–777. ADS: 2009ApJ...692..758G. doi: 10.1088/0004-637X/692/1/758.

Gini, C. (1921). Measurement of inequality of incomes. *The Economic Journal*, 31(121), 124–126.

Goad, M. & Wanders, I. (1996). The Effect of a Variable Anisotropic Continuum Source upon the Broad Emission Line Profiles and Responses. *ApJ*, 469, 113. ADS: 1996ApJ...469..113G. doi: 10.1086/177764.

Goad, M. R., Korista, K. T., & Ruff, A. J. (2012). The broad emission-line region: the confluence of the outer accretion disc with the inner edge of the dusty torus. *MNRAS*, 426, 3086–3111. ADS: 2012MNRAS.426.3086G. doi: 10.1111/j.1365-2966.2012.21808.x.

Golub, G. H. & van Loan, C. F. (1980). An Analysis of the Total Least Squares Problem. *SIAM Journal on Numerical Analysis*, 17, 883–893. ADS: 1980SJNA...17..883G. doi: 10.1137/0717073.

Goodrich, R. W. (1997). On the Fraction of Broad Absorption Line Quasi-stellar Objects. *ApJ*, 474, 606–611. ADS: 1997ApJ...474..606G. doi: 10.1086/303481.

Goodrich, R. W. & Miller, J. S. (1995). Polarization Clues to the Structure of Broad Absorption Line Quasi-stellar Objects. *ApJ*, 448, L73. ADS: 1995ApJ...448L..73G. doi: 10.1086/309600.

Graham, A. W., Erwin, P., Caon, N., & Trujillo, I. (2001). A Correlation between Galaxy Light Concentration and Supermassive Black Hole Mass. *ApJ*, 563, L11–L14. ADS: 2001ApJ...563L..11G. doi: 10.1086/338500.

Graham, A. W., Onken, C. A., Athanassoula, E., & Combes, F. (2011). An expanded M_{bh}-σ diagram, and a new calibration of active galactic nuclei masses. *MNRAS*, 412, 2211–2228. ADS: 2011MNRAS.412.2211G. doi: 10.1111/j.1365-2966.2010.18045.x.

Granato, G. L., De Zotti, G., Silva, L., Bressan, A., & Danese, L. (2004). A Physical Model for the Coevolution of QSOs and Their Spheroidal Hosts. *ApJ*, 600, 580–594. ADS: 2004ApJ...600..580G. doi: 10.1086/379875.

Greene, J. E. & Ho, L. C. (2005). Estimating Black Hole Masses in Active Galaxies Using the Hα Emission Line. *ApJ*, 630, 122–129. ADS: 2005ApJ...630..122G. doi: 10.1086/431897.

Greene, J. E., Hood, C. E., Barth, A. J., Bennert, V. N., Bentz, M. C., Filippenko, A. V., Gates, E., Malkan, M. A., Treu, T., Walsh, J. L., & Woo, J.-H. (2010). The Lick AGN Monitoring Project: Alternate Routes to a Broad-line Region Radius. *ApJ*, 723, 409–416. ADS: 2010ApJ...723..409G. doi: 10.1088/0004-637X/723/1/409.

Gregg, M. D., Becker, R. H., & de Vries, W. (2006). FR II Broad Absorption Line Quasars and the Life Cycle of Quasars. *ApJ*, 641, 210–216. ADS: 2006ApJ...641..210G. doi: 10.1086/500381.

Grier, C. J. (2013). *Active galactic nuclei: Masses and dynamics*. PhD thesis, The Ohio State University. ADS: 2013PhDT.......332G.

Grier, C. J., Hall, P. B., Brandt, W. N., Trump, J. R., Shen, Y., Vivek, M., Filiz Ak, N., Chen, Y., Dawson, K. S., Denney, K. D., Green, P. J., Jiang, L., Kochanek, C. S., McGreer, I. D., Pâris, I., Peterson, B. M., Schneider, D. P., Tao, C., Wood-Vasey, W. M., Bizyaev, D., Ge, J., Kinemuchi, K., Oravetz, D., Pan, K., & Simmons, A. (2015). The Sloan Digital Sky Survey Reverberation Mapping Project: Rapid CIV Broad Absorption Line Variability. *ApJ*, 806, 111. ADS: 2015ApJ...806..111G. doi: 10.1088/0004-637X/806/1/111.

Grier, C. J., Peterson, B. M., Horne, K., Bentz, M. C., Pogge, R. W., Denney, K. D., De Rosa, G., Martini, P., Kochanek, C. S., Zu, Y., Shappee, B., Siverd, R., Beatty, T. G., Sergeev, S. G., Kaspi, S., Araya Salvo, C., Bird, J. C., Bord, D. J., Borman, G. A., Che, X., Chen, C., Cohen, S. A., Dietrich, M., Doroshenko, V. T., Efimov, Y. S., Free, N., Ginsburg, I., Henderson, C. B., King, A. L., Mogren, K., Molina, M., Mosquera, A. M., Nazarov, S. V., Okhmat, D. N., Pejcha, O., Rafter, S., Shields, J. C., Skowron, J., Szczygiel, D. M., Valluri, M., & van Saders, J. L. (2013). The Structure of the Broad-line Region in Active Galactic Nuclei. I. Reconstructed Velocity-delay Maps. *ApJ*, 764, 47. ADS: 2013ApJ...764...47G. doi: 10.1088/0004-637X/764/1/47.

Gu, Q., Maiolino, R., & Dultzin-Hacyan, D. (2001). Nuclear obscuration and scattering in Seyfert 2 galaxies. *A&A*, 366, 765–770. ADS: 2001A&A...366..765G. doi: 10.1051/0004-6361:20000302.

Guainazzi, M. (2002). The formerly X-ray reflection-dominated Seyfert 2 galaxy NGC 6300. *MNRAS*, 329, L13–L17. ADS: 2002MNRAS.329L..13G. doi: 10.1046/j.1365-8711.2002.05132.x.

Gültekin, K., Richstone, D. O., Gebhardt, K., Lauer, T. R., Tremaine, S., Aller, M. C., Bender, R., Dressler, A., Faber, S. M., Filippenko, A. V., Green, R., Ho, L. C., Kormendy, J., Magorrian, J., Pinkney, J., & Siopis, C. (2009). The M-σ and M-L Relations in Galactic Bulges, and Determinations of Their Intrinsic Scatter. *ApJ*, 698, 198–221. ADS: 2009ApJ...698..198G. doi: 10.1088/0004-637X/698/1/198.

Gürkan, G., Hardcastle, M. J., & Jarvis, M. J. (2014). The Wide-field Infrared Survey Explorer properties of complete samples of radio-loud active galactic nucleus. *MNRAS*, 438, 1149–1161. ADS: 2014MNRAS.438.1149G. doi: 10.1093/mnras/stt2264.

Hall, P. B., Anderson, S. F., Strauss, M. A., York, D. G., Richards, G. T., Fan, X., Knapp, G. R., Schneider, D. P., Vanden Berk, D. E., Geballe, T. R., Bauer, A. E., Becker, R. H., Davis, M., Rix, H.-W., Nichol, R. C., Bahcall, N. A., Brinkmann, J., Brunner, R., Connolly, A. J., Csabai, I., Doi, M., Fukugita, M., Gunn, J. E., Haiman, Z., Harvanek, M., Heckman, T. M., Hennessy, G. S., Inada, N., Ivezić, Ž., Johnston, D., Kleinman, S., Krolik, J. H., Krzesinski, J., Kunszt, P. Z., Lamb, D. Q., Long, D. C., Lupton, R. H., Miknaitis, G., Munn, J. A., Narayanan, V. K., Neilsen, E., Newman, P. R., Nitta, A., Okamura, S., Pentericci, L., Pier, J. R., Schlegel, D. J., Snedden, S., Szalay, A. S., Thakar, A. R., Tsvetanov, Z., White, R. L., & Zheng, W. (2002). Unusual Broad Absorption Line Quasars from the Sloan Digital Sky Survey. *ApJS*, 141, 267–309. ADS: 2002ApJS..141..267H. doi: 10.1086/340546.

Hall, P. B., Brandt, W. N., Petitjean, P., Pâris, I., Filiz Ak, N., Shen, Y., Gibson, R. R., Aubourg, É., Anderson, S. F., Schneider, D. P., Bizyaev, D., Brinkmann, J., Malanushenko, E., Malanushenko, V., Myers, A. D., Oravetz, D. J., Ross, N. P., Shelden, A., Simmons, A. E., Streblyanska, A., Weaver, B. A., & York, D. G. (2013). Broad absorption line quasars with redshifted troughs: high-velocity infall or rotationally dominated outflows? *MNRAS*, 434, 222–256. ADS: 2013MNRAS.434..222H. doi: 10.1093/mnras/stt1012.

Halpern, J. P. (1984). Variable X-ray absorption in the QSO MR 2251 - 178. *ApJ*, 281, 90–94. ADS: 1984ApJ...281...90H. doi: 10.1086/162077.

Halpern, J. P., Eracleous, M., Filippenko, A. V., & Chen, K. (1996). Hubble Space Telescope Ultraviolet Spectrum of ARP 102B, the Prototypical Double-peaked Emission-Line AGN. *ApJ*, 464, 704. ADS: 1996ApJ...464..704H. doi: 10.1086/177357.

Hamann, F. (1997). Metal Abundances and Ionization in Quasar Intrinsic Absorbers. *ApJS*, 109, 279–305. ADS: 1997ApJS..109..279H. doi: 10.1086/312980.

Hamann, F. (1998). Broad P V Absorption in the QSO PG 1254+047: Column Densities, Ionizations, and Metal Abundances in Broad Absorption Line Winds. *ApJ*, 500, 798–809. ADS: 1998ApJ...500..798H. doi: 10.1086/305776.

Hamann, F., Barlow, T. A., & Junkkarinen, V. (1997). Time-variable Intrinsic Absorption Lines in the Quasi-stellar Object Q2343+125. *ApJ*, 478, 87–93. ADS: 1997ApJ...478...87H. doi: 10.1086/303782.

Hamann, F., Chartas, G., McGraw, S., Rodriguez Hidalgo, P., Shields, J., Capellupo, D., Charlton, J., & Eracleous, M. (2013). Extreme-velocity quasar outflows and the role of X-ray shielding. *MNRAS*, 435, 133–148. ADS: 2013MNRAS.435..133H. doi: 10.1093/mnras/stt1231.

Hamann, F. & Ferland, G. (1993). The Chemical Evolution of QSOs and the Implications for Cosmology and Galaxy Formation. *ApJ*, 418, 11. ADS: 1993ApJ...418...11H. doi: 10.1086/173366.

Hamann, F., Simon, L., Rodriguez Hidalgo, P., & Capellupo, D. (2012). Narrow UV Absorption Line Outflows from Quasars. In G. Chartas, F. Hamann, & K. M. Leighly (Eds.), *AGN Winds in Charleston*, volume 460 of *Astronomical Society of the Pacific Conference Series* (pp.47). ADS: 2012ASPC..460...47H. arXiv: 1204.3791.

Hamann, W.-R., Feldmeier, A., & Oskinova, L. M., Eds. (2008). *Clumping in hot-star winds*. Universit'atsverlag Potsdam. ADS: 2008cihw.conf.....H.

Hao, L., Spoon, H. W. W., Sloan, G. C., Marshall, J. A., Armus, L., Tielens, A. G. G. M., Sargent, B., van Bemmel, I. M., Charmandaris, V., Weedman, D. W., & Houck, J. R. (2005). The Detection of Silicate Emission from Quasars at 10 and 18 Microns. *ApJ*, 625, L75–L78. ADS: 2005ApJ...625L..75H. doi: 10.1086/431227.

Hardcastle, M. J., Evans, D. A., & Croston, J. H. (2007). Hot and cold gas accretion and feedback in radio-loud active galaxies. *MNRAS*, 376, 1849–1856. ADS: 2007MNRAS.376.1849H. doi: 10.1111/j.1365-2966.2007.11572.x.

Heckman, T. M. & Best, P. N. (2014). The Coevolution of Galaxies and Supermassive Black Holes: Insights from Surveys of the Contemporary Universe. *ARA&A*, 52, 589–660. ADS: 2014ARA&A..52..589H. doi: 10.1146/annurev-astro-081913-035722.

Heisler, C. A., Lumsden, S. L., & Bailey, J. A. (1997). Visibility of scattered broad-line emission in Seyfert 2 galaxies. *Nature*, 385, 700–702. ADS: 1997Natur.385..700H. doi: 10.1038/385700a0.

Hewett, P. C. & Foltz, C. B. (2003). The Frequency and Radio Properties of Broad Absorption Line Quasars. *AJ*, 125, 1784–1794. ADS: 2003AJ....125.1784H. doi: 10.1086/368392.

Hewett, P. C. & Wild, V. (2010). Improved redshifts for SDSS quasar spectra. *MNRAS*, 405, 2302–2316. ADS: 2010MNRAS.405.2302H. doi: 10.1111/j.1365-2966.2010.16648.x.

Hickox, R. C., Jones, C., Forman, W. R., Murray, S. S., Kochanek, C. S., Eisenstein, D., Jannuzi, B. T., Dey, A., Brown, M. J. I., Stern, D., Eisenhardt, P. R., Gorjian, V., Brodwin, M., Narayan, R., Cool, R. J., Kenter, A., Caldwell, N., & Anderson, M. E. (2009). Host Galaxies, Clustering, Eddington Ratios, and Evolution of Radio, X-Ray, and Infrared-Selected AGNs. *ApJ*, 696, 891–919. ADS: 2009ApJ...696..891H. doi: 10.1088/0004-637X/696/1/891.

Higginbottom, N., Knigge, C., Long, K. S., Sim, S. A., & Matthews, J. H. (2013). A simple disc wind model for broad absorption line quasars. *MNRAS*, 436, 1390–1407. ADS: 2013MNRAS.436.1390H. doi: 10.1093/mnras/stt1658.

Higginbottom, N., Proga, D., Knigge, C., Long, K. S., Matthews, J. H., & Sim, S. A. (2014).

Line-driven Disk Winds in Active Galactic Nuclei: The Critical Importance of Ionization and Radiative Transfer. *ApJ*, 789, 19. ADS: 2014ApJ...789...19H. doi: 10.1088/0004-637X/789/1/19.

Hine, R. G. & Longair, M. S. (1979). Optical spectra of 3CR radio galaxies. *MNRAS*, 188, 111–130. ADS: 1979MNRAS.188..111H. doi: 10.1093/mnras/188.1.111.

Ho, L. C. (2002). On the Relationship between Radio Emission and Black Hole Mass in Galactic Nuclei. *ApJ*, 564, 120–132. ADS: 2002ApJ...564..120H. doi: 10.1086/324399.

Hönig, S. F., Beckert, T., Ohnaka, K., & Weigelt, G. (2006). Radiative transfer modeling of three-dimensional clumpy AGN tori and its application to NGC 1068. *A&A*, 452, 459–471. ADS: 2006A&A...452..459H. doi: 10.1051/0004-6361:20054622.

Hönig, S. F., Kishimoto, M., Antonucci, R., Marconi, A., Prieto, M. A., Tristram, K., & Weigelt, G. (2012). Parsec-scale Dust Emission from the Polar Region in the Type 2 Nucleus of NGC 424. *ApJ*, 755, 149. ADS: 2012ApJ...755..149H. doi: 10.1088/0004-637X/755/2/149.

Horne, K. & Marsh, T. R. (1986). Emission line formation in accretion discs. *MNRAS*, 218, 761–773. ADS: 1986MNRAS.218..761H. doi: 10.1093/mnras/218.4.761.

Horne, K., Peterson, B. M., Collier, S. J., & Netzer, H. (2004). Observational Requirements for High-Fidelity Reverberation Mapping. *PASP*, 116, 465–476. ADS: 2004PASP..116..465H. doi: 10.1086/420755.

Huchra, J. & Burg, R. (1992). The spatial distribution of active galactic nuclei. I - The density of Seyfert galaxies and liners. *ApJ*, 393, 90–97. ADS: 1992ApJ...393...90H. doi: 10.1086/171488.

Hunter, J. D. (2007). Matplotlib: A 2d graphics environment. *Computing In Science & Engineering*, 9(3), 90–95. doi: 10.1109/MCSE.2007.55.

Hutchings, J. B., Gower, A. C., & Price, R. (1987). 21 CM emission in QSOs and active galaxies. *AJ*, 93, 6–13. ADS: 1987AJ.....93....6H. doi: 10.1086/114284.

Ivezić, Ž., Menou, K., Knapp, G. R., Strauss, M. A., Lupton, R. H., Vanden Berk, D. E., Richards, G. T., Tremonti, C., Weinstein, M. A., Anderson, S., Bahcall, N. A., Becker, R. H., Bernardi, M., Blanton, M., Eisenstein, D., Fan, X., Finkbeiner, D., Finlator, K., Frieman, J., Gunn, J. E., Hall, P. B., Kim, R. S. J., Kinkhabwala, A., Narayanan, V. K., Rockosi, C. M., Schlegel, D., Schneider, D. P., Strateva, I., SubbaRao, M., Thakar, A. R., Voges, W., White, R. L., Yanny, B., Brinkmann, J., Doi, M., Fukugita, M., Hennessy, G. S., Munn, J. A., Nichol, R. C., & York, D. G. (2002). Optical and Radio Properties of Extragalactic Sources Observed by the FIRST Survey and the Sloan Digital Sky Survey. *AJ*, 124, 2364–2400. ADS: 2002AJ....124.2364I. doi: 10.1086/344069.

Jackson, N., Perez, E., & Penston, M. V. (1991). Quasar H-beta profiles and discs. *MNRAS*, 249, 577–583. ADS: 1991MNRAS.249..577J. doi: 10.1093/mnras/249.4.577.

Jackson, N. & Rawlings, S. (1997). [O III] 500.7 spectroscopy of 3C galaxies and quasars at redshift z>1. *MNRAS*, 286, 241–256. ADS: 1997MNRAS.286..241J. doi: 10.1093/mnras/286.1.241.

Jaffe, W., Meisenheimer, K., Röttgering, H. J. A., Leinert, C., Richichi, A., Chesneau, O., Fraix-Burnet, D., Glazenborg-Kluttig, A., Granato, G.-L., Graser, U., Heijligers, B., Köhler, R., Malbet, F., Miley, G. K., Paresce, F., Pel, J.-W., Perrin, G., Przygodda, F., Schoeller, M., Sol, H., Waters, L. B. F. M., Weigelt, G., Woillez, J., & de Zeeuw, P. T. (2004). The central dusty torus in the active nucleus of NGC 1068. *Nature*, 429, 47–49. ADS: 2004Natur.429...47J. doi: 10.1038/nature02531.

Jannuzi, B. T., Hartig, G. F., Kirhakos, S., Sargent, W. L. W., Turnshek, D. A., Weymann, R. J., Bahcall, J. N., Bergeron, J., Boksenberg, A., Savage, B. D., Schneider, D. P., & Wolfe, A. M. (1996). The Hubble Space Telescope Quasar Absorption Line Key Project: The Unusual Absorption-Line System in the Spectrum of PG 2302+029—Ejected or Intervening? *ApJ*, 470, L11. ADS: 1996ApJ...470L..11J. doi: 10.1086/310301.

Janssen, R. M. J., Röttgering, H. J. A., Best, P. N., & Brinchmann, J. (2012). The triggering probability of radio-loud AGN. A comparison of high and low excitation radio galaxies in hosts of different colors. *A&A*, 541, A62. ADS: 2012A&A...541A..62J. doi: 10.1051/0004-6361/201219052.

Jarvis, M. J. & McLure, R. J. (2006). Orientation dependency of broad-line widths in quasars and consequences for black hole mass estimation. *MNRAS*, 369, 182–188. ADS: 2006MNRAS.369..182J. doi: 10.1111/j.1365-2966.2006.10295.x.

Jones, E., Oliphant, T., Peterson, P., et al. (2001). SciPy: Open source scientific tools for Python. http://www.scipy.org/.

Jovanović, P., Popović, L. Č., Stalevski, M., & Shapovalova, A. I. (2010). Variability of the Hβ Line Profiles as an Indicator of Orbiting Bright Spots in Accretion Disks of Quasars: A Case Study of 3C 390.3. *ApJ*, 718, 168–176. ADS: 2010ApJ...718..168J. doi: 10.1088/0004-637X/718/1/168.

Kaastra, J. S., Mewe, R., Liedahl, D. A., Komossa, S., & Brinkman, A. C. (2000). X-ray absorption lines in the Seyfert 1 galaxy NGC 5548 discovered with Chandra-LETGS. *A&A*, 354, L83–L86. ADS: 2000A&A...354L..83K.

Kashi, A., Proga, D., Nagamine, K., Greene, J., & Barth, A. J. (2013). On the Virialization of Disk Winds: Implications for the Black Hole Mass Estimates in Active Galactic Nuclei. *ApJ*, 778, 50. ADS: 2013ApJ...778...50K. doi: 10.1088/0004-637X/778/1/50.

Kaspi, S., Brandt, W. N., George, I. M., Netzer, H., Crenshaw, D. M., Gabel, J. R., Hamann, F. W., Kaiser, M. E., Koratkar, A., Kraemer, S. B., Kriss, G. A., Mathur, S., Mushotzky, R. F., Nandra, K., Peterson, B. M., Shields, J. C., Turner, T. J., & Zheng, W. (2002). The Ionized Gas and Nuclear Environment in NGC 3783. I. Time-averaged 900 Kilosecond Chandra Grating Spectroscopy. *ApJ*, 574, 643–662. ADS: 2002ApJ...574..643K. doi: 10.1086/341113.

Kaspi, S., Brandt, W. N., Maoz, D., Netzer, H., Schneider, D. P., & Shemmer, O. (2007). Reverberation Mapping of High-Luminosity Quasars: First Results. *ApJ*, 659, 997–1007. ADS: 2007ApJ...659..997K. doi: 10.1086/512094.

Kaspi, S., Maoz, D., Netzer, H., Peterson, B. M., Vestergaard, M., & Jannuzi, B. T. (2005). The Relationship between Luminosity and Broad-Line Region Size in Active Galactic Nuclei. *ApJ*,

629, 61–71. ADS: 2005ApJ...629...61K. doi: 10.1086/431275.

Kaspi, S., Smith, P. S., Netzer, H., Maoz, D., Jannuzi, B. T., & Giveon, U. (2000). Reverberation Measurements for 17 Quasars and the Size-Mass-Luminosity Relations in Active Galactic Nuclei. *ApJ*, 533, 631–649. ADS: 2000ApJ...533..631K. doi: 10.1086/308704.

Katgert, P., Katgert-Merkelijn, J. K., Le Poole, R. S., & van der Laan, H. (1973). A first 1415 MHz survey with the Westerbork Synthesis Radio Telescope: An attempt to detect radio emission from quasi-stellar objects. *A&A*, 23, 171–194. ADS: 1973A&A....23..171K.

Kauffmann, G. & Haehnelt, M. (2000). A unified model for the evolution of galaxies and quasars. *MNRAS*, 311, 576–588. ADS: 2000MNRAS.311..576K. doi: 10.1046/j.1365-8711.2000.03077.x.

Keating, S. K., Everett, J. E., Gallagher, S. C., & Deo, R. P. (2012). Sweeping Away the Mysteries of Dusty Continuous Winds in Active Galactic Nuclei. *ApJ*, 749, 32. ADS: 2012ApJ...749...32K. doi: 10.1088/0004-637X/749/1/32.

Kellermann, K. I. & Pauliny-Toth, I. I. K. (1966). A Search for Radio Emission from Blue Stellar Objects and Seyfert Galaxies. *Nature*, 212, 781–782. ADS: 1966Natur.212..781K. doi: 10.1038/212781a0.

Kellermann, K. I., Sramek, R., Schmidt, M., Shaffer, D. B., & Green, R. (1989). VLA observations of objects in the Palomar Bright Quasar Survey. *AJ*, 98, 1195–1207. ADS: 1989AJ.....98.1195K. doi: 10.1086/115207.

Kelly, B. C. & Bechtold, J. (2007). Virial Masses of Black Holes from Single Epoch Spectra of Active Galactic Nuclei. *ApJS*, 168, 1–18. ADS: 2007ApJS..168....1K. doi: 10.1086/509725.

Kelly, B. C. & Shen, Y. (2013). The Demographics of Broad-line Quasars in the Mass-Luminosity Plane. II. Black Hole Mass and Eddington Ratio Functions. *ApJ*, 764, 45. ADS: 2013ApJ...764...45K. doi: 10.1088/0004-637X/764/1/45.

Khachikian, E. Y. & Weedman, D. W. (1974). An atlas of Seyfert galaxies. *ApJ*, 192, 581–589. ADS: 1974ApJ...192..581K. doi: 10.1086/153093.

Kimball, A. E., Ivezić, Ž., Wiita, P. J., & Schneider, D. P. (2011). Correlations of Quasar Optical Spectra with Radio Morphology. *AJ*, 141, 182. ADS: 2011AJ....141..182K. doi: 10.1088/0004-6256/141/6/182.

King, A. (2003). Black Holes, Galaxy Formation, and the M_{BH}-σ Relation. *ApJ*, 596, L27–L29. ADS: 2003ApJ...596L..27K. doi: 10.1086/379143.

King, A. (2005). The AGN-Starburst Connection, Galactic Superwinds, and M_{BH}-σ. *ApJ*, 635, L121–L123. ADS: 2005ApJ...635L.121K. doi: 10.1086/499430.

King, A. & Pounds, K. (2015). Powerful Outflows and Feedback from Active Galactic Nuclei. *A&A*, 53, 115–154. ADS: 2015ARA&A..53..115K. doi: 10.1146/annurev-astro-082214-122316.

Kishimoto, M., Hönig, S. F., Antonucci, R., Barvainis, R., Kotani, T., Tristram, K. R. W., Weigelt, G., & Levin, K. (2011). The innermost dusty structure in active galactic nuclei

as probed by the Keck interferometer. *A&A*, 527, A121. ADS: 2011A&A...527A.121K. doi: 10.1051/0004-6361/201016054.

Kishimoto, M., Hönig, S. F., Antonucci, R., Kotani, T., Barvainis, R., Tristram, K. R. W., & Weigelt, G. (2009). Exploring the inner region of type 1 AGNs with the Keck interferometer. *A&A*, 507, L57–L60. ADS: 2009A&A...507L..57K. doi: 10.1051/0004-6361/200913512.

Kishimoto, M., Hönig, S. F., Antonucci, R., Millan-Gabet, R., Barvainis, R., Millour, F., Kotani, T., Tristram, K. R. W., & Weigelt, G. (2013). Evidence for a Receding Dust Sublimation Region around a Supermassive Black Hole. *ApJ*, 775, L36. ADS: 2013ApJ...775L..36K. doi: 10.1088/2041-8205/775/2/L36.

Kleinmann, S. G., Hamilton, D., Keel, W. C., Wynn-Williams, C. G., Eales, S. A., Becklin, E. E., & Kuntz, K. D. (1988). The properties and environment of the giant, infrared-luminous galaxy IRAS 09104 + 4109. *ApJ*, 328, 161–169. ADS: 1988ApJ...328..161K. doi: 10.1086/166276.

Knigge, C., Scaringi, S., Goad, M. R., & Cottis, C. E. (2008). The intrinsic fraction of broad-absorption line quasars. *MNRAS*, 386, 1426–1435. ADS: 2008MNRAS.386.1426K. doi: 10.1111/j.1365-2966.2008.13081.x.

Kohavi, R. (1995). A study of cross-validation and bootstrap for accuracy estimation and model selection. In *Proceedings of the Fourteenth International Joint Conference on Artificial Intelligence* (pp. 1137–1143).: Morgan Kaufmann.

Kollatschny, W. (2003). Accretion disk wind in the AGN broad-line region: Spectroscopically resolved line profile variations in Mrk 110. *A&A*, 407, 461–472. ADS: 2003A&A...407..461K. doi: 10.1051/0004-6361:20030928.

Kollmeier, J. A., Onken, C. A., Kochanek, C. S., Gould, A., Weinberg, D. H., Dietrich, M., Cool, R., Dey, A., Eisenstein, D. J., Jannuzi, B. T., Le Floc'h, E., & Stern, D. (2006). Black Hole Masses and Eddington Ratios at 0.3 < z < 4. *ApJ*, 648(1), 128–139. ADS: 2006ApJ...648..128K. doi: 10.1086/505646.

Kolmogorov, A. (1933). Sulla determinazione empirica di una lgge di distribuzione. *Inst. Ital. Attuari, Giorn.*, 4, 83–91.

Kolmogorov, A. (1941). Confidence limits for an unknown distribution function. *The annals of mathematical statistics*, 12(4), 461–463.

Konigl, A. & Kartje, J. F. (1994). Disk-driven hydromagnetic winds as a key ingredient of active galactic nuclei unification schemes. *ApJ*, 434, 446–467. ADS: 1994ApJ...434..446K. doi: 10.1086/174746.

Koratkar, A. & Blaes, O. (1999). The Ultraviolet and Optical Continuum Emission in Active Galactic Nuclei: The Status of Accretion Disks. *PASP*, 111, 1–30. ADS: 1999PASP..111...1K. doi: 10.1086/316294.

Koratkar, A. P. & Gaskell, C. M. (1989). Emission-line variability of Fairall 9 - Determination of the size of the broad-line region and the direction of gas motion. *ApJ*, 345, 637–646. ADS: 1989ApJ...345..637K. doi: 10.1086/167937.

Korista, K. (1999). What's Emitting the Broad Emission Lines? In G. Ferland & J. Baldwin (Eds.), *Quasars and Cosmology*, volume 162 of *Astronomical Society of the Pacific Conference Series* (pp. 165). ADS: 1999ASPC..162..165K.

Korista, K., Baldwin, J., Ferland, G., & Verner, D. (1997). An Atlas of Computed Equivalent Widths of Quasar Broad Emission Lines. *ApJS*, 108, 401–415. ADS: 1997ApJS..108..401K. doi: 10.1086/312966.

Korista, K. T., Alloin, D., Barr, P., Clavel, J., Cohen, R. D., Crenshaw, D. M., Evans, I. N., Horne, K., Koratkar, A. P., Kriss, G. A., Krolik, J. H., Malkan, M. A., Morris, S. L., Netzer, H., O'Brien, P. T., Peterson, B. M., Reichert, G. A., Rodriguez-Pascual, P. M., Wamsteker, W., Anderson, K. S. J., Axon, D. J., Benitez, E., Berlind, P., Bertram, R., Blackwell, Jr., J. H., Bochkarev, N. G., Boisson, C., Carini, M., Carrillo, R., Carone, T. E., Cheng, F.-Z., Christensen, J. A., Chuvaev, K. K., Dietrich, M., Dokter, J. J., Doroshenko, V., Dultzin-Hacyan, D., England, M. N., Espey, B. R., Filippenko, A. V., Gaskell, C. M., Goad, M. R., Ho, L. C., Huchra, J. P., Jiang, X. J., Kaspi, S., Kollatschny, W., Laor, A., Luminet, J.-P., MacAlpine, G. M., MacKenty, J. W., Malkov, Y. F., Maoz, D., Martin, P. G., Matheson, T., McCollum, B., Merkulova, N., Metik, L., Mignoli, M., Miller, H. R., Pastoriza, M. G., Pelat, D., Penfold, J., Perez, M., Perola, G. C., Persaud, J. L., Peters, J., Pitts, R., Pogge, R. W., Pronik, I., Pronik, V. I., Ptak, R. L., Rawley, L., Recondo-Gonzalez, M. C., Rodriguez-Espinosa, J. M., Romanishin, W., Sadun, A. C., Salamanca, I., Santos-Lleo, M., Sekiguchi, K., Sergeev, S. G., Shapovalova, A. I., Shields, J. C., Shrader, C., Shull, J. M., Silbermann, N. A., Sitko, M. L., Skillman, D. R., Smith, H. A., Smith, S. M., Snijders, M. A. J., Sparke, L. S., Stirpe, G. M., Stoner, R. E., Sun, W.-H., Thiele, U., Tokarz, S., Tsvetanov, Z. I., Turnshek, D. A., Veilleux, S., Wagner, R. M., Wagner, S. J., Wanders, I., Wang, T., Welsh, W. F., Weymann, R. J., White, R. J., Wilkes, B. J., Wills, B. J., Winge, C., Wu, H., & Zou, Z. L. (1995). Steps toward determination of the size and structure of the broad-line region in active galatic nuclei. 8: an intensive HST, IUE, and ground-based study of NGC 5548. *ApJS*, 97, 285–330. ADS: 1995ApJS...97..285K. doi: 10.1086/192144.

Korista, K. T. & Goad, M. R. (2000). Locally Optimally Emitting Clouds and the Variable Broad Emission Line Spectrum of NGC 5548. *ApJ*, 536, 284–298. ADS: 2000ApJ...536..284K. doi: 10.1086/308930.

Korista, K. T. & Goad, M. R. (2004). What the Optical Recombination Lines Can Tell Us about the Broad-Line Regions of Active Galactic Nuclei. *ApJ*, 606, 749–762. ADS: 2004ApJ...606..749K. doi: 10.1086/383193.

Korista, K. T., Voit, G. M., Morris, S. L., & Weymann, R. J. (1993). Double troughs in broad absorption line quasars and Ly-alpha-N V line-locking. *ApJS*, 88, 357–381. ADS: 1993ApJS...88..357K. doi: 10.1086/191825.

Korista, K. T., Weymann, R. J., Morris, S. L., Kopko, Jr., M., Turnshek, D. A., Hartig, G. F., Foltz, C. B., Burbidge, E. M., & Junkkarinen, V. T. (1992). Hubble Space Telescope Faint Object Spectrograph and ground-based observations of the broad absorption line quasar 0226-1024. *ApJ*, 401, 529–542. ADS: 1992ApJ...401..529K. doi: 10.1086/172084.

Kormendy, J. & Ho, L. C. (2013). Coevolution (Or Not) of Supermassive Black Holes and Host Galaxies. *ARA&A*, 51, 511–653. ADS: 2013ARA&A..51..511K. doi: 10.1146/

annurev-astro-082708-101811.

Kormendy, J. & Richstone, D. (1995). Inward Bound—The Search For Supermassive Black Holes In Galactic Nuclei. *ARA&A*, 33, 581. ADS: 1995ARA&A..33..581K. doi: 10.1146/annurev.aa.33.090195.003053.

Krasnopolsky, R., Li, Z.-Y., & Blandford, R. (1999). Magnetocentrifugal Launching of Jets from Accretion Disks. I. Cold Axisymmetric Flows. *ApJ*, 526, 631–642. ADS: 1999ApJ...526..631K. doi: 10.1086/308023.

Krolik, J. H. & Begelman, M. C. (1988). Molecular tori in Seyfert galaxies - Feeding the monster and hiding it. *ApJ*, 329, 702–711. ADS: 1988ApJ...329..702K. doi: 10.1086/166414.

Krolik, J. H. & Kriss, G. A. (1995). Observable Properties of X-Ray–heated Winds in Active Galactic Nuclei: Warm Reflectors and Warm Absorbers. *ApJ*, 447, 512. ADS: 1995ApJ...447..512K. doi: 10.1086/175896.

Krolik, J. H. & McKee, C. F. (1978). Hydrogen emission-line spectra in quasars and active galactic nuclei. *ApJS*, 37, 459–483. ADS: 1978ApJS...37..459K. doi: 10.1086/190538.

Krolik, J. H., McKee, C. F., & Tarter, C. B. (1981). Two-phase models of quasar emission line regions. *ApJ*, 249, 422–442. ADS: 1981ApJ...249..422K. doi: 10.1086/159303.

Krolik, J. H. & Voit, G. M. (1998). What Is the True Covering Factor of Absorbing Matter in BALQSOs? *ApJ*, 497, L5–L8. ADS: 1998ApJ...497L...5K. doi: 10.1086/311274.

Kuźmicz, A. & Jamrozy, M. (2012). Optical and radio properties of giant radio quasars: central black hole characteristics. *MNRAS*, 426, 851–867. ADS: 2012MNRAS.426..851K. doi: 10.1111/j.1365-2966.2012.21576.x.

Laha, S., Guainazzi, M., Dewangan, G. C., Chakravorty, S., & Kembhavi, A. K. (2014). Warm absorbers in X-rays (WAX), a comprehensive high-resolution grating spectral study of a sample of Seyfert galaxies - I. A global view and frequency of occurrence of warm absorbers. *MNRAS*, 441, 2613–2643. ADS: 2014MNRAS.441.2613L. doi: 10.1093/mnras/stu669.

Laing, R. A., Jenkins, C. R., Wall, J. V., & Unger, S. W. (1994). Spectrophotometry of a Complete Sample of 3CR Radio Sources: Implications for Unified Models. In G. V. Bicknell, M. A. Dopita, & P. J. Quinn (Eds.), *The Physics of Active Galaxies*, volume 54 of *Astronomical Society of the Pacific Conference Series* (pp. 201). ADS: 1994ASPC...54..201L.

Lal, D. V. & Ho, L. C. (2010). The Radio Properties of Type 2 Quasars. *AJ*, 139, 1089–1105. ADS: 2010AJ....139.1089L. doi: 10.1088/0004-6256/139/3/1089.

LaMassa, S. M., Cales, S., Moran, E. C., Myers, A. D., Richards, G. T., Eracleous, M., Heckman, T. M., Gallo, L., & Urry, C. M. (2015). The Discovery of the First "Changing Look" Quasar: New Insights Into the Physics and Phenomenology of Active Galactic Nucleus. *ApJ*, 800, 144. ADS: 2015ApJ...800..144L. doi: 10.1088/0004-637X/800/2/144.

Lamers, H. J. G. L. M. & Cassinelli, J. P. (1999). *Introduction to Stellar Winds*. ADS: 1999isw..book.....L.

Lamy, H. & Hutsemékers, D. (2004). Polarization properties of broad absorption line QSOs: New

statistical clues. *A&A*, 427, 107–123. ADS: 2004A&A...427..107L. doi: 10.1051/0004-6361:20041066.

Laor, A. (1998). On Quasar Masses and Quasar Host Galaxies. *ApJ*, 505, L83–L86. ADS: 1998ApJ...505L..83L. doi: 10.1086/311619.

Laor, A. (2000). On Black Hole Masses and Radio Loudness in Active Galactic Nuclei. *ApJ*, 543, L111–L114. ADS: 2000ApJ...543L.111L. doi: 10.1086/317280.

Laor, A. & Brandt, W. N. (2002). The Luminosity Dependence of Ultraviolet Absorption in Active Galactic Nuclei. *ApJ*, 569, 641–654. ADS: 2002ApJ...569..641L. doi: 10.1086/339476.

Lawrence, A. (1991). The relative frequency of broad-lined and narrow-lined active galactic nuclei - Implications for unified schemes. *MNRAS*, 252, 586–592. ADS: 1991MNRAS.252..586L. doi: 10.1093/mnras/252.4.586.

Lawrence, A. & Elvis, M. (2010). Misaligned Disks as Obscurers in Active Galaxies. *ApJ*, 714, 561–570. ADS: 2010ApJ...714..561L. doi: 10.1088/0004-637X/714/1/561.

Lawther, D., Vestergaard, M., & Fan, X. (2018). A Hubble Space Telescope imaging study of four FeLoBAL quasar host galaxies. *MNRAS*, 475, 3213–3239. ADS: 2018MNRAS.475.3213L. doi: 10.1093/mnras/stx3203.

Lee, L. W. & Turnshek, D. A. (1995). On Correlations between the Broad Absorption Lines and Adjacent Broad Emission Lines in QSO Spectra. *ApJ*, 453, L61. ADS: 1995ApJ...453L..61L. doi: 10.1086/309753.

Legendre, A. (1805). *Nouvelles méthodes pour la détermination des orbites des comètes*. Nineteenth Century Collections Online (NCCO): Science, Technology, and Medicine: 1780-1925. F. Didot. https://books.google.com.au/books?id=FRcOAAAAQAAJ.

Leighly, K. M. (2004). Hubble Space Telescope STIS Ultraviolet Spectral Evidence of Outflow in Extreme Narrow-Line Seyfert 1 Galaxies. II. Modeling and Interpretation. *ApJ*, 611, 125–152. ADS: 2004ApJ...611..125L. doi: 10.1086/422089.

Leighly, K. M., Hamann, F., Casebeer, D. A., & Grupe, D. (2009). Emergence of a Broad Absorption Line Outflow in the Narrow-line Seyfert 1 Galaxy WPVS 007. *ApJ*, 701, 176–199. ADS: 2009ApJ...701..176L. doi: 10.1088/0004-637X/701/1/176.

Liu, W.-J., Zhou, H., Ji, T., Yuan, W., Wang, T.-G., Jian, G., Shi, X., Zhang, S., Jiang, P., Shu, X., Wang, H., Wang, S.-F., Sun, L., Yang, C., Liu, B., & Zhao, W. (2015). A Comprehensive Study of Broad Absorption Line Quasars. I. Prevalence of HeI* Absorption Line Multiplets in Low-ionization Objects. *ApJS*, 217, 11. ADS: 2015ApJS..217...11L. doi: 10.1088/0067-0049/217/1/11.

Lucy, L. B. & Solomon, P. M. (1970). Mass Loss by Hot Stars. *ApJ*, 159, 879. ADS: 1970ApJ...159..879L. doi: 10.1086/150365.

Lucy, L. B. & White, R. L. (1980). X-ray emission from the winds of hot stars. *ApJ*, 241, 300–305. ADS: 1980ApJ...241..300L. doi: 10.1086/158342.

Lumsden, S. L. & Alexander, D. M. (2001). The infrared luminosity of the torus and the

visibility of scattered broad line emission in Seyfert 2 galaxies. *MNRAS*, 328, L32–L36. ADS: 2001MNRAS.328L..32L. doi: 10.1046/j.1365-8711.2001.05074.x.

Lusso, E., Piedipalumbo, E., Risaliti, G., Paolillo, M., Bisogni, S., Nardini, E., & Amati, L. (2019). Tension with the flat ΛCDM model from a high-redshift Hubble diagram of supernovae, quasars, and gamma-ray bursts. *A&A*, 628, L4. ADS: 2019A&A...628L...4L. doi: 10.1051/0004-6361/201936223.

MacGregor, K. B., Hartmann, L., & Raymond, J. C. (1979). Radiative amplification of sound waves in the winds of O and B stars. *ApJ*, 231, 514–523. ADS: 1979ApJ...231..514M. doi: 10.1086/157213.

MacLeod, C. L., Ivezić, Ž., Kochanek, C. S., Kozłowski, S., Kelly, B., Bullock, E., Kimball, A., Sesar, B., Westman, D., Brooks, K., Gibson, R., Becker, A. C., & de Vries, W. H. (2010). Modeling the Time Variability of SDSS Stripe 82 Quasars as a Damped Random Walk. *ApJ*, 721, 1014–1033. ADS: 2010ApJ...721.1014M. doi: 10.1088/0004-637X/721/2/1014.

MacLeod, C. L., Ivezić, Ž., Sesar, B., de Vries, W., Kochanek, C. S., Kelly, B. C., Becker, A. C., Lupton, R. H., Hall, P. B., Richards, G. T., Anderson, S. F., & Schneider, D. P. (2012). A Description of Quasar Variability Measured Using Repeated SDSS and POSS Imaging. *ApJ*, 753, 106. ADS: 2012ApJ...753..106M. doi: 10.1088/0004-637X/753/2/106.

Magorrian, J., Tremaine, S., Richstone, D., Bender, R., Bower, G., Dressler, A., Faber, S. M., Gebhardt, K., Green, R., Grillmair, C., Kormendy, J., & Lauer, T. (1998). The Demography of Massive Dark Objects in Galaxy Centers. *AJ*, 115, 2285–2305. ADS: 1998AJ....115.2285M. doi: 10.1086/300353.

Maiolino, R. & Rieke, G. H. (1995). Low-Luminosity and Obscured Seyfert Nuclei in Nearby Galaxies. *ApJ*, 454, 95. ADS: 1995ApJ...454...95M. doi: 10.1086/176468.

Maiolino, R., Risaliti, G., Salvati, M., Pietrini, P., Torricelli-Ciamponi, G., Elvis, M., Fabbiano, G., Braito, V., & Reeves, J. (2010). "Comets" orbiting a black hole. *A&A*, 517, A47. ADS: 2010A&A...517A..47M. doi: 10.1051/0004-6361/200913985.

Malkan, M. A. & Sargent, W. L. W. (1982). The ultraviolet excess of Seyfert 1 galaxies and quasars. *ApJ*, 254, 22–37. ADS: 1982ApJ...254...22M. doi: 10.1086/159701.

Mangham, S. W., Knigge, C., Matthews, J. H., Long, K. S., Sim, S. A., & Higginbottom, N. (2017). The reverberation signatures of rotating disc winds in active galactic nuclei. *MNRAS*, 471, 4788–4801. ADS: 2017MNRAS.471.4788M. doi: 10.1093/mnras/stx1863.

Marchese, E., Braito, V., Della Ceca, R., Caccianiga, A., & Severgnini, P. (2012). NGC 454: unveiling a new 'changing look' active galactic nucleus. *MNRAS*, 421, 1803–1812. ADS: 2012MNRAS.421.1803M. doi: 10.1111/j.1365-2966.2012.20445.x.

Marconi, A., Axon, D. J., Maiolino, R., Nagao, T., Pastorini, G., Pietrini, P., Robinson, A., & Torricelli, G. (2008). The Effect of Radiation Pressure on Virial Black Hole Mass Estimates and the Case of Narrow-Line Seyfert 1 Galaxies. *ApJ*, 678, 693–700. ADS: 2008ApJ...678..693M. doi: 10.1086/529360.

Marconi, A. & Hunt, L. K. (2003). The Relation between Black Hole Mass, Bulge Mass, and Near-

Infrared Luminosity. *ApJ*, 589, L21–L24. ADS: 2003ApJ...589L..21M. doi: 10.1086/375804.

Marin, F. (2016). Are there reliable methods to estimate the nuclear orientation of Seyfert galaxies? *MNRAS*, 460, 3679–3705. ADS: 2016MNRAS.460.3679M. doi: 10.1093/mnras/stw1131.

Marin, F. & Antonucci, R. (2016). A Robust Derivation of the Tight Relationship of Radio Core Dominance to Inclination Angle in High Redshift 3CRR Sources. *ApJ*, 830, 82. ADS: 2016ApJ...830...82M. doi: 10.3847/0004-637X/830/2/82.

Marin, F., Goosmann, R. W., & Gaskell, C. M. (2015). Modeling optical and UV polarization of AGNs. III. From uniform-density to clumpy regions. *A&A*, 577, A66. ADS: 2015A&A...577A..66M. doi: 10.1051/0004-6361/201525628.

Marziani, P., del Olmo, A., Martínez-Carballo, M. A., Martínez-Aldama, M. L., Stirpe, G. M., Negrete, C. A., Dultzin, D., D'Onofrio, M., Bon, E., & Bon, N. (2019). Black hole mass estimates in quasars. A comparative analysis of high- and low-ionization lines. *A&A*, 627, A88. ADS: 2019A&A...627A..88M. doi: 10.1051/0004-6361/201935265.

Marziani, P., Dultzin, D., Sulentic, J. W., Del Olmo, A., Negrete, C. A., Martínez-Aldama, M. L., D'Onofrio, M., Bon, E., Bon, N., & Stirpe, G. M. (2018). A main sequence for quasars. *Frontiers in Astronomy and Space Sciences*, 5, 6. ADS: 2018FrASS...5....6M. doi: 10.3389/fspas.2018.00006.

Marziani, P. & Sulentic, J. W. (2014). Highly accreting quasars: sample definition and possible cosmological implications. *MNRAS*, 442(2), 1211–1229. ADS: 2014MNRAS.442.1211M. doi: 10.1093/mnras/stu951.

Marziani, P., Sulentic, J. W., Dultzin-Hacyan, D., Calvani, M., & Moles, M. (1996). Comparative Analysis of the High- and Low-Ionization Lines in the Broad-Line Region of Active Galactic Nuclei. *ApJS*, 104, 37. ADS: 1996ApJS..104...37M. doi: 10.1086/192291.

Marziani, P., Sulentic, J. W., Plauchu-Frayn, I., & del Olmo, A. (2013). Is MgIIλ2800 a reliable virial broadening estimator for quasars? *A&A*, 555, A89. ADS: 2013A&A...555A..89M. doi: 10.1051/0004-6361/201321374.

Marziani, P., Sulentic, J. W., Zwitter, T., Dultzin-Hacyan, D., & Calvani, M. (2001). Searching for the Physical Drivers of the Eigenvector 1 Correlation Space. *ApJ*, 558, 553–560. ADS: 2001ApJ...558..553M. doi: 10.1086/322286.

Mateos, S., Carrera, F. J., Alonso-Herrero, A., Hernán-Caballero, A., Barcons, X., Asensio Ramos, A., Watson, M. G., Blain, A., Caccianiga, A., Ballo, L., Braito, V., & Ramos Almeida, C. (2016). X-Ray Absorption, Nuclear Infrared Emission, and Dust Covering Factors of AGNs: Testing Unification Schemes. *ApJ*, 819, 166. ADS: 2016ApJ...819..166M. doi: 10.3847/0004-637X/819/2/166.

Mateos, S., Carrera, F. J., Barcons, X., Alonso-Herrero, A., Hernán-Caballero, A., Page, M., Ramos Almeida, C., Caccianiga, A., Miyaji, T., & Blain, A. (2017). Survival of the Obscuring Torus in the Most Powerful Active Galactic Nuclei. *ApJ*, 841, L18. ADS: 2017ApJ...841L..18M. doi: 10.3847/2041-8213/aa7268.

Mathews, W. G. & Capriotti, E. R. (1985). Structure and dynamics of the broad line region. In J. S. Miller (Ed.), *Astrophysics of Active Galaxies and Quasi-Stellar Objects* (pp. 185–233). ADS: 1985aagq.conf..185M.

Mathews, W. G. & Wampler, E. J. (1985). Evidence for kinematic variation with ionization level in quasars. *PASP*, 97, 966–969. ADS: 1985PASP...97..966M. doi: 10.1086/131649.

Matt, G., Guainazzi, M., & Maiolino, R. (2003). Changing look: from Compton-thick to Compton-thin, or the rebirth of fossil active galactic nuclei. *MNRAS*, 342, 422–426. ADS: 2003MNRAS.342..422M. doi: 10.1046/j.1365-8711.2003.06539.x.

Matthews, J. H., Knigge, C., & Long, K. S. (2017). Quasar emission lines as probes of orientation: implications for disc wind geometries and unification. *MNRAS*, 467, 2571–2584. ADS: 2017MNRAS.467.2571M. doi: 10.1093/mnras/stx231.

Matthews, J. H., Knigge, C., Long, K. S., Sim, S. A., Higginbottom, N., & Mangham, S. W. (2016). Testing quasar unification: radiative transfer in clumpy winds. *MNRAS*, 458, 293–305. ADS: 2016MNRAS.458..293M. doi: 10.1093/mnras/stw323.

McConnell, N. J. & Ma, C.-P. (2013). Revisiting the Scaling Relations of Black Hole Masses and Host Galaxy Properties. *ApJ*, 764, 184. ADS: 2013ApJ...764..184M. doi: 10.1088/0004-637X/764/2/184.

McElroy, R. E., Husemann, B., Croom, S. M., Davis, T. A., Bennert, V. N., Busch, G., Combes, F., Eckart, A., Perez-Torres, M., Powell, M., Scharwächter, J., Tremblay, G. R., & Urrutia, T. (2016). The Close AGN Reference Survey (CARS). Mrk 1018 returns to the shadows after 30 years as a Seyfert 1. *A&A*, 593, L8. ADS: 2016A&A...593L...8M. doi: 10.1051/0004-6361/201629102.

McGill, K. L., Woo, J.-H., Treu, T., & Malkan, M. A. (2008). Comparing and Calibrating Black Hole Mass Estimators for Distant Active Galactic Nuclei. *ApJ*, 673, 703–714. ADS: 2008ApJ...673..703M. doi: 10.1086/524349.

McGovern, A. & Wagstaff, K. L. (2011). Machine learning in space: extending our reach. *Machine Learning*, 84(3), 335–340. doi: 10.1007/s10994-011-5249-4.

McIntosh, D. H., Rix, H.-W., Rieke, M. J., & Foltz, C. B. (1999). Redshifted and Blueshifted Broad Lines in Luminous Quasars. *ApJ*, 517, L73–L76. ADS: 1999ApJ...517L..73M. doi: 10.1086/312033.

McKernan, B., Yaqoob, T., & Reynolds, C. S. (2007). A soft X-ray study of type I active galactic nuclei observed with Chandra high-energy transmission grating spectrometer. *MNRAS*, 379, 1359–1372. ADS: 2007MNRAS.379.1359M. doi: 10.1111/j.1365-2966.2007.11993.x.

McKinney, W. (2010). Data structures for statistical computing in python. In S. van der Walt & J. Millman (Eds.), *Proceedings of the 9th Python in Science Conference* (pp. 51 – 56).

McLure, R. J. & Dunlop, J. S. (2002). On the black hole-bulge mass relation in active and inactive galaxies. *MNRAS*, 331, 795–804. ADS: 2002MNRAS.331..795M. doi: 10.1046/j.1365-8711.2002.05236.x.

McLure, R. J. & Dunlop, J. S. (2004). The cosmological evolution of quasar black hole masses. *MNRAS*, 352, 1390–1404. ADS: 2004MNRAS.352.1390M. doi: 10.1111/j.1365-2966.2004.08034.x.

McLure, R. J. & Jarvis, M. J. (2002). Measuring the black hole masses of high-redshift quasars. *MNRAS*, 337, 109–116. ADS: 2002MNRAS.337..109M. doi: 10.1046/j.1365-8711.2002.05871.x.

Mejía-Restrepo, J. E., Trakhtenbrot, B., Lira, P., Netzer, H., & Capellupo, D. M. (2016). Active galactic nuclei at z $\sim$ 1.5 - II. Black hole mass estimation by means of broad emission lines. *MNRAS*, 460, 187–211. ADS: 2016MNRAS.460..187M. doi: 10.1093/mnras/stw568.

Menou, K., Vanden Berk, D. E., Ivezić, Ž., Kim, R. S. J., Knapp, G. R., Richards, G. T., Strateva, I., Fan, X., Gunn, J. E., Hall, P. B., Heckman, T., Krolik, J., Lupton, R. H., Schneider, D. P., York, D. G., Anderson, S. F., Bahcall, N. A., Brinkmann, J., Brunner, R., Csabai, I., Fukugita, M., Hennessy, G. S., Kunszt, P. Z., Lamb, D. Q., Munn, J. A., Nichol, R. C., & Szokoly, G. P. (2001). Broad Absorption Line Quasars in the Sloan Digital Sky Survey with VLA FIRST Radio Detections. *ApJ*, 561, 645–652. ADS: 2001ApJ...561..645M. doi: 10.1086/323218.

Merloni, A., Dwelly, T., Salvato, M., Georgakakis, A., Greiner, J., Krumpe, M., Nandra, K., Ponti, G., & Rau, A. (2015). A tidal disruption flare in a massive galaxy? Implications for the fuelling mechanisms of nuclear black holes. *MNRAS*, 452, 69–87. ADS: 2015MNRAS.452...69M. doi: 10.1093/mnras/stv1095.

Merloni, A. & Heinz, S. (2007). Measuring the kinetic power of active galactic nuclei in the radio mode. *MNRAS*, 381, 589–601. ADS: 2007MNRAS.381..589M. doi: 10.1111/j.1365-2966.2007.12253.x.

Miller, J. S. & Goodrich, R. W. (1990). Spectropolarimetry of high-polarization Seyfert 2 galaxies and unified Seyfert theories. *ApJ*, 355, 456–467. ADS: 1990ApJ...355..456M. doi: 10.1086/168780.

Miller, L., Peacock, J. A., & Mead, A. R. G. (1990). The bimodal radio luminosity function of quasars. *MNRAS*, 244, 207–213. ADS: 1990MNRAS.244..207M.

Mingo, B., Hardcastle, M. J., Croston, J. H., Dicken, D., Evans, D. A., Morganti, R., & Tadhunter, C. (2014). An X-ray survey of the 2 Jy sample - I. Is there an accretion mode dichotomy in radio-loud AGN? *MNRAS*, 440, 269–297. ADS: 2014MNRAS.440..269M. doi: 10.1093/mnras/stu263.

Miniutti, G., Sanfrutos, M., Beuchert, T., Agís-González, B., Longinotti, A. L., Piconcelli, E., Krongold, Y., Guainazzi, M., Bianchi, S., Matt, G., & Jiménez-Bailón, E. (2014). The properties of the clumpy torus and BLR in the polar-scattered Seyfert 1 galaxy ESO 323-G77 through X-ray absorption variability. *MNRAS*, 437, 1776–1790. ADS: 2014MNRAS.437.1776M. doi: 10.1093/mnras/stt2005.

Montenegro-Montes, F. M., Mack, K.-H., Vigotti, M., Benn, C. R., Carballo, R., González-Serrano, J. I., Holt, J., & Jiménez-Luján, F. (2008). Radio spectra and polarization properties of radio-loud broad absorption-line quasars. *MNRAS*, 388, 1853–1868. ADS: 2008MNRAS.388.

1853M. doi: 10.1111/j.1365-2966.2008.13520.x.

Mor, R., Netzer, H., & Elitzur, M. (2009). Dusty Structure Around Type-I Active Galactic Nuclei: Clumpy Torus Narrow-line Region and Near-nucleus Hot Dust. *ApJ*, 705, 298–313. ADS: 2009ApJ...705..298M. doi: 10.1088/0004-637X/705/1/298.

Moran, E. C., Barth, A. J., Kay, L. E., & Filippenko, A. V. (2000). The Frequency of Polarized Broad Emission Lines in Type 2 Seyfert Galaxies. *ApJ*, 540, L73–L77. ADS: 2000ApJ...540L..73M. doi: 10.1086/312876.

Mortlock, D. J., Warren, S. J., Venemans, B. P., Patel, M., Hewett, P. C., McMahon, R. G., Simpson, C., Theuns, T., Gonzáles-Solares, E. A., Adamson, A., Dye, S., Hambly, N. C., Hirst, P., Irwin, M. J., Kuiper, E., Lawrence, A., & Röttgering, H. J. A. (2011). A luminous quasar at a redshift of z = 7.085. *Nature*, 474, 616–619. ADS: 2011Natur.474..616M. doi: 10.1038/nature10159.

Mukaka, M. M. (2012). A guide to appropriate use of correlation coefficient in medical research. *Malawi Medical Journal*, 24(3), 69–71.

Mulchaey, J. S., Koratkar, A., Ward, M. J., Wilson, A. S., Whittle, M., Antonucci, R. R. J., Kinney, A. L., & Hurt, T. (1994). Multiwavelength tests of the dusty torus model for Seyfert galaxies. *ApJ*, 436, 586–598. ADS: 1994ApJ...436..586M. doi: 10.1086/174933.

Murray, N. & Chiang, J. (1997). Disk Winds and Disk Emission Lines. *ApJ*, 474, 91. ADS: 1997ApJ...474...91M. doi: 10.1086/303443.

Murray, N., Chiang, J., Grossman, S. A., & Voit, G. M. (1995). Accretion Disk Winds from Active Galactic Nuclei. *ApJ*, 451, 498. ADS: 1995ApJ...451..498M. doi: 10.1086/176238.

Murray, N., Quataert, E., & Thompson, T. A. (2005). On the Maximum Luminosity of Galaxies and Their Central Black Holes: Feedback from Momentum-driven Winds. *ApJ*, 618, 569–585. ADS: 2005ApJ...618..569M. doi: 10.1086/426067.

Mushotzky, R. F. & Wandel, A. (1989). On the ratio of the infrared-to-ultraviolet continuum to the X-rays in quasars and active galaxies. *ApJ*, 339, 674–688. ADS: 1989ApJ...339..674M. doi: 10.1086/167327.

Nandra, K., George, I. M., Mushotzky, R. F., Turner, T. J., & Yaqoob, T. (1997). ASCA Observations of Seyfert 1 Galaxies. II. Relativistic Iron Kα Emission. *ApJ*, 477, 602–622. ADS: 1997ApJ...477..602N. doi: 10.1086/303721.

Nandra, K., O'Neill, P. M., George, I. M., & Reeves, J. N. (2007). An XMM-Newton survey of broad iron lines in Seyfert galaxies. *MNRAS*, 382, 194–228. ADS: 2007MNRAS.382..194N. doi: 10.1111/j.1365-2966.2007.12331.x.

Narayan, R. & Yi, I. (1994). Advection-dominated accretion: A self-similar solution. *ApJ*, 428, L13–L16. ADS: 1994ApJ...428L..13N. doi: 10.1086/187381.

Narayanan, D., Hamann, F., Barlow, T., Burbidge, E. M., Cohen, R. D., Junkkarinen, V., & Lyons, R. (2004). Variability Tests for Intrinsic Absorption Lines in Quasar Spectra. *ApJ*, 601, 715–722. ADS: 2004ApJ...601..715N. doi: 10.1086/380781.

Nayakshin, S. (2005). Warped accretion discs and the unification of active galactic nuclei. *MNRAS*, 359(2), 545–550. ADS: 2005MNRAS.359..545N. doi: 10.1111/j.1365-2966.2005.08913.x.

Nemmen, R. S., Georganopoulos, M., Guiriec, S., Meyer, E. T., Gehrels, N., & Sambruna, R. M. (2012). A Universal Scaling for the Energetics of Relativistic Jets from Black Hole Systems. *Science*, 338(6113), 1445. ADS: 2012Sci...338.1445N. doi: 10.1126/science.1227416.

Nenkova, M., Ivezić, Ž., & Elitzur, M. (2002). Dust Emission from Active Galactic Nuclei. *ApJ*, 570, L9–L12. ADS: 2002ApJ...570L...9N. doi: 10.1086/340857.

Nenkova, M., Sirocky, M. M., Nikutta, R., Ivezić, Ž., & Elitzur, M. (2008). AGN Dusty Tori. II. Observational Implications of Clumpiness. *ApJ*, 685, 160–180. ADS: 2008ApJ...685..160N. doi: 10.1086/590483.

Netzer, H. (1987). Quasar discs. II - A composite model for the broad-line region. *MNRAS*, 225, 55–72. ADS: 1987MNRAS.225...55N. doi: 10.1093/mnras/225.1.55.

Netzer, H. (1990). AGN emission lines. In R. D. Blandford, H. Netzer, L. Woltjer, T. J.-L. Courvoisier, & M. Mayor (Eds.), *Active Galactic Nuclei* (pp. 57–160). ADS: 1990agn..conf...57N.

Netzer, H. (1996). X-Ray Lines in Active Galactic Nuclei and Photoionized Gases. *ApJ*, 473, 781. ADS: 1996ApJ...473..781N. doi: 10.1086/178190.

Netzer, H. (2013). *The Physics and Evolution of Active Galactic Nuclei*. ADS: 2013peag.book....N.

Netzer, H. (2015). Revisiting the Unified Model of Active Galactic Nuclei. *ARA&A*, 53, 365–408. ADS: 2015ARA&A..53..365N. doi: 10.1146/annurev-astro-082214-122302.

Netzer, H. & Laor, A. (1993). Dust in the narrow-line region of active galactic nuclei. *ApJ*, 404, L51–L54. ADS: 1993ApJ...404L..51N. doi: 10.1086/186741.

Netzer, H. & Marziani, P. (2010). The Effect of Radiation Pressure on Emission-line Profiles and Black Hole Mass Determination in Active Galactic Nuclei. *ApJ*, 724, 318–328. ADS: 2010ApJ...724..318N. doi: 10.1088/0004-637X/724/1/318.

Nicastro, F. (2000). Broad Emission Line Regions in Active Galactic Nuclei: The Link with the Accretion Power. *ApJ*, 530, L65–L68. ADS: 2000ApJ...530L..65N. doi: 10.1086/312491.

Nicastro, F., Martocchia, A., & Matt, G. (2003). The Lack of Broad-Line Regions in Low Accretion Rate Active Galactic Nuclei as Evidence of Their Origin in the Accretion Disk. *ApJ*, 589, L13–L16. ADS: 2003ApJ...589L..13N. doi: 10.1086/375715.

Ochsenbein, F., Bauer, P., & Marcout, J. (2000). The VizieR database of astronomical catalogues. *A&AS*, 143, 23–32. ADS: 2000A&AS..143...23O. doi: 10.1051/aas:2000169.

O'Dea, C. P. (1998). The Compact Steep-Spectrum and Gigahertz Peaked-Spectrum Radio Sources. *PASP*, 110, 493–532. ADS: 1998PASP..110..493O. doi: 10.1086/316162.

O'Dowd, M. J., Bate, N. F., Webster, R. L., Labrie, K., & Rogers, J. (2015). Microlensing Constraints on Broad Absorption and Emission Line Flows in the Quasar H1413+117. *ApJ*,

813, 62. ADS: 2015ApJ...813...62O. doi: 10.1088/0004-637X/813/1/62.

Ogle, P. M., Cohen, M. H., Miller, J. S., Tran, H. D., Goodrich, R. W., & Martel, A. R. (1999). Polarization of Broad Absorption Line QSOS. I. A Spectropolarimetric Atlas. *ApJS*, 125, 1–34. ADS: 1999ApJS..125....1O. doi: 10.1086/313272.

Onken, C. A., Ferrarese, L., Merritt, D., Peterson, B. M., Pogge, R. W., Vestergaard, M., & Wandel, A. (2004). Supermassive Black Holes in Active Galactic Nuclei. II. Calibration of the Black Hole Mass-Velocity Dispersion Relationship for Active Galactic Nuclei. *ApJ*, 615, 645–651. ADS: 2004ApJ...615..645O. doi: 10.1086/424655.

Onken, C. A. & Kollmeier, J. A. (2008). An Improved Method for Using Mg II to Estimate Black Hole Masses in Active Galactic Nuclei. *ApJ*, 689, L13. ADS: 2008ApJ...689L..13O. doi: 10.1086/595746.

Orr, M. J. L. & Browne, I. W. A. (1982). Relativistic beaming and quasar statistics. *MNRAS*, 200, 1067–1080. ADS: 1982MNRAS.200.1067O. doi: 10.1093/mnras/200.4.1067.

Osterbrock, D. E. (1977). Spectrophotometry of Seyfert 1 galaxies. *ApJ*, 215, 733–745. ADS: 1977ApJ...215..733O. doi: 10.1086/155407.

Osterbrock, D. E. (1981). Seyfert galaxies with weak broad H alpha emission lines. *ApJ*, 249, 462–470. ADS: 1981ApJ...249..462O. doi: 10.1086/159306.

Osterbrock, D. E. (1989). *Astrophysics of gaseous nebulae and active galactic nuclei*. ADS: 1989agna.book.....O.

Osterbrock, D. E. & Ferland, G. J. (2006). *Astrophysics of gaseous nebulae and active galactic nuclei*. ADS: 2006agna.book.....O.

Osterbrock, D. E. & Shaw, R. A. (1988). The relative number of Seyfert 2 galaxies. I - Spectra of emission-line galaxies in the Wasilewski field. *ApJ*, 327, 89–98. ADS: 1988ApJ...327...89O. doi: 10.1086/166172.

Osterbrock, D. E. & Shuder, J. M. (1982). Emission-line profiles in Seyfert 1 galaxies. *ApJS*, 49, 149–174. ADS: 1982ApJS...49..149O. doi: 10.1086/190793.

Otani, C., Kii, T., Reynolds, C. S., Fabian, A. C., Iwasawa, K., Hayashida, K., Inoue, H., Kunieda, H., Makino, F., Matsuoka, M., & Tanaka, Y. (1996). The Variable O,VIII Warm Absorber in MCG-6-30-15. *PASJ*, 48, 211–218. ADS: 1996PASJ...48..211O. doi: 10.1093/pasj/48.2.211.

Ouyed, R. & Pudritz, R. E. (1997). Numerical Simulations of Astrophysical Jets from Keplerian Disks. I. Stationary Models. *ApJ*, 482, 712–732. ADS: 1997ApJ...482..712O. doi: 10.1086/304170.

Owocki, S. P., Castor, J. I., & Rybicki, G. B. (1988). Time-dependent models of radiatively driven stellar winds. I - Nonlinear evolution of instabilities for a pure absorption model. *ApJ*, 335, 914–930. ADS: 1988ApJ...335..914O. doi: 10.1086/166977.

Owocki, S. P. & Rybicki, G. B. (1984). Instabilities in line-driven stellar winds. I - Dependence on perturbation wavelength. *ApJ*, 284, 337–350. ADS: 1984ApJ...284..337O. doi: 10.1086/

162412.

Padovani, P. (2016). The faint radio sky: radio astronomy becomes mainstream. *A&ARv*, 24, 13. ADS: 2016A&ARv..24...13P. doi: 10.1007/s00159-016-0098-6.

Padovani, P. (2017). On the two main classes of active galactic nuclei. *Nature Astronomy*, 1, 0194. ADS: 2017NatAs...1E.194P. doi: 10.1038/s41550-017-0194.

Padovani, P., Alexander, D. M., Assef, R. J., De Marco, B., Giommi, P., Hickox, R. C., Richards, G. T., Smolčić, V., Hatziminaoglou, E., Mainieri, V., & Salvato, M. (2017). Active galactic nuclei: what's in a name? *A&ARv*, 25, 2. ADS: 2017A&ARv..25....2P. doi: 10.1007/s00159-017-0102-9.

Padovani, P. & Urry, C. M. (1992). Luminosity functions, relativistic beaming, and unified theories of high-luminosity radio sources. *ApJ*, 387, 449–457. ADS: 1992ApJ...387..449P. doi: 10.1086/171098.

Pancoast, A., Brewer, B. J., & Treu, T. (2011). Geometric and Dynamical Models of Reverberation Mapping Data. *ApJ*, 730, 139. ADS: 2011ApJ...730..139P. doi: 10.1088/0004-637X/730/2/139.

Pancoast, A., Brewer, B. J., Treu, T., Park, D., Barth, A. J., Bentz, M. C., & Woo, J.-H. (2014). Modelling reverberation mapping data - II. Dynamical modelling of the Lick AGN Monitoring Project 2008 data set. *MNRAS*, 445, 3073–3091. ADS: 2014MNRAS.445.3073P. doi: 10.1093/mnras/stu1419.

Pâris, I., Petitjean, P., Aubourg, É., Bailey, S., Ross, N. P., Myers, A. D., Strauss, M. A., Anderson, S. F., Arnau, E., Bautista, J., Bizyaev, D., Bolton, A. S., Bovy, J., Brandt, W. N., Brewington, H., Browstein, J. R., Busca, N., Capellupo, D., Carithers, W., Croft, R. A. C., Dawson, K., Delubac, T., Ebelke, G., Eisenstein, D. J., Engelke, P., Fan, X., Filiz Ak, N., Finley, H., Font-Ribera, A., Ge, J., Gibson, R. R., Hall, P. B., Hamann, F., Hennawi, J. F., Ho, S., Hogg, D. W., Ivezić, Ž., Jiang, L., Kimball, A. E., Kirkby, D., Kirkpatrick, J. A., Lee, K.-G., Le Goff, J.-M., Lundgren, B., MacLeod, C. L., Malanushenko, E., Malanushenko, V., Maraston, C., McGreer, I. D., McMahon, R. G., Miralda-Escudé, J., Muna, D., Noterdaeme, P., Oravetz, D., Palanque-Delabrouille, N., Pan, K., Perez-Fournon, I., Pieri, M. M., Richards, G. T., Rollinde, E., Sheldon, E. S., Schlegel, D. J., Schneider, D. P., Slosar, A., Shelden, A., Shen, Y., Simmons, A., Snedden, S., Suzuki, N., Tinker, J., Viel, M., Weaver, B. A., Weinberg, D. H., White, M., Wood-Vasey, W. M., & Yèche, C. (2012). The Sloan Digital Sky Survey quasar catalog: ninth data release. *A&A*, 548, A66. ADS: 2012A&A...548A..66P. doi: 10.1051/0004-6361/201220142.

Pâris, I., Petitjean, P., Ross, N. P., Myers, A. D., Aubourg, É., Streblyanska, A., Bailey, S., Armengaud, É., Palanque-Delabrouille, N., Yèche, C., Hamann, F., Strauss, M. A., Albareti, F. D., Bovy, J., Bizyaev, D., Niel Brandt, W., Brusa, M., Buchner, J., Comparat, J., Croft, R. A. C., Dwelly, T., Fan, X., Font-Ribera, A., Ge, J., Georgakakis, A., Hall, P. B., Jiang, L., Kinemuchi, K., Malanushenko, E., Malanushenko, V., McMahon, R. G., Menzel, M.-L., Merloni, A., Nandra, K., Noterdaeme, P., Oravetz, D., Pan, K., Pieri, M. M., Prada, F., Salvato, M., Schlegel, D. J., Schneider, D. P., Simmons, A., Viel, M., Weinberg, D. H., & Zhu, L. (2017). The Sloan Digital Sky Survey Quasar Catalog: Twelfth data release. *A&A*,

597, A79. ADS: 2017A&A...597A..79P. doi: 10.1051/0004-6361/201527999.

Park, D., Barth, A. J., Woo, J.-H., Malkan, M. A., Treu, T., Bennert, V. N., Assef, R. J., & Pancoast, A. (2017). Extending the Calibration of C iv-based Single-epoch Black Hole Mass Estimators for Active Galactic Nuclei. *ApJ*, 839, 93. ADS: 2017ApJ...839...93P. doi: 10.3847/1538-4357/aa6a53.

Park, D., Kelly, B. C., Woo, J.-H., & Treu, T. (2012a). Recalibration of the Virial Factor and M $_{BH}$-σ_* Relation for Local Active Galaxies. *ApJS*, 203, 6. ADS: 2012ApJS..203....6P. doi: 10.1088/0067-0049/203/1/6.

Park, D., Woo, J.-H., Bennert, V. N., Treu, T., Auger, M. W., & Malkan, M. A. (2015). Cosmic Evolution of Black Holes and Spheroids. V. The Relation between Black Hole Mass and Host Galaxy Luminosity for a Sample of 79 Active Galaxies. *ApJ*, 799, 164. ADS: 2015ApJ...799..164P. doi: 10.1088/0004-637X/799/2/164.

Park, D., Woo, J.-H., Denney, K. D., & Shin, J. (2013). Calibrating C-IV-based Black Hole Mass Estimators. *ApJ*, 770, 87. ADS: 2013ApJ...770...87P. doi: 10.1088/0004-637X/770/2/87.

Park, D., Woo, J.-H., Treu, T., Barth, A. J., Bentz, M. C., Bennert, V. N., Canalizo, G., Filippenko, A. V., Gates, E., Greene, J. E., Malkan, M. A., & Walsh, J. (2012b). The Lick AGN Monitoring Project: Recalibrating Single-epoch Virial Black Hole Mass Estimates. *ApJ*, 747, 30. ADS: 2012ApJ...747...30P. doi: 10.1088/0004-637X/747/1/30.

Pauldrach, A., Puls, J., & Kudritzki, R. P. (1986). Radiation-driven winds of hot luminous stars - Improvements of the theory and first results. *A&A*, 164, 86–100. ADS: 1986A&A...164...86P.

Peacock, J. A., Miller, L., & Longair, M. S. (1986). The statistics of radio emission from quasars. *MNRAS*, 218, 265–278. ADS: 1986MNRAS.218..265P. doi: 10.1093/mnras/218.2.265.

Pedregosa, F., Varoquaux, G., Gramfort, A., Michel, V., Thirion, B., Grisel, O., Blondel, M., Prettenhofer, P., Weiss, R., Dubourg, V., Vanderplas, J., Passos, A., Cournapeau, D., Brucher, M., Perrot, M., & Duchesnay, E. (2011). Scikit-learn: Machine learning in Python. *Journal of Machine Learning Research*, 12, 2825–2830.

Pelletier, G. & Pudritz, R. E. (1992). Hydromagnetic disk winds in young stellar objects and active galactic nuclei. *ApJ*, 394, 117–138. ADS: 1992ApJ...394..117P. doi: 10.1086/171565.

Penston, M. V. & Perez, E. (1984). An evolutionary link between Seyfert I and II galaxies? *MNRAS*, 211, 33P–39P. ADS: 1984MNRAS.211P..33P. doi: 10.1093/mnras/211.1.33P.

Pérez, F. & Granger, B. E. (2007). IPython: a system for interactive scientific computing. *Computing in Science and Engineering*, 9(3), 21–29. doi: 10.1109/MCSE.2007.53.

Peterson, B. M. (1993). Reverberation mapping of active galactic nuclei. *PASP*, 105, 247–268. ADS: 1993PASP..105..247P. doi: 10.1086/133140.

Peterson, B. M. (1997). *An Introduction to Active Galactic Nuclei*. ADS: 1997iagn.book.....P.

Peterson, B. M. (2006). The Broad-Line Region in Active Galactic Nuclei. In D. Alloin (Ed.), *Physics of Active Galactic Nuclei at all Scales*, volume 693 of *Lecture Notes in Physics, Berlin Springer Verlag* (pp.77). ADS: 2006LNP...693...77P. doi: 10.1007/3-540-34621-X_3.

Peterson, B. M. (2010). Toward Precision Measurement of Central Black Hole Masses. In B. M. Peterson, R. S. Somerville, & T. Storchi-Bergmann (Eds.), *IAU Symposium*, volume 267 of *IAU Symposium* (pp. 151–160). ADS: 2010IAUS..267..151P. doi: 10.1017/S1743921310006095.

Peterson, B. M. (2011). Masses of Black Holes in Active Galactic Nuclei: Implications for NLS1s. *ArXiv e-prints*. ADS: 2011arXiv1109.4181P. arXiv: 1109.4181.

Peterson, B. M. (2014). Measuring the Masses of Supermassive Black Holes. *SSRv*, 183, 253–275. ADS: 2014SSRv..183..253P. doi: 10.1007/s11214-013-9987-4.

Peterson, B. M., Denney, K. D., De Rosa, G., Grier, C. J., Pogge, R. W., Bentz, M. C., Kochanek, C. S., Vestergaard, M., Kilerci-Eser, E., Dalla Bontà, E., & Ciroi, S. (2013). The Size of the Narrow-line-emitting Region in the Seyfert 1 Galaxy NGC 5548 from Emission-line Variability. *ApJ*, 779, 109. ADS: 2013ApJ...779..109P. doi: 10.1088/0004-637X/779/2/109.

Peterson, B. M., Ferrarese, L., Gilbert, K. M., Kaspi, S., Malkan, M. A., Maoz, D., Merritt, D., Netzer, H., Onken, C. A., Pogge, R. W., Vestergaard, M., & Wandel, A. (2004). Central Masses and Broad-Line Region Sizes of Active Galactic Nuclei. II. A Homogeneous Analysis of a Large Reverberation-Mapping Database. *ApJ*, 613, 682–699. ADS: 2004ApJ...613..682P. doi: 10.1086/423269.

Peterson, B. M., Grier, C. J., Horne, K., Pogge, R. W., Bentz, M. C., De Rosa, G., Denney, K. D., Martini, P., Sergeev, S. G., Kaspi, S., Minezaki, T., Zu, Y., Kochanek, C. S., Siverd, R. J., Shappee, B., Araya Salvo, C., Beatty, T. G., Bird, J. C., Bord, D. J., Borman, G. A., Che, X., Chen, C.-T., Cohen, S. A., Dietrich, M., Doroshenko, V. T., Drake, T., Efimov, Y. S., Free, N., Ginsburg, I., Henderson, C. B., King, A. L., Koshida, S., Mogren, K., Molina, M., Mosquera, A. M., Motohara, K., Nazarov, S. V., Okhmat, D. N., Pejcha, O., Rafter, S., Shields, J. C., Skowron, D. M., Skowron, J., Valluri, M., van Saders, J. L., & Yoshii, Y. (2014). Reverberation Mapping of the Seyfert 1 Galaxy NGC 7469. *ApJ*, 795, 149. ADS: 2014ApJ...795..149P. doi: 10.1088/0004-637X/795/2/149.

Peterson, B. M., Korista, K. T., & Cota, S. A. (1987). The double broad-line emitting regions in NGC 5548 as possible evidence for a supermassive binary. *ApJ*, 312, L1–L4. ADS: 1987ApJ...312L...1P. doi: 10.1086/184808.

Peterson, B. M. & Wandel, A. (1999). Keplerian Motion of Broad-Line Region Gas as Evidence for Supermassive Black Holes in Active Galactic Nuclei. *ApJ*, 521, L95–L98. ADS: 1999ApJ...521L..95P. doi: 10.1086/312190.

Pettitt, A. N. (1976). A two-sample anderson–darling rank statistic. *Biometrika*, 63(1), 161–168.

Pier, E. A. & Krolik, J. H. (1992). Infrared spectra of obscuring dust tori around active galactic nuclei. I - Calculational method and basic trends. *ApJ*, 401, 99–109. ADS: 1992ApJ...401...99P. doi: 10.1086/172042.

Pier, E. A. & Krolik, J. H. (1993). Infrared Spectra of Obscuring Dust Tori around Active Galactic Nuclei. II. Comparison with Observations. *ApJ*, 418, 673. ADS: 1993ApJ...418..673P. doi: 10.1086/173427.

Pogge, R. W. (1989). The circumnuclear environment of nearby, noninteracting Seyfert galaxies.

ApJ, 345, 730–751. ADS: 1989ApJ...345..730P. doi: 10.1086/167945.

Ponti, G., Fender, R. P., Begelman, M. C., Dunn, R. J. H., Neilsen, J., & Coriat, M. (2012). Ubiquitous equatorial accretion disc winds in black hole soft states. *MNRAS*, 422, L11–L15. ADS: 2012MNRAS.422L..11P. doi: 10.1111/j.1745-3933.2012.01224.x.

Popović, L. Č., Shapovalova, A. I., Ilić, D., Kovačević, A., Kollatschny, W., Burenkov, A. N., Chavushyan, V. H., Bochkarev, N. G., & León-Tavares, J. (2011). Spectral optical monitoring of 3C 390.3 in 1995-2007. II. Variability of the spectral line parameters. *A&A*, 528, A130. ADS: 2011A&A...528A.130P. doi: 10.1051/0004-6361/201016317.

Pounds, K. A., Reeves, J. N., King, A. R., Page, K. L., O'Brien, P. T., & Turner, M. J. L. (2003). A high-velocity ionized outflow and XUV photosphere in the narrow emission line quasar PG1211+143. *MNRAS*, 345, 705–713. ADS: 2003MNRAS.345..705P. doi: 10.1046/j.1365-8711.2003.07006.x.

Pringle, J. E. (1996). Self-induced warping of accretion discs. *MNRAS*, 281(1), 357–361. ADS: 1996MNRAS.281..357P. doi: 10.1093/mnras/281.1.357.

Proga, D. (2003). Numerical Simulations of Mass Outflows Driven from Accretion Disks by Radiation and Magnetic Forces. *ApJ*, 585, 406–417. ADS: 2003ApJ...585..406P. doi: 10.1086/345897.

Proga, D. (2007). Theory of Winds in AGNs. In L. C. Ho & J.-W. Wang (Eds.), *The Central Engine of Active Galactic Nuclei*, volume 373 of *Astronomical Society of the Pacific Conference Series* (pp. 267). ADS: 2007ASPC..373..267P.

Proga, D. & Kallman, T. R. (2004). Dynamics of Line-driven Disk Winds in Active Galactic Nuclei. II. Effects of Disk Radiation. *ApJ*, 616, 688–695. ADS: 2004ApJ...616..688P. doi: 10.1086/425117.

Proga, D., Stone, J. M., & Drew, J. E. (1998). Radiation-driven winds from luminous accretion discs. *MNRAS*, 295, 595. ADS: 1998MNRAS.295..595P. doi: 10.1046/j.1365-8711.1998.01337.x.

Proga, D., Stone, J. M., & Drew, J. E. (1999). Line-driven disc wind models with an improved line force. *MNRAS*, 310, 476–482. ADS: 1999MNRAS.310..476P. doi: 10.1046/j.1365-8711.1999.02935.x.

Proga, D., Stone, J. M., & Kallman, T. R. (2000). Dynamics of Line-driven Disk Winds in Active Galactic Nuclei. *ApJ*, 543, 686–696. ADS: 2000ApJ...543..686P. doi: 10.1086/317154.

Puccetti, S., Fiore, F., Risaliti, G., Capalbi, M., Elvis, M., & Nicastro, F. (2007). Rapid N_H changes in NGC 4151. *MNRAS*, 377, 607–616. ADS: 2007MNRAS.377..607P. doi: 10.1111/j.1365-2966.2007.11634.x.

Puchnarewicz, E. M., Mason, K. O., Carrera, F. J., Brandt, W. N., Cabrera-Guera, F., Carballo, R., Hasinger, G., McMahon, R. G., Mittaz, J. P. D., Page, M. J., Perez-Fournon, I., & Schwope, A. (1997). Optical and X-ray properties of the RIXOS AGN - II. Emission lines. *MNRAS*, 291, 177–202. ADS: 1997MNRAS.291..177P. doi: 10.1093/mnras/291.1.177.

Puchnarewicz, E. M., Mason, K. O., Romero-Colmenero, E., Carrera, F. J., Hasinger, G., McMahon, R., Mittaz, J. P. D., Page, M. J., & Carballo, R. (1996). Optical and X-ray properties of the RIXOS active galactic nuclei - I. The continua. *MNRAS*, 281, 1243–1266. ADS: 1996MNRAS.281.1243P. doi: 10.1093/mnras/281.4.1243.

Punsly, B. & Zhang, S. (2010). Hβ Line Widths as an Orientation Indicator for Low-ionization Broad Absorption Line Quasars. *ApJ*, 725, 1928–1937. ADS: 2010ApJ...725.1928P. doi: 10.1088/0004-637X/725/2/1928.

Rafiee, A. & Hall, P. B. (2011). Supermassive Black Hole Mass Estimates Using Sloan Digital Sky Survey Quasar Spectra at $0.7 < z < 2$. *ApJS*, 194, 42. ADS: 2011ApJS..194...42R. doi: 10.1088/0067-0049/194/2/42.

Ramos Almeida, C. & Ricci, C. (2017). Nuclear obscuration in active galactic nuclei. *Nature Astronomy*, 1, 679–689. ADS: 2017NatAs...1..679R. doi: 10.1038/s41550-017-0232-z.

Rawlings, S. & Saunders, R. (1991). Evidence for a common central-engine mechanism in all extragalactic radio sources. *Nature*, 349, 138–140. ADS: 1991Natur.349..138R. doi: 10.1038/349138a0.

Rees, M. J. (1987). Magnetic confinement of broad-line clouds in active galactic nuclei. *MNRAS*, 228, 47P–50P. ADS: 1987MNRAS.228P..47R. doi: 10.1093/mnras/228.1.47P.

Reeves, J. N., O'Brien, P. T., & Ward, M. J. (2003). A Massive X-Ray Outflow from the Quasar PDS 456. *ApJ*, 593, L65–L68. ADS: 2003ApJ...593L..65R. doi: 10.1086/378218.

Reichard, T. A., Richards, G. T., Hall, P. B., Schneider, D. P., Vanden Berk, D. E., Fan, X., York, D. G., Knapp, G. R., & Brinkmann, J. (2003). Continuum and Emission-Line Properties of Broad Absorption Line Quasars. *AJ*, 126, 2594–2607. ADS: 2003AJ....126.2594R. doi: 10.1086/379293.

Reyes, R., Zakamska, N. L., Strauss, M. A., Green, J., Krolik, J. H., Shen, Y., Richards, G. T., Anderson, S. F., & Schneider, D. P. (2008). Space Density of Optically Selected Type 2 Quasars. *AJ*, 136, 2373–2390. ADS: 2008AJ....136.2373R. doi: 10.1088/0004-6256/136/6/2373.

Reynolds, C. S. (1997). An X-ray spectral study of 24 type 1 active galactic nuclei. *MNRAS*, 286, 513–537. ADS: 1997MNRAS.286..513R. doi: 10.1093/mnras/286.3.513.

Reynolds, C. S. & Fabian, A. C. (1995). Warm absorbers in active galactic nuclei. *MNRAS*, 273, 1167–1176. ADS: 1995MNRAS.273.1167R. doi: 10.1093/mnras/273.4.1167.

Ricci, C., Bauer, F. E., Arevalo, P., Boggs, S., Brandt, W. N., Christensen, F. E., Craig, W. W., Gandhi, P., Hailey, C. J., Harrison, F. A., Koss, M., Markwardt, C. B., Stern, D., Treister, E., & Zhang, W. W. (2016). IC 751: A New Changing Look AGN Discovered by NuSTAR. *ApJ*, 820, 5. ADS: 2016ApJ...820....5R. doi: 10.3847/0004-637X/820/1/5.

Richards, G. T., Kruczek, N. E., Gallagher, S. C., Hall, P. B., Hewett, P. C., Leighly, K. M., Deo, R. P., Kratzer, R. M., & Shen, Y. (2011). Unification of Luminous Type 1 Quasars through C IV Emission. *AJ*, 141, 167. ADS: 2011AJ....141..167R. doi: 10.1088/0004-6256/141/5/167.

Richards, G. T., Strauss, M. A., Fan, X., Hall, P. B., Jester, S., Schneider, D. P., Vanden Berk,

D. E., Stoughton, C., Anderson, S. F., Brunner, R. J., Gray, J., Gunn, J. E., Ivezić, Ž., Kirkland, M. K., Knapp, G. R., Loveday, J., Meiksin, A., Pope, A., Szalay, A. S., Thakar, A. R., Yanny, B., York, D. G., Barentine, J. C., Brewington, H. J., Brinkmann, J., Fukugita, M., Harvanek, M., Kent, S. M., Kleinman, S. J., Krzesiński, J., Long, D. C., Lupton, R. H., Nash, T., Neilsen, Jr., E. H., Nitta, A., Schlegel, D. J., & Snedden, S. A. (2006). The Sloan Digital Sky Survey Quasar Survey: Quasar Luminosity Function from Data Release 3. *AJ*, 131, 2766–2787. ADS: 2006AJ....131.2766R. doi: 10.1086/503559.

Richards, G. T., Vanden Berk, D. E., Reichard, T. A., Hall, P. B., Schneider, D. P., SubbaRao, M., Thakar, A. R., & York, D. G. (2002). Broad Emission-Line Shifts in Quasars: An Orientation Measure for Radio-Quiet Quasars? *AJ*, 124, 1–17. ADS: 2002AJ....124....1R. doi: 10.1086/341167.

Richstone, D. (1998). Black holes and galaxy centers (Review). In Y. Sofue (Ed.), *The Central Regions of the Galaxy and Galaxies*, volume 184 of *IAU Symposium* (pp. 451). ADS: 1998IAUS..184..451R.

Risaliti, G. & Lusso, E. (2015). A Hubble Diagram for Quasars. *ApJ*, 815, 33. ADS: 2015ApJ...815...33R. doi: 10.1088/0004-637X/815/1/33.

Risaliti, G. & Lusso, E. (2019). Cosmological Constraints from the Hubble Diagram of Quasars at High Redshifts. *Nature Astronomy*, 3, 272–277. ADS: 2019NatAs...3..272R. doi: 10.1038/s41550-018-0657-z.

Risaliti, G., Miniutti, G., Elvis, M., Fabbiano, G., Salvati, M., Baldi, A., Braito, V., Bianchi, S., Matt, G., Reeves, J., Soria, R., & Zezas, A. (2009). Variable Partial Covering and A Relativistic Iron Line in NGC 1365. *ApJ*, 696, 160–171. ADS: 2009ApJ...696..160R. doi: 10.1088/0004-637X/696/1/160.

Risaliti, G., Salvati, M., & Marconi, A. (2011). [O III] equivalent width and orientation effects in quasars. *MNRAS*, 411, 2223–2229. ADS: 2011MNRAS.411.2223R. doi: 10.1111/j.1365-2966.2010.17843.x.

Rochais, T. B., DiPompeo, M. A., Myers, A. D., Brotherton, M. S., Runnoe, J. C., & Hall, S. W. (2014). Radio-loud and radio-quiet BAL quasars: a detailed ultraviolet comparison. *MNRAS*, 444, 2498–2506. ADS: 2014MNRAS.444.2498R. doi: 10.1093/mnras/stu1635.

Roettgering, H. J. A., Lacy, M., Miley, G. K., Chambers, K. C., & Saunders, R. (1994). Samples of ultra-steep spectrum radio sources. *A&AS*, 108, 79–141. ADS: 1994A&AS..108...79R.

Roettgering, H. J. A., van Ojik, R., Miley, G. K., Chambers, K. C., van Breugel, W. J. M., & de Koff, S. (1997). Spectroscopy of ultra-steep spectrum radio sources: a sample of z>2 radio galaxies. *A&AS*, 326, 505–527. ADS: 1997A&A...326..505R.

Rokaki, E., Boisson, C., & Collin-Souffrin, S. (1992). Fitting the broad line spectrum and UV continuum by accretion discs in active galactic nuclei. *A&A*, 253, 57–73. ADS: 1992A&A...253...57R.

Ruff, A. J., Floyd, D. J. E., Webster, R. L., Korista, K. T., & Landt, H. (2012). New Constraints on the Quasar Broad Emission Line Region. *ApJ*, 754, 18. ADS: 2012ApJ...754...18R.

doi: 10.1088/0004-637X/754/1/18.

Runnoe, J. C., Brotherton, M. S., DiPompeo, M. A., & Shang, Z. (2014). The behaviour of quasar C IV emission-line properties with orientation. *MNRAS*, 438, 3263–3274. ADS: 2014MNRAS.438.3263R. doi: 10.1093/mnras/stt2429.

Runnoe, J. C., Brotherton, M. S., Shang, Z., & DiPompeo, M. A. (2013a). Rehabilitating C IV-based black hole mass estimates in quasars. *MNRAS*, 434, 848–861. ADS: 2013MNRAS.434..848R. doi: 10.1093/mnras/stt1077.

Runnoe, J. C., Brotherton, M. S., Shang, Z., Wills, B. J., & DiPompeo, M. A. (2013b). The orientation dependence of quasar single-epoch black hole mass scaling relationships. *MNRAS*, 429, 135–149. ADS: 2013MNRAS.429..135R. doi: 10.1093/mnras/sts322.

Runnoe, J. C., Cales, S., Ruan, J. J., Eracleous, M., Anderson, S. F., Shen, Y., Green, P. J., Morganson, E., LaMassa, S., Greene, J. E., Dwelly, T., Schneider, D. P., Merloni, A., Georgakakis, A., & Roman-Lopes, A. (2016). Now you see it, now you don't: the disappearing central engine of the quasar J1011+5442. *MNRAS*, 455, 1691–1701. ADS: 2016MNRAS.455.1691R. doi: 10.1093/mnras/stv2385.

Ruschel-Dutra, D., Pastoriza, M., Riffel, R., Sales, D. A., & Winge, C. (2014). A mid-IR comparative analysis of the Seyfert galaxies NGC 7213 and NGC 1386. *MNRAS*, 438, 3434–3442. ADS: 2014MNRAS.438.3434R. doi: 10.1093/mnras/stt2448.

Russell, H. R., McNamara, B. R., Edge, A. C., Hogan, M. T., Main, R. A., & Vantyghem, A. N. (2013). Radiative efficiency, variability and Bondi accretion on to massive black holes: the transition from radio AGN to quasars in brightest cluster galaxies. *MNRAS*, 432, 530–553. ADS: 2013MNRAS.432..530R. doi: 10.1093/mnras/stt490.

Rybicki, G. B. & Hummer, D. G. (1978). A generalization of the Sobolev method for flows with nonlocal radiative coupling. *ApJ*, 219, 654–675. ADS: 1978ApJ...219..654R. doi: 10.1086/155826.

Rybicki, G. B. & Hummer, D. G. (1983). The specific luminosity of a three-dimensional medium in terms of the escape probability. *ApJ*, 274, 380–398. ADS: 1983ApJ...274..380R. doi: 10.1086/161454.

Sadler, E. M. (2016). GPS/CSS radio sources and their relation to other AGN. *Astronomische Nachrichten*, 337, 105. ADS: 2016AN....337..105S. doi: 10.1002/asna.201512274.

Sales, D. A., Pastoriza, M. G., Riffel, R., Winge, C., Rodríguez-Ardila, A., & Carciofi, A. C. (2011). The Compton-thick Seyfert 2 Nucleus of NGC 3281: Torus Constraints from the 9.7 μm Silicate Absorption. *ApJ*, 738, 109. ADS: 2011ApJ...738..109S. doi: 10.1088/0004-637X/738/1/109.

Salviander, S., Shields, G. A., Gebhardt, K., & Bonning, E. W. (2007). The Black Hole Mass-Galaxy Bulge Relationship for QSOs in the Sloan Digital Sky Survey Data Release 3. *ApJ*, 662, 131–144. ADS: 2007ApJ...662..131S. doi: 10.1086/513086.

Sandage, A. (1965). The Existence of a Major New Constituent of the Universe: the Quasistellar Galaxies. *ApJ*, 141, 1560. ADS: 1965ApJ...141.1560S. doi: 10.1086/148245.

Sanders, D. B., Phinney, E. S., Neugebauer, G., Soifer, B. T., & Matthews, K. (1989). Continuum Energy Distributions of Quasars: Shapes and Origins. *ApJ*, 347, 29. ADS: 1989ApJ...347..29S. doi: 10.1086/168094.

Sazonov, S., Churazov, E., & Krivonos, R. (2015). Does the obscured AGN fraction really depend on luminosity? *MNRAS*, 454, 1202–1220. ADS: 2015MNRAS.454.1202S. doi: 10.1093/mnras/stv2069.

Schartmann, M., Meisenheimer, K., Camenzind, M., Wolf, S., Tristram, K. R. W., & Henning, T. (2008). Three-dimensional radiative transfer models of clumpy tori in Seyfert galaxies. *A&A*, 482, 67–80. ADS: 2008A&A...482...67S. doi: 10.1051/0004-6361:20078907.

Scheuer, P. A. G. (1987). Tests of beaming models. In J. A. Zensus & T. J. Pearson (Eds.), *Superluminal Radio Sources* (pp. 104–113). ADS: 1987slrs.work..104S.

Schmidt, M. (1963). 3C 273 : A Star-Like Object with Large Red-Shift. *Nature*, 197, 1040. ADS: 1963Natur.197.1040S. doi: 10.1038/1971040a0.

Schmidt, M. (1970). Space Distribution and Luminosity Functions of Quasars. *ApJ*, 162, 371. ADS: 1970ApJ...162..371S. doi: 10.1086/150668.

Schneider, D. P., Hall, P. B., Richards, G. T., Strauss, M. A., Vanden Berk, D. E., Anderson, S. F., Brandt, W. N., Fan, X., Jester, S., Gray, J., Gunn, J. E., SubbaRao, M. U., Thakar, A. R., Stoughton, C., Szalay, A. S., Yanny, B., York, D. G., Bahcall, N. A., Barentine, J., Blanton, M. R., Brewington, H., Brinkmann, J., Brunner, R. J., Castander, F. J., Csabai, I., Frieman, J. A., Fukugita, M., Harvanek, M., Hogg, D. W., Ivezić, Ž., Kent, S. M., Kleinman, S. J., Knapp, G. R., Kron, R. G., Krzesiński, J., Long, D. C., Lupton, R. H., Nitta, A., Pier, J. R., Saxe, D. H., Shen, Y., Snedden, S. A., Weinberg, D. H., & Wu, J. (2007). The Sloan Digital Sky Survey Quasar Catalog. IV. Fifth Data Release. *AJ*, 134, 102–117. ADS: 2007AJ....134..102S. doi: 10.1086/518474.

Schneider, D. P., Richards, G. T., Hall, P. B., Strauss, M. A., Anderson, S. F., Boroson, T. A., Ross, N. P., Shen, Y., Brandt, W. N., Fan, X., Inada, N., Jester, S., Knapp, G. R., Krawczyk, C. M., Thakar, A. R., Vanden Berk, D. E., Voges, W., Yanny, B., York, D. G., Bahcall, N. A., Bizyaev, D., Blanton, M. R., Brewington, H., Brinkmann, J., Eisenstein, D., Frieman, J. A., Fukugita, M., Gray, J., Gunn, J. E., Hibon, P., Ivezić, Ž., Kent, S. M., Kron, R. G., Lee, M. G., Lupton, R. H., Malanushenko, E., Malanushenko, V., Oravetz, D., Pan, K., Pier, J. R., Price, III, T. N., Saxe, D. H., Schlegel, D. J., Simmons, A., Snedden, S. A., SubbaRao, M. U., Szalay, A. S., & Weinberg, D. H. (2010). The Sloan Digital Sky Survey Quasar Catalog. V. Seventh Data Release. *AJ*, 139, 2360. ADS: 2010AJ....139.2360S. doi: 10.1088/0004-6256/139/6/2360.

Schulze, A. & Wisotzki, L. (2010). Low redshift AGN in the Hamburg/ESO Survey . II. The active black hole mass function and the distribution function of Eddington ratios. *A&A*, 516, A87. ADS: 2010A&A...516A..87S. doi: 10.1051/0004-6361/201014193.

Sergeev, S. G., Klimanov, S. A., Doroshenko, V. T., Efimov, Y. S., Nazarov, S. V., & Pronik, V. I. (2011). Variability of the 3C 390.3 nucleus in 2000-2007 and a new estimate of the central black hole mass. *MNRAS*, 410, 1877–1885. ADS: 2011MNRAS.410.1877S. doi: 10.1111/j.1365-2966.2010.17569.x.

Sergeev, S. G., Pronik, V. I., Peterson, B. M., Sergeeva, E. A., & Zheng, W. (2002). Variability of the Broad Balmer Emission Lines in 3C 390.3 from 1992 to 2000. *ApJ*, 576, 660–672. ADS: 2002ApJ...576..660S. doi: 10.1086/341791.

Sergeev, S. G., Pronik, V. I., & Sergeeva, E. A. (2000). Arp 102B: variability patterns of the Hα line profile as evidence for gas rotation in the broad-line region. *A&A*, 356, 41–49. ADS: 2000A&A...356...41S.

Sergeev, S. G., Pronik, V. I., Sergeeva, E. A., & Malkov, Y. F. (1999). A Link between the Hβ Equivalent Width, Profile Width, BLR Size, and Optical Luminosity from a Small Sample of Well-studied Active Galactic Nuclei. *AJ*, 118, 2658–2667. ADS: 1999AJ....118.2658S. doi: 10.1086/301124.

Sesar, B., Ivezić, Ž., Lupton, R. H., Jurić, M., Gunn, J. E., Knapp, G. R., DeLee, N., Smith, J. A., Miknaitis, G., Lin, H., Tucker, D., Doi, M., Tanaka, M., Fukugita, M., Holtzman, J., Kent, S., Yanny, B., Schlegel, D., Finkbeiner, D., Padmanabhan, N., Rockosi, C. M., Bond, N., Lee, B., Stoughton, C., Jester, S., Harris, H., Harding, P., Brinkmann, J., Schneider, D. P., York, D., Richmond, M. W., & Vanden Berk, D. (2007). Exploring the Variable Sky with the Sloan Digital Sky Survey. *AJ*, 134, 2236–2251. ADS: 2007AJ....134.2236S. doi: 10.1086/521819.

Seyfert, C. K. (1943). Nuclear Emission in Spiral Nebulae. *ApJ*, 97, 28. ADS: 1943ApJ....97...28S. doi: 10.1086/144488.

Shakura, N. I. & Sunyaev, R. A. (1973). Black holes in binary systems. Observational appearance. *A&A*, 24, 337–355. ADS: 1973A&A....24..337S.

Shankar, F., Dai, X., & Sivakoff, G. R. (2008). Dependence of the Broad Absorption Line Quasar Fraction on Radio Luminosity. *ApJ*, 687, 859–868. ADS: 2008ApJ...687..859S. doi: 10.1086/591488.

Shannon, C. (1948). A mathematical theory of communication. *The Bell System Technical Journal*, 27(3), 379–423.

Shapovalova, A. I., Doroshenko, V. T., Bochkarev, N. G., Burenkov, A. N., Carrasco, L., Chavushyan, V. H., Collin, S., Valdés, J. R., Borisov, N., Dumont, A.-M., Vlasuyk, V. V., Chilingarian, I., Fioktistova, I. S., & Martinez, O. M. (2004). Profile variability of the Hα and Hβ broad emission lines in NGC 5548. *A&A*, 422, 925–940. ADS: 2004A&A...422..925S. doi: 10.1051/0004-6361:20035652.

Shapovalova, A. I., Popović, L. Č., Burenkov, A. N., Chavushyan, V. H., Ilić, D., Kollatschny, W., Kovačević, A., Bochkarev, N. G., Carrasco, L., León-Tavares, J., Mercado, A., Valdes, J. R., Vlasuyk, V. V., & de La Fuente, E. (2010). Spectral optical monitoring of 3C 390.3 in 1995-2007. I. Light curves and flux variation in the continuum and broad lines. *A&A*, 517, A42. ADS: 2010A&A...517A..42S. doi: 10.1051/0004-6361/201014118.

Shapovalova, A. I., Popović, L. Č., Burenkov, A. N., Chavushyan, V. H., Ilić, D., Kollatschny, W., Kovačević, A., Bochkarev, N. G., Valdés, J. R., Torrealba, J., Patiño-Álvarez, V., León-Tavares, J., Benitez, E., Carrasco, L., Dultzin, D., Mercado, A., & Zhdanova, V. E. (2013). Spectral optical monitoring of a double-peaked emission line AGN Arp 102B. Variability of

spectral lines and continuum. *A&A*, 559, A10. ADS: 2013A&A...559A..10S. doi: 10.1051/0004-6361/201321781.

Shappee, B. J., Prieto, J. L., Grupe, D., Kochanek, C. S., Stanek, K. Z., De Rosa, G., Mathur, S., Zu, Y., Peterson, B. M., Pogge, R. W., Komossa, S., Im, M., Jencson, J., Holoien, T. W.-S., Basu, U., Beacom, J. F., Szczygieł, D. M., Brimacombe, J., Adams, S., Campillay, A., Choi, C., Contreras, C., Dietrich, M., Dubberley, M., Elphick, M., Foale, S., Giustini, M., Gonzalez, C., Hawkins, E., Howell, D. A., Hsiao, E. Y., Koss, M., Leighly, K. M., Morrell, N., Mudd, D., Mullins, D., Nugent, J. M., Parrent, J., Phillips, M. M., Pojmanski, G., Rosing, W., Ross, R., Sand, D., Terndrup, D. M., Valenti, S., Walker, Z., & Yoon, Y. (2014). The Man behind the Curtain: X-Rays Drive the UV through NIR Variability in the 2013 Active Galactic Nucleus Outburst in NGC 2617. *ApJ*, 788, 48. ADS: 2014ApJ...788...48S. doi: 10.1088/0004-637X/788/1/48.

Shen, Y. (2016). Rest-frame Optical Properties of Luminous $1.5 < Z < 3.5$ Quasars: The Hβ-[O III] Region. *ApJ*, 817, 55. ADS: 2016ApJ...817...55S. doi: 10.3847/0004-637X/817/1/55.

Shen, Y., Brandt, W. N., Richards, G. T., Denney, K. D., Greene, J. E., Grier, C. J., Ho, L. C., Peterson, B. M., Petitjean, P., Schneider, D. P., Tao, C., & Trump, J. R. (2016). The Sloan Digital Sky Survey Reverberation Mapping Project: Velocity Shifts of Quasar Emission Lines. *ApJ*, 831, 7. ADS: 2016ApJ...831....7S. doi: 10.3847/0004-637X/831/1/7.

Shen, Y., Greene, J. E., Strauss, M. A., Richards, G. T., & Schneider, D. P. (2008). Biases in Virial Black Hole Masses: An SDSS Perspective. *ApJ*, 680, 169–190. ADS: 2008ApJ...680..169S. doi: 10.1086/587475.

Shen, Y. & Ho, L. C. (2014). The diversity of quasars unified by accretion and orientation. *Nature*, 513, 210–213. ADS: 2014Natur.513..210S. doi: 10.1038/nature13712.

Shen, Y. & Liu, X. (2012). Comparing Single-epoch Virial Black Hole Mass Estimators for Luminous Quasars. *ApJ*, 753, 125. ADS: 2012ApJ...753..125S. doi: 10.1088/0004-637X/753/2/125.

Shen, Y., Richards, G. T., Strauss, M. A., Hall, P. B., Schneider, D. P., Snedden, S., Bizyaev, D., Brewington, H., Malanushenko, V., Malanushenko, E., Oravetz, D., Pan, K., & Simmons, A. (2011). A Catalog of Quasar Properties from Sloan Digital Sky Survey Data Release 7. *ApJS*, 194, 45. ADS: 2011ApJS..194...45S. doi: 10.1088/0067-0049/194/2/45.

Shields, G. A. (1978). Thermal continuum from acretion disks in quasars. *Nature*, 272, 706–708. ADS: 1978Natur.272..706S. doi: 10.1038/272706a0.

Shlosman, I. & Vitello, P. (1993). Winds from accretion disks - Ultraviolet line formation in cataclysmic variables. *ApJ*, 409, 372–386. ADS: 1993ApJ...409..372S. doi: 10.1086/172670.

Shlosman, I., Vitello, P. A., & Shaviv, G. (1985). Active galactic nuclei - Internal dynamics and formation of emission clouds. *ApJ*, 294, 96–105. ADS: 1985ApJ...294...96S. doi: 10.1086/163278.

Shuder, J. M. (1982). On the physical conditions and the velocity fields in Seyfert 1 galaxies and QSOs. *ApJ*, 259, 48–54. ADS: 1982ApJ...259...48S. doi: 10.1086/160145.

Siebenmorgen, R., Haas, M., Krügel, E., & Schulz, B. (2005). Discovery of 10 μm silicate emission in quasars. Evidence of the AGN unification scheme. *A&A*, 436, L5–L8. ADS: 2005A&A...436L...5S. doi: 10.1051/0004-6361:200500109.

Silk, J. & Rees, M. J. (1998). Quasars and galaxy formation. *A&A*, 331, L1–L4. ADS: 1998A&A...331L...1S.

Sim, S. A., Proga, D., Miller, L., Long, K. S., & Turner, T. J. (2010). Multidimensional modelling of X-ray spectra for AGN accretion disc outflows - III. Application to a hydrodynamical simulation. *MNRAS*, 408, 1396–1408. ADS: 2010MNRAS.408.1396S. doi: 10.1111/j.1365-2966.2010.17215.x.

Simon, L. E. & Hamann, F. (2010). The origins of a rich absorption line complex in a quasar at redshift 3.45. *MNRAS*, 409, 269–283. ADS: 2010MNRAS.409..269S. doi: 10.1111/j.1365-2966.2010.17306.x.

Simpson, C. (2005). The luminosity dependence of the type 1 active galactic nucleus fraction. *MNRAS*, 360, 565–572. ADS: 2005MNRAS.360..565S. doi: 10.1111/j.1365-2966.2005.09043.x.

Sluse, D., Schmidt, R., Courbin, F., Hutsemékers, D., Meylan, G., Eigenbrod, A., Anguita, T., Agol, E., & Wambsganss, J. (2011). Zooming into the broad line region of the gravitationally lensed quasar QSO 2237 + 0305 ≡ the Einstein Cross. III. Determination of the size and structure of the C iv and C iii] emitting regions using microlensing. *A&A*, 528, A100. ADS: 2011A&A...528A.100S. doi: 10.1051/0004-6361/201016110.

Smirnov, N. (1939). Sur les écarts de la courbe de distribution empirique. *Matematicheskii Sbornik*, 48(1), 3–26.

Smith, M. G. & Wright, A. E. (1980). A radio study of optically selected QSOs. *MNRAS*, 191, 871–886. ADS: 1980MNRAS.191..871S. doi: 10.1093/mnras/191.4.871.

Smolčić, V. (2009). The Radio AGN Population Dichotomy: Green Valley Seyferts Versus Red Sequence Low-Excitation Active Galactic Nuclei. *ApJ*, 699, L43–L47. ADS: 2009ApJ...699L..43S. doi: 10.1088/0004-637X/699/1/L43.

Spearman, C. (1904). The proof and measurement of association between two things. *The American Journal of Psychology*, 15(1), 72–101.

Spergel, D. N., Verde, L., Peiris, H. V., Komatsu, E., Nolta, M. R., Bennett, C. L., Halpern, M., Hinshaw, G., Jarosik, N., Kogut, A., Limon, M., Meyer, S. S., Page, L., Tucker, G. S., Weiland, J. L., Wollack, E., & Wright, E. L. (2003). First-Year Wilkinson Microwave Anisotropy Probe (WMAP) Observations: Determination of Cosmological Parameters. *ApJS*, 148, 175–194. ADS: 2003ApJS..148..175S. doi: 10.1086/377226.

Sprayberry, D. & Foltz, C. B. (1992). Extinction in low-ionization broad absorption line quasi-stellar objects. *ApJ*, 390, 39–45. ADS: 1992ApJ...390...39S. doi: 10.1086/171257.

Sramek, R. A. & Weedman, D. W. (1980). The radio properties of optically discovered quasars. *ApJ*, 238, 435–444. ADS: 1980ApJ...238..435S. doi: 10.1086/158000.

Stalevski, M., Fritz, J., Baes, M., Nakos, T., & Popović, L. Č. (2012). 3D radiative transfer modelling of the dusty tori around active galactic nuclei as a clumpy two-phase medium. *MNRAS*, 420, 2756–2772. ADS: 2012MNRAS.420.2756S. doi: 10.1111/j.1365-2966.2011.19775.x.

Stalevski, M., Ricci, C., Ueda, Y., Lira, P., Fritz, J., & Baes, M. (2016). The dust covering factor in active galactic nuclei. *MNRAS*, 458, 2288–2302. ADS: 2016MNRAS.458.2288S. doi: 10.1093/mnras/stw444.

Stern, D., Djorgovski, S. G., Perley, R. A., de Carvalho, R. R., & Wall, J. V. (2000). Radio Properties of Z>4 Optically Selected Quasars. *AJ*, 119, 1526–1533. ADS: 2000AJ....119.1526S. doi: 10.1086/301316.

Stocke, J. T., Morris, S. L., Weymann, R. J., & Foltz, C. B. (1992). The radio properties of the broad-absorption-line QSOs. *ApJ*, 396, 487–503. ADS: 1992ApJ...396..487S. doi: 10.1086/171735.

Storchi-Bergmann, T., Baldwin, J. A., & Wilson, A. S. (1993). Double-peaked broad line emission from the LINER nucleus of NGC 1097. *ApJ*, 410, L11–L14. ADS: 1993ApJ...410L..11S. doi: 10.1086/186867.

Storchi-Bergmann, T., Nemmen da Silva, R., Eracleous, M., Halpern, J. P., Wilson, A. S., Filippenko, A. V., Ruiz, M. T., Smith, R. C., & Nagar, N. M. (2003). Evolution of the Nuclear Accretion Disk Emission in NGC 1097: Getting Closer to the Black Hole. *ApJ*, 598, 956–968. ADS: 2003ApJ...598..956S. doi: 10.1086/378938.

Strateva, I. V., Strauss, M. A., Hao, L., Schlegel, D. J., Hall, P. B., Gunn, J. E., Li, L.-X., Ivezić, Ž., Richards, G. T., Zakamska, N. L., Voges, W., Anderson, S. F., Lupton, R. H., Schneider, D. P., Brinkmann, J., & Nichol, R. C. (2003). Double-peaked Low-Ionization Emission Lines in Active Galactic Nuclei. *AJ*, 126, 1720–1749. ADS: 2003AJ....126.1720S. doi: 10.1086/378367.

Strittmatter, P. A., Hill, P., Pauliny-Toth, I. I. K., Steppe, H., & Witzel, A. (1980). Radio observations of optically selected quasars. *A&A*, 88, L12–L15. ADS: 1980A&A....88L..12S.

Sturm, E., Schweitzer, M., Lutz, D., Contursi, A., Genzel, R., Lehnert, M. D., Tacconi, L. J., Veilleux, S., Rupke, D. S., Kim, D.-C., Sternberg, A., Maoz, D., Lord, S., Mazzarella, J., & Sanders, D. B. (2005). Silicate Emissions in Active Galaxies: From LINERs to QSOs. *ApJ*, 629, L21–L23. ADS: 2005ApJ...629L..21S. doi: 10.1086/444359.

Suganuma, M., Yoshii, Y., Kobayashi, Y., Minezaki, T., Enya, K., Tomita, H., Aoki, T., Koshida, S., & Peterson, B. A. (2006). Reverberation Measurements of the Inner Radius of the Dust Torus in Nearby Seyfert 1 Galaxies. *ApJ*, 639, 46–63. ADS: 2006ApJ...639...46S. doi: 10.1086/499326.

Sulentic, J., Marziani, P., & Zamfir, S. (2011). The Case for Two Quasar Populations. *Baltic Astronomy*, 20, 427–434. ADS: 2011BaltA..20..427S. doi: 10.1515/astro-2017-0314.

Sulentic, J. W., Bachev, R., Marziani, P., Negrete, C. A., & Dultzin, D. (2007). C IV λ1549 as an Eigenvector 1 Parameter for Active Galactic Nuclei. *ApJ*, 666, 757–777. ADS: 2007ApJ...

666..757S. doi: 10.1086/519916.

Sulentic, J. W., Marziani, P., & Dultzin-Hacyan, D. (2000). Phenomenology of Broad Emission Lines in Active Galactic Nuclei. *ARA&A*, 38, 521–571. ADS: 2000ARA&A..38..521S. doi: 10.1146/annurev.astro.38.1.521.

Sulentic, J. W., Marziani, P., Zamfir, S., & Meadows, Z. A. (2012). No Evidence for a Systematic Fe II Emission Line Redshift in Type 1 Active Galactic Nuclei. *ApJ*, 752, L7. ADS: 2012ApJ...752L...7S. doi: 10.1088/2041-8205/752/1/L7.

Sulentic, J. W., Zamfir, S., Marziani, P., Bachev, R., Calvani, M., & Dultzin-Hacyan, D. (2003). Radio-loud Active Galactic Nuclei in the Context of the Eigenvector 1 Parameter Space. *ApJ*, 597, L17–L20. ADS: 2003ApJ...597L..17S. doi: 10.1086/379754.

Sundqvist, J. O., Owocki, S. P., & Puls, J. (2012). The Nature and Consequences of Clumping in Hot, Massive Star Winds. In L. Drissen, C. Robert, N. St-Louis, & A. F. J. Moffat (Eds.), *Proceedings of a Scientific Meeting in Honor of Anthony F. J. Moffat*, volume 465 of *Astronomical Society of the Pacific Conference Series* (pp. 119). ADS: 2012ASPC..465..119S. arXiv: 1110.0485.

Tadhunter, C. & Tsvetanov, Z. (1989). Anisotropic ionizing radiation in NGC5252. *Nature*, 341, 422–424. ADS: 1989Natur.341..422T. doi: 10.1038/341422a0.

Tang, B., Shang, Z., Gu, Q., Brotherton, M. S., & Runnoe, J. C. (2012). The Optical and Ultraviolet Emission-line Properties of Bright Quasars with Detailed Spectral Energy Distributions. *ApJS*, 201, 38. ADS: 2012ApJS..201...38T. doi: 10.1088/0067-0049/201/2/38.

Tasse, C., Best, P. N., Röttgering, H., & Le Borgne, D. (2008). Radio-loud AGN in the XMM-LSS field. II. A dichotomy in environment and accretion mode? *A&A*, 490, 893–904. ADS: 2008A&A...490..893T. doi: 10.1051/0004-6361:20079299.

Teng, S. H., Mushotzky, R. F., Sambruna, R. M., Davis, D. S., & Reynolds, C. S. (2011). Fermi/LAT Observations of Swift/BAT Seyfert Galaxies: On the Contribution of Radio-quiet Active Galactic Nuclei to the Extragalactic γ-Ray Background. *ApJ*, 742, 66. ADS: 2011ApJ...742...66T. doi: 10.1088/0004-637X/742/2/66.

Tohline, J. E. & Osterbrock, D. E. (1976). Variation of the spectrum of the Seyfert galaxy NGC 7603. *ApJ*, 210, L117–L120. ADS: 1976ApJ...210L.117T. doi: 10.1086/182317.

Tombesi, F., Cappi, M., Reeves, J. N., Nemmen, R. S., Braito, V., Gaspari, M., & Reynolds, C. S. (2013). Unification of X-ray winds in Seyfert galaxies: from ultra-fast outflows to warm absorbers. *MNRAS*, 430, 1102–1117. ADS: 2013MNRAS.430.1102T. doi: 10.1093/mnras/sts692.

Trakhtenbrot, B. (2014). The Most Massive Active Black Holes at z ˜ 1.5-3.5 have High Spins and Radiative Efficiencies. *ApJ*, 789, L9. ADS: 2014ApJ...789L...9T. doi: 10.1088/2041-8205/789/1/L9.

Trakhtenbrot, B. & Netzer, H. (2012). Black hole growth to z = 2 - I. Improved virial methods for measuring M_{BH} and L/L_{Edd}. *MNRAS*, 427, 3081–3102. ADS: 2012MNRAS.427.3081T.

doi: 10.1111/j.1365-2966.2012.22056.x.

Tran, H. D. (1995). The Nature of Seyfert 2 Galaxies with Obscured Broad-Line Regions. I. Observations. *ApJ*, 440, 565. ADS: 1995ApJ...440..565T. doi: 10.1086/175296.

Tran, H. D. (2001). Hidden Broad-Line Seyfert 2 Galaxies in the CFA and 12 μM Samples. *ApJ*, 554, L19–L23. ADS: 2001ApJ...554L..19T. doi: 10.1086/320926.

Tran, H. D. (2003). The Unified Model and Evolution of Active Galaxies: Implications from a Spectropolarimetric Study. *ApJ*, 583, 632–648. ADS: 2003ApJ...583..632T. doi: 10.1086/345473.

Tran, H. D., Miller, J. S., & Kay, L. E. (1992). Detection of obscured broad-line regions in four Seyfert 2 galaxies. *ApJ*, 397, 452–456. ADS: 1992ApJ...397..452T. doi: 10.1086/171801.

Tremaine, S. & Davis, S. W. (2014). Dynamics of warped accretion discs. *MNRAS*, 441(2), 1408–1434. ADS: 2014MNRAS.441.1408T. doi: 10.1093/mnras/stu663.

Tristram, K. R. W., Meisenheimer, K., Jaffe, W., Schartmann, M., Rix, H.-W., Leinert, C., Morel, S., Wittkowski, M., Röttgering, H., Perrin, G., Lopez, B., Raban, D., Cotton, W. D., Graser, U., Paresce, F., & Henning, T. (2007). Resolving the complex structure of the dust torus in the active nucleus of the Circinus galaxy. *A&A*, 474, 837–850. ADS: 2007A&A...474..837T. doi: 10.1051/0004-6361:20078369.

Trump, J. R., Hall, P. B., Reichard, T. A., Richards, G. T., Schneider, D. P., Vanden Berk, D. E., Knapp, G. R., Anderson, S. F., Fan, X., Brinkman, J., Kleinman, S. J., & Nitta, A. (2006). A Catalog of Broad Absorption Line Quasars from the Sloan Digital Sky Survey Third Data Release. *ApJS*, 165, 1–18. ADS: 2006ApJS..165....1T. doi: 10.1086/503834.

Trump, J. R., Impey, C. D., Kelly, B. C., Civano, F., Gabor, J. M., Diamond-Stanic, A. M., Merloni, A., Urry, C. M., Hao, H., Jahnke, K., Nagao, T., Taniguchi, Y., Koekemoer, A. M., Lanzuisi, G., Liu, C., Mainieri, V., Salvato, M., & Scoville, N. Z. (2011). Accretion Rate and the Physical Nature of Unobscured Active Galaxies. *ApJ*, 733, 60. ADS: 2011ApJ...733...60T. doi: 10.1088/0004-637X/733/1/60.

Tukey, J. W. (1977). *Exploratory data analysis*. ADS: 1977eda..book.....T.

Turnshek, D. A. (1984). Properties of the broad absorption-line QSOs. *ApJ*, 280, 51–65. ADS: 1984ApJ...280...51T. doi: 10.1086/161967.

Turnshek, D. A., Espey, B. R., Kopko, Jr., M., Rauch, M., Weymann, R. J., Jannuzi, B. T., Boksenberg, A., Bergeron, J., Hartig, G. F., Sargent, W. L. W., Savage, B. D., Schneider, D. P., & Wolfe, A. M. (1994). The HST quasar absorption line key project. 4: HST faint-object spectrograph and ground-based observations of the unusual low-redshift broad absorption-line quasi-stellar object PG 0043+039. *ApJ*, 428, 93–112. ADS: 1994ApJ...428...93T. doi: 10.1086/174223.

Turnshek, D. A., Kopko, Jr., M., Monier, E., Noll, D., Espey, B. R., & Weymann, R. J. (1996). Far-Ultraviolet Spectra of Broad Absorption Line QSOs and Constraints on Models for the Ionization Structure and Metallicity of the BAL-Region Gas. *ApJ*, 463, 110. ADS: 1996ApJ...463..110T. doi: 10.1086/177227.

Turriziani, S., Cavazzuti, E., & Giommi, P. (2007). ROXA: a new multi-frequency large sample of blazars selected with SDSS and 2dF optical spectroscopy. *A&A*, 472, 699–704. ADS: 2007A&A...472..699T. doi: 10.1051/0004-6361:20077114.

Tytler, D. & Fan, X.-M. (1992). Systematic QSO emission-line velocity shifts and new unbiased redshifts. *ApJS*, 79, 1–36. ADS: 1992ApJS...79....1T. doi: 10.1086/191642.

Ulrich, M.-H. & Horne, K. (1996). A month in the life of NGC 4151: velocity-delay maps of the broad-line region. *MNRAS*, 283, 748–758. ADS: 1996MNRAS.283..748U. doi: 10.1093/mnras/283.3.748.

Urry, C. M. & Padovani, P. (1995). Unified Schemes for Radio-Loud Active Galactic Nuclei. *PASP*, 107, 803. ADS: 1995PASP..107..803U. doi: 10.1086/133630.

Ustyugova, G. V., Koldoba, A. V., Romanova, M. M., Chechetkin, V. M., & Lovelace, R. V. E. (1999). Magnetocentrifugally Driven Winds: Comparison of MHD Simulations with Theory. *ApJ*, 516, 221–235. ADS: 1999ApJ...516..221U. doi: 10.1086/307093.

van der Walt, S., Colbert, S. C., & Varoquaux, G. (2011). The numpy array: A structure for efficient numerical computation. *Computing in Science & Engineering*, 13(2), 22–30. doi: 10.1109/MCSE.2011.37.

Van Gorkom, K. J., Wardle, J. F. C., Rauch, A. P., & Gobeille, D. B. (2015). Comparing different indicators of quasar orientation. *MNRAS*, 450, 4240–4247. ADS: 2015MNRAS.450.4240V. doi: 10.1093/mnras/stv912.

Vanden Berk, D. E., Richards, G. T., Bauer, A., Strauss, M. A., Schneider, D. P., Heckman, T. M., York, D. G., Hall, P. B., Fan, X., Knapp, G. R., Anderson, S. F., Annis, J., Bahcall, N. A., Bernardi, M., Briggs, J. W., Brinkmann, J., Brunner, R., Burles, S., Carey, L., Castander, F. J., Connolly, A. J., Crocker, J. H., Csabai, I., Doi, M., Finkbeiner, D., Friedman, S., Frieman, J. A., Fukugita, M., Gunn, J. E., Hennessy, G. S., Ivezić, Ž., Kent, S., Kunszt, P. Z., Lamb, D. Q., Leger, R. F., Long, D. C., Loveday, J., Lupton, R. H., Meiksin, A., Merelli, A., Munn, J. A., Newberg, H. J., Newcomb, M., Nichol, R. C., Owen, R., Pier, J. R., Pope, A., Rockosi, C. M., Schlegel, D. J., Siegmund, W. A., Smee, S., Snir, Y., Stoughton, C., Stubbs, C., SubbaRao, M., Szalay, A. S., Szokoly, G. P., Tremonti, C., Uomoto, A., Waddell, P., Yanny, B., & Zheng, W. (2001). Composite Quasar Spectra from the Sloan Digital Sky Survey. *AJ*, 122, 549–564. ADS: 2001AJ....122..549V. doi: 10.1086/321167.

Veilleux, S. & Zheng, W. (1991). Unique broad-line profile variations in the radio galaxy 3C 390.3. *ApJ*, 377, 89–99. ADS: 1991ApJ...377...89V. doi: 10.1086/170338.

Vestergaard, M. (2002). Determining Central Black Hole Masses in Distant Active Galaxies. *ApJ*, 571, 733–752. ADS: 2002ApJ...571..733V. doi: 10.1086/340045.

Vestergaard, M., Fan, X., Tremonti, C. A., Osmer, P. S., & Richards, G. T. (2008). Mass Functions of the Active Black Holes in Distant Quasars from the Sloan Digital Sky Survey Data Release 3. *ApJ*, 674, L1–L4. ADS: 2008ApJ...674L...1V. doi: 10.1086/528981.

Vestergaard, M. & Osmer, P. S. (2009). Mass Functions of the Active Black Holes in Distant Quasars from the Large Bright Quasar Survey, the Bright Quasar Survey, and the Color-

selected Sample of the SDSS Fall Equatorial Stripe. *ApJ*, 699, 800–816. ADS: 2009ApJ...699..800V. doi: 10.1088/0004-637X/699/1/800.

Vestergaard, M. & Peterson, B. M. (2006). Determining Central Black Hole Masses in Distant Active Galaxies and Quasars. II. Improved Optical and UV Scaling Relationships. *ApJ*, 641, 689–709. ADS: 2006ApJ...641..689V. doi: 10.1086/500572.

Vestergaard, M., Wilkes, B. J., & Barthel, P. D. (2000). Clues to Quasar Broad-Line Region Geometry and Kinematics. *ApJ*, 538, L103–L106. ADS: 2000ApJ...538L.103V. doi: 10.1086/312805.

Voit, G. M., Weymann, R. J., & Korista, K. T. (1993). Low-ionization broad absorption lines in quasars. *ApJ*, 413, 95–109. ADS: 1993ApJ...413...95V. doi: 10.1086/172980.

Wandel, A., Peterson, B. M., & Malkan, M. A. (1999). Central Masses and Broad-Line Region Sizes of Active Galactic Nuclei. I. Comparing the Photoionization and Reverberation Techniques. *ApJ*, 526, 579–591. ADS: 1999ApJ...526..579W. doi: 10.1086/308017.

Wanders, I., Goad, M. R., Korista, K. T., Peterson, B. M., Horne, K., Ferland, G. J., Koratkar, A. P., Pogge, R. W., & Shields, J. C. (1995). The Geometry and Kinematics of the Broad-Line Region in NGC 5548 from HST and IUE Observations. *ApJ*, 453, L87. ADS: 1995ApJ...453L..87W. doi: 10.1086/309750.

Wang, J.-G., Dong, X.-B., Wang, T.-G., Ho, L. C., Yuan, W., Wang, H., Zhang, K., Zhang, S., & Zhou, H. (2009). Estimating Black Hole Masses in Active Galactic Nuclei Using the Mg II λ2800 Emission Line. *ApJ*, 707, 1334–1346. ADS: 2009ApJ...707.1334W. doi: 10.1088/0004-637X/707/2/1334.

Wang, T., Brinkmann, W., & Bergeron, J. (1996). X-ray properties of active galactic nuclei with optical FeII emission. *A&A*, 309, 81–96. ADS: 1996A&A...309...81W.

Wardle, J. F. C. & Aaron, S. E. (1997). How fast are the large-scale jets in quasars? Constraints on both Doppler beaming and intrinsic asymmetries. *MNRAS*, 286, 425–435. ADS: 1997MNRAS.286..425W. doi: 10.1093/mnras/286.2.425.

Warner, C., Hamann, F., & Dietrich, M. (2003). A Relation between Supermassive Black Hole Mass and Quasar Metallicity? *ApJ*, 596, 72–84. ADS: 2003ApJ...596...72W. doi: 10.1086/377710.

Waters, T., Kashi, A., Proga, D., Eracleous, M., Barth, A. J., & Greene, J. (2016). Reverberation Mapping of the Broad Line Region: Application to a Hydrodynamical Line-driven Disk Wind Solution. *ApJ*, 827, 53. ADS: 2016ApJ...827...53W. doi: 10.3847/0004-637X/827/1/53.

Weymann, R. J., Morris, S. L., Foltz, C. B., & Hewett, P. C. (1991). Comparisons of the emission-line and continuum properties of broad absorption line and normal quasi-stellar objects. *ApJ*, 373, 23–53. ADS: 1991ApJ...373...23W. doi: 10.1086/170020.

Weymann, R. J., Scott, J. S., Schiano, A. V. R., & Christiansen, W. A. (1982). A thermal wind model for the broad emission line region of quasars. *ApJ*, 262, 497–510. ADS: 1982ApJ...262..497W. doi: 10.1086/160443.

Weymann, R. J., Williams, R. E., Peterson, B. M., & Turnshek, D. A. (1979). Results of a homogeneous survey of absorption lines in QSOs of small and intermediate emission redshift. *ApJ*, 234, 33–46. ADS: 1979ApJ...234...33W. doi: 10.1086/157470.

White, R. L., Becker, R. H., Helfand, D. J., & Gregg, M. D. (1997). A Catalog of 1.4 GHz Radio Sources from the FIRST Survey. *ApJ*, 475, 479–493. ADS: 1997ApJ...475..479W. doi: 10.1086/303564.

Whittle, M. (1992). Virial and jet-induced velocities in Seyfert galaxies. I - A compilation of narrow line region and host galaxy properties. *ApJS*, 79, 49–75. ADS: 1992ApJS...79...49W. doi: 10.1086/191644.

Wilhite, B. C., Brunner, R. J., Schneider, D. P., & Vanden Berk, D. E. (2007). The Effect of Variability on the Estimation of Quasar Black Hole Masses. *ApJ*, 669, 791–800. ADS: 2007ApJ...669..791W. doi: 10.1086/521713.

Wilkes, B. J. (1986). Studies of broad emission line profiles in QSOs. II - Properties of a large, predominantly radio selected sample. *MNRAS*, 218, 331–361. ADS: 1986MNRAS.218..331W. doi: 10.1093/mnras/218.2.331.

Wilkes, B. J., Kuraszkiewicz, J., Haas, M., Barthel, P., Leipski, C., Willner, S. P., Worrall, D. M., Birkinshaw, M., Antonucci, R., Ashby, M. L. N., Chini, R., Fazio, G. G., Lawrence, C., Ogle, P., & Schulz, B. (2013). Revealing the Heavily Obscured Active Galactic Nucleus Population of High-redshift 3CRR Sources with Chandra X-Ray Observations. *ApJ*, 773, 15. ADS: 2013ApJ...773...15W. doi: 10.1088/0004-637X/773/1/15.

Willott, C. J., Albert, L., Arzoumanian, D., Bergeron, J., Crampton, D., Delorme, P., Hutchings, J. B., Omont, A., Reylé, C., & Schade, D. (2010). Eddington-limited Accretion and the Black Hole Mass Function at Redshift 6. *AJ*, 140, 546–560. ADS: 2010AJ....140..546W. doi: 10.1088/0004-6256/140/2/546.

Willott, C. J., Rawlings, S., Blundell, K. M., & Lacy, M. (1999). The emission line-radio correlation for radio sources using the 7C Redshift Survey. *MNRAS*, 309, 1017–1033. ADS: 1999MNRAS.309.1017W. doi: 10.1046/j.1365-8711.1999.02907.x.

Willott, C. J., Rawlings, S., Blundell, K. M., & Lacy, M. (2000). The quasar fraction in low-frequency-selected complete samples and implications for unified schemes. *MNRAS*, 316, 449–458. ADS: 2000MNRAS.316..449W. doi: 10.1046/j.1365-8711.2000.03447.x.

Willott, C. J., Rawlings, S., & Grimes, J. A. (2003). The Submillimeter Properties of Broad Absorption Line Quasars. *ApJ*, 598, 909–915. ADS: 2003ApJ...598..909W. doi: 10.1086/379066.

Wills, B. J. & Brotherton, M. S. (1995). An Improved Measure of Quasar Orientation. *ApJ*, 448, L81. ADS: 1995ApJ...448L..81W. doi: 10.1086/309614.

Wills, B. J., Brotherton, M. S., Fang, D., Steidel, C. C., & Sargent, W. L. W. (1993). Statistics of QSO Broad Emission-Line Profiles. I. The C IV lambda 1549 Line and the lambda 1400 Feature. *ApJ*, 415, 563. ADS: 1993ApJ...415..563W. doi: 10.1086/173186.

Wills, B. J. & Browne, I. W. A. (1986). Relativistic beaming and quasar emission lines. *ApJ*,

302, 56–63. ADS: 1986ApJ...302...56W. doi: 10.1086/163973.

Wilson, A. S. & Tsvetanov, Z. I. (1994). Ionization cones and radio ejecta in active galaxies. *AJ*, 107, 1227–1234. ADS: 1994AJ....107.1227W. doi: 10.1086/116935.

Winkler, H. (1992). Variability studies of Seyfert galaxies. II - Spectroscopy. *MNRAS*, 257, 677–688. ADS: 1992MNRAS.257..677W. doi: 10.1093/mnras/257.4.677.

Wolpert, D. H. (1996). The lack of a priori distinctions between learning algorithms. *Neural Computation*, 8(7), 1341–1390. doi: 10.1162/neco.1996.8.7.1341.

Wolpert, D. H. & Macready, W. G. (1997). No free lunch theorems for optimization. *IEEE transactions on evolutionary computation*, 1(1), 67–82.

Woo, J.-H., Le, H. A. N., Karouzos, M., Park, D., Park, D., Malkan, M. A., Treu, T., & Bennert, V. N. (2018). Calibration and Limitations of the Mg II Line-based Black Hole Masses. *ApJ*, 859(2), 138. ADS: 2018ApJ...859..138W. doi: 10.3847/1538-4357/aabf3e.

Woo, J.-H., Schulze, A., Park, D., Kang, W.-R., Kim, S. C., & Riechers, D. A. (2013). Do Quiescent and Active Galaxies Have Different M $_{BH}$-σ_* Relations? *ApJ*, 772, 49. ADS: 2013ApJ...772...49W. doi: 10.1088/0004-637X/772/1/49.

Woo, J.-H., Treu, T., Barth, A. J., Wright, S. A., Walsh, J. L., Bentz, M. C., Martini, P., Bennert, V. N., Canalizo, G., Filippenko, A. V., Gates, E., Greene, J., Li, W., Malkan, M. A., Stern, D., & Minezaki, T. (2010). The Lick AGN Monitoring Project: The M $_{BH}$-σ_* Relation for Reverberation-mapped Active Galaxies. *ApJ*, 716, 269–280. ADS: 2010ApJ...716..269W. doi: 10.1088/0004-637X/716/1/269.

Woo, J.-H., Yoon, Y., Park, S., Park, D., & Kim, S. C. (2015). The Black Hole Mass-Stellar Velocity Dispersion Relation of Narrow-line Seyfert 1 Galaxies. *ApJ*, 801, 38. ADS: 2015ApJ...801...38W. doi: 10.1088/0004-637X/801/1/38.

Wu, X.-B. & Han, J. L. (2001). Inclinations and Black Hole Masses of Seyfert 1 Galaxies. *ApJ*, 561, L59–L62. ADS: 2001ApJ...561L..59W. doi: 10.1086/324408.

Wu, X.-B., Wang, R., Kong, M. Z., Liu, F. K., & Han, J. L. (2004). Black hole mass estimation using a relation between the BLR size and emission line luminosity of AGN. *A&A*, 424, 793–798. ADS: 2004A&A...424..793W. doi: 10.1051/0004-6361:20035845.

Yong, S. Y., King, A. L., Webster, R. L., Bate, N. F., O'Dowd, M. J., & Labrie, K. (2018). Using the Properties of Broad Absorption Line Quasars to Illuminate Quasar Structure. *MNRAS*, 479, 4153–4171. ADS: 2018MNRAS.479.4153Y. doi: 10.1093/mnras/sty1540.

Yong, S. Y. & Webster, R. L. (2019). Black hole mass estimation: Modelling the biases. In *2019 6th International Conference on Space Science and Communication (IconSpace)* (pp. 139–143). doi: 10.1109/IconSpace.2019.8905923.

Yong, S. Y., Webster, R. L., & King, A. L. (2016). Black Hole Mass Estimation: How Good is the Virial Estimate? *PASA*, 33, e009. ADS: 2016PASA...33....9Y. doi: 10.1017/pasa.2016.8.

Yong, S. Y., Webster, R. L., King, A. L., Bate, N. F., Labrie, K., & O'Dowd, M. J. (2020). Determining quasar orientation. *MNRAS*, 491(1), 1320–1334. ADS: 2020MNRAS.491.1320Y.

doi: 10.1093/mnras/stz3074.

Yong, S. Y., Webster, R. L., King, A. L., Bate, N. F., O'Dowd, M. J., & Labrie, K. (2017). The Kinematics of Quasar Broad Emission Line Regions Using a Disk-Wind Model. *PASA*, 34, e042. ADS: 2017PASA...34...42Y. doi: 10.1017/pasa.2017.37.

Young, P. & Schneider, D. P. (1980). Emission line eclipse phenomena in nova DQ Herculis /1934/. *ApJ*, 238, 955–963. ADS: 1980ApJ...238..955Y. doi: 10.1086/158060.

Young, S., Axon, D. J., Robinson, A., Hough, J. H., & Smith, J. E. (2007). The rotating wind of the quasar PG 1700+518. *Nature*, 450, 74–76. ADS: 2007Natur.450...74Y. doi: 10.1038/nature06319.

Young, S., Hough, J. H., Efstathiou, A., Wills, B. J., Bailey, J. A., Ward, M. J., & Axon, D. J. (1996). Polarimetry and modelling of narrow-line active galaxies. *MNRAS*, 281, 1206–1242. ADS: 1996MNRAS.281.1206Y. doi: 10.1093/mnras/281.4.1206.

Zakamska, N. L., Schmidt, G. D., Smith, P. S., Strauss, M. A., Krolik, J. H., Hall, P. B., Richards, G. T., Schneider, D. P., Brinkmann, J., & Szokoly, G. P. (2005). Candidate Type II Quasars from the Sloan Digital Sky Survey. III. Spectropolarimetry Reveals Hidden Type I Nuclei. *AJ*, 129, 1212–1224. ADS: 2005AJ....129.1212Z. doi: 10.1086/427543.

Zakamska, N. L., Strauss, M. A., Krolik, J. H., Collinge, M. J., Hall, P. B., Hao, L., Heckman, T. M., Ivezić, Ž., Richards, G. T., Schlegel, D. J., Schneider, D. P., Strateva, I., Vanden Berk, D. E., Anderson, S. F., & Brinkmann, J. (2003). Candidate Type II Quasars from the Sloan Digital Sky Survey. I. Selection and Optical Properties of a Sample at 0.3<Z<0.83. *AJ*, 126, 2125–2144. ADS: 2003AJ....126.2125Z. doi: 10.1086/378610.

Zamfir, S., Sulentic, J. W., & Marziani, P. (2008). New insights on the QSO radio-loud/radio-quiet dichotomy: SDSS spectra in the context of the 4D eigenvector1 parameter space. *MNRAS*, 387, 856–870. ADS: 2008MNRAS.387..856Z. doi: 10.1111/j.1365-2966.2008.13290.x.

Zamfir, S., Sulentic, J. W., Marziani, P., & Dultzin, D. (2010). Detailed characterization of Hβ emission line profile in low-z SDSS quasars. *MNRAS*, 403, 1759–1786. ADS: 2010MNRAS.403.1759Z. doi: 10.1111/j.1365-2966.2009.16236.x.

Zhang, S., Wang, T.-G., Wang, H., Zhou, H., Dong, X.-B., & Wang, J.-G. (2010). Low-z Mg II Broad Absorption-line Quasars from the Sloan Digital Sky Survey. *ApJ*, 714, 367–383. ADS: 2010ApJ...714..367Z. doi: 10.1088/0004-637X/714/1/367.

Zhang, T.-Z. & Wu, X.-B. (2002). Inclination of Broad Line Region in Narrow Line and Broad Line Seyfert 1 Galaxies. *ChJAA*, 2, 487–500. ADS: 2002ChJAA...2..487Z. doi: 10.1088/1009-9271/2/6/487.

Zheng, W. & Malkan, M. A. (1993). Does a Luminosity-dependent Continuum Shape Cause the Baldwin Effect? *ApJ*, 415, 517. ADS: 1993ApJ...415..517Z. doi: 10.1086/173182.

Zheng, W., Sulentic, J. W., & Binette, L. (1990). A double-stream model for line profiles. *ApJ*, 365, 115–118. ADS: 1990ApJ...365..115Z. doi: 10.1086/169462.

Zhou, H., Wang, T., Wang, H., Wang, J., Yuan, W., & Lu, Y. (2006). Polar Outflows in

Six Broad Absorption Line Quasars. *ApJ*, 639, 716–723. ADS: 2006ApJ...639..716Z. doi: 10.1086/499768.